



# **Use of Serial Block Face-Scanning Electron Microscopy to Study the Ultrastructure of Vertebrate and Invertebrate Biology**

**Erin Twynham Cocks**

**BSc (Hons), MSc**

This thesis is submitted for the degree of Doctor of Philosophy at  
Newcastle University

Institute of Genetic Medicine

April 2021





## **Abstract**

The development of Serial Block Face Scanning Electron Microscopy (SBF-SEM) allows for acquisition of serially sectioned, imaged data of ultrastructure at high resolution. In this project, optimisation of both SBF-SEM methodology and 3-D image segmentation analysis was applied to the ultrastructural examination of two types of biological tissues, each requiring a different experimental approach. The first project was a connectomic based study, to determine the relationship between the neurons that synapse upon the Lobula Giant Movement Detector 2 (LGMD 2) neuron, within the optic lobe of the locust. A substantial portion of the LGMD 2 neuron was reconstructed along with the afferent neurons, enabling the discovery of retinotopic mapping from the photoreceptors of the eye onto the LGMD 2 neuron. A sub-class of afferent neurons was also found, most likely vital in the process of signal integration across the large LGMD 2 neuron. For the second project, two types of skeletal muscle (psoas and soleus) obtained from fetal and adult guinea pigs were analysed to assess tissue-specific changes in mitochondrial morphology with muscle maturation. Distinct mitochondrial shapes were found across both muscles and age groups and a classification system was developed. It was found that, in both muscles, by late fetal gestation the mitochondrial network is well developed and akin to that found in the adult. Quantitative and qualitative differences in mitochondria morphology and complexity were found between the two muscles in the adult group. These differences are likely to be related to functional specialisation. All data collected during the experiments have also been made available online on Zenodo, roughly 240GB, which can be used for further studies. Overall SBF-SEM was proven to be a robust method of gaining new insights into the ultrastructure in both models and has wide ranging capabilities for a variety of experimental objectives.

## **Declaration**

I declare that this thesis is my own work, unless otherwise stated, and has not been submitted in any form for another degree at this or any other university. Information from published and unpublished work of others has been acknowledged in the text and references given.

## **Acknowledgements**

Firstly, I would like to thank all of my supervisors, Professor Michael Taggart, Dr Claire Rind, and Dr Kathryn White for their guidance and help throughout my PhD. In particular to Dr Kathryn White who has kept the balance (peace) between the two halves of my PhD.

Thanks to everyone in the EM research services here at Newcastle. To Tracey Davey who trained me in all things EM, always willing to fight in my corner and has made me laugh every day. To Ross Laws who I could always go to for any questions relating to analysis and would always help figure out a solution (not always the simplest). Also, for finally dragging me along to climbing, forcing me to take time off my work, and will miss our random discussions, from politics to funny animal videos.

Would like to thank everyone at Newcastle hockey club for welcoming me to the North East. I have always looked forward to the Wednesday night training sessions and weekend matches. While playing and coaching hockey I was able to forget the stresses of my PhD and have fun. I have enjoyed my time at the club and have made some great memories and friends for life.

Finally, to all my friends and family that have supported me throughout all of my studies so far. To Rose who was always a willing to listen to my complaints and was always ready to go on holiday. To my Father who always came and visited and provided food (pick 'n' mix) to keep me going. Lastly to my Mother, who has encouraged me every step of the way throughout all of my studies and adventures, no matter how crazy they were.

## Table of Contents

<b>ABSTRACT .....</b>	<b>I</b>
<b>DECLARATION.....</b>	<b>II</b>
<b>ACKNOWLEDGEMENTS .....</b>	<b>III</b>
<b>TABLE OF CONTENTS .....</b>	<b>IV</b>
<b>ABBREVIATIONS .....</b>	<b>1</b>
<b>FIGURES AND TABLES.....</b>	<b>2</b>
Figures .....	2
Tables .....	7
<b>CHAPTER 1. INTRODUCTION.....</b>	<b>8</b>
<b>1.1. Electron Microscopy .....</b>	<b>8</b>
1.1.1. Development of Electron Microscopy and 3D-Electron Microscopy .....	8
1.1.2. Serial Block Face-Scanning Electron Microscopy .....	14
<b>1.2. Locust Visual System .....</b>	<b>23</b>
1.2.1. Choice of experimental animal rationale (Locust).....	31
1.2.2. Hypothesis/Aims .....	32
<b>1.3. Skeletal Muscle.....</b>	<b>33</b>
1.3.1. Structure and Function .....	33
1.3.2. Skeletal Muscle Development .....	39
1.3.3. Nucleus.....	41
1.3.4. Mitochondria .....	42
1.3.5. Choice of experimental animal rationale (Guinea pig).....	45
1.3.6. Hypothesis/Aims .....	46

<b>CHAPTER 2. METHODS .....</b>	<b>47</b>
<b>2.1. Staining Protocol and Pin Preparation.....</b>	<b>47</b>
2.1.1. Locust Optic Lobe.....	47
2.1.2. Guinea Pig Skeletal Muscle.....	49
<b>2.2. Imaging Parameters Refinement .....</b>	<b>52</b>
2.2.1. Locust Optic Lobe Parameters .....	58
2.2.2. Muscle Parameters.....	60
<b>2.3. Optimisation of Image Analysis.....</b>	<b>61</b>
2.3.1. Software Comparison .....	62
2.3.2. Segmentation Workflow.....	65
2.3.3. Validation of Workflow .....	76
<b>2.4. Segmentation, Reconstruction and Analysis of Locust Optic Lobe .....</b>	<b>82</b>
2.4.1. Identification of LGMD 2 neuron.....	82
2.4.2. Identification of Synapses.....	84
2.4.3. Segmentation and Reconstruction.....	86
2.4.4. Statistical Analysis .....	92
<b>2.5. Optimised Procedure for Segmentation, Reconstruction and Analysis of Guinea Pig Skeletal Muscle.....</b>	<b>93</b>
2.5.1. Identification of skeletal muscle cell components.....	93
2.5.2. Segmentation and Reconstruction of nuclei .....	96
2.5.3. Segmentation and Reconstruction of mitochondrial network.....	98
2.5.4. Segmentation and reconstruction of individual mitochondria .....	102
2.5.5. Statistical Analysis .....	104
<b>CHAPTER 3. RESULTS .....</b>	<b>111</b>
<b>3.1. Locust Results.....</b>	<b>111</b>
3.1.1. Reconstructions .....	111
3.1.2. Synapse Distribution Across the LGMD 2 Neuron Branch .....	113
3.1.3. Connectivity in Z Direction .....	116
3.1.4. Connectivity in X and Y Direction .....	130
3.1.5. Summary .....	140

<b>3.2. Muscle Results .....</b>	<b>141</b>
3.2.1. Reconstructions .....	141
3.2.2. Mitochondrial Network Analysis .....	142
3.2.3. Individual Mitochondria Analysis.....	156
3.2.4. Nuclei Analysis .....	173
3.2.5. Summary .....	178
 <b>CHAPTER 4. DISCUSSION .....</b>	 <b>179</b>
<b>4.1. Locust.....</b>	<b>180</b>
4.1.1. Summary .....	180
4.1.2. Synaptic Density .....	182
4.1.3. The TmA Neuron Network .....	183
4.1.4. Conclusion .....	189
4.1.5. Future Work .....	190
 <b>4.2. Skeletal Muscle.....</b>	 <b>192</b>
4.2.1. Summary .....	192
4.2.2. Mitochondrial Volume, Surface Area and Location.....	193
4.2.3. Branching and Shape analysis of mitochondria.....	195
4.2.4. Nuclei Analysis .....	202
4.2.5. Conclusion .....	204
4.2.6. Future Work .....	205
 <b>4.3. Consideration of the utility of SBF-SEM for the study of neuron and skeletal muscle biology .....</b>	 <b>207</b>
4.3.1. Summary .....	207
4.3.2. 3D-Electron Microscopy (Microscopy) .....	208
4.3.3. Analysis .....	209
4.3.4. Conclusion and Future Work .....	211
 <b>CHAPTER 5. REFERENCES.....</b>	 <b>213</b>
 <b>APPENDIX .....</b>	 <b>246</b>
 <b>Appendix A – Literature Review. ....</b>	 <b>246</b>

<b>Appendix B – Locust Protocol .....</b>	<b>282</b>
<b>Appendix C – Guinea Pig Protocol .....</b>	<b>284</b>
<b>Appendix D – Chemical List .....</b>	<b>286</b>
<b>Appendix E – Image Analysis Protocol.....</b>	<b>287</b>
1.1 Conversion from DM3 to Tiff.....	287
1.2. Fiji/TrakEM2 Analysis Method .....	288
1.3. Blender Reconstruction .....	289
1.4. Microscopy Image Browser (MIB).....	290
1.5. Amira .....	293
<b>Appendix F – Published Paper.....</b>	<b>295</b>

## **Abbreviations**

EM – Electron Microscopy

TEM – Transmission Electron Microscopy

SEM – Scanning Electron Microscopy

SBF-SEM – Serial Block-Face Scanning Electron Microscopy

FIB-SEM – Focused Ion-Beam Scanning Electron Microscopy

mSEM – Multi-Beam Scanning Electron Microscopy

ssTEM – Serial Section Transmission Electron Microscopy

ssSEM – Serial Section Scanning Electron Microscopy

CLEM – Correlative Light and Electron Microscopy

MIB – Microscopy Image Browser

LMC – Lamina Monopolar Cell

LGMD – Lobula Giant Movement Detector

DCMD – Descending Contralateral Movement Detector

TmA – Trans-Medullary Afferent

OLO – Outer Lobula Region

IMF – Intermyo-fibrillar

SS – Sub-Sarcolemmal

PN – Peri-Nuclear

ROI – Region of Interest



## Figures and Tables

### Figures

Figure 1.1 – Diagram of 3D-EM techniques.....	11
Figure 1.2 – Graph showing number of publications using SBF-SEM per year from 2004-2019.....	19
Figure 1.3 – Graphs showing number of publications divided by sample type and category.....	21
Figure 1.4 – Diagram of Locust eye with pathway from retina to lobula.....	24
Figure 1.5 – Schematic of TmA neuron synapses onto the LGMD 2 neuron in the lobula of the locust.....	27
Figure 1.6 – Diagram of muscle structure.....	34
Figure 1.7 – Schematic of muscle contraction.....	36
Figure 1.8 – Location of psoas and soleus muscles in the rodent.....	38
Figure 1.9 – Schematic of myogenesis during fetal development.....	40
Figure 2.1 – Sample preparation of locust brain for SBF-SEM.....	48
Figure 2.2 – Sample preparation of skeletal muscle for SBF-SEM.....	51
Figure 2.3 – Examples of resin degradation and methods used to overcome.....	53
Figure 2.4 – Impact of pressure on image contrast.....	54
Figure 2.5 – Pixel dwell time alterations and noise.....	55
Figure 2.6 – Relationship between magnification, resolution and image size.....	56
Figure 2.7 – Example of SBF-SEM image series.....	62
Figure 2.8 – Examples of digital reconstruction of nuclear volume.....	66
Figure 2.9 – Analysis of accuracy of interpolation method for segmentation.....	67
Figure 2.10 – Examples of reconstruction of chromatin and nucleoli.....	69
Figure 2.11 – Examples showing the complex morphology of mitochondria.....	71
Figure 2.12 – Examples of reconstructions of the mitochondrial network.....	72
Figure 2.13 – Examples of 3D reconstructions of segmented structures.....	74

Figure 2.14 – Proposed workflow to aid in decision making when choosing appropriate segmentation methods for analysis of SBF-SEM data.....	75
Figure 2.15 – Segmentation and reconstruction of mitochondria from cardiac muscle.....	77
Figure 2.16 – Segmentation and reconstruction of nucleus from cardiac muscle.....	79
Figure 2.17 – Segmentation and reconstruction of the LGMD 2 neuron from the optic lobe of the locust.....	81
Figure 2.18 – Process of finding the region of interest and the LGMD 2 neuron.....	83
Figure 2.19 – Identifying synapses using TEM and SBF-SEM.....	85
Figure 2.20 – Steps of image processing from raw to segmented images.....	87
Figure 2.21 – Segmentation and reconstruction of LGMD 2 neuron branches and TmA neurons.....	89
Figure 2.22 – Analysis of the main and sub-branches of a portion of LGMD 2 neuron.....	90
Figure 2.23 – Reconstructions of incomplete arbors of TmA neurons.....	91
Figure 2.24 – Examples of high resolution TEM images of mitochondria from analysed samples.....	94
Figure 2.25 – Steps of image processing from raw images to segmentations.....	95
Figure 2.26 – Example of segmentation of mitochondria and nuclei from 50 sections.....	97
Figure 2.27 – Labelled single section of intermyofibrillar, subsarcolemmal and perinuclear mitochondria.....	99
Figure 2.28 – Angle measurement of skeletonised mitochondrial network.....	101
Figure 2.29 – Random selection of mitochondria for analysis of individual whole mitochondria.....	103
Figure 3.1 – Overview of reconstructed LGMD 2 branches and TmA neuron segmentations.....	112

Figure 3.2 – Distribution of synapses along larger and smaller branches of a portion of the LGMD 2 neuron.....	114
Figure 3.3 – Results from distribution of synapses along larger and smaller branches.....	115
Figure 3.4 – Formation of TmA neuron network via different synaptic partners.....	116
Figure 3.5 – Connectomes of TmA Neuron v TmA Neuron.....	118
Figure 3.6 – Total number of synapses from individual TmA neurons.....	120
Figure 3.7 – Number of synaptic partners found for individual TmA neurons.....	121
Figure 3.8 – Frequency of TmA neurons synapsing with the same partner.....	122
Figure 3.9 – Schematic of a portion of the network of TmA neurons synapsing onto the LGMD 2 neuron.....	124
Figure 3.10 – Analysis of total number of synaptic connections against number of unique connections for each of the TmA neurons.....	126
Figure 3.11 – Comparison of ‘hub’ and non-hub neurons.....	127
Figure 3.12 – Reconstructions of the ‘hub’ neurons.....	129
Figure 3.13 – Synapse distribution on multiple branches of LGMD 2 neuron.....	131
Figure 3.14 – Connectome of TmA neuron V LGMD 2 neuron Branches.....	133
Figure 3.15 – Analyses of branch frequency and distribution.....	135
Figure 3.16 – Comparison of single-branch innervating TmA neurons and multi-branch innervating TmA neurons.....	136
Figure 3.17 – TmA network diagram.....	138
Figure 3.18 – TmA network diagram with ‘hub’ neurons removed.....	139
Figure 3.19 – Examples of total mitochondria segmented from 50 sections of psoas.....	143
Figure 3.20 – Examples of total mitochondria segmented from 50 sections of soleus.....	144
Figure 3.21 – Results of percentage of portion of cell volume occupied by mitochondria.....	145

Figure 3.22 – Results of portion of cell volume.....	146
Figure 3.23 – Examples of mitochondrial segmentation and reconstructions divided by location for psoas.....	148
Figure 3.24 – Examples of mitochondrial segmentation and reconstructions divided by location for soleus.....	149
Figure 3.25 – Results of the mitochondrial volume for each location and age group in the psoas. ....	151
Figure 3.26 – Results of the mitochondrial volume for each location and age group in the soleus.....	152
Figure 3.27 – Branching analysis of mitochondrial network, percentage of segments >50 degrees.....	154
Figure 3.28 – Reconstructions of mitochondrial network from adult psoas and soleus cells.....	155
Figure 3.29 – Surface area and volume of individual whole mitochondria.....	157
Figure 3.30 – Results of volume and surface area of whole mitochondria for psoas and soleus divided by location.....	159
Figure 3.31 – Examples of types of shapes found in the central portion of mitochondria.....	160
Figure 3.32 – Results from analysis of central shapes for individual mitochondria for psoas and soleus.....	162
Figure 3.33 – Comparison of central shape analysis between psoas and soleus for all age groups.....	164
Figure 3.34 – Percentage of central shapes divided by location for psoas muscle.....	166
Figure 3.35 – Percentage of central shapes divided by location for soleus muscle.....	167
Figure 3.36 – Results of the percentage of branching and non-branching mitochondria for psoas and soleus.....	168

Figure 3.37 – Comparison of the percentage of branching and non-branching mitochondria between the psoas and soleus muscle.....	169
Figure 3.38 – Percentage of branching and non-branching mitochondria divided by location for psoas muscle.....	171
Figure 3.39 – Percentage of branching and non-branching mitochondria divided by location for soleus muscle.....	172
Figure 3.40 – Examples of whole and partially reconstructed nuclei for psoas muscle for each age group.....	174
Figure 3.41 – Examples of whole and partially reconstructed nuclei for soleus muscle for each age group.....	175
Figure 3.42 – Volume and percentage results of partially reconstructed nuclei for psoas and soleus for all age groups.....	177
Figure 4.1 – Summary diagram of TmA Neuron interaction onto the LGMD 2 neuron.....	181

## **Tables**

Table 2.1 – Imaging parameters used.....	59
Table 2.2 – Comparison of imaging programs.....	63
Table 2.3 – Timing analysis results.....	64
Table 2.4 – Mitochondria Volume Test Results.....	98
Table 2.5 – Access links to skeletal muscle datasets.....	105
Table 4.1 – Overview of results of mitochondrial complexity and morphology compared to previous studies.....	200

## Chapter 1. Introduction

### 1.1. Electron Microscopy

#### *1.1.1. Development of Electron Microscopy and 3D-Electron Microscopy*

The ambition of scientists to visualise subcellular structures at nanometre (nm) resolution led to the development of Electron Microscopy (EM). An electron beam to image was first utilised in the early 1930s with the development of the Transmission Electron Microscope (TEM) (Knoll and Ruska, 1932) and followed by the invention of the Scanning Electron Microscope (SEM) (von Ardenne, 1938). Since these first introductions of electron microscopes in the 1930s they have continued to develop and are now commonly used in a wide range of research areas. Both methods produce high resolution images of the ultrastructure of biological tissues and have answered many questions about the structure and function of cells and their organelles.

Although both TEM and SEM each use electrons as their energy source, the principles of application and subsequent images differ between the two techniques. TEM, as the name suggests, works by transmitting electrons through a thin section of tissue. The intention is to reveal spatial detail at nanometre resolution of intracellular and intercellular structures in biological specimens. To do this, the tissue has to be less than 100nm thick, and the electron beam has to be presented at a high voltage for the electrons to penetrate through the tissue. In areas of higher electron density, such as cell membranes, fewer electrons are transmitted through and these areas appear darker in the 2D image produced. Whereas areas of lower electron density, meaning more electrons pass through, appear lighter.

In the early stages of TEM, one of the major limitations was the need to have the specimen to be thin for the beam to penetrate the sample and for tissue fixation and staining procedures to be optimised to this end (Hall et al., 1946). A new embedding method, using methacrylic resin as a medium, (Newman et al., 1949) combined with a microtome and glass knife (Porter and Blum, 1953) allowed for thinner sections of the resin embedded fixed tissue to be reliably prepared for analysis by TEM. The fixation and preservation of sample membranes were first improved with the use of Osmium Tetroxide, which both fixes and stains biological material (Palade, 1952). This was followed by the development of the dual fixation method, where primary aldehyde fixation is followed by post-fixation with osmium tetroxide (Sabatini et al.,

1963). Improved contrasting and staining of samples for visualisation started with the shadow staining method developed by Williams and Wyckoff (1946), using metals to stain samples. Following this it was found that the heavy metals lead and uranyl acetate greatly improved membrane contrast (Cattini and Davies, 1983, Cattini and Davies, 1984). The combination of dual fixation with subsequent staining with heavy metals is the most commonly used method for sample preparation for TEM at present. Fixation and staining are discussed in further sections of this Introduction and for a review of developments in conventional TEM see Harris (2015).

In contrast to TEM, SEM uses an electron beam at a lower voltage. For SEM studies the electrons need only to interact with the surface of the specimen, with minimal penetration, so as to either examine the surface topology or the composition of the samples. Within the SEM there are two types of electrons that are detectable, which produce different images. These are backscattered and secondary electrons. Backscattered electrons occur when electrons, originating from the beam, interact with the sample surface, subsequently losing some of their energy and are scattered backwards. These back-scattered electrons are then detected and indicate the composition of the sample. Areas of the sample containing heavier elements will result in the incident electrons having a higher energy loss, shown as lighter regions in the final image. On the other hand, the secondary electrons originate from the sample. When the electron beam interacts with the sample, electrons within the sample become ionised and leave the sample. The topology of the sample will affect the number of secondary electrons that leave the sample and are detected. Areas of 'rises' or 'peaks' in the sample produce more secondary electrons, as they have more routes to exit the sample, whereas flatter surfaces produce fewer secondary electrons. The higher surfaces will appear lighter and the flatter surfaces darker, giving an indication of the overall shape of the sample as the beam scans the sample and producing a 3D image. As with the TEM, techniques and protocols required for the SEM have been optimised over time, for a review of these see Pawley (1997).

Both TEM and SEM share a restriction in the z direction that limits the ability of the EM community to obtain data in three spatial dimensions (x-y-z) at the ultrastructural level. Serial microtome sectioning and sequential TEM imaging of the sections, has been used to try and overcome this. It results in a stack of images that can be analysed to produce information in the z-axis (White et al., 1986, Kristen and Stevens, 1988, Chklovskii et al., 2010, Rivera-Alba et al., 2011). However manually



sectioning and imaging consecutive sections is extremely time consuming and challenging (e.g., aligning serial images and accounting for missing or damaged sections). Recently serial section TEM (ssTEM) was used to create a dataset encompassing the entire brain of *Drosophila melongaster* (Zheng et al., 2018), around 7062 sections at 40nm thickness and 21 million images at 4nm resolution were taken to produce the dataset: this took around 16 months.

To combat the limitations of using ssTEM, a method combining automated sectioning and imaging was developed. This has been termed Serial Block Face Scanning Electron Microscopy (SBF-SEM). The principle of combining a microtome within an SEM was first rudimentary developed by Kuzirian and Leighton (1983) and opened the way towards further developments of SBF-SEM (Denk and Horstmann, 2004). The SBF-SEM combines an ultra-microtome with an SEM. The knife cuts ultrathin sections from a piece of tissue embedded in a resin block, an electron beam scans the block surface, and a detector records the back-scattered electrons, producing a digital image. This process is repeated at an operator-specified depth to produce a digitised stack of aligned images. It is possible to obtain tens to hundreds of serial sections from resin blocks, and aligned digitised images, in a few hours. Since the development of SBF-SEM there have been other 3D-EM methods formed, shown in Figure 1.1.

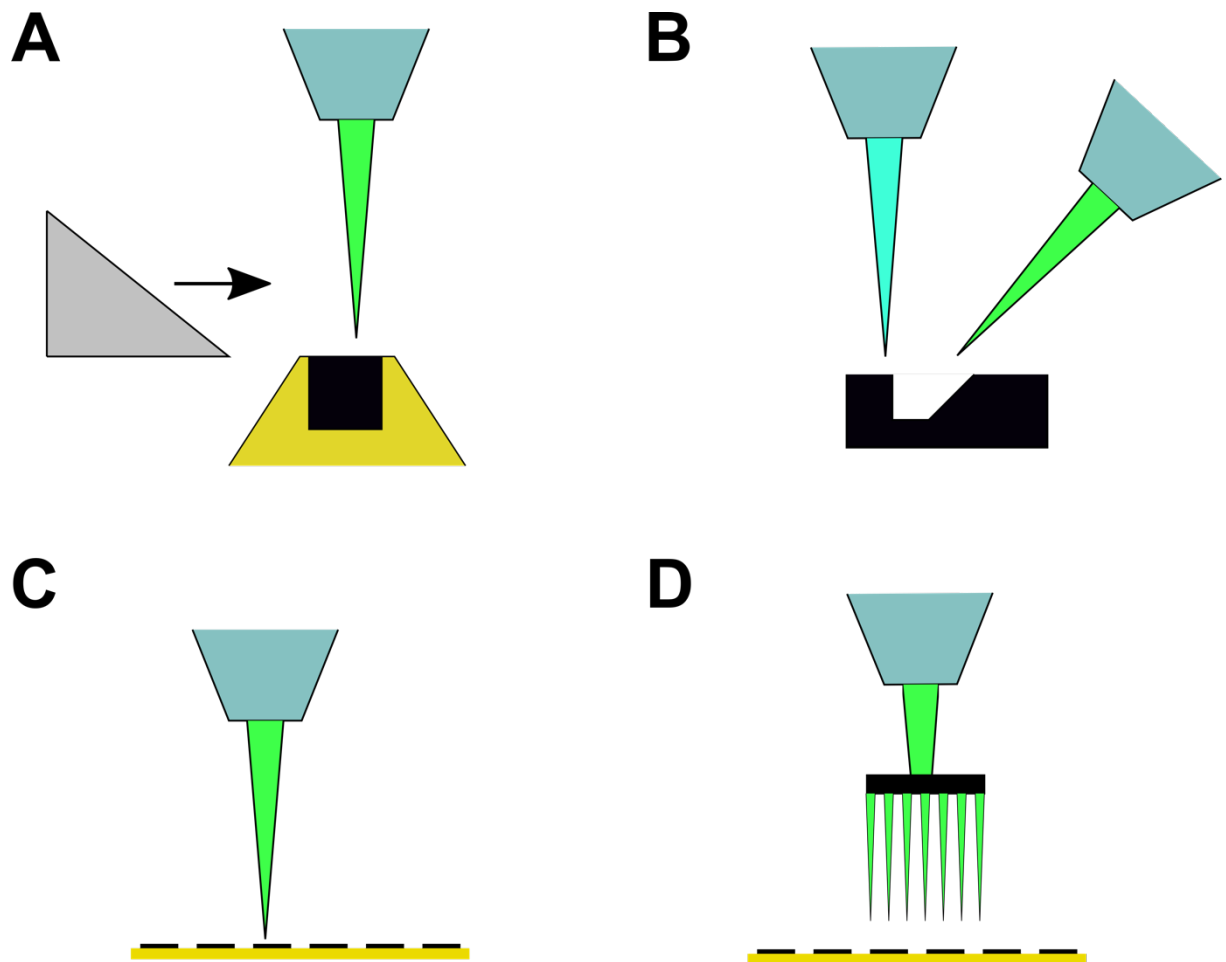


**Figure 1.1 – Diagram of 3D-EM techniques.** (A) Shows SBF-SEM, with the block face being imaged using electron interaction from an electron beam (green) upon the sample surface being detected and producing an image. This is followed by a knife-cut and the new face imaged and repeated to get the stack. (B) Shows FIB-SEM, where the block is milled by an ion beam (blue) and then imaged using an electron beam (green). (C) Principle behind serial section SEM or TEM, where multiple sections are produced on a microtome and then taken into an electron microscope to be imaged. (D) The multi-beam SEM (mSEM) splits the beam so that a larger area of a single section can be imaged at high resolution.

A similar method to SBF-SEM is the Focused Ion Beam-SEM (FIB-SEM), in that it combines sectioning and imaging in one modality. Unlike in the SBF-SEM system, the FIB-SEM system has an ion beam that mills the sample creating a trench followed by an electron beam that scans the surface (Knott et al., 2011). By using an ion beam instead of a diamond knife, thinner areas of the sample can be removed. Initially 20nm thickness was achieved (Knott et al., 2008) but more recent FIB-SEM studies have shown sections of the tissue, 5nm and below can be milled by the beam (Rennie et al., 2014, Vanslembrouck et al., 2018). The FIB-SEM can produce isotropic voxels, meaning they are the same length in x, y and Z, and this reduces any loss of detail in the Z resolution. However, the FIB-SEM is limited in the size of the area that can be milled away by the beam, roughly 100µm by 100µm, restricting the area available for imaging to this size. This is significantly smaller than SBF-SEM, which has a cutting area dependent on the width of the knife, which is 2mm in standard SBF-SEM machines, although it is recommended for samples in SBF-SEM to be below this.

A disadvantage of both SBF-SEM and FIB-SEM is that no physical section remains after the cutting or milling, and the sample is lost and cannot be re-imaged for additional analysis. Serial sectioning has previously been combined with SEM to try and address this (Horstmann et al., 2012, Kuwajima et al., 2013a, Kuwajima et al., 2013b, Hildebrand et al., 2017) but, as with serial sectioning for TEM, errors can occur in collection of the sections. To reduce the error rate, an automated method for sectioning was developed, the ATUMtome. The ATUMtome combines a tape collection system with a microtome (Hayworth et al., 2014, Kasthuri et al., 2015, Joesch et al., 2016, Vishwanathan et al., 2017). As sections are cut, they are deposited onto the tape situated close to the knife. The tape is constantly moving as the sample is sectioned, resulting in a reel of tape with sections in their cutting order on top. The number and thickness of sections to be taken can be programmed into the microtome and left to run. As the sectioning occurs without the presence of an electron beam, the resin remains stable allowing for acquisition of thin sections, roughly 30nm. The tape is collected, cut and placed on specially designed wafers, which are then imaged in a SEM. The sections of the sample can be kept and re-imaged multiple times without damage. The tape mechanism reduces the rate of error seen in the manual sectioning used for 3D TEM work, but there is still compression on the sections caused by the knife (Jesior, 1989, Studer and Gnaegi, 2000) and potential for missing or damaged sections. In contrast, as SBF microscopy

images the block face and not the sections, this problem does not occur and is only seen in the ATUMtome and serial section TEM or SEM methods.

For serial sectioning, as with the SBF-SEM, the size of the sample is restricted to the width of the knife and the cutting window although this can be up to 4mm wide for the ATUMtome. With the ability to cut larger samples there is a need to be able to increase imaging size and output from the serial section methods. For this, a new technique was developed known as the multi-beam SEM (mSEM) (Eberle et al., 2015, Pereira et al., 2016, Haehn et al., 2017). The mSEM works by splitting the electron beam into multi-beams which can scan an area of the section and collect data simultaneously. This allows for acquisition of a larger area of a sample, up to 3mm<sup>2</sup> has been achieved so far (Eberle et al., 2015), with a 1mm<sup>3</sup> of rat cortex also acquired using mSEM (Schalek et al., 2016). Another limitation for all 3D-EM techniques is the preparation of the sample. Currently the size of the samples that can be reliably stained with heavy metals is limited to around 1µm<sup>3</sup> (Hua et al., 2015), however this is continually being improved upon (Mikula and Denk, 2015). Overall, current automated methods for collection of 3D-EM data are continually being improved upon and new methods developed.

### *1.1.2. Serial Block Face-Scanning Electron Microscopy*

When comparing the automated 3D-EM techniques widely available, SBF-SEM is the most applicable technique to be used for a range of experiments. It has a wider field of view than FIB-SEM and larger datasets, in x, y and z, can be collected. A single SBF-SEM dataset can cover a larger area of the sample and reduce the need for multiple datasets, samples and animals for experiments. Although FIB-SEM has superior resolution capabilities in both directions, a single SBF-SEM block face can be imaged multiple times at different magnifications and resolutions, taking both low- and high-resolution images if needed. This makes SBF-SEM appropriate for imaging structures that are both large and small within the same dataset, such as a large neuron ( $>7\mu\text{m}$  in diameter) and the smaller neurons and processes extending from it ( $<1\mu\text{m}$  in diameter) or a large muscle cell ( $>40\mu\text{m}$  in diameter) and small organelles such as mitochondria ( $0.5\text{--}2\mu\text{m}$  in diameter). To cover as many potential experiments as possible SBF-SEM is the most appropriate technique to use and was chosen for this reason.

With the development of any new technique the steps required to obtain information using it have to be developed. This is the case for how a sample is processed for imaging using SBF-SEM and the data collected analysed. A sample for SBF-SEM has to be processed accordingly to withstand the serial sectioning and imaging it undergoes within the microscope. First, the tissue is fixed. For EM tissue fixation is with glutaraldehyde (Hayat, 1986) or a combination of glutaraldehyde and formaldehyde or paraformaldehyde (Wilke et al., 2013, Wernitznig et al., 2016), depending on the sample type. Another option of fixation that has been used to fix material is high pressure freezing (McDonald, 2007, Möbius, 2009) or freeze substitution has also been used to fix material for SBF-SEM (McDonald and Webb, 2011). Following fixation, the samples are then processed with a number of heavy metals, so that the membranes and organelles can be visualised under the SEM beam.

Processing the sample for SBF-SEM depends upon sample type and specific staining requirements for the experiment. The most common protocol followed is the reduced osmium, thiocarbohydrazide, osmium (rOTO) with lead and uranyl acetate (Wilke et al., 2013). The first step is reduced osmium tetroxide, a combination of osmium with either potassium ferricyanide (Rivlin and Raymond, 1987) or ferrocyanide (Goldfischer et al., 1981), a reducing agent (White et al., 1979). Osmium

tetroxide acts as both a fixative and a stain, readily binding to and staining cellular structures and membranes (Litman and Barnett, 1972, Geissinger et al., 1983). The first step is followed by thiocarbohydrazide (TCH) and a secondary osmium step (Friedman and Ellisman, 1981, Furness and Hackney, 1986). The TCH acts as a ligand, bridging membrane bound osmium (from the first step) with osmium from the second osmium infiltration, increasing the amount of osmium present in the sample (Seligman et al., 1966). Following rOTO, uranyl acetate is added, which interacts with osmium tetroxide, preserving structure and adding additional staining (Hayat, 1981, Cattini and Davies, 1984). The last heavy metal is lead, added in combination with an acid to increase penetration and stability of the metal (Karnovsky, 1961). As with the other heavy metals, lead stains the sample and improves conductivity of the sample (Walton, 1979, Cattini and Davies, 1983).

The heavy metal protocol layers the chemicals on top of samples which can thicken the appearances of membranes. This can reduce the visibility of smaller structures (e.g., ribosomes) and make it more difficult to determine separate cells in dense areas, differentiate between membranes, and visualise small structures such as synaptic vesicles and smaller organelles within cells. Thus, there are continual developments in the heavy metal protocol being adapted to different tissue types and also with experimental need. The size of a sample is becoming less of a restriction due to the development of large tissue staining procedures such as that applied to whole mouse brain staining (Mikula and Denk, 2015, Hua et al., 2015). The addition or change of specific metals can also improve the visibility of certain structures, such as addition of tannic acid to improve membrane visibility (Geissinger et al., 1983, Stirling, 1993), platinum blue for chromosomes (Yusuf et al., 2014) and dithizone for staining islets in the pancreas (Laif et al., 1988, Pisanía et al., 2010). The introduction of microwave processing decreases the sample preparation time and is becoming commonly used. However, it has to be treated with caution as to how it may affect the heavy metal interactions with structures, with each other and also the sample type. It is a benefit of the heavy metal staining procedure that it still lends the sample open to examination, should the experimenter wish (e.g., to obtain highest resolution images of specific areas of interest), by TEM.

Once the tissue samples are processed with the heavy metals and dehydrated with acetone or ethanol they are embedded into a hard resin and polymerised. The resin used has to be hard to account for the time spent under the electron beam and the

sectioning within the chamber. Once embedded the resin block is trimmed, so as to fit on pins specially designed for SBF-SEM. The size of the block on the pin is limited by the size of the knife (2mm) and cutting area (1-2mm) and is typically  $\leq 0.75\text{mm}$  by  $\leq 0.75\text{mm}$ . The sample and the pin are then coated in silver and/or gold, to increase conductivity of the sample and reduce the charging due to the electron beam interaction with the sample (Bråten, 1978, Titze and Denk, 2013).

The entire process from sample collection to sectioning can last more than 5 days, using the standard bench processing. The heavy metal staining and resin embedding steps take 3 to 4 days, followed by at least 48 hours in the oven for the resin polymerisation step. However the use of a microwave can speed up the processing greatly (Webster, 2014). Microwave assisted processing has been widely used in electron microscopy to improve fixation and staining penetration into the sample, reducing the time and allowing for larger sample sizes.

Once placed inside the microscope, the electron beam interacts with the heavy metals within the sample, and this produces the back-scattered electrons that are detected to form an image of the sample surface (Pawley, 1997, Denk and Horstmann, 2004, Wilke et al., 2013). As mentioned previously, the heavier elements appear lighter, so in the resulting image the electron dense areas have been stained more by the heavy metals and so appear white. The result is then inverted into a TEM-like image, which biologists are accustomed to (Denk and Horstmann, 2004). the imaging parameters and cutting thickness all depend upon the objectives of the experiment and also the type of sample. This is discussed further in the methods.

In many ways the challenges of 3D-EM have now shifted from how to capture the difficult-to-measure to what to do with all this data? At the outset of an experiment one, ideally, needs to know how the resultant images are to be analysed. These considerations vary from simple to complex, depending upon the experimental question, the tissue or cell constituency, the resolutions of structures of interest and their contrast to neighbouring structures.

The dataset obtained can be visualised in a number of ways. The series of images can be viewed sequentially to gain information on appearance of the tissue, cells and organelles. The 3D stack can be further analysed by segmenting the structures of interest and creating 3D reconstructions, which can yield volumetric, surface area and length measurements. There are a number of software packages available to

perform this type of analysis, ranging from freeware to licensed software (Borrett and Hughes, 2016). Segmentation is the process of annotating a specific structure on each image so as to follow it in each consecutive image in the z-axis.

The segmentation can be achieved using a variety of tools, primarily depending upon the nature of the subject, for example its contrast and size (Tsai et al., 2014, Cocks et al., 2018). The labelling of the structure can occur in two ways, depending on the software being used and regardless of the method of segmentation. In the first method, the object is segmented by adding a coloured layer on top of the image. A single structure can be attributed to multiple labels if the structures overlap, for example a nucleolus within a nucleus. In the other labelling process, the individual image pixels are assigned to one structure. If a pixel is reselected during further segmentation, it will be reassigned to the new model. This allows for mistakes made during segmentation, such as incorrect labelling, to be corrected. However, when segmenting a larger object and smaller target structures contained within, such as a cell and its' organelles, if the cell is segmented first, then followed by the organelles the resulting cell model will be minus the pixels selected after during segmentation of organelles. The method of labelling utilised has to be known and understood by the user prior to starting segmentation.

The methods of segmentation can be divided into manual, semi-automated and automated categories. Manual segmentation tools require the user to annotate the object by hand, e.g., by colouring the object in over every section. Semi-automated tools use a combination of user input and program predictions, to highlight a structure. An example of this is interpolation. The user manually annotates the structure every  $n$ th slice and the program will fill in the empty slices using the annotated image as a guide to predict the possible shape of the object. Another is the thresholding tool, which selects pixels based on the contrast limits set by the user. These limits allow for the selection of light or dark pixels depending on the appearance of the object. There is the option available in some programs for machine learning automated segmentation. Here, the program 'learns' object selection based on trial runs performed by the user on a sample dataset. These settings are then automatically applied to the full dataset to be analysed and can be implemented on other datasets as well. There has been a rise in the development and use of semi-automated and automated segmentation programs for analysing SBF-SEM data (Berning et al., 2015, Kasthuri et al., 2015, Kaynig et al., 2015,



Hussain et al., 2018, Krasowski et al., 2018). Although the majority of these programs are targeted towards segmentation of neural data.

Manual segmentation requires an individual or individuals to draw around a structure of interest over each section, which is time consuming and is currently the largest limitation for all 3D-EM techniques. Hence the drive in recent years to develop software for more automated methods of segmentation (Berning et al., 2015, Kasthuri et al., 2015, Kaynig et al., 2015, Beier et al., 2017, Dorkenwald et al., 2017, Hussain et al., 2018). However, some the programs developed and made available to people to use can be difficult for novices or those with limited computing background, often requiring some knowledge of coding to run the software. In addition, the majority of the newer software is based solely on neuronal datasets and focuses on the dense segmentation these types of experiments need, such as webknossos (Boergens et al., 2017) and SegEM (Berning et al., 2015). However, with the increasing use of 3D-EM for experiments outside of the brain and nervous system a program that can be used to segment a range of datasets is needed.

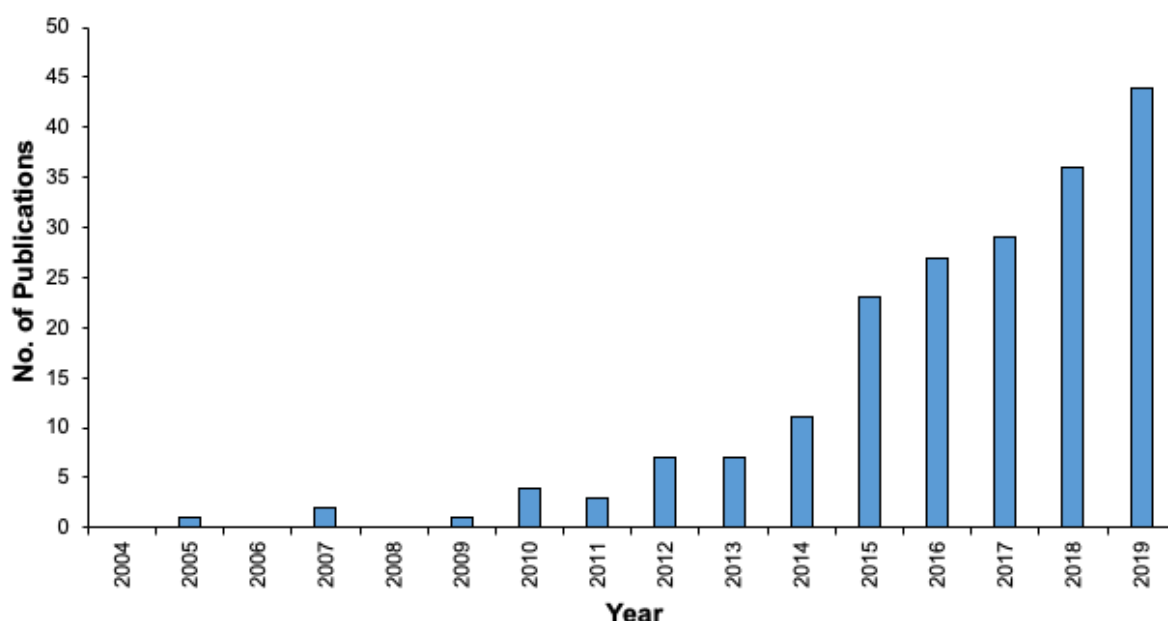
A subsequent factor in the imaging parameters is the computing power available. Both an image at high resolution and low magnification and a long series of images (regardless of size) will result in large data. Large datasets can be difficult to store and for analysing, due to small computer processing or graphics card memory size, for example <16GB RAM. This can be alleviated by the use of cloud storage for storing the data and running analysis and use of high-powered computers (>32GB RAM) with multiple graphics cards.

Overall, analysis of SBF-SEM data is the most time-consuming portion. Datasets can range in size from a few sections (<50), to several 1000 sections. The most popular segmentation method is manual, and sometimes used in conjunction with semi-automated or automated methods as well. From a review of literature using SBF-SEM (Appendix A) around half of the publications used manual segmentation solely or in combination with other semi-automated methods. The most popular pieces of software for analysis used are TrakEM2 (Fiji) (Cardona et al., 2012), IMOD (Kremer et al., 1996) and Amira (Thermofisher).

To provide an indication of the increased application of SBF-SEM in biological research and assess the types of experiments and sample type analysed, a review of SBF-SEM literatures was performed. Publications were found using the search term:

((((((((serial block face) OR sbfsem) OR sbf-sem) OR sbem) OR sbf-em) OR 3VIEW) OR volume scope)) AND microscopy

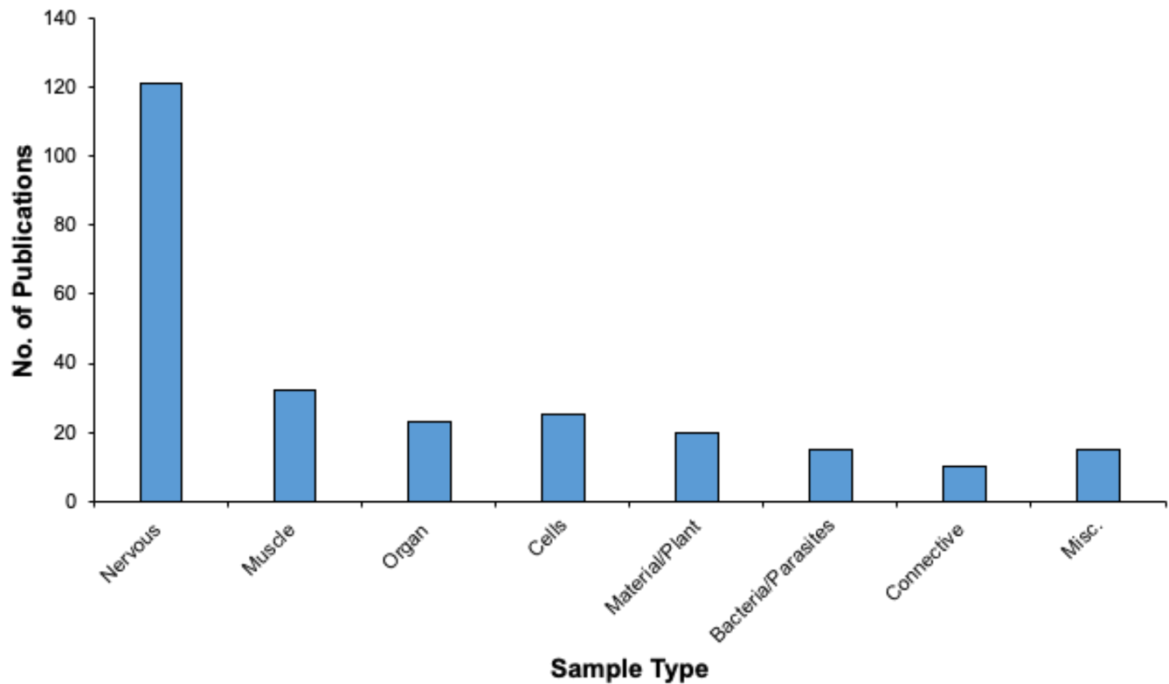
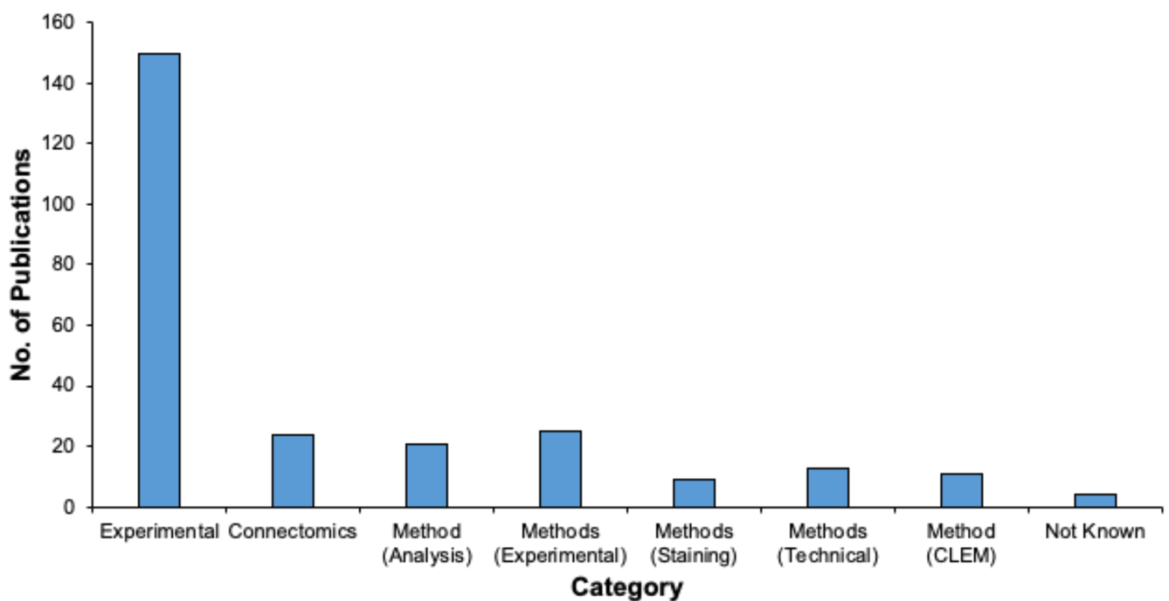
in PubMed, and checked that SBF-SEM was used, from 2004 to 2019. All the publications are compiled in table in Appendix A. From the development of SBF-SEM to the beginning of this project (2004 – 2015), there were 84 publications using SBF-SEM, Figure 1.2. Between 2015 and 2019 the number of publications increased up to 234. Although there has been a large increase in the number of publications using SBF-SEM per year, in comparison to other microscopy techniques it is still not as widely used even within the EM field, a search in PubMed for publications using TEM (search term used is transmission electron microscopy) for the year 2019 yields 7345 results. This is most likely due to the large cost and limited availability of SBF-SEM instruments.



**Figure 1.2 – Graph showing number of publications using SBF-SEM per year from 2004-2019.** Graph shows the number of publications per year from 2004 to 2019 using the search term '((((((((serial block face) OR SBFSEM) OR SBF-SEM) OR SBEM) OR SBF-EM) OR 3VIEW) OR volumescope)) AND microscopy' in PubMed.

From these publications the most common sample type studied using SBF-SEM was nervous tissue (46%) followed by muscle, including skeletal, smooth and cardiac (14%) (Figure 1.3(A)). In half of the publications SBF-SEM was used in conjunction with other methods or 'experimental'. For the purpose of this comparison 'experimental' was used to describe the projects in which SBF-SEM was used to compare between groups, such as between control cases and mutants or disease models, differences between ages groups and/or exploratory analysis of known structures. The majority of the other publications were methods papers; detailing how to use SBF-SEM to study specific sample types, sample preparation, analysis of the data, and technical papers, due to the new nature of the technique.

As SBF-SEM was developed by neuroscientists for connectomic based studies it is most commonly used in the neuroscience field (as detailed already). Connectomic studies map the connections between neurons within an area of the brain. However, connectomic studies are a small proportion of studies, Figure 1.3(B). This is most likely due to the time it takes to collect the large datasets and analyse the data for these types of studies (see Helmstaedter et al. (2011), Briggman et al. (2011) for examples). SBF-SEM is primarily used for experimental studies, mostly in conjunction with other methods and often just to show a small portion of structural data. In a lot of the publications the authors use one dataset and sometimes it is a small portion of the tissue or sample of interest. Use of one dataset is standard in connectomic studies, due to the size of the projects and the robust nature of the results from the extensive reconstruction and analysis of a neuronal network, which can extend into the 1000s. Within the publications that use SBF-SEM in conjunction with other methods often only 1 dataset is analysed or presented, and often the datasets are small. There are few publications that use SBF-SEM solely or extensively, for example comparing different experimental conditions. Even though the usage of SBF-SEM has grown since 2015 the publications available using the technique are still limited.

**A****B**

**Figure 1.3 – Graphs showing number of publications divided by sample type and category.** (A) Shows the number of publications by sample type, including nervous tissue (cornea, retina and brain), muscle (skeletal, smooth and cardiac), organ (kidney, liver, lung, pancreas and skin), cells (single and cultured cells), material or plant, bacteria or parasites, connective tissue (bone, tendons and cartilage) and others that could not fit into the other categories. (B) The number of publications by purpose, including experimental and connectomic studies and methods (analysis, staining and technical).

Overall, the development and usage of 3D-Electron Microscopy has increased over the past decade. Although the majority of the electron microscopy techniques were developed by neuroscientists for studying the brain, they have now been expanded to other areas of biology and material sciences. It is for this flexibility that SBF-SEM is being applied here to the study of two different tissue types with two different objectives, the connectomics of a neural network within the locust brain and changes over development in the ultrastructure of guinea pig skeletal muscle. With an overall aim to compare and contrast the different approaches required and applicability of the technique for each project. With the continued development of the techniques and greater knowledge in the subject area there will continue to be an increase in studies using 3D-EM and in a range of sample types.

## 1.2. Locust Visual System

The simplicity of the insect nervous system has led to it being widely used as a system for studying neuronal networks and computation. Insect eyes are compound, made up of thousands of lenses, each with the same dedicated circuit interpreting the image seen at one point before circuits come together in various combinations. Their crystalline structure, made up of simple repeated and ordered components, makes insect visual systems amenable to circuit analysis (Meinertzhagen and O'Neil, 1991). The locust visual system is one such system and has been studied for over 40 years. One aspect that is of particular interest is the neurons and the network involved in collision avoidance behaviour. When an object approaches the locust, on a collision course, a jumping, escaping or hiding behaviour is produced in adult and juvenile locusts (O'Shea et al., 1974, O'Shea and Williams, 1974, Sztarker and Rind, 2014). Collision avoidance pathways can be found in many insects and in the locust serves two main functions, one for predator evasion and the other for avoiding approaching objects. Avoiding approaching objects is especially important in locusts, as they fly in swarms that may contain millions of individuals. Some of the neurons involved in these specific behaviours have been studied extensively, although at the ultrastructural level there are still unanswered questions. The development of 3D-EM techniques allows for the visualisation of neurons and small processes simultaneously with the synapses between them.

The visual system of the locust consists of the eye and the optic lobe. The eye is estimated to be made up of 8134 individual facets (Simmons et al., 2013). Locusts have a fused rhabdome, made up of the light absorbing microvilli of all 8 photoreceptors. Photoreceptors 1-6 project into the lamina, while the photoreceptors 7 and 8 project into the medulla (Nowel and Shelton, 1981, Schmeling et al., 2015). The photoreceptors that extend into the lamina synapse with the lamina monopolar cell (LMC) (Nowel and Shelton, 1981). LMC neurons project into the medulla, where they synapse with a Trans-medullary afferent (TmA) neuron (Rind and Simmons, 1998, Rind et al., 2016). These TmA neurons cross the chiasm, from the medulla neuropil to the lobula neuropil, to synapse upon the Lobula Giant Movement Detector (LGMD) neurons, of which there are two, the LGMD 1 (O'Shea and Williams, 1974) and the LGMD 2 neuron (Rind, 1987, Simmons and Rind, 1997). A diagram of the input network onto the LGMD 2 neuron can be seen in Figure 1.4. The LGMD 1 in turn synapses onto the Descending Contralateral Movement Detector (DCMD)

neuron (Rowell, 1971, O'Shea et al., 1974), within the protocerebrum of the locust. . As there is a one-to-one transmission of spikes from the LGMD 1 to the DCMD and DCMD spikes can be recorded in behaving locusts (Rind, 1984, Santer et al., 2005). However, the postsynaptic partner of the LGMD 2 neuron is still unknown. Overall, the collision avoidance network is small, consisting of around 4 synaptic levels of neurons, from eye to protocerebrum (Rind and Bramwell, 1996, Peron et al., 2009, Jones and Gabbiani, 2010).

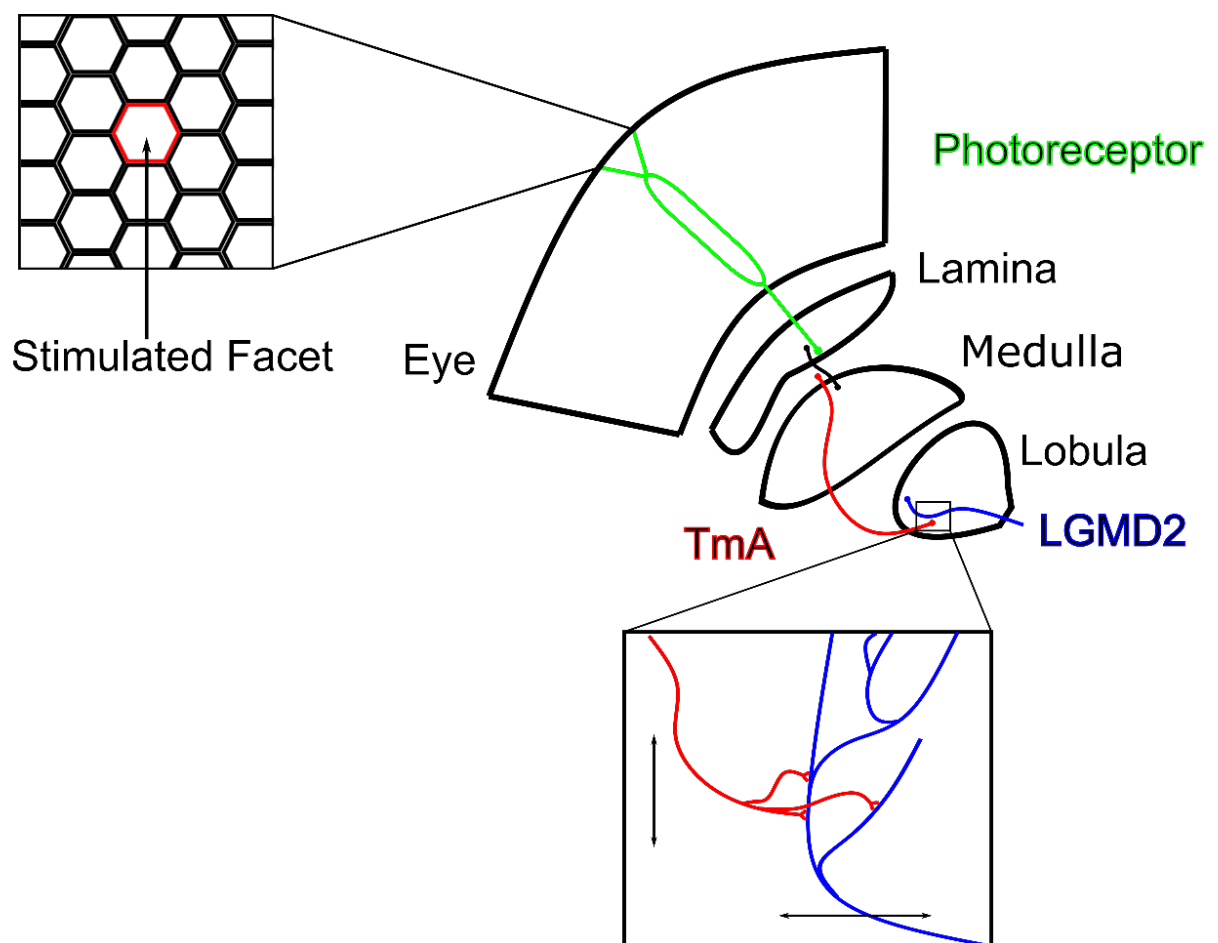


**Figure 1.4 – Diagram of Locust eye with pathway from retina to lobula.** The diagram shows the structure of the 6-sided facets present on the eye of the locust. Each facet is associated with 8 photoreceptors (green) which extends into the lamina. When a facet is stimulated the associated photoreceptor is as well. Then via a connective neuron between the lamina and medulla (black), a specific TmA neuron (red) becomes excited. This TmA neuron travels across the medulla and enters into the lobula region and synapses upon the LGMD 2 neuron (blue). These synapses are excitatory and thought to occur along a branch, (up-down arrows) and across other branches (left-right arrows), based on LGMD 1 neuron evidence.

Both neurons respond to looming objects. The LGMD 1 exhibits invariance, it responds to a looming object regardless of its texture, shape, angular subtense or trajectory (Gabbiani et al., 2001b, Gabbiani et al., 2004).. The LGMD 2 neuron has also been shown to respond selectively to looming objects but it has a preference for dark approaching objects (Simmons and Rind, 1997). Behavioural studies on flightless immature locust instars have used the LGMD 2 neuron's preference for dark objects to show that the LGMD 2 neuron is involved in hiding behaviour (Sztarker and Rind, 2014). Physiological recordings show the DCMD neuron, and hence the LGMD 1 neuron is selective for looming from the time the locust first hatches, through the 5 juvenile instars until adulthood, although its responses sharpen as the locust matures. EM studies show that synapses onto the LGMD 1 and 2 neurons in the first instar resemble the back-to-back, reciprocal pattern seen in adult synapses (Simmons et al., 2013). This suggests that the LGMD neurons are also well developed upon hatching to produce this behaviour via the looming selective network. 3D reconstructions, using light microscopy and silver-stained sections (see Sztarker and Rind (2013) figure 1), of both the LGMD 1 and LGMD 2 neurons and behavioural studies show this to be the case (Simmons et al 2013; Sztarker and Rind, 2014).

Each spike in the LGMD neuron elicits a spike in the DCMD neuron; this means that the spike rate of the DCMD neuron represents the spike rate of the LGMD neuron. The action of excitation is well documented onto the LGMD 1 neuron dendritic field (Krapp and Gabbiani, 2005). The LGMD neurons are able to discriminate between approaching and translating objects (Rind and Simmons, 1992, Simmons and Rind, 1992, Judge and Rind, 1997, Rind and Simmons, 1997). If the object alters direction and moves across the eye the excitation decreases and the threshold for signal propagation is not met and the action is not triggered (Rowell and O'Shea, 1976, O'Shea and Rowell, 1976, Rowell et al., 1977). The object approaching stimulates multiple facets and causes a spread of excitation across the dendritic field of the LGMD neurons, the signals converge in the larger dendrites and spikes are produced when the threshold for spiking is exceeded (Jones and Gabbiani, 2010, Jones and Gabbiani, 2012).

The excitatory inputs onto the LGMD 1 and 2 neurons, the TmA neurons, cross the medulla and enter into the lobula to synapse upon the LGMD neurons (O'Shea and Rowell, 1976, Rind et al., 2016). One of the main neurotransmitters found in insect



sensory nervous system synapses is acetylcholine (ACh) (Sattelle, 1980, Trimmer, 1995). ACh can either be excitatory or inhibitory depending on the receptors present on the postsynaptic neurons (Le Corronc et al., 1991, Parker and Newland, 1995). There are two main types of receptors involved in the cholinergic synapses in insects, the fast excitatory nicotinic synapses (Sattelle, 1980) and the slower muscarinic receptors, which can cause inhibition or excitation based on the type of receptor (Trimmer, 1995, Collin et al., 2013). Through staining it was determined that the transmitter present at the TmA neuron synapses on the LGMD neurons is acetylcholine, based on the presence of the enzyme acetylcholine esterase (Rind and Simmons, 1998) found at cholinergic synapses. This was, subsequently verified using antibodies against choline-protein conjugates and a polyclonal antiserum against choline acetyltransferase, that the LGMD 1 and 2 neurons and their pre-synaptic neurons contain ACh (Rind and Leitinger, 2000). It has been determined that the excitatory nicotinic ACh receptors are activated by the TmA neurons that synapse upon them (Rind and Simmons, 1998, Rind and Leitinger, 2000, Jones and Gabbiani, 2010).

Unlike mammalian synapses, synapses in an insect nervous system have been found to be dyadic and reciprocal (Watson and Burrows, 1985). A dyadic synapse occurs when one pre-synaptic cell has two post-synaptic targets. Back-to-back dyadic synapses where two presynaptic neurons share the same post-synaptic target and where each is the target of the other one, and both share the same synaptic cleft has currently only been found in the lobula and mushroom bodies of the locust (Rind and Simmons, 1998, Leiss et al., 2009, Rind et al., 2016). Within the lobula, these types of back-to-back synapses have been seen between the TmA neurons and the LGMD neurons (Rind and Simmons, 1998, Rind et al., 2016). Each TmA has two post-synaptic targets, the LGMD neuron and a secondary TmA neuron with which it forms a reciprocal dyadic synapse (Figure 1.5) (Rind and Simmons, 1998, Rind et al., 2016).

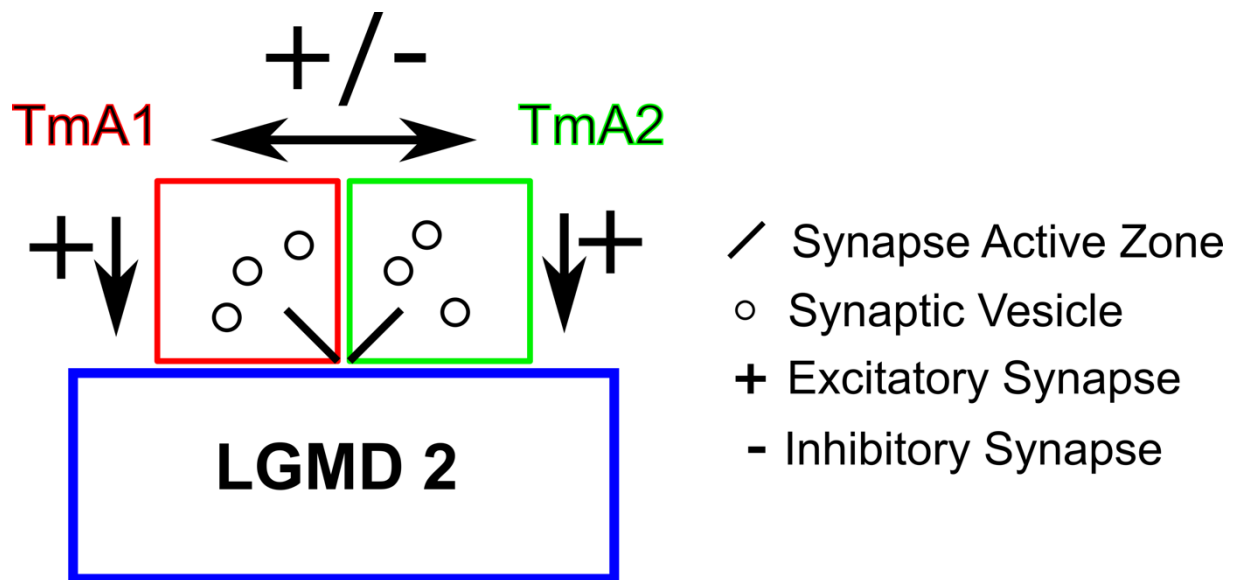


**Figure 1.5 – Schematic of TmA neuron synapses onto the LGMD 2 neuron in the lobula of the locust.** A schematic of two TmA neurons (blue and red) forming a dyadic and reciprocal synapse upon the LGMD 2 neuron (blue). The arrows show the direction of the synapse and the identity of the synapse, excitatory or inhibitory, is indicated.

The connection between the two TmA neurons occurs at the same point, that is when the two TmA neurons synapse upon a portion of the LGMD neuron. Evidence shows that release of acetylcholine from one of the TmAs also affects the neighbouring TmA neuron, and vice versa (Rind and Simmons, 1998, Rind et al., 2016, Zhu et al., 2018). It was originally proposed that inhibitory cholinergic receptors are present on the TmA neurons, enabling each TmA neuron to inhibit its neighbours at the reciprocal synapse (Rind et al., 2016). However, excitation occurring through excitatory muscarinic acetylcholine receptors has also been shown (Zhu et al., 2018). Although the presence of these receptors on the TmA neurons potentially explains the existence of the overlap of excitation over the branches of the LGMD 1 neuron (Zhu and Gabbiani, 2016) but the presence of inhibition between the TmA neurons has not been ruled out (Zhu et al., 2018). Overall, the identity of the TmA neuron to TmA neuron interaction is still debated.

There are a number of proposed methods for protection of the circuit against habituation. One such way, and most well-known, is via post-synaptic inhibition (Hatsopoulos et al., 1995, Gabbiani et al., 1999, Gabbiani et al., 2001a, O'Shea and Rowell, 1975). The post-synaptic inhibition occurs due to inhibitory inputs onto the dendritic sub-fields (B and C) of the LGMD 1 neuron (Rind and Bramwell, 1996, Gabbiani et al., 2005). It is proposed that the spike in the LGMD 1 neuron, in response to a stimulus, is due to computation of combination of excitatory and inhibitory inputs onto the dendritic fields (Gabbiani et al., 2001a, Gabbiani et al., 2004). It was proposed that, when a large part of the visual field becomes excited, there is a rise in inhibitory potentials across the sub-fields B and C; stopping the spiking of the LGMD 1 neuron (Rind, 1996). As the LGMD 2 neuron does not have distinct sub-fields, it is thought that direct inhibition is non-specific and occurs across the entire area of the dendritic branches (Rind et al., 2016).

Another method for the protection of the circuit against habituation is through the action of lateral inhibition which would act to protect decrement prone TmA synapses by preventing them spiking to non-looming stimuli (O'Shea and Rowell, 1975, Rowell and O'Shea, 1976, Rind and Bramwell, 1996, Rind and Simmons, 1998, Rind et al., 2016). Lateral inhibition is thought to occur between or onto the pre-synaptic cells prior to the synapse on the LGMD 1 neuron branches (O'Shea and Rowell, 1975, Rowell and O'Shea, 1976, Rind and Bramwell, 1996, Rind and Simmons, 1998, Rind et al., 2016). Lateral inhibition was proposed to form part of the network of the excitatory and inhibitory potentials that all play a role in controlling the output from the LGMD 1 neuron but is not essential (Rind and Bramwell, 1996).

The action of lateral inhibition, besides preventing habituation at the decrement prone synapses of the TmA neurons onto the main dendritic fan of the LGMD 1 neuron, is most likely due to the inhibitory muscarinic receptors on the TmA neurons. The reaction from these receptors is slower than the excitatory synapses. As an object approaches, the rate of excitation increases and the action of inhibition lags, causing a spike in the LGMD neuron. However, if the object moves away from a collision course the excitation does not increase, allowing for inhibition to overtake and stop the signal. The purpose of this lateral inhibition was thought to distinguish approaching and passing objects (Rind and Bramwell, 1996). Although it is now thought, that the action of lateral inhibition helps to sharpen the response of the LGMD neurons, in combination with other factors such as spike frequency adaptation

and locally synchronised input caused by a looming object that reinforce the preference for motion caused by looming objects.(Rind et al., 2016).

Although, the exact identity of the ACh receptors at the TmA neuron to TmA neuron synapses is not known, a recent study provides evidence that the main lateral effect is excitation occurring, through excitatory muscarinic acetylcholine receptors on the TmA neurons, but does not rule out the presence of inhibition between the TmA neurons (Zhu et al., 2018). Although the presence of these receptors on the TmA neurons potentially explains the existence of the overlap of excitation over the branches of the LGMD 1 neuron (Zhu and Gabbiani, 2016).

For the LGMD neurons, a retinotopic map is preserved from the locust eye facets, via the TmA neurons and onto the branches of the LGMD neurons. An individual facet is assumed to be associated with a single TmA neuron, which in turn synapses onto branches in a specific area of the LGMD neurons (Rowell et al., 1977, Rind and Bramwell, 1996, Rind and Simmons, 1998, Krapp and Gabbiani, 2005, Peron et al., 2009, Rind et al., 2016, Zhu and Gabbiani, 2016). However, a similar study has to be performed on the LGMD 2 neuron to determine whether it is conserved for both LGMD neurons.

Currently the LGMD 1 neuron has been studied far more than the LGMD 2 because of the ease of recording from the LGMD 1 neuron via the DCMD axon. The majority of the knowledge of the LGMD neurons' input network, and the action of excitation and inhibition, is based upon studies of the LGMD 1 neuron, but TmA neurons also form excitatory synapses onto the LGMD 2 neuron as they do onto the LGMD 1 neuron (Rind et al., 2016). The LGMD 1 and 2 neurons share some similarities but differ in their structure in the lobula. The LGMD 1 neuron has three distinct dendritic fields, the larger sub-field receives excitatory inputs and the two smaller sub-fields receive inhibitory inputs (Rind and Bramwell, 1996, Gabbiani et al., 2005). Whereas the LGMD 2 neuron only has a single large dendritic field (Simmons and Rind, 1997, Rind et al., 2016).

The nature of synapses within the lobula region of locust's optic lobe (and that of other insects) indicate a potential network between the TmA neurons as they synapse with the LGMD 1 or 2 neurons. Studying the connectomics of the TmA neurons could elucidate more information about the TmA neurons and how they confer on the LGMD neurons the tuning for approaching objects. Within the locust

visual system understanding the principles behind signal integration and the TmA neuron network can be applied to other visual systems (Fotowat and Gabbiani, 2011) but also within the field of robotics (Yue and Rind, 2006).

The output of the LGMD 2 neuron is not known and the mechanism of inhibition onto the neuron is unknown. As shown by other studies (Kasthuri et al., 2015, Kaynig et al., 2015, Zheng et al., 2018) SBF-SEM can be used to map the connectomics of neural circuits. For this study SBF-SEM will be used to map the TmA neuron circuitry onto the LGMD 2 neuron, with the objective of discovering how the degree of TmA neuron connectedness may confer the tuning for approaching objects and the position invariance of this tuning on the LGMD 2 neuron.

### *1.2.1. Choice of Experimental Animal Rationale (Locust)*

Motion detection can be found in other insects, like *Drosophila* with some variation (Vogt and Desplan, 2007) and in a more complex form in primates (Appleby and Manookin, 2020). The locust is a simple organism when compared to other animals used to study the neuronal system, such as mice and rats. The collision avoidance network can be used to study the integration of sensory information within a neural circuit and for studying the behavioural output based on the sensory input. The relative simplicity of the circuit lends itself to easy experimentation. It is well conserved across locust populations, as without the network they would not survive, so there is little to no variation between individuals. (Santer et al., 2008, Fotowat and Gabbiani, 2011, Santer et al., 2012). This means that it can be studied using connectome based dense reconstruction without the need of multiple individuals to account for variation.

### *1.2.2. Hypothesis/Aims*

The LGMD 1 responds to changes in light across the locust retina, with inputs occurring from retinotopic units. It is thought that the TmA neurons retain the retinotopy from the facets of the eye onto the dendritic trees of the LGMD 1 neurons. The processes of the LGMD 1 neuron are responsible for the summation of the inputs. It can be hypothesised that the TmA neurons also maintain retinotopic mapping onto the LGMD 2 neuron. Each of these TmA neurons synapses upon the LGMD 2 neuron are reciprocal, with a single TmA neuron having two synaptic partners at each location of a single synapse upon the LGMD 2 neuron (one partner is the LGMD 2 neuron and second partner is neighbouring TmA neuron). Each TmA neuron is responsible for one facet and are evenly weighted across the dendritic trees, with all of them synapsing upon the same number of times, covering the same area of the LGMD 2 neuron and with the same number of TmA neuron partners.

To map the connections of the TmA neurons onto the LGMD 2 neuron over a large area, in x, y and z, a 3D electron microscopy technique is required, such as SBF-SEM. It provides the resolution needed to identify synapses and follow the TmA neurons through a sample and has a large field of view to be able to image an extensive area of the lobula. Mapping the inputs onto a portion of the LGMD 2 neuron will show whether the TmA neuron synapses are all reciprocal and by identifying the neurons involved the neural network can be mapped. Mapping the network of the TmA neurons onto the LGMD 2 neuron will determine the structural organisation and subsequently whether there is even retinotopic mapping.

Additionally, the relationship between TmA neurons can be determined and this will indicate the weighting of individual TmA neurons onto the LGMD 2 neuron. The objective will be to discover how the degree of TmA neuron connectedness may confer the tuning for approaching objects, which expand outwards in all directions and the position invariance of this tuning on the LGMD 2 neuron. The steps to performing a connectomic analysis on the LGMD 2 neuron using SBF-SEM have yet to be undertaken. SBF-SEM will be used, and analysis provided in detail to ensure that further connectomic type studies can be performed on less common systems.

### **1.3. Skeletal Muscle**

#### *1.3.1. Structure and Function*

The skeletal muscles provide support to the skeletal frame as well as being vital for limb and body movement via muscle contractions and relaxations. The structure of skeletal muscle is well-known (Rozsa et al., 1950, Spicer and Rozsa, 1953). It is made up of groups of individual muscle fibres, each of these fibres consists of bundles of myofibrils. These are made-up of thin actin- and thick myosin-containing filaments (Frontera and Ochala, 2015). The thin and thick filaments are arranged within the myofibril with overlapping and non-overlapping regions, each contained within defined boundaries of structures known as sarcomeres. A single sarcomere is denoted by 'Z-lines', structures that serve as anchorage points for other proteins involved in holding the thick and thin filaments in line (Hall et al., 1946, Draper and Hodge, 1949, Frontera and Ochala, 2015), Figure 1.6. This arrangement of structures gives rise to the light and dark (striated) sarcomeric banding pattern evident under light and electron microscopy.



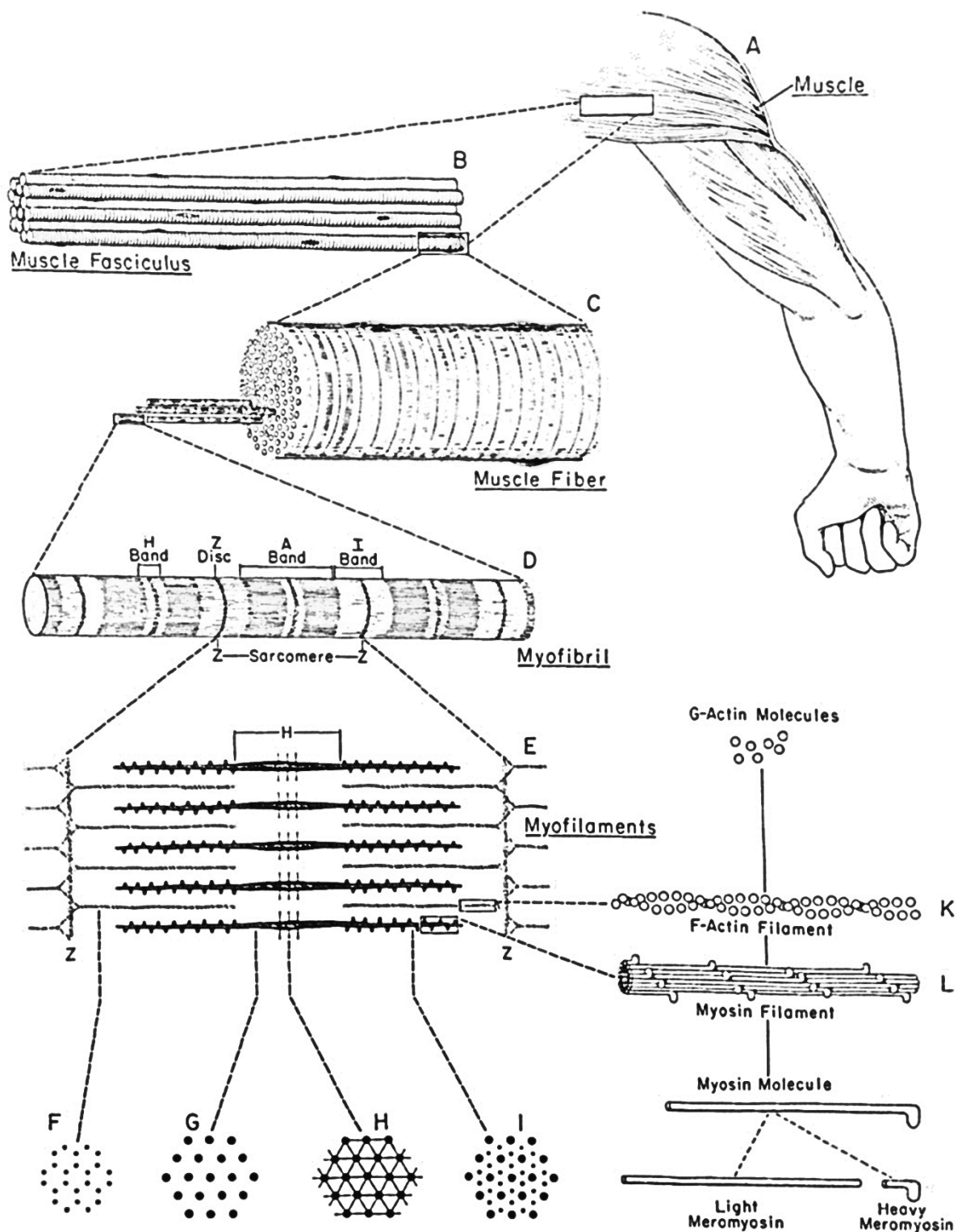


**Figure 1.6 – Diagram of muscle structure.** The diagram shows the components of a muscle (A). Muscles consist of bundles of muscle fibres (B) and a single muscle fibre (C) is made of numerous myofibrils (D). Each myofibril consists of myofilaments (E), actin (K) and myosin (L), the myofilaments are arranged in overlapping and non-overlapping regions, which form the sarcomeres. Diagram taken from Fawcett and Bloom (1994).

Within the muscle fibres there is a complex organellar system, the sarcoplasmic reticulum (SR) (Porter and Palade, 1957, Andersson-Cedergren, 1959) and transverse tubular (T-Tubule) system. The latter is part of the plasmalemmal continuum and therefore open to the extra cellular matrix (Endo, 1964, Franzini-armstrong and Porter, 1964, Huxley, 1964, Endo, 1966). Both of these systems play a vital role in the mechanism of contraction in skeletal muscle. Unlike other cell types, skeletal muscle cells are multi-nucleated (Cheek et al., 1971, Cheek, 1985, Hall and Ralston, 1989, Frontera and Ochala, 2015) and have a complex network of mitochondria that runs through the length of the muscle fibre (Miyazaki et al., 2014, Dahl et al., 2015).

The mechanism underlying muscle contraction is known as the 'Sliding Filament Theory' (Huxley, 1974). As the name suggests the contraction of the muscle is caused by the action of the actin- and myosin-containing thin and thick filaments 'sliding' over one another. A number of EM studies have shown that the width of the sarcomere, as well as the A and I band within the sarcomere, alters during contraction (Hall et al., 1946, Draper and Hodge, 1949, Rozsa et al., 1950, Spicer and Rozsa, 1953, Huxley, 1967) due to the action of the filaments moving past one another, Figure 1.7.

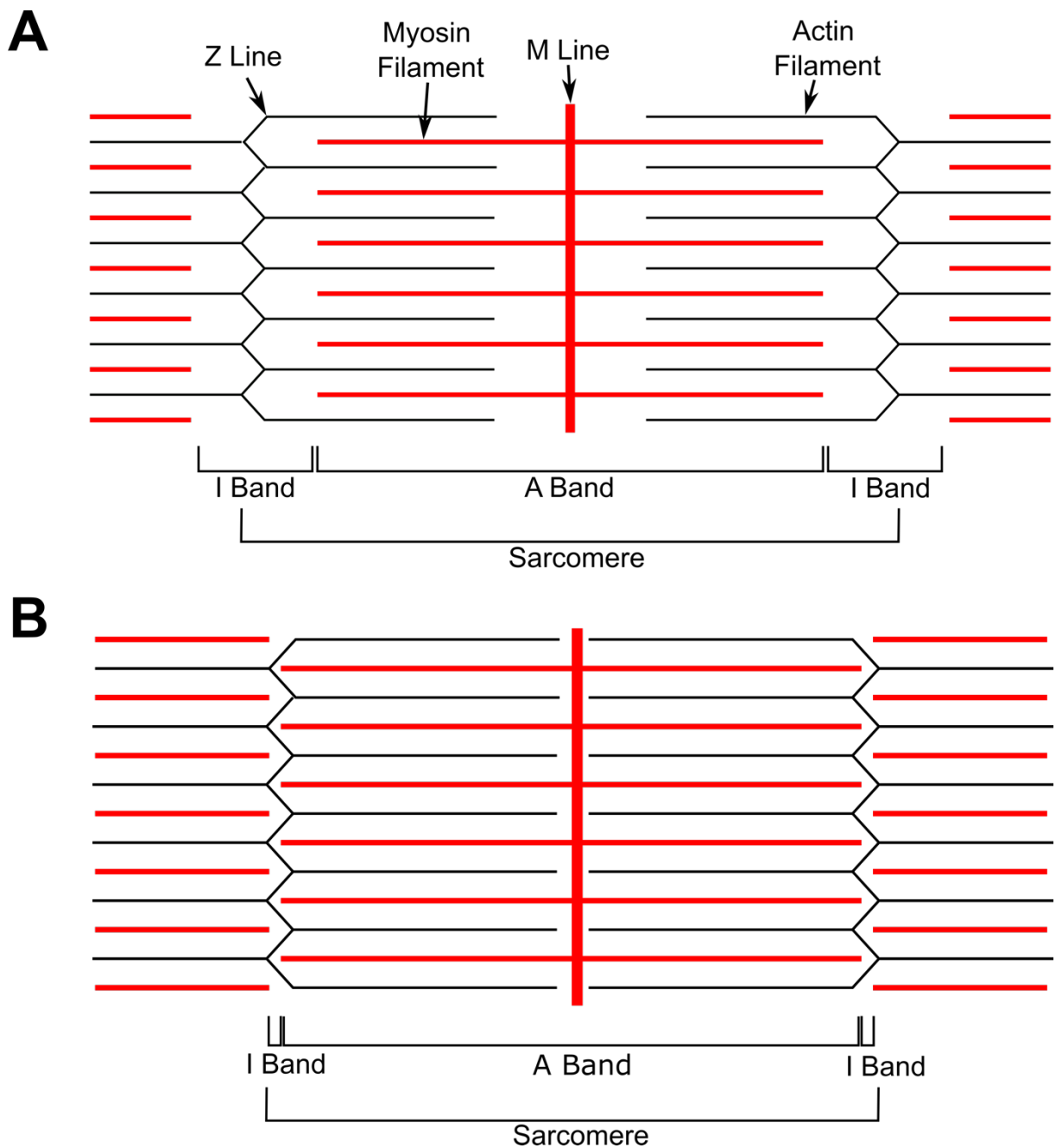


**Figure 1.7 – Schematic of muscle contraction.** (A) Shows schematic of non-contracted muscle with myofilaments, actin and myosin. The A band is the area that consists of myosin filament, including areas of solely myosin and overlapping areas with actin. The I band consists of only actin filaments. A sarcomere is the area from Z line to Z line. (B) Shows the shortening of the I band and sarcomere width during muscle contraction.

This contraction is known to occur in the presence of adenosine triphosphate (ATP) and a rise in intracellular  $\text{Ca}^{2+}$  levels due to the entry of  $\text{Ca}^{2+}$  from the sarcolemmal t-tubules during an electrical action potential (Spicer and Rozsa, 1953). A dedicated method of transference has to be present to account for the speed at which the electrical impulse is linked to muscle contraction (Hill, 1949). This process became known as 'Excitation-Contraction' (E-C) Coupling (Sandow, 1952). For recent reviews on this topic see Rebbeck et al. (2014) and Frontera and Ochala (2015).

There are two main groups of fibre type found in skeletal muscle. The slow twitch type, type 1, rich in myoglobin for continuous activity (red muscle) and the fast twitch type, type 2, specialising in phasic activity and glycolytic metabolism (white muscle) (Needham, 1926). Fast muscle fibres have been found to have three distinct sub-types, -2A, -2B and -2X. Fast fibres-2A and -2B were first defined by morphology (Schiaffino et al., 1970) and histochemical analysis of myosin ATPase (Guth and Samaha, 1969). Through immunohistochemical examination a third type of fast twitch muscle, type 2X, was identified and characterised later (Schiaffino et al., 1988, Schiaffino et al., 1989). Advancements in proteomic studies now ensures that characteristics of single fibres are not overlooked. Studies on Myosin Heavy Chain (MyHC) expression and variation have shown that a single muscle fibre is not just one type but can be heterogenous (Gorza, 1990, DeNardi et al., 1993, Bottinelli et al., 1994). Further review on this topic can be found at Schiaffino et al. (2020).

Two well-studied muscles include the soleus (leg muscle) and the psoas (back muscle), location shown in Figure 1.8. The soleus is involved in the movement of the ankle, knee and hip, working in conjunction with the gastrocnemius muscle (Lenhart et al., 2014). The psoas muscle is both a hip flexor and stabilises the lumbar area of the spine (Arbanas et al., 2009). It is well established across multiple mammalian species that the soleus is primarily slow twitch (~80%), supplemented with fast twitch, as found in guinea pigs (Peter et al., 1972, Gorza, 1990), rabbits (Peter et al., 1972), mice and rats (Gorza, 1990, Soukup et al., 2002) and humans (Johnson et al., 1973, Gollnick et al., 1974). On the other hand, in the psoas there is a heterogeneous distribution of both slow and fast twitch fibres, as found in human studies (Johnson et al., 1973, Parkkola et al., 1993). Although, recent publications show a higher percentage of fast twitch, specifically Type IIA, at ~60% (Arbanas et al., 2009). Fibre typing in rats show that there is a higher proportion of fast type fibre (Erdström et al., 1982, Härmäläinen and Pette, 1993, Vlahovic et al., 2017).

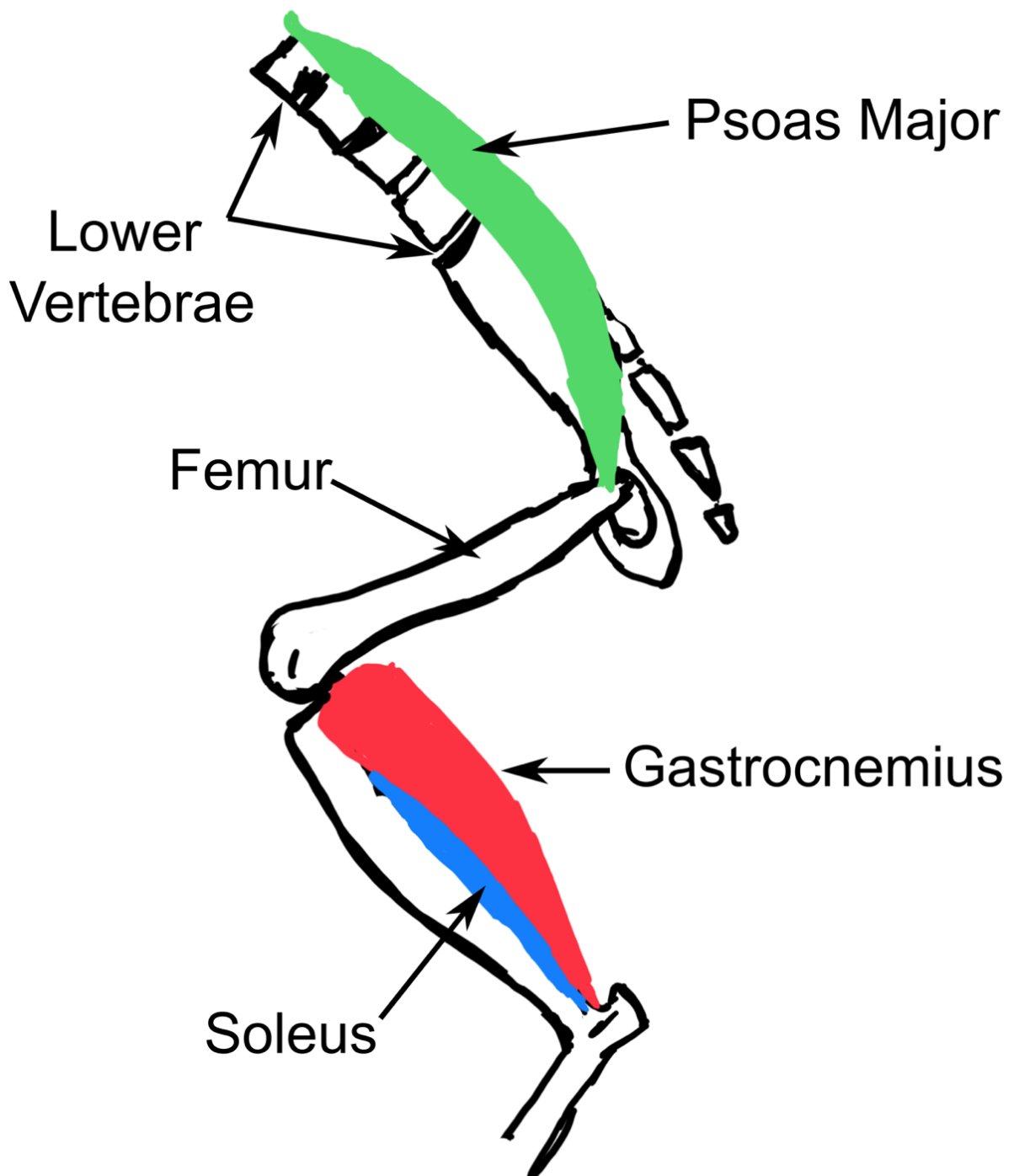


**Figure 1.8 – Location of psoas and soleus muscle in the rodent.** The diagram shows the hind limb, pelvis and portion of the lower vertebrae and the location of the soleus and psoas muscle. The soleus sits behind the larger gastrocnemius muscle, connecting with the fibula bone. The psoas is located in the lower back and pelvic region, connecting with the lower vertebrae and the femur. Schematic was drawn based on Charles et al. (2016).

### *1.3.2. Skeletal Muscle Development*

The formation of muscle comes from the fusing of myoblasts, muscle precursor cells, to form nascent myotubes, which go on to form muscle cells. Myogenesis occurs in a number of steps during embryonic, fetal and neonatal development. The first wave of myogenesis occurs from the embryonic wave, with the formation of the myotome (Ordahl and Le Douarin, 1992). Myocytes then start to form from the myotome and become early myofibres, driven by the expression of specific skeletal muscle cell factors and proteins (Sassoon et al., 1988, Babai et al., 1990, Lyons et al., 1990, Lyons et al., 1991). The role of these primary fibres is to act as a scaffold, dictating the position and orientation of the individual muscles in a highly regulated process (Buckingham et al., 2003, Abmayr and Pavlath, 2012, Fiorotto, 2012) and also form the early limb muscles (Murphy and Kardon, 2011). Following the primary phase comes the second wave of myogenesis. In this phase fetal myoblasts proliferate under the basal lamina of the primary fibres, then fuse and form the secondary fibres, these new fibres then separate from the primary fibres (Keller et al., 1992, Messina et al., 2010, Fiorotto, 2012). This occurs in the neonatal stages of development. Post-natal growth of muscle is facilitated by the addition of myofibrils in length and width (Gokhin et al., 2008, Sparrow and Schöck, 2009, Keefe et al., 2015) and myonuclei (White et al., 2010). An overview of this is shown in a schematic in Figure 1.9.

The post-natal stages are vital for the development of the muscle fibres and differentiation as they start to perform more functions related to their position and specific role in the musculoskeletal system. In most mammals at birth, the system is immature and requires a combination of factors to become adult muscle cells. The post-natal specification is dictated by intrinsic factors, such as gene programming, and extrinsic factors, like hormones (Gambke et al., 1983, d'Albis et al., 1990) and neural influence with the formation of distinct motor units, an area of muscle cells associated with a specific motor neuron (Slater, 1982, Fladby and Jansen, 1990, Jansen and Fladby, 1990). Post-natal neural innervation and hormone interaction drives the specification of fibres (Narusawa et al., 1987), shown by an accumulation of associated proteins during this stage in development (Butler-Browne and Whalen, 1984). By post-natal weeks 2 to 4 developmental fibres have disappeared in rats, mice and guinea pigs, the muscle fibres have formed distinct populations directly related to the required function (d'Albis et al., 1989, Agbulut et al., 2003),

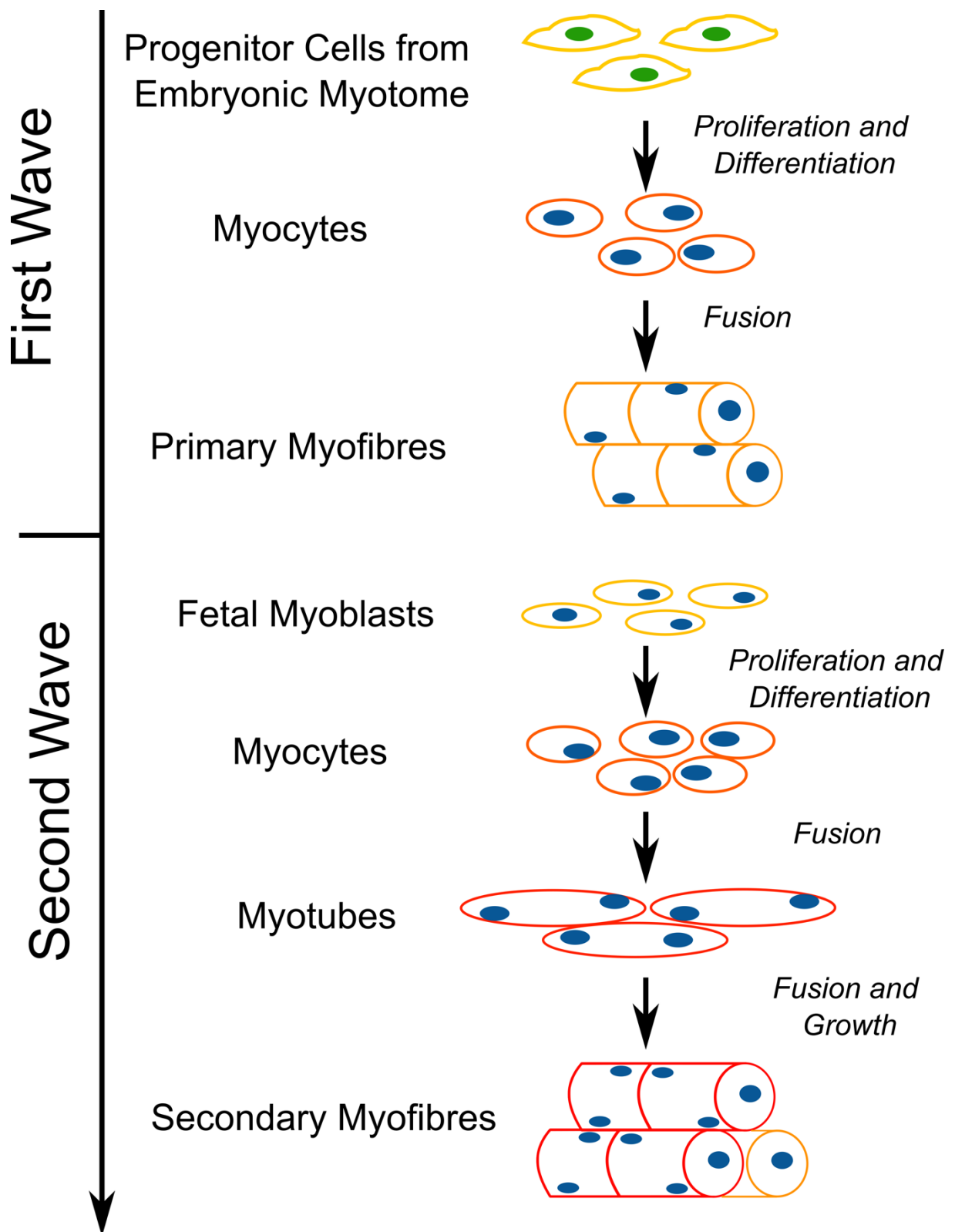


**Figure 1.9 – Schematic of myogenesis during fetal development.** Myogenesis starts with the proliferation of early myocytes from progenitor cells in the embryonic myotome. These differentiate and fuse to form primary myofibres (orange). During the second wave myoblasts differentiate into myocytes, which fuse to form nascent myotubes. The myotubes undergo further fusion and growth to form secondary myofibres (red), using the primary fibres as a scaffold.

### 1.3.3. Nucleus

Skeletal muscle cells are multinucleated (Cheek et al., 1971, Cheek, 1985, Hall and Ralston, 1989, Frontera and Ochala, 2015). Skeletal muscle cells are one of the largest cells found in vertebrates, making the nuclei important in maintaining a variety of cell functions over a large area (Cheek et al., 1971, Hall and Ralston, 1989). One theory as to how this is achieved is through the existence of nuclear domains, whereby a single nucleus occupies and maintains a given volume of the cytoplasm acting like a unit (Cheek, 1985, Hall and Ralston, 1989, Cheek et al., 1971). This is further corroborated by evidence suggesting that the ratio of nucleus to cytoplasm, by volume, is maintained during the action of hypertrophy of muscle cells (Allen et al., 1995, Allen et al., 1999, Shenkman et al., 2010).

Nuclei in skeletal muscle are known to follow distinct developmental stages. They develop centrally and migrate to the periphery (Gundersen and Worman, 2013, Bone and Starr, 2016). During development, myoblasts fuse and the nuclei align themselves in the centre of the newly formed myocyte (Capers, 1960, Cadot et al., 2012, Folker and Baylies, 2013, Falcone et al., 2014, Roman and Gomes, 2017). Recent studies suggest that the movement of the nuclei to the periphery is driven by myofibrils cross-linking, in a 'zip-like' fashion, altering the shape of the nuclei and pushing them to the outer regions of the cell (Roman et al., 2017, Rosen and Baylies, 2017, Roman et al., 2018). Once at the periphery, they anchor to the region of the cell they have moved to (Roman and Gomes, 2017). The distance between the nuclei is proposed to be maintained by cytoskeletal interactions with the nuclear envelope (D'Alessandro et al., 2015, Roman and Gomes, 2017, Manhart et al., 2018). Then in adult skeletal muscle cells the nuclei are all located on the periphery of the cell (Bruusgaard et al., 2003, Bruusgaard et al., 2006), except for in disease cases of central nuclear myopathy (Chapman et al., 2014, Falcone et al., 2014, Jungbluth and Gautel, 2014, Iyer et al., 2017).

There has been limited studies analysing the relationship between nuclei size (e.g., surface area or volume) and whole cell size (surface area or volume) across different stages of fetal development. From the current studies, a ratio of cell area to nuclei is thought to be maintained during the process of muscle damage and regeneration that occurs in mature muscle cells, as described above, but whether this ratio is seen during development is unknown. With the use of SBF-SEM both nuclei and the cell can be reconstructed in 3D to determine this.



#### 1.3.4. Mitochondria

Skeletal muscles require a significant amount of energy to produce its contractile function and mitochondria therefore are important organelles. Mitochondria contain the enzymatic system for oxidation of sugars, fats and proteins for Adenosine Triphosphate (ATP) production (Ryan and Hoogenraad, 2007). For example, after undergoing glycolysis sugar substrates enter the citric acid cycle within the mitochondrial matrix (Bartlett and Eaton, 2004, Maechler et al., 2006). Following the citric acid cycle the reduced Nicotinamide Adenine Dinucleotide (NADH) or Flavin Adenine Dinucleotide (FADH<sub>2</sub>) produced move to the electron transport chain in the inner mitochondrial membrane. This powers the transmembrane movement of protons that helps for the synthesis of ATP via oxidative phosphorylation (Osellame et al., 2012). The balance of energy requirements and production is maintained in part via calcium signalling. Calcium from the cytosol can be taken up into the mitochondria via the Mitochondrial Calcium Uniporter (MCU) (Kirichok et al., 2004, Baughman et al., 2011, De Stefani et al., 2011). This regulates enzymes involved in NADH uptake into the electron transport chain which increases respiration, conversion of oxygen and other nutrients into ATP, and thus ATP production (Duchen, 1992, Jouaville et al., 1999).

As well as producing ATP mitochondria contains a portion of DNA, mitochondrial DNA (mtDNA) of maternal origin, which code for a small portion of proteins, specifically involved in the electron transport chain (Picard et al., 2011, Picard et al., 2012, Russell et al., 2014). Another major role for mitochondria is involvement in apoptosis. Mitochondrial-associated proteins are able to directly stimulate the process of apoptosis via regulating the permeabilisation of the outer mitochondrial membrane (Li et al., 1997, Li et al., 1999, Susin et al., 1999, Li et al., 2000). These factors play important roles in, for example, cellular responses in ischemia and reperfusion injuries (Hunter and Haworth, 1979, Nakagawa et al., 2005, Forte et al., 2007).

Light microscopy studies have revealed that mitochondria change morphology by the action of fusion, two mitochondria coming together, and fission, the division of a mitochondrion (Sugioka et al., 2004, Berman et al., 2008, Galloway et al., 2012). As such, mitochondria are polymorphic organelles, although studies into the 3D shape of single mitochondria are uncommon and light microscopy methods often, and TEM certainly, do not provide the detail required to study the 3D shape. Not only do fusion

and fission serve to regulate mitochondrial number and morphology but they are also vital for distribution of mitochondrial DNA (mtDNA), and the maintenance of bio-energetic functionality (Griparic and van der Bliek, 2001, Osellame et al., 2012). Imbalance of fusion and fission leads to shifts in the morphology and loss of cell viability (Palmer et al., 2011). If left unregulated, increases in fission can lead to increased fragmentation, resulting in heterogeneous distribution of mtDNA, varied ATP production capabilities, increase in reactive oxygen species (rOS) production and an increase in the likelihood of apoptosis (Parone et al., 2008).

Fusion and fission will influence the individual shape of the mitochondria and also the overall morphology of the network. The functional requirements of the muscle, linked to fibre type, drive the action of fusion and fission. It is proposed that differences observed are due to differing metabolic constraints in the different fibres, for example the slow twitch fibres have a higher rate of fusion (Anderson and Neufer, 2006, Picard et al., 2008, Mitra et al., 2009, Tondera et al., 2009, Gomes et al., 2011, Mishra et al., 2015). In slow twitch fibres the mitochondria have been shown to be more elongated parallel to the sarcomeres with a higher proportion of branching (extensions from a mitochondrion) across the A band and I band (Kayar et al., 1988, Ogata and Yamasaki, 1997, Picard et al., 2012, Fujioka et al., 2013, Mishra et al., 2015). In comparison, the mitochondrial network in fast twitch fibres have been shown to be thinner and primarily along the sarcomeric I band, with limited branching across the A band (Ogata and Yamasaki, 1997, Picard et al., 2012, Mishra et al., 2015).

The location of mitochondria within the cell may also impact on the function, and possibly morphology, of the organelle. The skeletal muscle cell can be divided into 3 distinct areas, the sub-sarcolemmal (SS), between the cell membrane and the first myofibrils, intermyo-fibrillar (IMF), the central portion of the cell, and peri-nuclear (PN), the area surrounding the nuclei (including SS and IMF). Varying rates of protein import and ATP production have been noted based on the location of the mitochondria, higher in mitochondria at the periphery and higher in centrally located mitochondria respectively (Takahashi and Hood, 1996, Mollica et al., 2006). The mitochondria at each of these locations are also affected differently by stressors, such as exercise, fasting and aging (Bizeau et al., 1998, Mollica et al., 2006, Holloszy, 2008, Little et al., 2010, Crescenzo et al., 2014). Light microscopy and TEM studies have suggested that the mitochondrial morphology may differ between

mitochondria located at the SS and those in the IMF regions (Bakeeva et al., 1978, Kayar et al., 1988, Ogata and Yamasaki, 1997, Picard et al., 2013). SS mitochondria are proposed to have a higher proportion of circular mitochondria (Picard et al., 2013) and IMF mitochondria are narrower and extend through the sarcomeres, with more branching (Fujioka et al., 2013). However, it is now known the proportion or number of mitochondria that are situated at each location and how may this be influence by developmental muscle changes in different fibre types.

The morphology of individual mitochondria has been studied with the use of SBF-SEM, primarily in the context of mitochondrial disease in humans skeletal muscle (Vincent et al., 2016, Vincent et al., 2017, Vincent et al., 2019) and in normal mammalian muscle (Bleck et al., 2018). These studies have emphasised a variation in morphology of mitochondria present in skeletal muscle, for example the presence of nanotunnels (Vincent et al., 2017), which are involved in sharing of information between individual mitochondria but increase in number in disease cases, and an decrease in the complexity of the mitochondria (Vincent et al., 2019). The morphology of the mitochondria will have an impact on their function. It has been proposed that longer mitochondria have an increased interaction with other organelles and increased signalling across the cell and the larger the volume of the mitochondrion the greater internal functional capacity (Glancy et al., 2020). However, studies of the relationship between function and specific 3D morphology of individual mitochondria have not been performed yet and currently only assumptions can be made based on functional studies and a limited number of morphological studies.

Although all of these studies are important, they have been performed in a limited number of experimental settings, with regards to tissue type, species and technique., they do point to a need to explore arrangements of mitochondria in a broader range of circumstances. There are very few studies on morphology of individual mitochondria and the network. The majority of imaging methods either do not have the resolution capabilities required to differentiate individual mitochondria (light microscopy) or are not able to image in 3D (TEM) both needed to image the complex nature of the organelles and their network. However, with SBF-SEM individual mitochondria and the network can be imaged and reconstructed. There is limited research using SBF-SEM to examine the 3D structure, size and shape, of individual mitochondria, or the main features of the mitochondrial network, during the important biological process of skeletal muscle development and maturation.

#### *1.3.5. Choice of Experimental Animal Rationale (Guinea pig)*

Guinea pigs were used as the primary animal for studying muscles in the early days of muscle research (Peter et al., 1972, Gulati, 1976, Powell et al., 1984, Gorza, 1990). This was due to their muscular development being closer to that of human muscle development, when compared to development in other rodents, which are now primarily used due to their genetic amenability (rats and mice). New-born guinea pigs (usually only 1-3 per litter) are fully mobile and have a fully developed central nervous system, whereas mice and rats give birth to numerous pups (10-12 commonly) that require marked post-natal muscle maturation. Also, many physiological features of guinea pig pregnancy, and thereby the in-utero environment for fetal development, are closer to that of humans than mice or rats (van Kan et al., 2009, Dyson et al., 2012). These factors make guinea pigs a good animal to study skeletal muscle development with possible implications for human skeletal muscle development.

### *1.3.6. Hypothesis/Aims*

As detailed, mitochondrial morphology is vital for the function of a cell and even more so in the energy intensive musculoskeletal system. However high-resolution spatial mapping of the mitochondrial morphology, individually and as a network, in different guinea pig skeletal muscles, and how this may change with skeletal muscle maturation, has not been performed.

The overall hypothesis is that guinea pig skeletal muscle development will be accompanied by changes in mitochondrial morphology. It is proposed that the shape, size and branching of individual mitochondria and the proportions of sub-cellular localised mitochondria will change during fetal-to-adult development and maturation. Differences in these features of mitochondria will also be found between psoas and soleus skeletal muscle types. Stemming from studies showing the progression of fibre type differentiation occurring during fetal skeletal muscle development. The progression from primary to secondary muscle fibres during early to middle gestation, followed by fibre type differentiation, will result in different mitochondria shape, size and branching during development. Mitochondria will go from simple to more complex organelles based on this. The progression of the psoas and soleus muscle will also differ due to the different fibre type composition present in the two muscles.

With the use of SBF-SEM and subsequent segmentation, 3D reconstruction and quantitative analysis, a comprehensive assessment of mitochondria shape and size (relative to cell size) will be performed. This will be done in conjunction with a similar analysis of size and shape changes with muscle maturation of another intracellular organelle, the nucleus. From studies into muscle growth and regeneration in adult muscle cells the ratio between nuclei and cell volume stays the same during these processes. It can be hypothesised that cell to nuclei volume ratio is set early in gestational age and maintained throughout fetal and into post-natal development.

A rigorous, quantitative analysis of this type has yet to be performed along with the deposition of all raw data for public access and future use. Doing so will enable testing of the above hypothesis to provide valuable biological information concerning the processes accompanying skeletal muscle development. Not only this, but it will also establish a protocol for the imaging and analysis of skeletal muscle mitochondria (applicable to other organelles and even other tissue types) in differing experimental scenarios.

## Chapter 2. Methods

### 2.1. Staining Protocol and Pin Preparation

#### 2.1.1. Locust Optic Lobe

An adult locust (*Locusta migratoria*) was anaesthetised on ice, the brain dissected out in cold insect ringer solution and placed in 2% formaldehyde, 2.5% glutaraldehyde in 0.1M sodium cacodylate buffer. The brain was then halved, as shown in Figure 2.1, and processed using an adapted version of the (Wilke et al., 2013) protocol described in (Wernitznig et al., 2016). The brains were washed in 0.1M sodium cacodylate pH7.4 followed by a solution of 3% potassium ferrocyanide with 1% aqueous osmium tetroxide in ddH<sub>2</sub>O for 30 minutes. This was followed by filtered 10% thiocarbohydrazide (TCH) for 1h and then secondary 1% osmium tetroxide for 30 minutes. The samples were then placed in 1% uranyl acetate at 60° for 2 hours followed by lead aspartate solution, 0.12g of lead nitrate in 20ml aspartic acid overnight. The samples were washed in several changes of ddH<sub>2</sub>O between each step.

The samples were dehydrated with acetone, 25%, 50%, 75% and 100%, and infiltrated with increasing concentrations of TAAB 812 hard resin, 25%, 50%, 75% and 100%, in acetone with several changes of 100% resin. The samples were embedded into 100% resin in coffin moulds and left to polymerise at 60°C for a minimum of 36 hours. The brains were orientated with the protocerebrum closest to the top of the resin block, example shown in Figure 2.1. Using an ultramicrotome (Reichert) and a diamond knife the block was serially sectioned, at 1µm, stained with toluidine blue and viewed under a light microscope. The protocerebrum and optic stalk were sectioned all the way through until the lobula was reached. At this point several 70nm sections were taken, placed on a copper grid and viewed on a CM100 TEM (FEI). This was done to check tissue morphology, orientation of the sample and penetration of the staining (detailed further in 2.4.1.-2.). The blocks were further trimmed to approximately 0.75mm by 0.75mm and glued onto a pin. To reduce charging within the SEM, the block was painted in silver paint and sputter-coated with a 10nm layer of gold, shown in Figure 2.1(E).

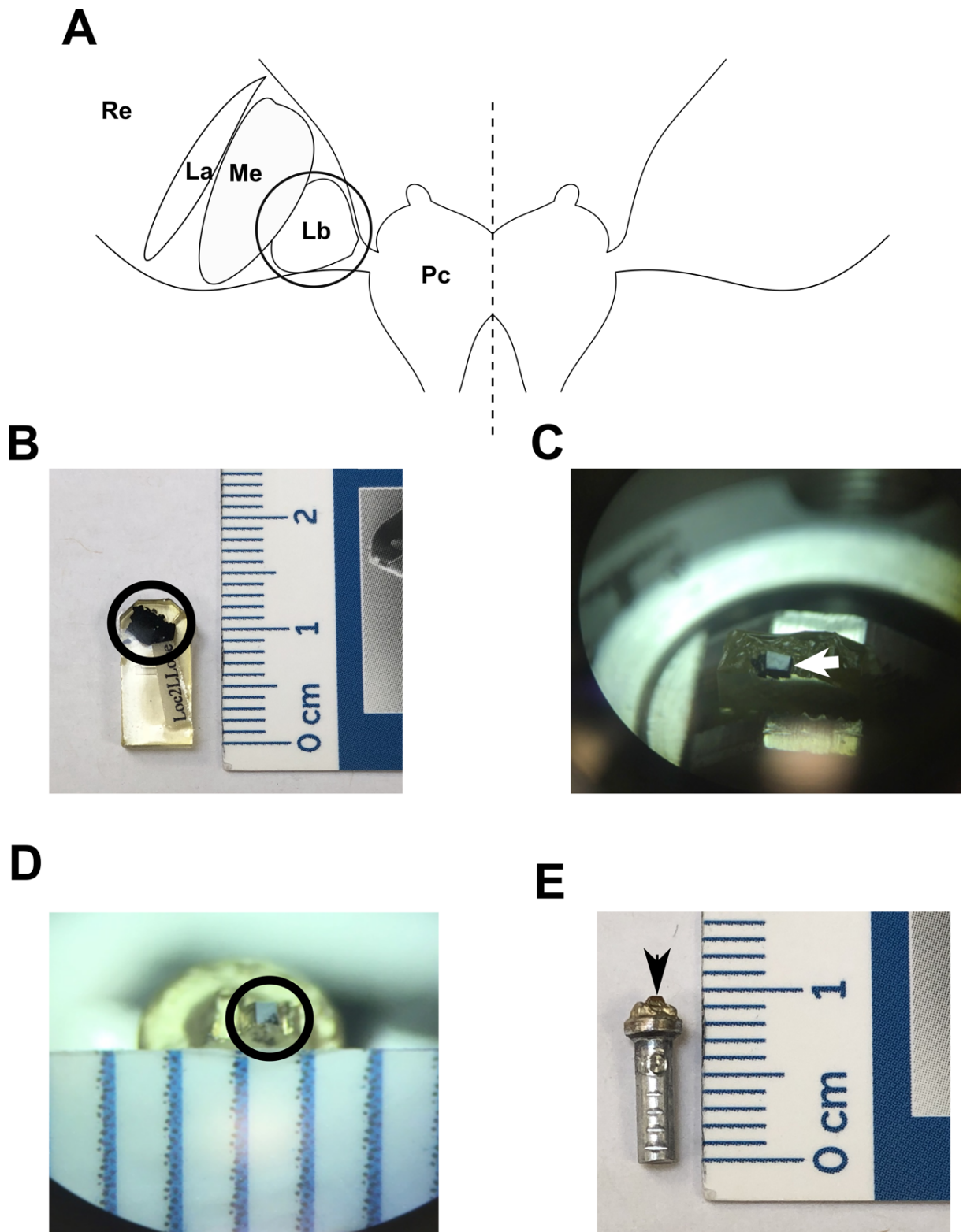


**Figure 2.1 – Sample preparation of locust brain for SBF-SEM.** (A) Diagram of locust brain. The brain is halved during dissection, indicated by the line. The lamina (*La*) is closest to the retina (*Re*), followed by the Medulla (*Me*) and the area of interest the Lobula (*Lb*), circled, closest to the protocerebrum (*Pc*). (B) Example of half a brain embedded in resin, circled. (C) Shows example of resin block trimmed to trapezium for ultrathin sectioning, indicated with white arrow, and (D) further trimming after being glued onto a pin, circled. (E) Is an example of a pin with sample that has been gold coated and is ready for viewing on 3View system. Arrow indicates where the sample is placed on the pin.

### *2.1.2. Guinea Pig Skeletal Muscle*

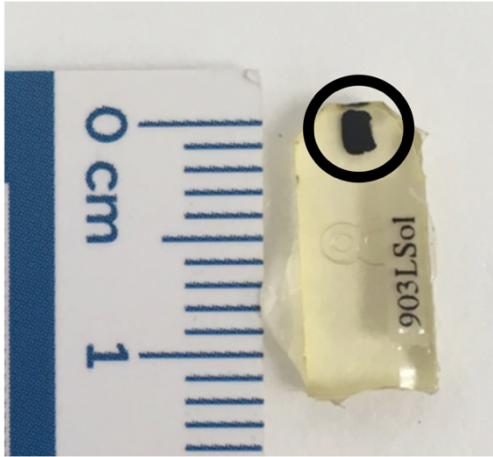
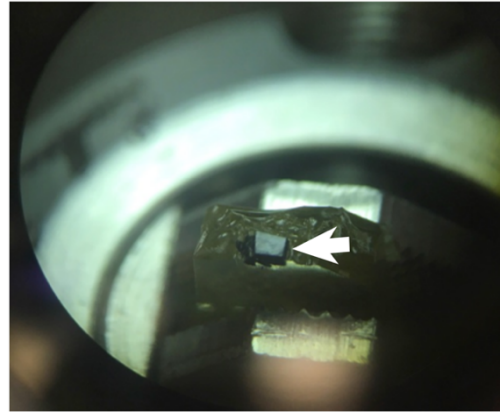
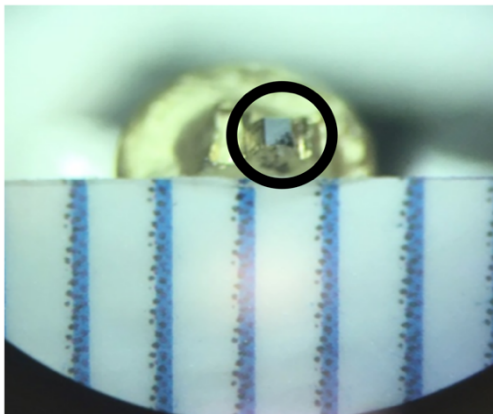
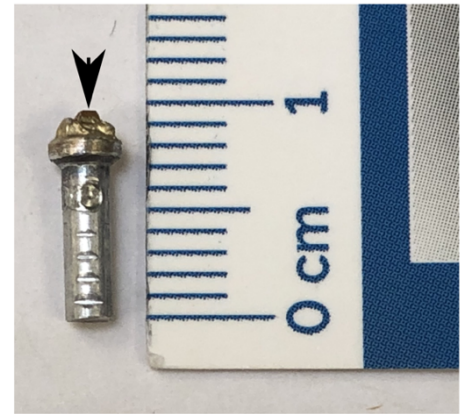
Skeletal tissue (psoas and soleus muscles) was collected from adult pregnant and non-pregnant females and piglets at gestational ages 50 to 65 days Duncan Hartley guinea pigs terminated under licensed procedures according to the Animals Scientific Procedures Act 1986 (ASPA). An incision was made in the skin at the point of the inner leg. With microdissection scissors, the skin was cut along the length of the inner leg to the thigh. The gastrocnemius muscle was teased apart to expose the underlying soleus muscle which removed and micro-dissected, ~2mm by 3mm rectangles, into 2% glutaraldehyde with 0.1M sodium cacodylate buffer pH7.4 and left for a minimum of 12hrs in the fixative at 4°C. The animal was placed on its front and an incision in the skin made from the abdomen down to the upper thigh. A portion of psoas muscle was carefully removed from the lower abdominal area and placed in the same buffer for microdissection. The samples then underwent a heavy metal staining protocol (Wilke et al., 2013). The tissues were washed in 0.1M sodium cacodylate pH7.4 and then a solution of 3% potassium ferrocyanide with 2% aqueous osmium tetroxide in ddH<sub>2</sub>O was added for 1 hour. This was followed by filtered 10% thiocarbohydrazide (TCH) for 20 minutes and then secondary 2% osmium tetroxide for 30 minutes. The samples were then placed in 1% uranyl acetate at 4°C overnight followed by lead aspartate solution (0.12gs of lead nitrate in 20ml aspartic acid) for 30 minutes. Between each step the samples were washed in several changes of ddH<sub>2</sub>O. The samples were dehydrated with acetone, 25%, 50%, 75% and 100% and then infiltrated with increasing concentrations of TAAB 812 hard resin in acetone, 25%, 50%, 75% and 100%, with several changes of 100% resin. The samples were embedded in transverse orientation into 100% resin and left to polymerise at 60°C for a minimum of 36 hours.

The resin blocks were trimmed using a razor blade to form a trapezoid block face, Figure 2.2. Using a diamond knife, 1µm sections were taken on a Reichert ultramicrotome and stained with 1% toluidine blue (until a gold ring forms around the toluidine blue) and viewed under a light microscope. Several 70nm sections were taken, placed on a copper grid and viewed on a TEM (Philips (FEI) CM100 100kV). This was done to check tissue orientation, which needed to be in transverse orientation, and morphology to ensure membranes and organelles had not been damaged during collection and processing, e.g., swollen or 'blown' mitochondria. The penetration of the heavy metal staining was also checked, making sure the contrast was consistent across cells and within the cells, particularly in deeper portions. The



blocks were then further trimmed to ~0.75mm by 0.75mm and glued on to a pin. In order to reduce sample charging within the SEM, the block was painted with silver paint and sputter-coated with a 10nm layer of gold, Figure 2.2(E).

Details of all protocols and chemicals used can be found in Appendix B – D.

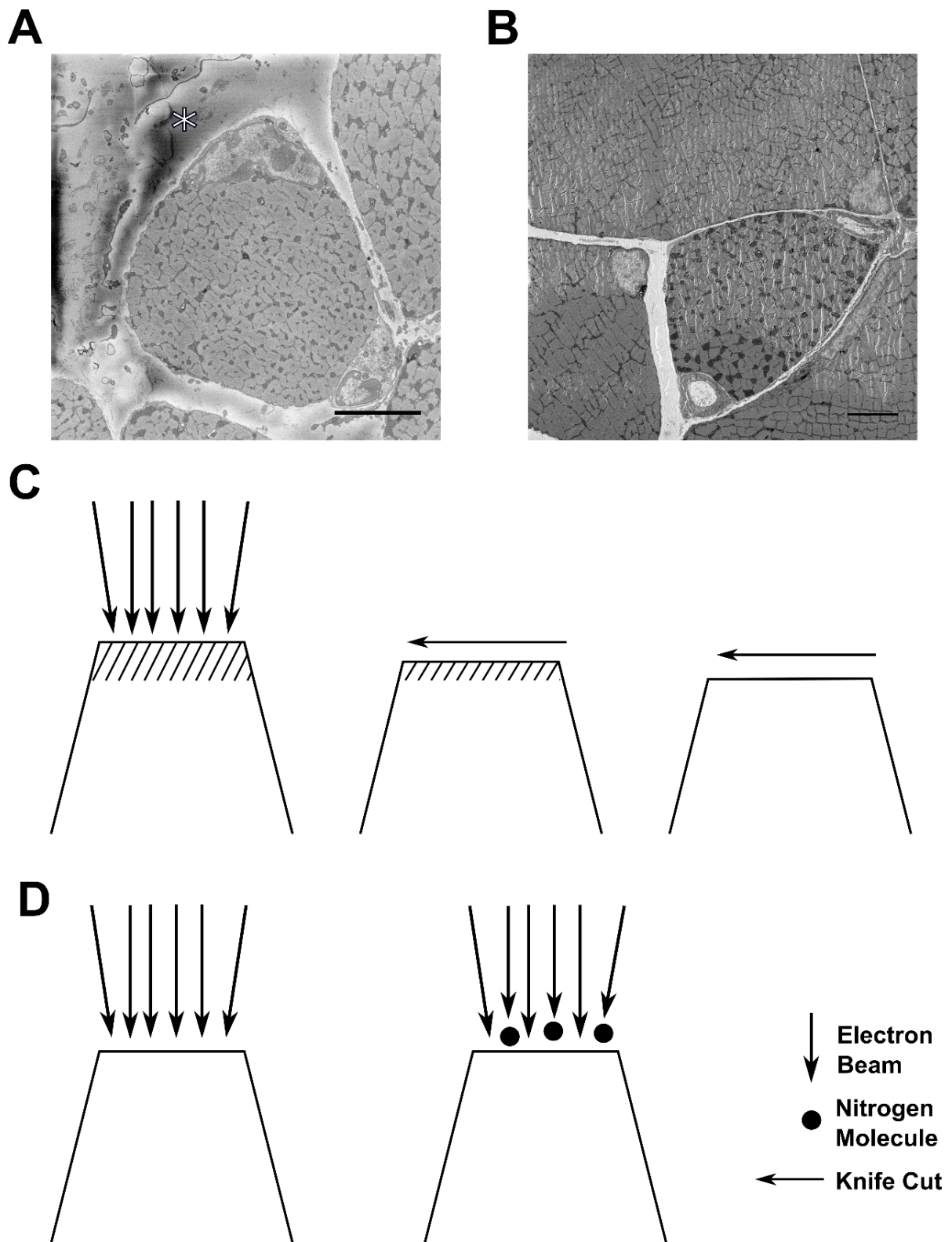
**A****B****C****D**

**Figure 2.2 – Sample preparation of skeletal muscle for SBF-SEM.** (A) The sample, *circled*, was embedded into hard resin and polymerised, placed as close to the edge of the resin block. (B) Using an ultramicrotome the block was trimmed and shaped into a trapezium for sectioning and viewing the sample, indicated with white arrow. (C) The tip of the block was sawn off, the sample was glued onto a pin, trimmed further, ~0.75mm by 0.75mm, painted with silver DAG and coated in gold, *circled*. (D) Shows an example of a gold coated pin ready for viewing on 3View system. Arrow indicates where the sample is placed on the pin.

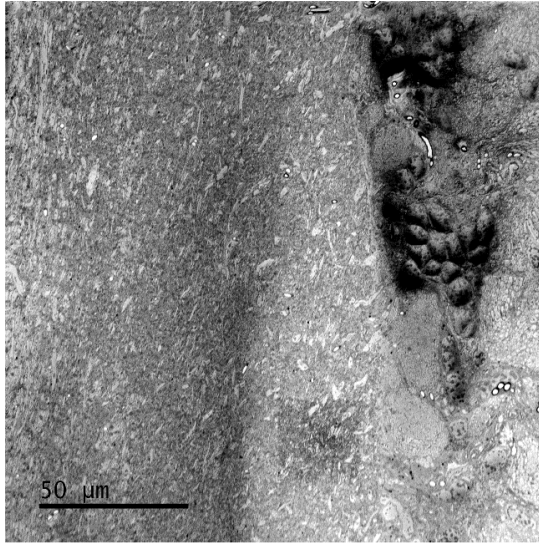
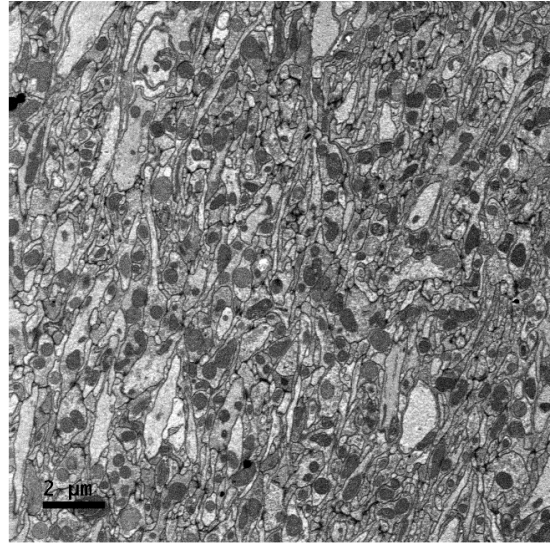
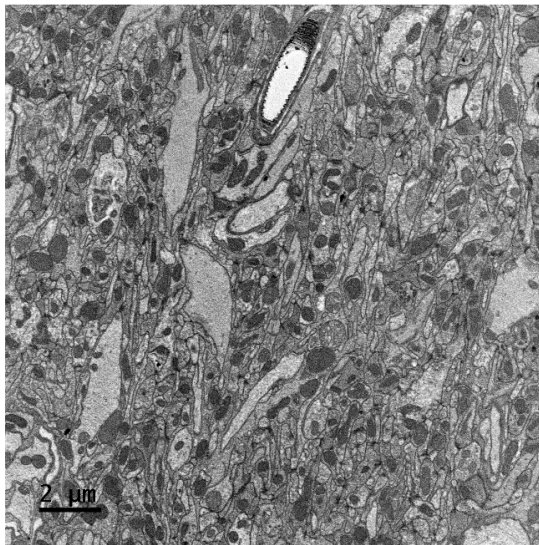
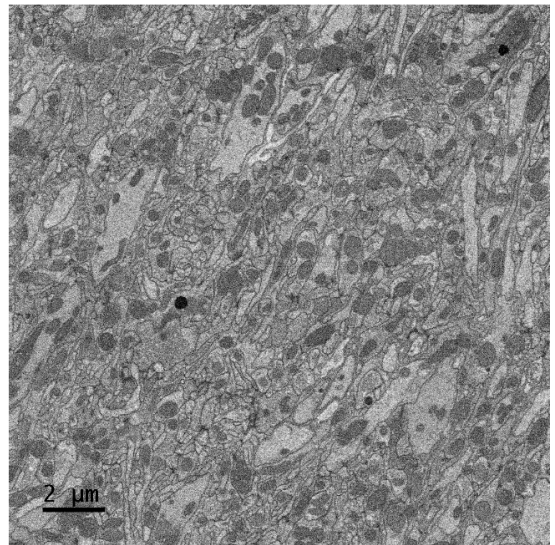
## 2.2. Imaging Parameters Refinement

All datasets were collected on a Zeiss Sigma SEM VP (Zeiss, Cambridge, UK) combined with Gatan 3View system (Gatan inc. Abingdon, UK). There are a number of different parameters that can be changed that relate to the sample to be collected. These are the accelerating voltage of the electron beam (kV), the variable pressure (pA) (specific to this setup), the pixel dwell time, resolution, image size and section thickness. A number of these parameters are related to each other, changing one will affect another, and can alter the image quality. The parameter settings were tested for both guinea pig muscle and locust brain samples and in regard to the aims of the respective experiments.

The first parameters to be tested were the kV and pA. Although SEMs can be operated under high vacuum, this can lead to a build-up of excess electrons in the resin block resulting in charging, even with the use of silver and gold to dissipate the charge. Charging manifests as an overly bright (dark in the resulting image) area that distorts the image and decreases the stability of the resin when cutting (Figure 2.3(A and B)). This can occur in samples with a high amount of resin (guinea pig skeletal muscle) or potentially poor resin infiltration, due to size and density of the sample (locust brain). The kV is an indicator of the depth at which the electrons will penetrate the sample, the higher the kV the higher the penetration depth. Resin will soften under the electron beam and the amount of resin that is affected will therefore depend on the penetration depth of the electron beam. Providing the section thickness is greater than the depth of beam penetration the softened resin will be removed, and the cutting of the sample will remain stable. If, when the section is cut, the full depth of the softened resin is not removed it can cause degradation of the resin and result in a build-up of charge. This can be counteracted by increasing the section thickness to remove the affected resin (Figure 2.3(D)). Another way to counteract the effect of the electron beam on the sample is by introducing a small amount of nitrogen into the SEM chamber. The excess electrons can be 'absorbed', and the charging removed (Figure 2.3(C)). However, increasing the amount of nitrogen molecules in the chamber will reduce the number of electrons that reach the detector. This will have an effect on image quality, most notably seen in the contrasting of the images, shown in Figure 2.4.



**Figure 2.3 – Examples of resin degradation and methods used to overcome.** (A) Shows example of charging that occurs in areas of empty resin surrounding a muscle cell (asterisk '\*'). (B) Example of continued impact of the electron beam on the tissue, causing wrinkling and damage to the resin. (C) One way in which to combat this is to increase the thickness of the section in order to remove all of the resin affected by the electron beam penetration, indicated by the shaded area. (D) Second method is to increase the nitrogen present in the chamber in order to limit the amount of electron beam interacting with the block surface. Scale bars are 5 $\mu$ m.

**A****B****C****D**

**Figure 2.4 – Impact of pressure on image contrast.** (A) – (D) Show examples of images taken at different pressures, pa, from high vacuum (A), 10pa (B), 20pa (C) and 30pa (D). As the pa increases there is a gradual loss of resolution and contrast from the images.

The next parameters tested were, magnification, resolution, image size and pixel dwell time. These factors have a direct impact on the quality of images acquired. Changing the dwell time will affect the noise of the final image, as the electron beam spends more time on the sample surface, the larger the number of resulting back scattered electrons and thus more information gained in regard to the structures in the sample. The result is an image where the contrast is starker between different structures but will increase acquisition time, shown in Figure 2.5. The magnification, resolution and image size are linked in such a way that changing one will affect another. When a resolution and magnification is chosen the size of the image required will be according to these two factors. If the magnification is altered, but the image size remains the same the resolution will change. Examples of this relationship are shown in Figure 2.6. Again, when taking images at high magnification, resolution and long dwell time this will affect the resin, which was taken into consideration when deciding these parameters.

**A**

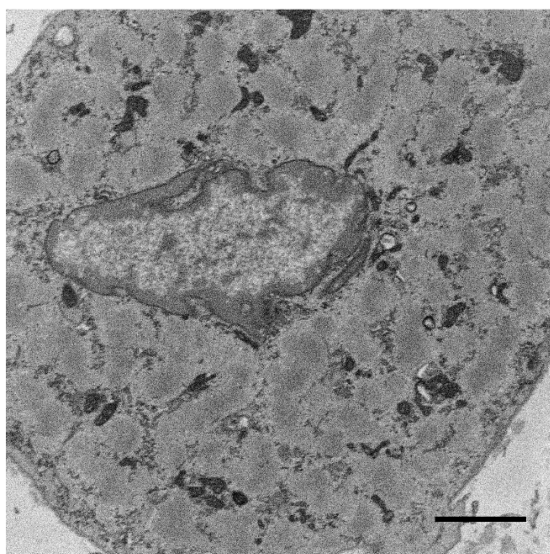


Image Size: 2000x2000  
Resolution: 6nm  
Magnification: 6.27kx  
Dwell Time: 5 $\mu$ s/pixel  
Time: 20.06secs

**B**

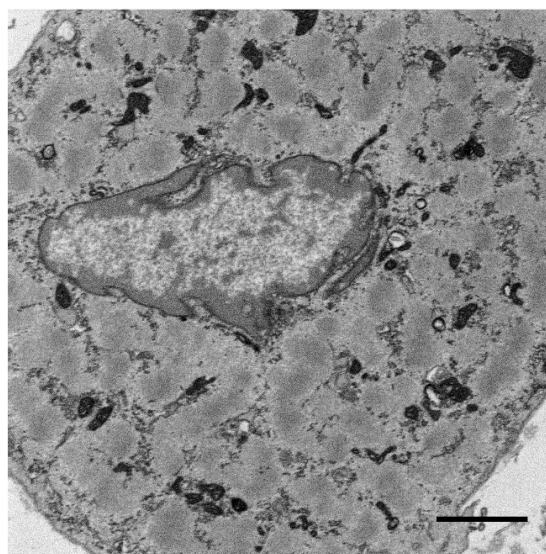
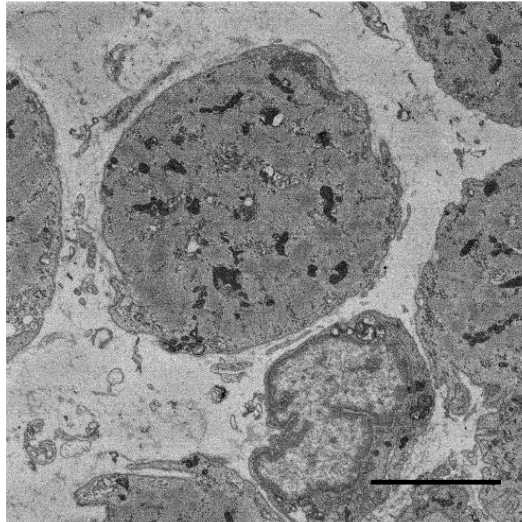


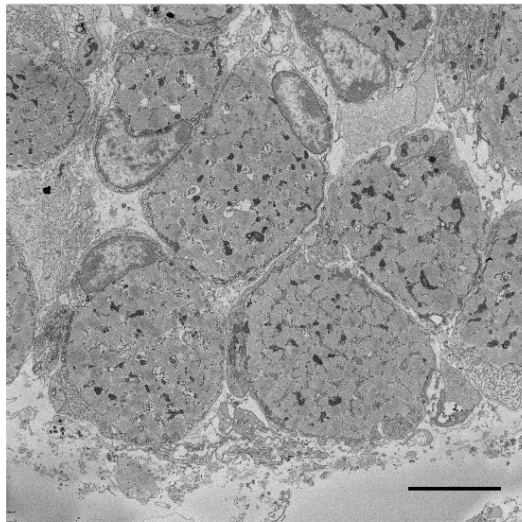
Image Size: 2000x2000  
Resolution: 6nm  
Magnification: 6.27kx  
Dwell Time: 20 $\mu$ s/pixel  
Time: 80.06secs

**Figure 2.5 – Pixel dwell time alterations and noise.** (A) An image of a muscle cell taken at 5 $\mu$ s per pixel and (B) the same area imaged at 20 $\mu$ s per pixel. The increase in dwell time decreases the noise but increases the time taken to scan a whole section. Scale bar is 5 $\mu$ m.

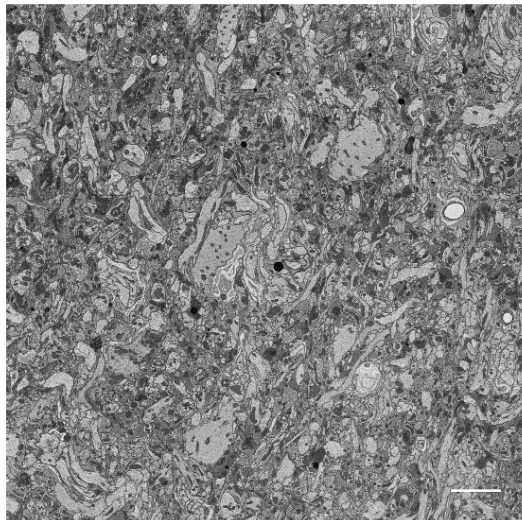


**A**

**Image Size: 2500x2500**  
**Resolution: 8nm**  
**Magnification 3.82Kx**

**B**

**Image Size: 3500x3500**  
**Resolution: 8nm**  
**Magnification 2.64Kx**

**C**

**Image Size: 6000x6000**  
**Resolution: 8nm**  
**Magnification 1.53Kx**

**Figure 2.6 – Relationship between magnification, resolution and image size.** (A) – (C) show examples of datasets collected at the same resolution but different image sizes and magnifications to highlight the relationship between the three parameters. If the magnification is reduced but the resolution is to be maintained, the image size has to change in accordance and vice versa for all the parameters. All Scale bars 5 $\mu$ m.

Another factor to consider when deciding upon the imaging parameters is the computing power available for the subsequent analysis. An image at high resolution and low magnification requires a large image size, therefore will be a large file, and a long series of images (regardless of size) can be difficult for the analysis software to handle. To decide upon all the different parameters, the type of information to be collected needs to be known. For the two biological questions the process of deciding upon the parameters used is discussed in the following sub-sections.



### 2.2.1. Locust Optic Lobe Parameters

The aim for the locust project was to follow identify and map the connections of the TmA neurons synapsing onto a portion of the LGMD 2 neuron. To undergo this, the LGMD 2 neuron had to be located and imaged, as well as the TmA neurons synapsing upon the LGMD 2 which had to be followed through the neuropil as far as possible to identify individual TmA neurons. For this a large area had to be imaged at a resolution at which synapses and small TmA neurons could be visualised. A range of resolutions was tested and the one at which both synapses and TmA neurons could be seen, and did not restrict the image size and magnification, was determined to be 8nm. Although arrived at independently, this was consistent with what had been used by other research groups working with *Drosophila* brains (Takemura et al., 2017). Once the resolution was decided upon, the size of the imaging area was tested and established. Firstly, the use of multiple regions of interest were tested. However, during the test imaging the resin became distorted at the areas of overlap, required for stitching the areas together. This occurred regardless of when the kV was decreased, the pA increased, or slice thickness increased. This was most likely due to lack of full resin infiltration, common in dense brain tissue. Therefore, it was decided that imaging a single large area was the best option. Short serial image runs were used to test different image sizes and stability of the imaging. From this, it was found that an image of 6000 by 6000 pixels at 8nm resolution gave a large enough area to follow a branch of the LGMD 2 neuron and the afferents synapsing with it.

After the imaging parameters had been decided upon, the next parameter to be tested was the slice thickness. As the synapses and processes of the afferent neurons are small, a thin section would ensure that the small processes could be followed (some studies of neurons have been sectioned at 25nm (Helmstaedter et al., 2013)). However, during the test runs cutting was not consistent and the resin became damaged when the thickness was dropped to 50nm or below. Thus, a section thickness of 60nm was chosen. At this thickness the cutting was stable and the synapses and TmA neurons could be seen and followed through the dataset.

Overall, the images were obtained at 2.5kV accelerating voltage, with an aperture of 30µm, at 20Pa. The block was sectioned at 60nm thickness, and the images recorded at a magnification of 1.5Kx, with an image size of 6000 by 6000 pixels, 20µs/pixel dwell time and a resolution of 8nm. The block was then imaged for 500 sections (Table 2.1).

**Table 2.1 – Imaging parameters used.** Comparison of parameters used for locust optic lobe and guinea pig skeletal muscle datasets.

	Accelerating Voltage (kV)	Pressure (pa)	Dwell Time ( $\mu\text{m}$ /s)	Image Size in X and Y (pixel)	Resolution (nm)	Section Thickness (nm)	Total Dataset Size
Locust Brain	2.5	20	20	6000x6000	8	60	16GB
Guinea Pig							224.4GB (4-
Skeletal	2.5-5	20-53	20	2500x2500-	7-28	70	12GB per
Muscle				5000x5000			dataset)

### *2.2.2. Muscle Parameters*

The muscle samples also underwent parameter testing. Once a sample was placed in the SBF-SEM the sample surface was visually scanned for muscle fibres in transverse orientation. Although the fibres had been orientated during resin embedding resin, the orientation of the tissue can change during polymerisation and pin preparation. For each run three muscle fibres were imaged simultaneously, using the multiple regions of interest function. The imaging parameters used were chosen based upon the size of the cell, the imaged area had to encompass the entire cross-section and portion of surrounding area of the cell. As the fibres were often oblique and truly vertical in the Z direction, the cell would not remain in the centre during imaging but 'drift'. The resolution required depended on the appearance of the mitochondria and nuclei, ensuring they were identifiable. The magnification and required resolution were decided upon and the final image size, which is dependent on these two factors, was adjusted accordingly (Table 2.1).

Thinner sections give more detail in the Z direction and show smaller changes in structures, for example the cristae of the mitochondria or the endoplasmic reticulum. From the aim of the muscle project only the overall 3D structure (shape, surface area and volume) of the mitochondria, nuclei and cell were needed. All of these structures can extend for a large number of sections, so a thick section was not required. The muscle samples also had a high amount of empty resin surrounding the cells. Therefore, the samples were at a higher risk of having a large amount of charging, resin distortion and inconsistent cutting. For this and the above reason 70nm section thickness was chosen.

Overall, the cells were imaged for a minimum of 250 sections at 70 nm section thickness, 2.5 to 5Kv accelerating voltage, a variable pressure between 20 and 53pa and a dwell time of 20µm/s. The size of the image ranged from 2500x2500 pixels up to 5000x5000 pixels and the resolution ranged from 7nm to 10nm with 8nm the average resolution used.

### 2.3. Optimisation of Image Analysis

Prior to analysis of the datasets collected, the best method(s) for analysing the data was found. Three software programs were chosen, based on accessibility, usage and segmentation and analyses tools available. The three chosen were TrakEM2, a Fiji plugin, (Cardona et al, 2012) combined with Blender, (Neuromorph tools, Jorstad et al. (2015)) an open software platform for reconstruction (collectively referred to in the Results as 'Fiji'); Microscopy Image Browser, MIB, a recently developed free software (Belevich et al., 2016); and Amira, a licensed software commonly used for analysis (<https://www.fei.com/software/amira-for-life-sciences/>). Then, using an example skeletal muscle dataset, each of the software packages and the segmentation tools were tested. Protocols were developed on how to use the programs (see Appendix E and in Cocks et al., 2018) and a workflow for choosing the best segmentation tools with respect to particular experimental objectives was created. The raw datasets used in this testing can be accessed via the EMPIAR website:

<http://www.ebi.ac.uk/pdbe/emdb/empiar/> (Accession code: EMPIAR-10092).

The analysis was performed on a Toshiba laptop with Intel® Core i7-5500U CPU, 2.40 GHz, 16 GB RAM and 64-bit processor. Videos pertaining to the steps can be found under Supporting Information at <https://doi.org/10.1111/jmi.12676>.

### 2.3.1. Software Comparison

Figure 2.7 shows a series of SBF-SEM images from the psoas skeletal muscle (fetal day 60-64). This example dataset was used to show different image analysis programs and protocols. From the data, the nucleus, nucleolus, chromatin and mitochondria were segmented using the segmentation tools detailed in Appendix E. The types of tools and functions can vary between the software available and a comparison between Fiji, Amira and MIB is shown in Table 2.2.

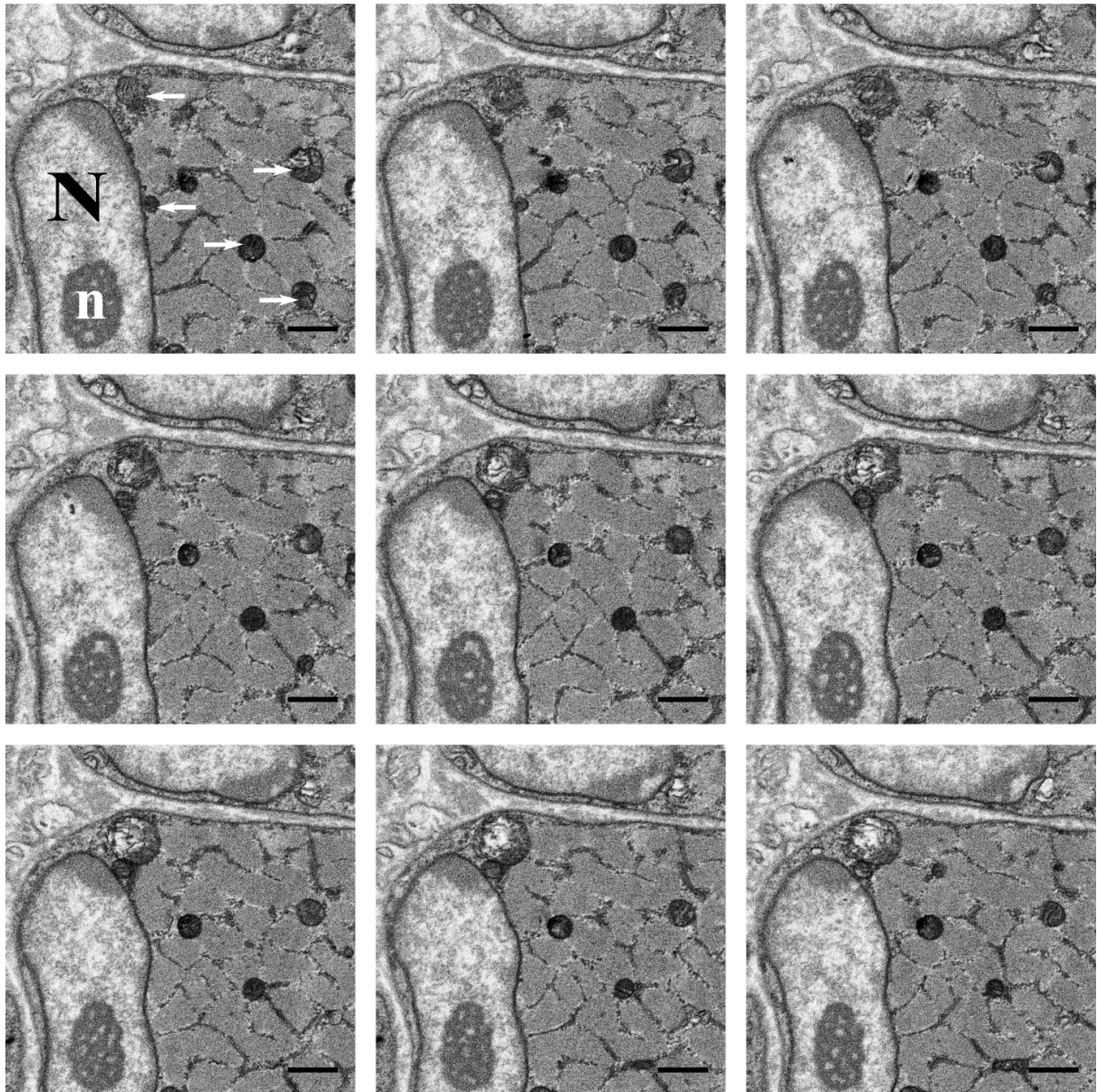


**Figure 2.7 – Example of SBF-SEM image series.** Nine consecutive images (viewed from left to right) at 70nm section thickness from a stack of 93 serial images of a portion of a skeletal muscle psoas cell from day 60-64 Fetal guinea pig. In the first image the nucleus can be seen, labelled with an 'N', as well as the nucleolus, white 'n', and the mitochondria, labelled with white arrows. All scale bars 1  $\mu$ m.

**Table 2.2 – Comparison of imaging programs.** Examples of the different types of image formats and segmentation tools offered by three analysis programs

	<b>Fiji</b>	<b>Amira</b>	<b>MIB</b>
<b>Image import format</b>	.tif, .dm3, .png, .bmp	.tif, .png, .bmp	.tif, .dm3, .dm4, .png, .bmp
<b>Object export format</b>	.obj	.am, .surf	.am, .tif, .mat, .model, .stl, .mrc, .mod, .nrrd, .h5
<b>Manual Brush</b>	✓	✓	✓
<b>Interpolation</b>		✓	✓
<b>B/W thresholding</b>		✓	✓
<b>Magic wand thresholding</b>		✓	✓
<b>Watershed/SLIC segmentation</b>			✓

A timing analysis was performed over 20 slices for each of the different methods used to segment an individual mitochondrion and a nucleus from adult or fetal skeletal (psoas) muscle (see Table 2.3). For Fiji (TrakEM2) the only method available for segmentation is the manual brush tool, which was used. For Amira and MIB manual segmentation (every 5<sup>th</sup> section) was combined with interpolation for the nucleus, which was faster than manual segmentation performed in Fiji. For the mitochondrion the fastest method found was the thresholding method used in Amira, Overall, the semi-automated tools segmented the structures fastest. However, it has to be noted that the speed of the semi-automated procedures is dependent on the computing power available.

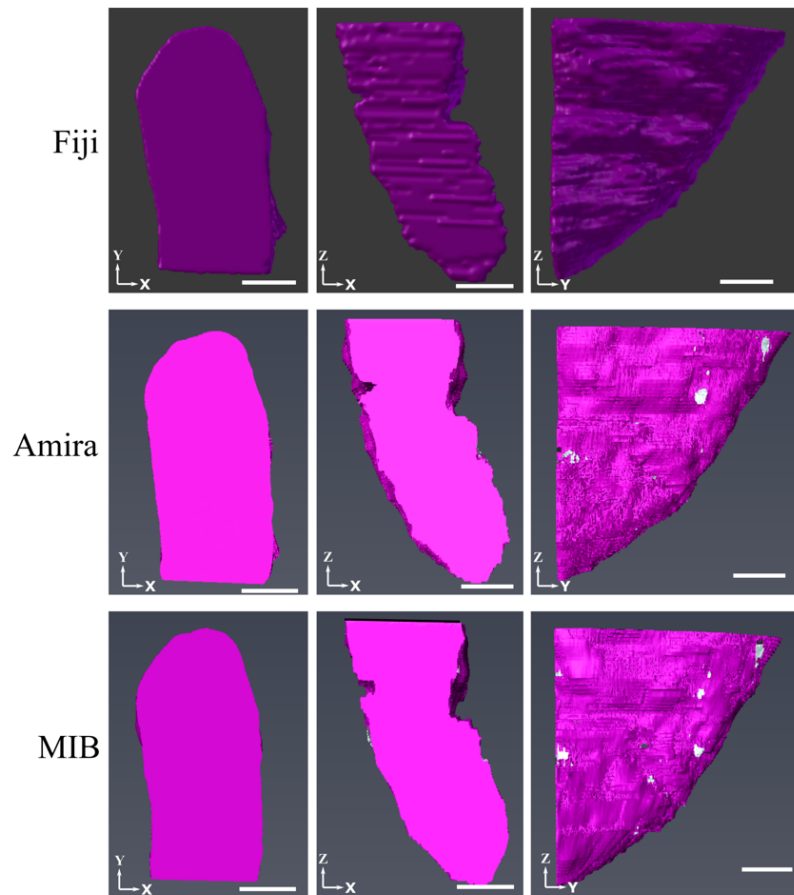
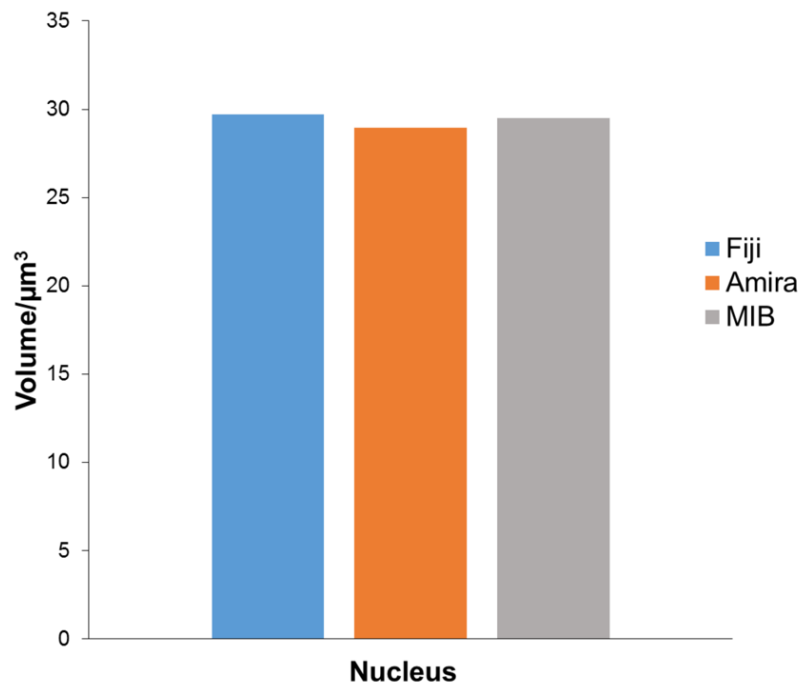
**Table 2.3 – Timing analysis results.** The table shows the results from the timing analysis (in seconds) performed on a small portion of the skeletal muscle dataset (20 slices) in each of the programs shown. It was performed on a Toshiba laptop with Intel® Core i7-5500U CPU, 2.40 GHz, 16 GB RAM and 64 bit.

		<b>Fiji</b>	<b>Amira</b>	<b>MIB</b>
<b>fetal</b>	Nucleus	6.29	3.21	2.12
	Mitochondrion	9.14	9.22	26.44
<b>Adult</b>	Nucleus	10.52	5.35	3.07
	Mitochondrion	37.14	4.28	62.39

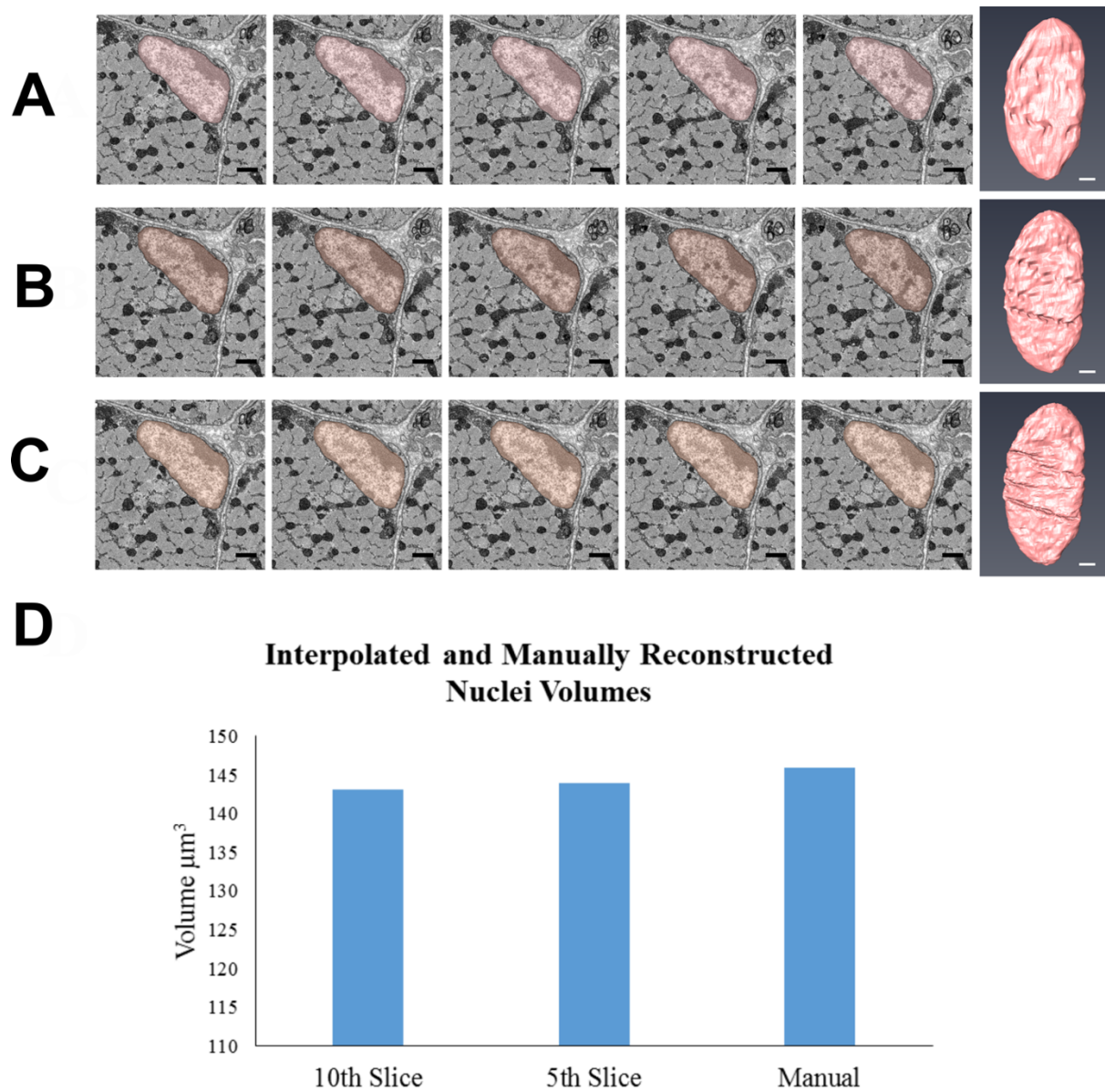
### *2.3.2. Segmentation Workflow*

The first structure to be segmented from the test dataset was the nucleus. It was segmented manually in Fiji and with the use of interpolation (semi-automated method) in Amira and MIB. Both the 3Dr reconstructions and volumes similar were are similar between each of the programs (Figure 2.8). Although interpolation sped up the segmentation process, errors occurred on the interpolated slices. These errors required manual correction and added to the overall time taken of the segmentation. Further analysis was performed to test the accuracy of the interpolation in MIB, comparing the uncorrected interpolated nuclei to a manually segmented one (Figure 2.9). The level of detail differed between each of the models; the folds of the nuclear membrane were not as detailed in the interpolated models as in the manually segmented one. However, the volumes of the nuclei from the quantification analysis were similar, with only 1.98% difference between the corrected and then every 10th slice (1.37% difference between the corrected and then every 5th slice). Overall, for bulk quantification analysis, interpolation without corrections can be used and if finer details are required a combination of interpolation and manual correction can be used.



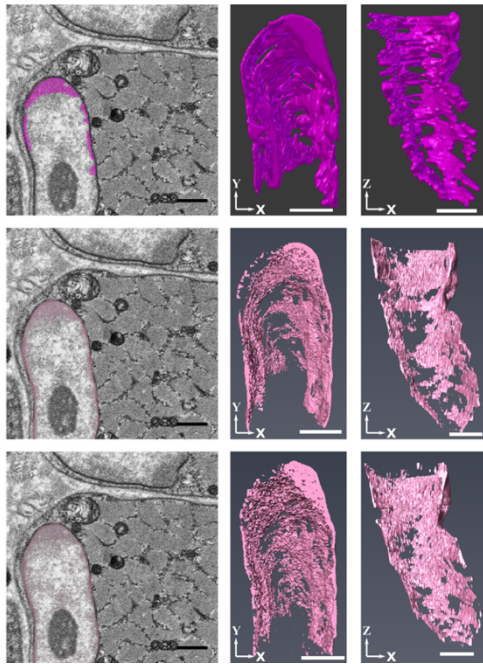
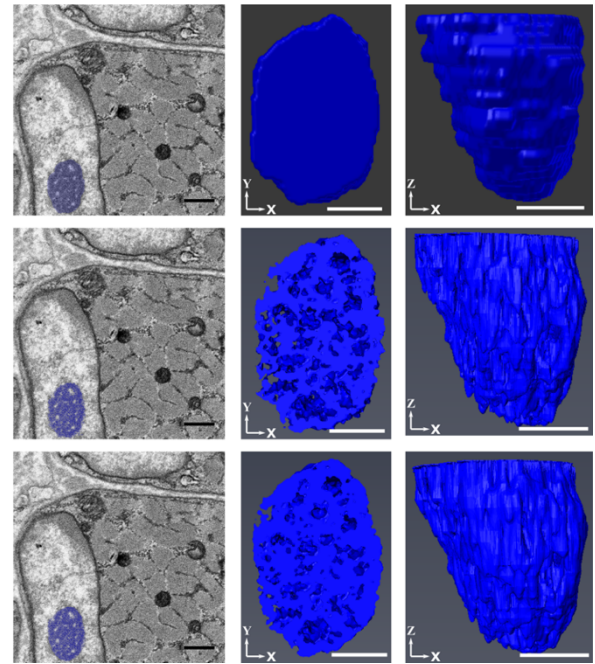
**A****B**

**Figure 2.8 – Examples of digital reconstruction of nuclear volume.** (A) Reconstructions of the nucleus from foetal psoas at different orientations from the segmentations performed in Fiji, Amira and MIB. (B) Shows the volume measurements of the nucleus from each of the programs. Scale bars 1  $\mu\text{m}$ .



**Figure 2.9 – Analysis of accuracy of interpolation method for segmentation.** (A), (B) and (C) each show 5 images with the nucleus segmented and the final reconstruction of the nucleus, from late foetal psoas, all performed in MIB. (A) Shows the nucleus segmented using interpolation when every 10th slice has been manually segmented, (B) from every 5th slice and (C) is a nucleus which has been segmented manually. Volumes from each of the segmentations. All Scale bars 1  $\mu\text{m}$ .

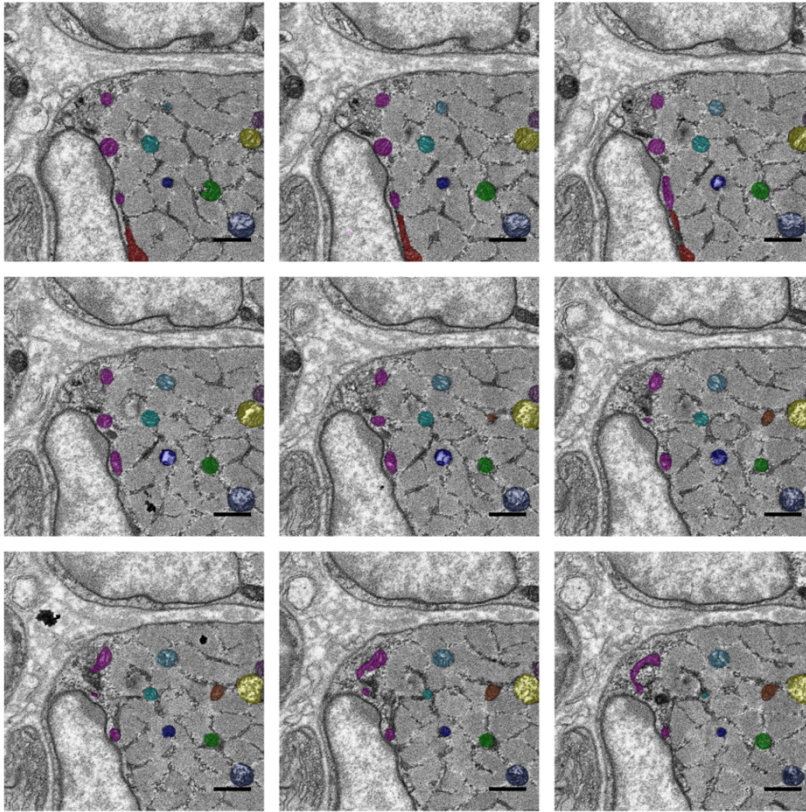
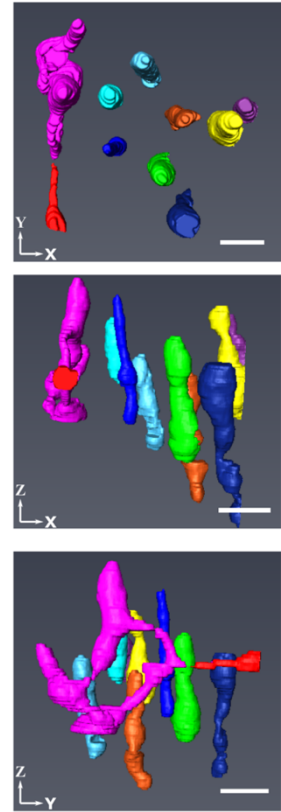
After the nucleus, the darker and dense chromatin and nucleolus within the nucleus was segmented. The segmentation and the final reconstruction can be seen in Figure 2.10. In Fiji, as with all of the structures, manual segmentation was used. In Fiji the object is segmented in layers whereas in MIB and Amira the pixels can only be assigned to a single object. When using MIB and Amira for inner structures, like chromatin and nucleolus, the order of the segmentation is important. In both MIB and Amira the chromatin and nucleolus were segmented using the thresholding tool, to select the darker pixels within the nucleus. The chromatin was thresholded first (Figure 2.10(A)). During this step the nucleolus was also selected, as the pixels are of a similar contrast. By then segmenting the nucleolus, the pixels were reassigned to the nucleolus object (Figure 2.10(B)). During the thresholding of the chromatin in both Amira and MIB, there were errors in the selection, often the dark nuclear boundary was also selected. These errors had to be corrected manually. As seen in the raw images, the nucleolus consists of both light and dark pixels and appears as a web-like structure. When thresholded, only the darker pixels were selected, causing gaps in the model, whereas during manual segmentation, the entire nucleolus area was segmented. The thresholded models in MIB and Amira showed the web-like appearance which was not seen in the manual segmentation. This is an example of when thresholding can be used to show intricate internal structures of an object. Overall, for the thresholding procedure to be effective, there needs to be sufficient contrast within the images and between structures. Although, manual alterations can be made after thresholding to ensure that the correct selection is made.

**A****B**

**Figure 2.10 – Examples of reconstruction of chromatin and nucleoli.** (A) 3 single images from the data series with the chromatin segmented and the reconstructions at different orientations performed in each of the image programs, Fiji, Amira and MIB, scale Bars are 1  $\mu\text{m}$ . (B) 3 single images from the data series with the nucleolus segmented and reconstructions of the nucleolus from the 3 programs. Scale Bars are 0.5  $\mu\text{m}$ .

Once the nuclei and associated structures were completed, the mitochondria were segmented. Mitochondrion can extend through many sections but due to their small size and complexity (Figures 2.11(A) and (B)) the decision was made not to interpolate. Instead, the mitochondria were thresholded in Amira and MIB and manually reconstructed in Fiji (Figure 2.12). In the raw images it can be seen that mitochondria consist of a range of contrasts due to the detail of the cristae (appearing as dark inner membranes)). During thresholding, only the darker pixels, the outer mitochondrial membrane and inner membrane (cristae), were selected. This gave the models from Amira and MIB a broken appearance compared to that from the manual segmentation in Fiji. However, the overall arrangement of the mitochondria could be seen and with further user input (e.g., using the fill feature), the appearance could be further improved. The quantitative volume analysis showed that the thresholded mitochondria resulted in a smaller volume than the manually segmented mitochondria, due to only the darker pixels being segmented (Figure 2.12(B)). This further proves that the thresholding tool should only be used in conjunction with other segmentation methods, to ensure that correct reconstructions and resulting measurements are made.



**A****B**

**Figure 2.11 – Examples showing the complex morphology of mitochondria.** (A) Nine consecutive images from the late foetal psoas (viewed from left to right). The mitochondria have been segmented individually in different colours, in MIB, and their corresponding 3D reconstructions, from Amira, can be seen in (B). All Scale Bars 1 $\mu$ m.

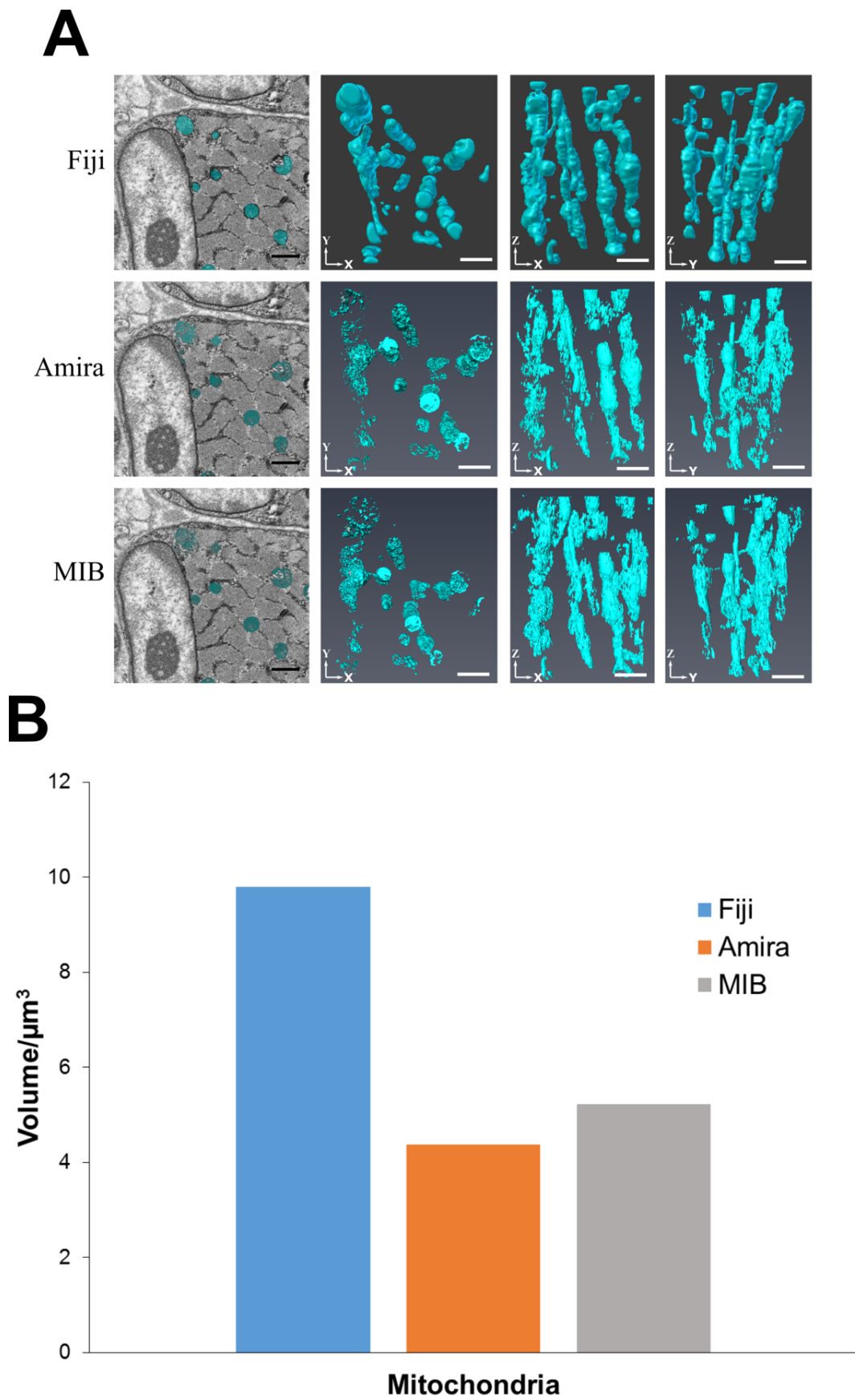


**Figure 2.12 – Examples of reconstructions of the mitochondrial network.** (C) 3 single images from the data series with the mitochondria segmented and the reconstructions of the mitochondria at different orientations. (D) Volume measurements of the mitochondria. All Scale Bars 1 $\mu\text{m}$ .

The final reconstructions incorporating all segmented features of the skeletal muscle are shown in Figure 2.13. Although the general appearances of the models were similar in each of the programs, there were some differences caused by the methods used to segment the structures of interest. For example, the mitochondria were more fragmented in the MIB and Amira models as they had been thresholded compared to the denser structures seen with Fiji's manual segmentation. The devised workflow from these analyses is shown in Figure 2.14.



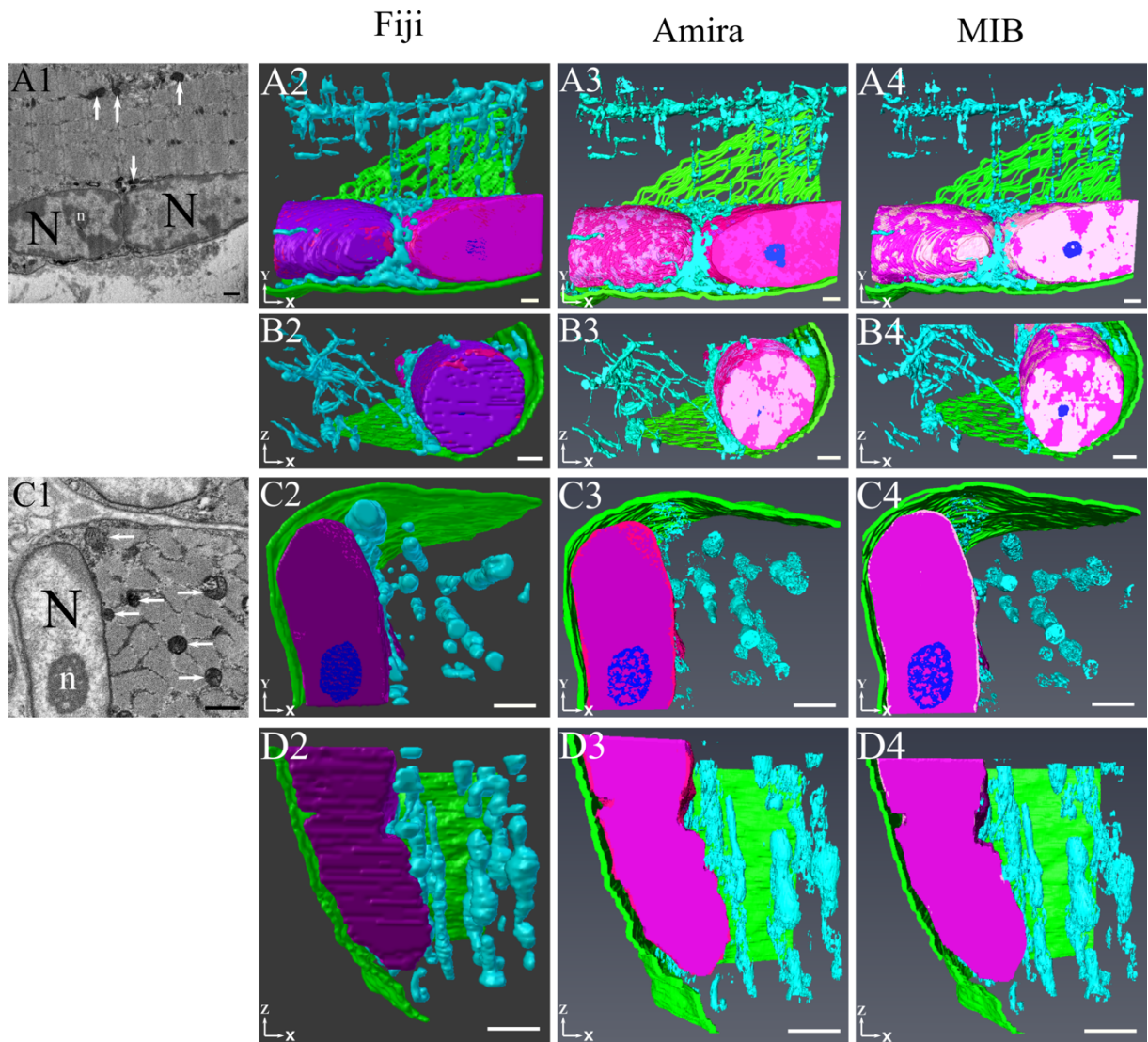


**Figure 2.13 – Examples of 3D reconstructions of segmented structures.** This diagram depicts examples of the assembled reconstructions of all segmented features from two separate skeletal muscle SBF-SEM datasets. Rows A and B show results from adult soleus muscle (from X serial sections; panel A1 indicates an SBF-SEM image). Rows C and D show results from foetal psoas muscle (from X serial sections; panel B1 indicates an SBF-SEM image). Rows (C) and (D) The following features are colour-coded in the reconstructions: mitochondria, light blue; nuclei, dark pink/purple; chromatin, light pink; nucleoli, dark blue; plasmalemma, green. All scale bars 1µm.

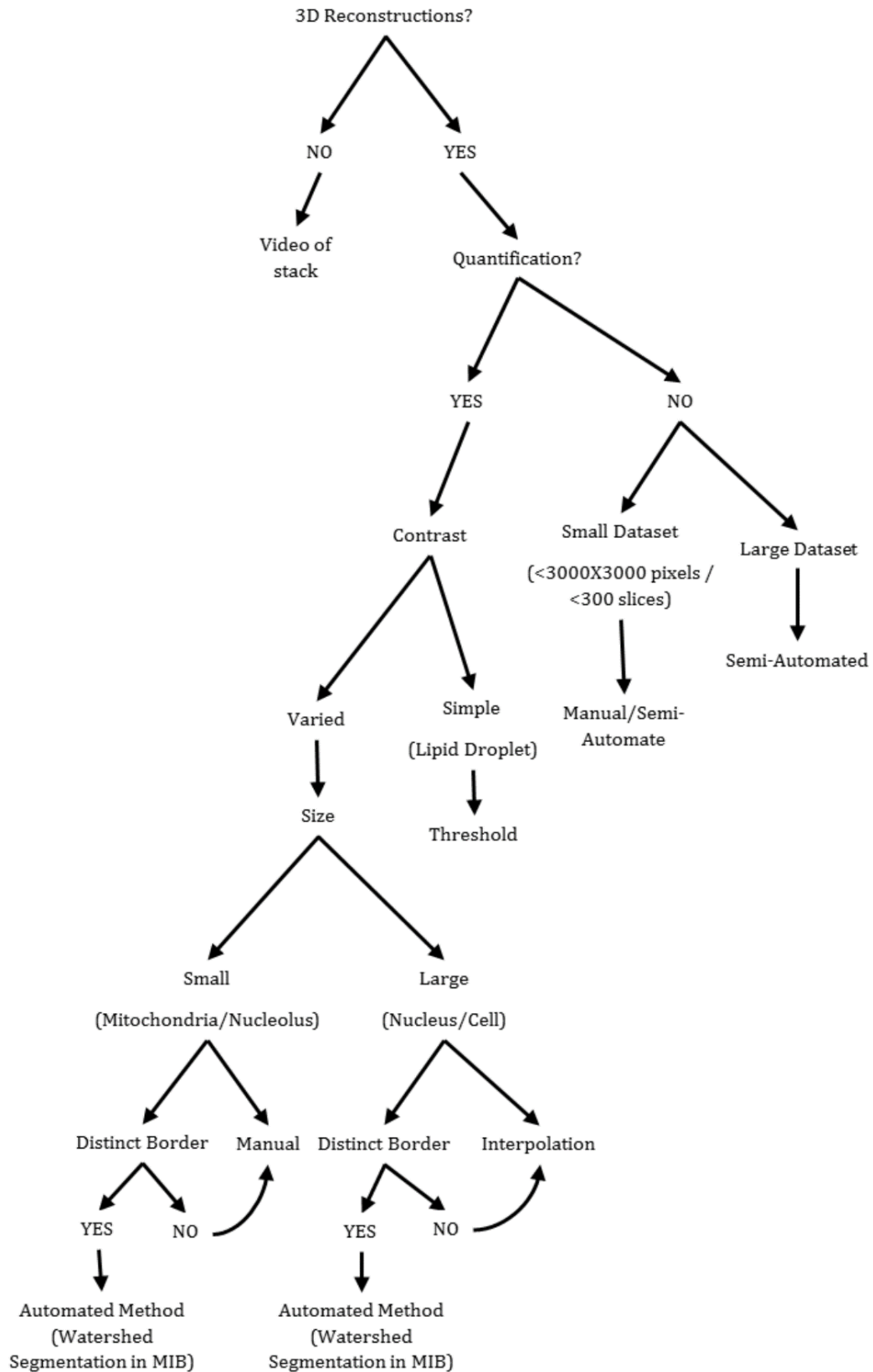


**Figure 2.14 – Proposed workflow to aid in decision making when choosing appropriate segmentation methods for analysis of SBF-SEM data.** The majority of these segmentation methods can be used in MIB and Amira, with some exceptions, the watershed segmentation which is not shown in this paper. The decision to use either MIB or Amira to perform the segmentations will depend on user preference and access to the software, as previously shown the two programs yield similar results.

### *2.3.3. Validation of Workflow*

The workflow was then implemented onto two other tissue types: guinea pig cardiac muscle (detailed below in this section) and a region of the optic lobe from locust brain (detailed in section 2.4). This was done to test the workflow and validate that it was applicable to other tissues and structures.

Cardiac muscle (dataset taken by Dr. Hanan Kashbour) was chosen as a good model system for this test because the mitochondria appeared darker and denser, compared to skeletal muscle, with high contrast to surrounding features (Figure 2.15(A)). It had a different appearance when compared to the mitochondria in the skeletal muscle, which, as shown already, exhibited varied contrasts. By following the workflow:

3D-Reconstruction>Yes>Quantification>Yes>Contrast>Simple>Threshold

it was determined that a form of thresholding, either b/w or the magic wand in MIB or Amira, could be used to segment the cardiac mitochondria. This was done and the successful segmentations and subsequent reconstructions are shown in Figures 2.15 (B) and (C).

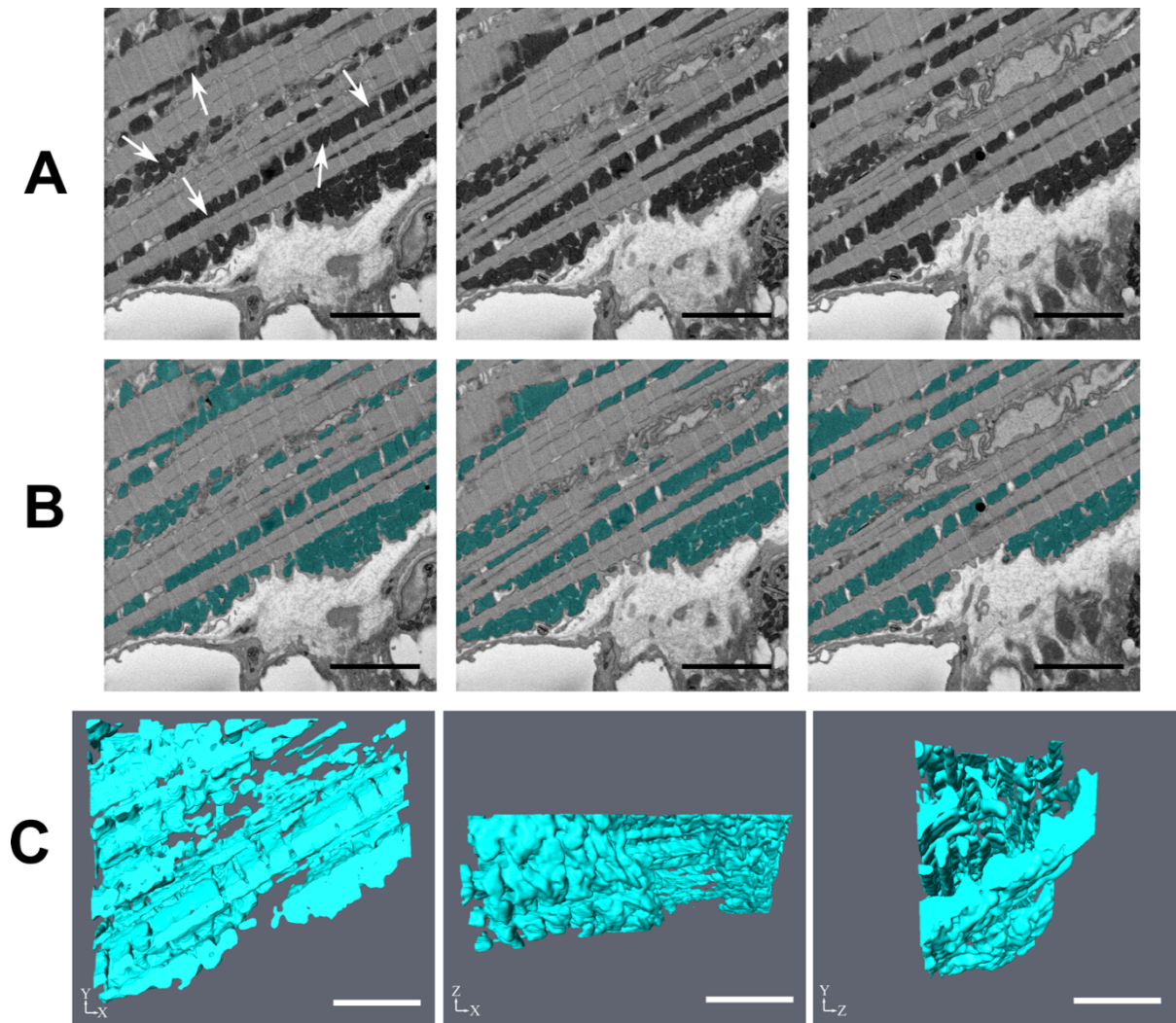


**Figure 2.15 – Segmentation and reconstruction of mitochondria from cardiac muscle.** (A) Shows 3 raw images that are 5 slices apart from each-other, mitochondria labelled with white arrows. (B) Are the same raw images with the segmentation of the mitochondria (blue) shown and (C) is the subsequent reconstructions at different orientations. Scale bars are 1 $\mu\text{m}$ .

For the cardiac muscle nucleus, the same segmentation procedure was used as for the skeletal muscle. The workflow was:

3D Reconstruction>Yes>Quantification>Yes>Contrast>Varied>Size> Large>Distinct Border>Yes>Automated Method (Watershed Segmentation in MIB)

The dataset was composed of only 100 slices, image size 1024x1024 pixels, and the nucleus was only present for a portion of the stack. As automated segmentation can be a time-consuming method due to computational demands, it is not efficient for small objects or datasets. Thus, the decision was made to use manual segmentation combined with interpolation. So, the nucleus was manually segmented over every fifth slice, interpolated in-between and any errors manually corrected (Figure 2.16).

These outcomes indicated the applicability of the workflow approach for mitochondrial analyses of muscle preparations.



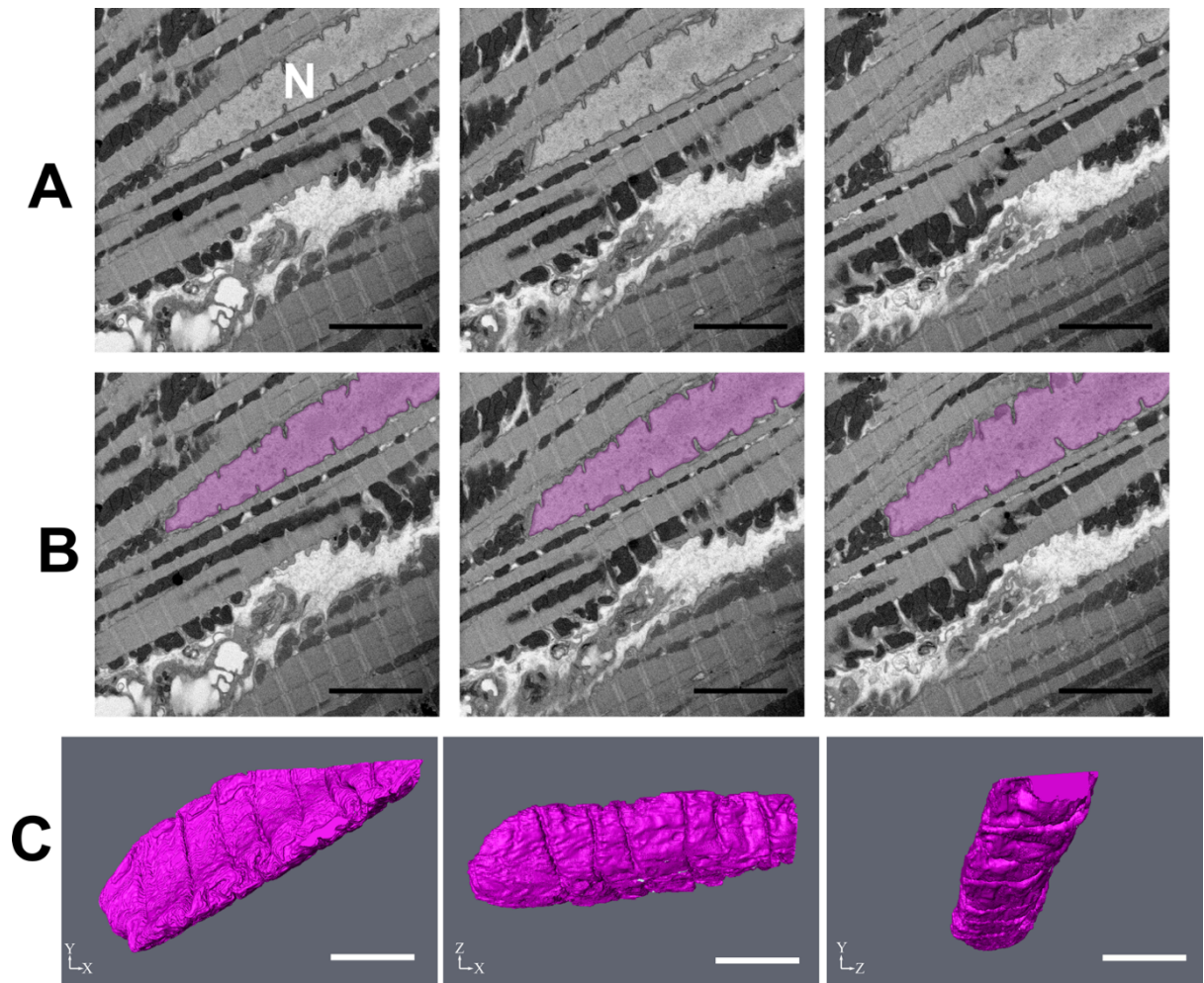


**Figure 2.16 – Segmentation and reconstruction of nucleus from cardiac muscle.** (A) Shows 3 raw images that are 5 slices apart from each-other, nucleus is labelled with white 'N'. (B) Are the same raw images with the segmentation of the nucleus (purple) shown and (C) is the subsequent reconstructions at different orientations. Scale bars are 1 $\mu$ m. (Data collected by Dr. Hanan Kasbour).

The dataset from the locust optic lobe of the LGMD 2 neuron also presented challenges for choosing the most appropriate analyses procedure. This tissue was vastly different from the skeletal and cardiac muscle already shown, as it was densely packed with a variety of cells. The dataset analysed (100 slices at 6000x6000 pixels) was also much larger than the muscle dataset. The aim, on this occasion, was rather different - to segment out an entire dendrite. The following workflow was followed:

3D Reconstruction>Yes>Quantification>Yes>Contrast>Varied>Size> Large>Distinct Border>Yes>Automated Method (Watershed Segmentation in MIB)

As mentioned earlier, this method takes time but there is a semi-automated version of the watershed segmentation combined with the brush tool in MIB, whereby voxels are grouped depending on the presence of boundaries. These larger voxels can be selected using the brush, all performed directly in the user interface. Using this method, the dendrite was selected, manually segmented repeated every fifth slice and interpolation used (Figure 2.17). This tool could be used when analysing nuclei, however, it is best used on larger and more complex structures that would take time to manually segment, such as large dendrites like the LGMD 2 neuron. This approach therefore also confirmed the adaptability of the workflow to the examination of neuronal tissue.

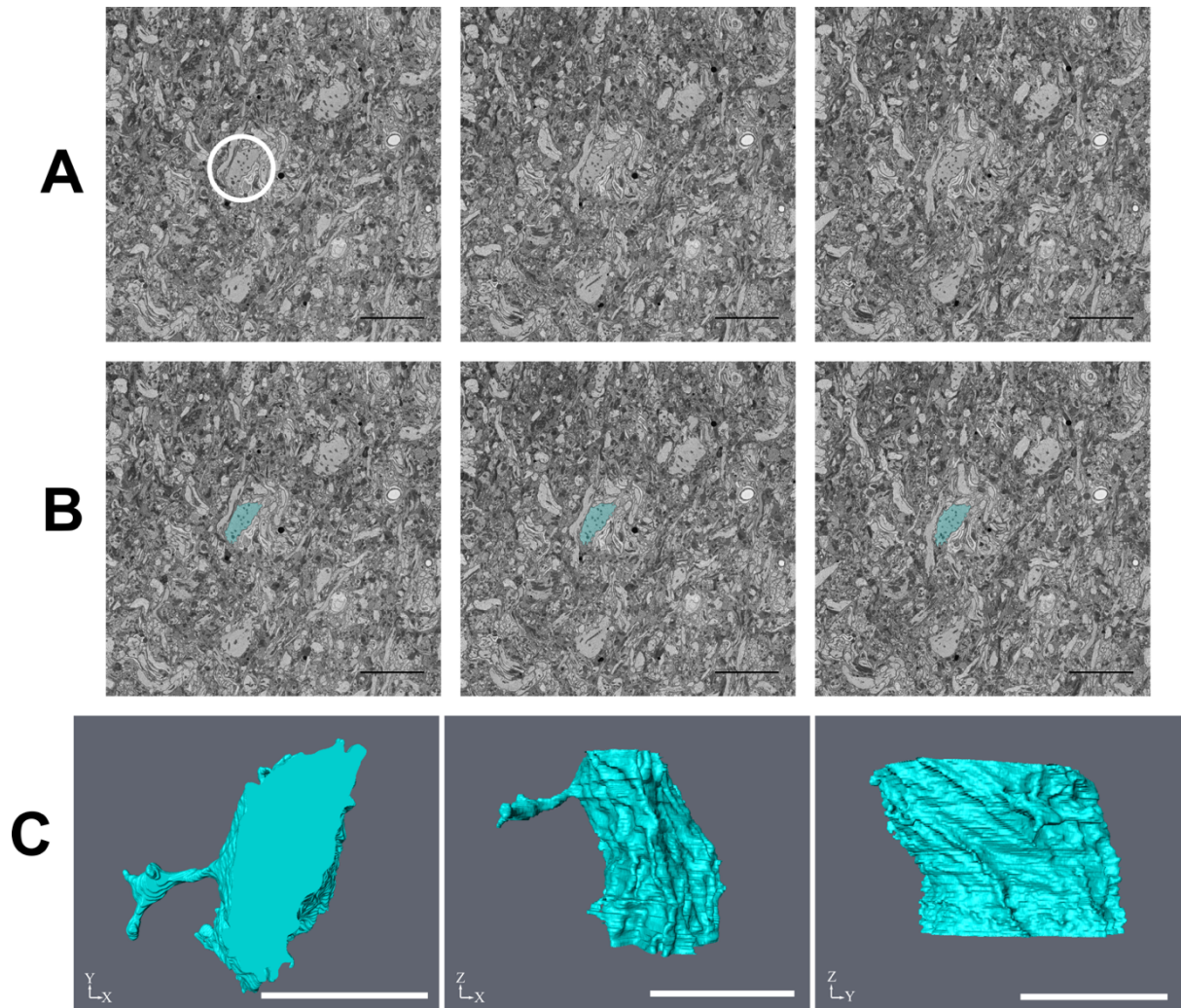


**Figure 2.17 – Segmentation and reconstruction of the LGMD 2 neuron from the optic lobe of the locust.** (A) Shows 3 raw images that are 5 slices apart from each other, with the neuron of interest circled in white. (B) Are the same raw images with the segmentation of the LGMD 2 shown and (C) is the subsequent reconstructions at different orientations. Scale bars on sections are 10 $\mu$ m and 5 $\mu$ m on 3D reconstructions



## **2.4. Segmentation, Reconstruction and Analysis of Locust Optic Lobe**

### *2.4.1. Identification of LGMD 2 neuron*

As described previously the block was serially sectioned at 1µm thickness, stained with toluidine blue and checked under the light microscope until the protocerebrum and optic stalk had been cut through. As soon as the optic stalk was cut through the subsequent sections were checked for the start of the lobula region of the optic lobe. The lobula region was identified by the presence of tracheae, groupings of cell or nuclear bodies, such as anterior body and ventral body. The LGMD 2 neuron dendrites are the outer crescent of two located within the lobula (Rind et al., 2016, Rind and Leitinger, 2000), examples of the sections taken and viewed are in Figure 2.18(A-B).

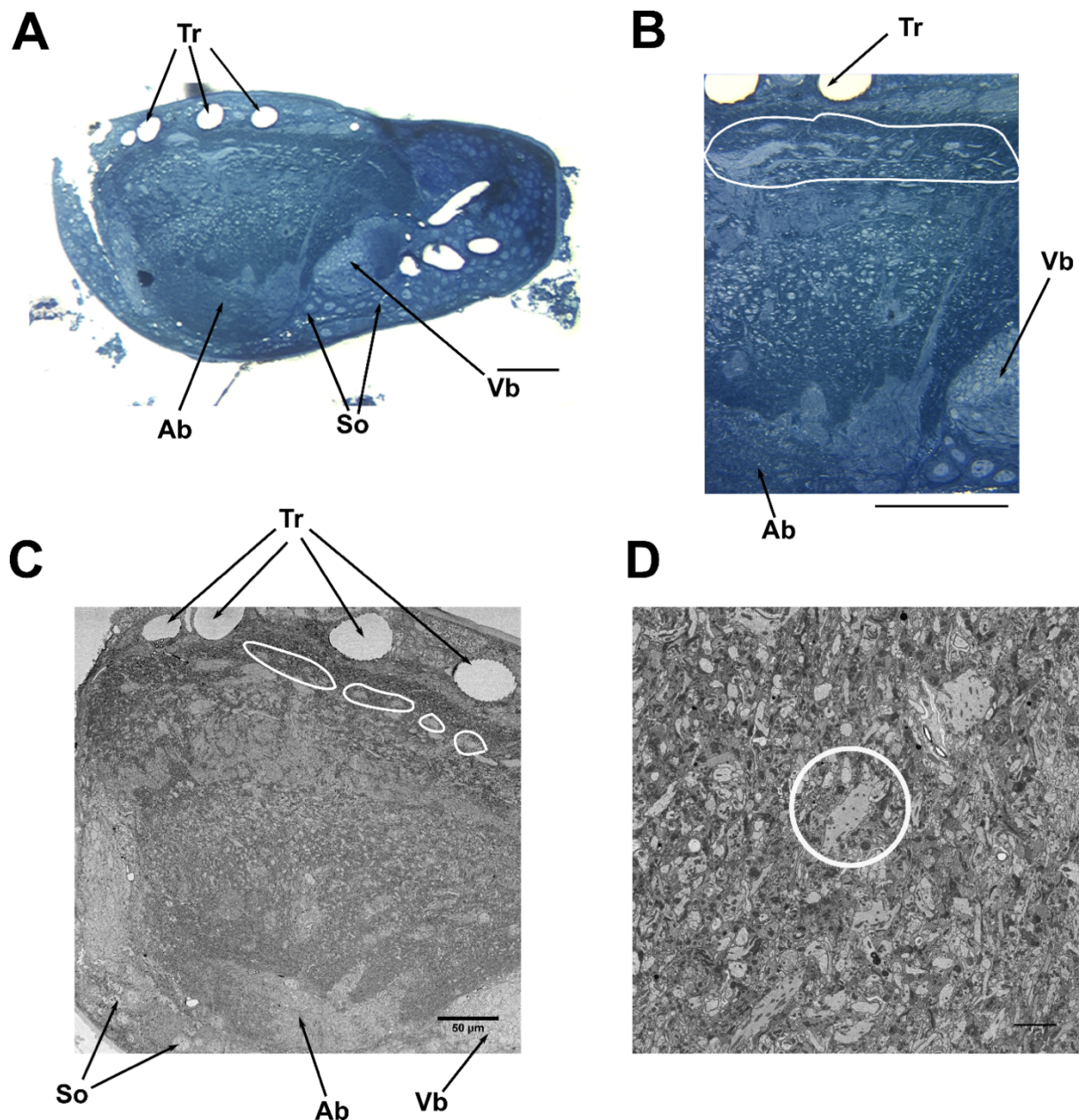


**Figure 2.18 – Process of finding the region of interest and the LGMD 2 neuron.** (A) Light microscope section, stained with toluidine blue, of the lobula with tracheae, *Tr*, somata, *So*, anterior body, *Ab*, and ventral body, *Vb*, labelled. Scale bar 100μm. (B) Higher resolution image of same section with area of interest circled. Scale bar 100μm. (C) Image from SBF-SEM of the lobula, with tracheae, *Tr*, somata, *So*, and the anterior body, *Ab*, labelled and branches of LGMD 2 neuron are circled in white. (D) Single section from the collected dataset (500 slices), with the LGMD 2 branch of interest circled. Scale bar 5μm.

#### *2.4.2. Identification of Synapses*

As described earlier once the crescent of the dendrites of the LGMD 2 neuron were identified in the lobula region, several 70nm sections were taken and viewed on the TEM. As the tissue processing protocol differs for the SBF-SEM compared to standard TEM the preservation and appearance of the synapses was checked (and later compared to the appearance of the synapses seen when viewing with the SBF-SEM), shown in Figure 2.19. Synapses were first recognised in the TEM, by the presence of presynaptic density and vesicles. At a synapse onto the LGMD 2 neuron, there is a dark pre-synaptic density present in both TmA neurons in a 'V' shape. The synapses found on the TEM also confirmed the location and identity of the LGMD 2 neuron, as characteristically all synapses found were reciprocal, with the synapses of two neighbouring TmA neurons occurring back-to-back synapses at the same location onto the LGMD 2 neuron branch and both sharing the same synaptic cleft (Rind et al., 2016, Rind and Leitinger, 2000).

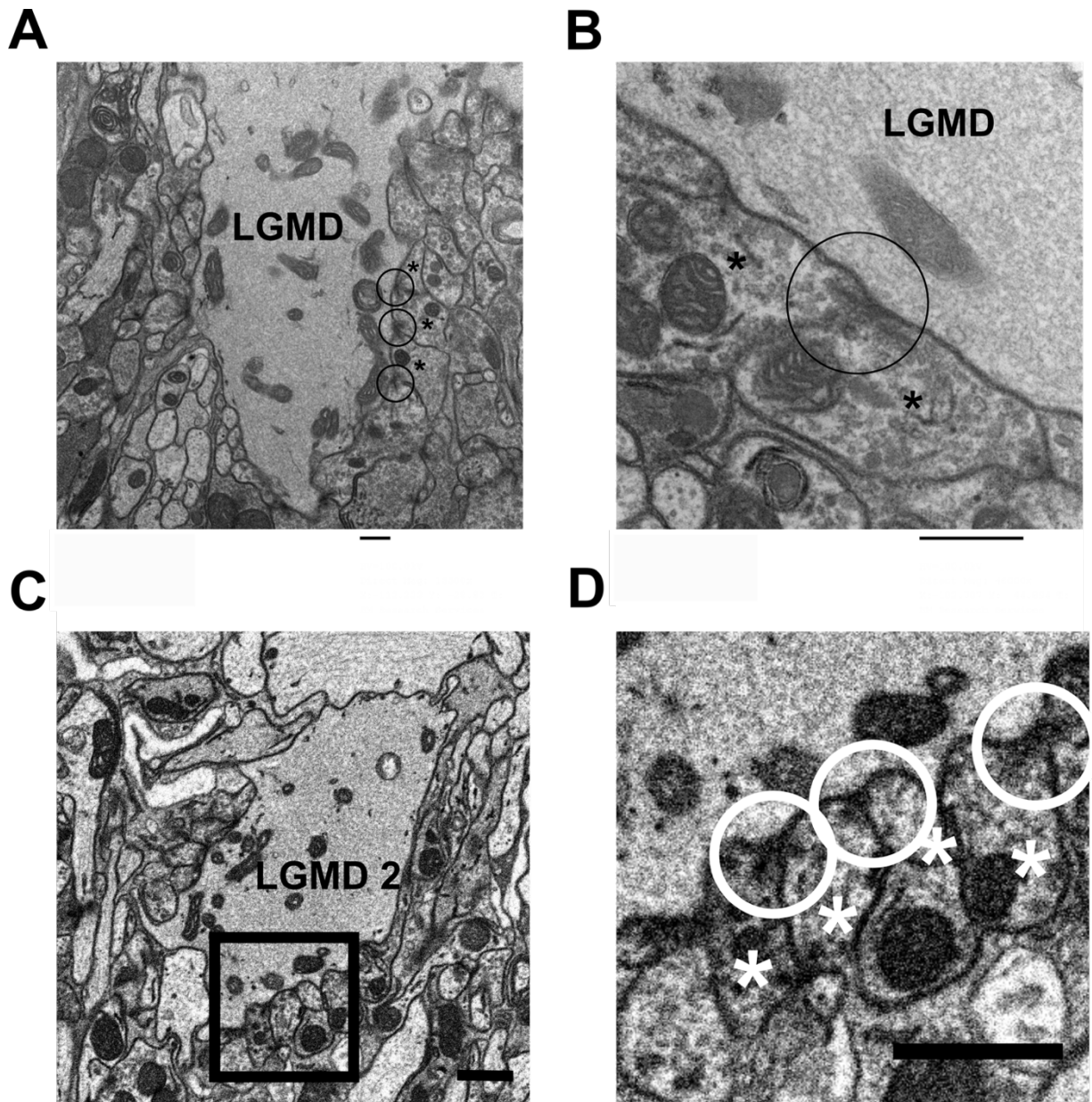


**Figure 2.19 – Identifying synapses using TEM and SBF-SEM.** (A) and (B) show TEM images of a 3view sample. The TmA neurons are labelled (\*) and the synapses are circled. The synapses are identified by their characteristic dark pre-synaptic densities present in both TmA neurons forming a 'V' shape relative to one another. Scale bar 500nm. (C) Shows a branch of the LGMD 2 neuron and (D) is an enlarged image of the area in the square imaged in the SBF-SEM. On (D) the TmA neurons are labelled (\*) and synapses circled. Scale bar is 1μm.

#### *2.4.3. Segmentation and Reconstruction*

The dataset collected was then converted from .DM3 to .TIF format using Fiji (<https://fiji.sc/>). During this step in Fiji the contrast was normalised across the stack. The dataset was then given to Dr Kristian Bredies (University of Graz, Austria), and further processed using a denoising filter to aid in semi-automated segmentation. The processed dataset was divided into two 200 and one 100 portions due to the overall size of the dataset (>16GB). The portions of the processed dataset were opened into Microscopy Image Browser (MIB) (<http://mib.helsinki.fi/>) (Belevich et al., 2016) and the contrast of the images were altered further, to visualise the dark cell boundaries and synapses easier. In MIB the larger LGMD 2 neuron branches were segmented using the watershed option of the manual brush tool and interpolation. The smaller LGMD 2 neuron processes and the TmA neurons had to be reconstructed manually, as they were too small for the semi-automated methods and too many errors were created. Examples of the appearance of the data at each of these steps is shown in Figure 2.20. Information about each of the TmA neurons and their respective synapses was also compiled, including location on the LGMD 2 neuron and which branch of the LGMD 2, as well as the identity of the neighbouring neuron, which the TmA neuron synapses with onto the LGMD 2 neuron.



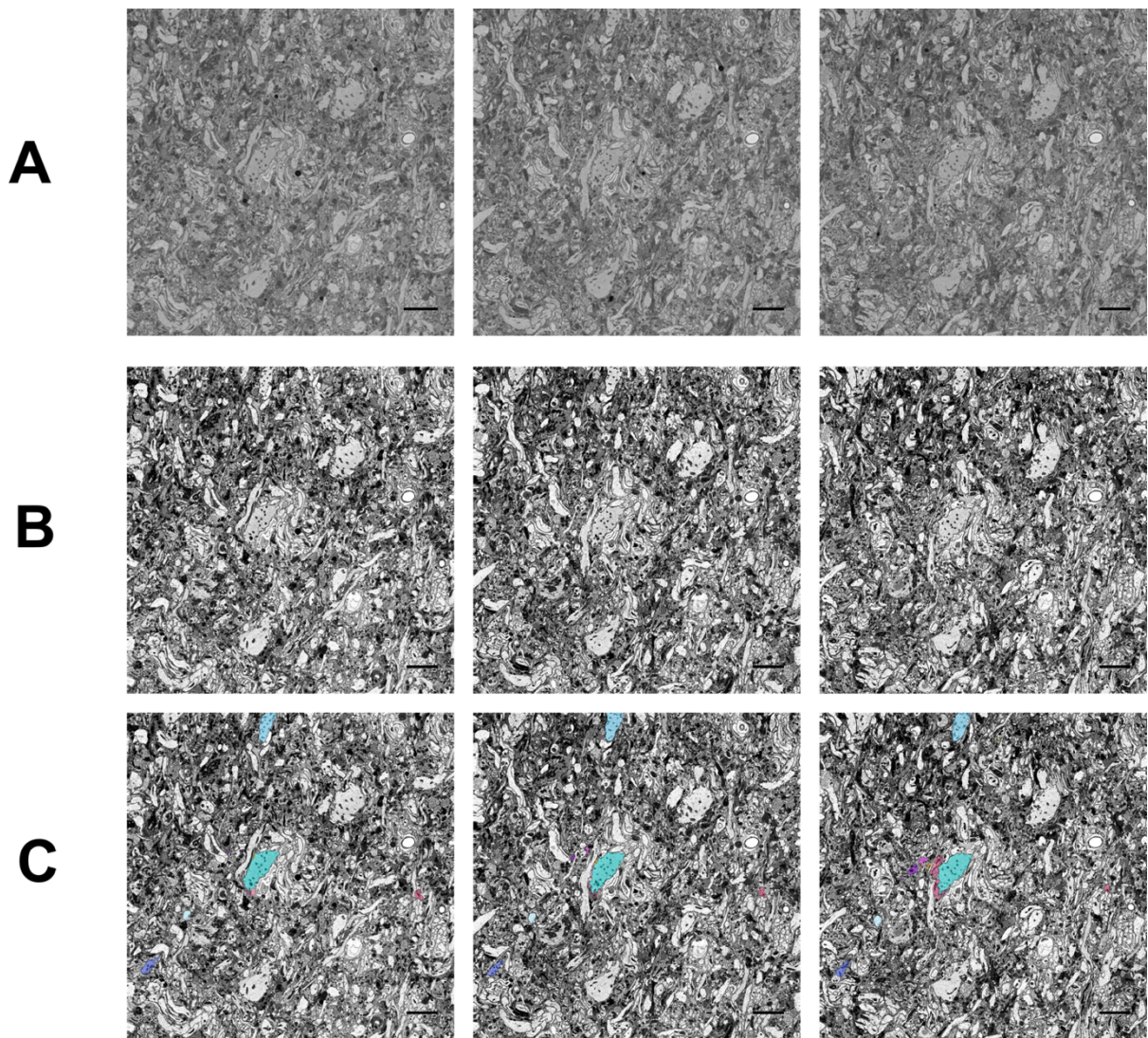
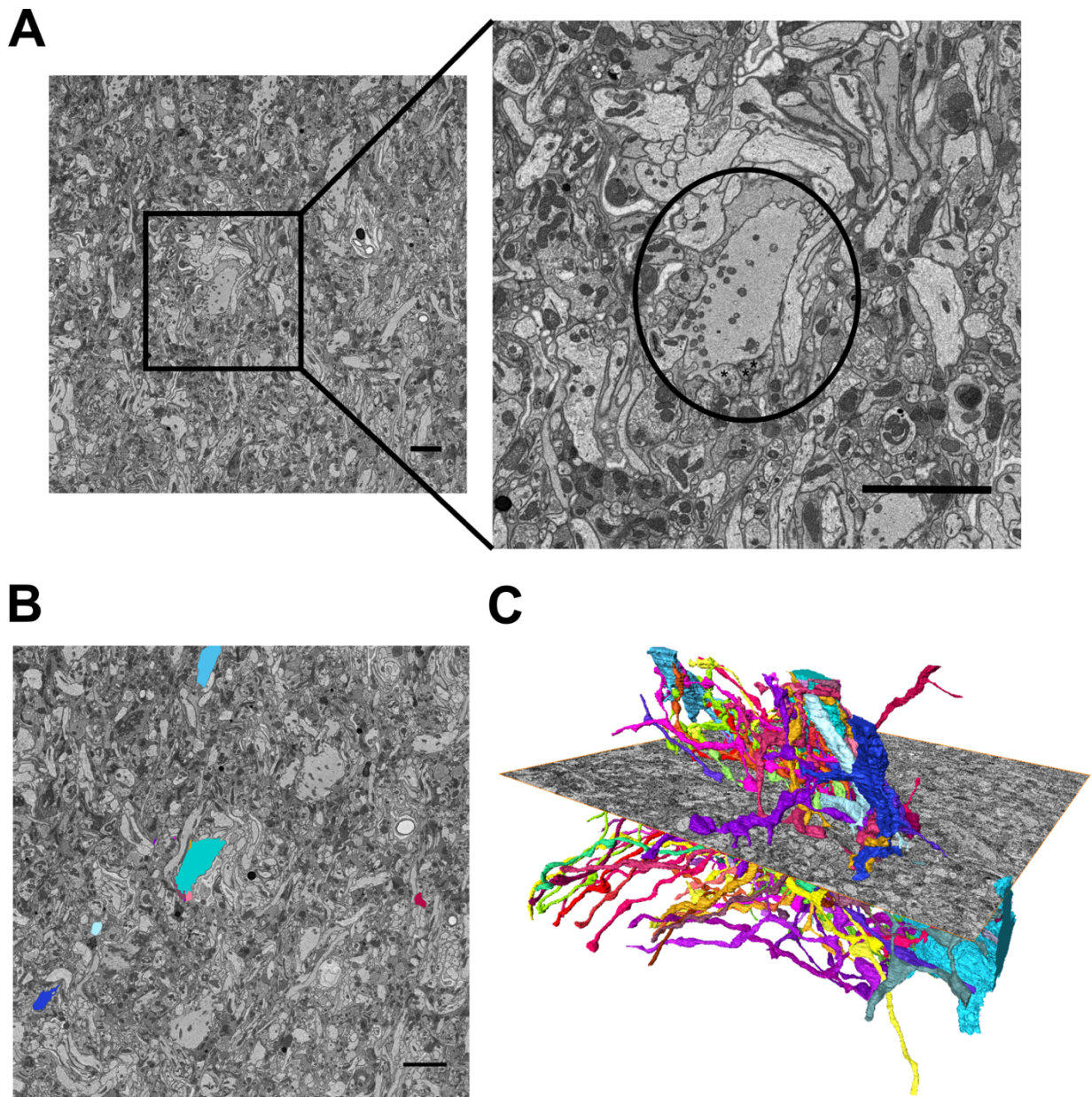


**Figure 2.20 – Steps of image processing from raw to segmented images.** (A) Shows slice 1, 10 and 20 from dataset of raw images collected from digital micrograph. (B) The denoised dataset (performed by Dr Kristian Bredies of Graz university) and after further contrast enhancement in MIB, to improve boundaries and synapses. (C) Examples of segmented dataset of LGMD 2 neuron branches, *blue*, and TmA neurons, *multi-coloured*. Scale bar 5 $\mu$ m.

Video: <https://doi.org/10.6084/m9.figshare.7172384.v5>

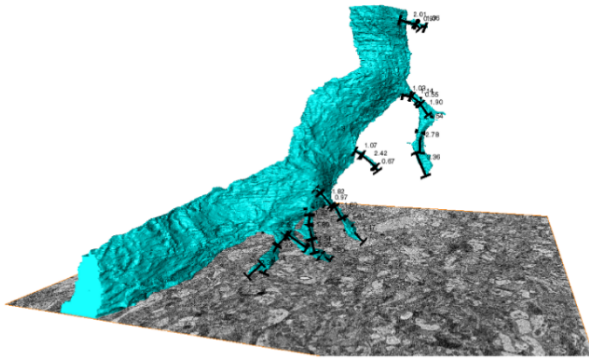
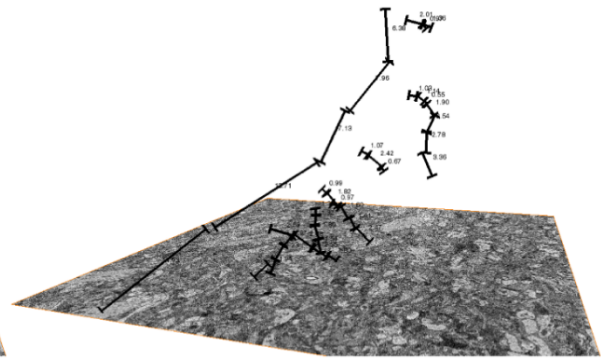
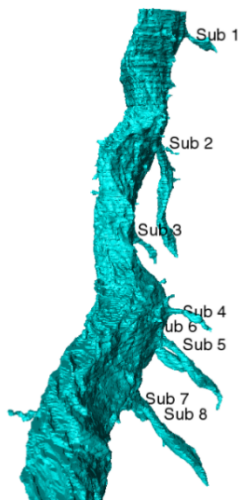
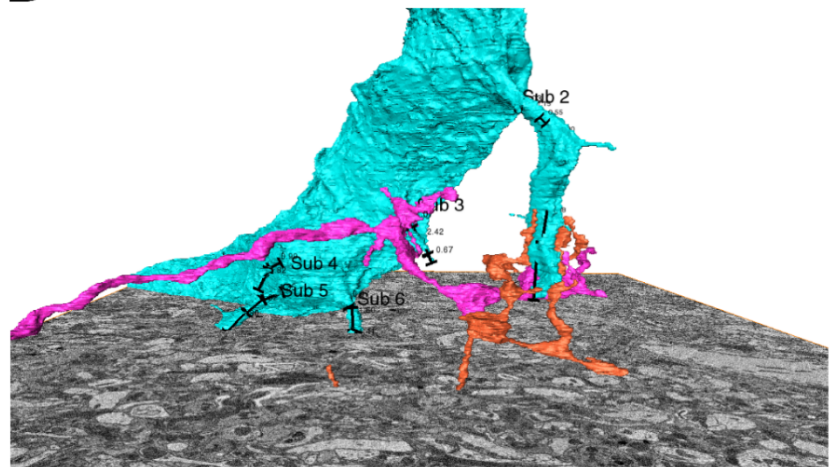
Once the segmentation of all the TmA neurons synapsing onto the nominated LGMD 2 neuron branches within the dataset was finished both the TmA neurons and LGMD 2 neuron branches were exported out of MIB and opened in Amira (<https://www.fei.com/software/amira-for-life-sciences/>). The models of the neurons over the three portions of the dataset were merged within Amira and visualised, Figure 2.21. Within Amira the lengths of the dendrite main and sub-branches were measured, Figure 2.22, as well as the surface areas of all the branches.





**Figure 2.21 – Segmentation and reconstruction of LGMD 2 neuron branches and TmA neurons.** (A) Single section from the dataset and enlarged area around the main branch of the LGMD 2 neuron analysed (circled). (B) Single section with the segmentation, LGMD 2 neuron branches are *blue* and TmA neurons *multi-coloured*. (C) Reconstruction of all of the segmented LGMD 2 neuron branches, *blue*, and TmA neurons, *multi-coloured*, with an orthoslice taken at the level shown in C with a shift in orientation. Scale bar 5 $\mu$ m. Video: <https://doi.org/10.6084/m9.figshare.7167998>



**A****B****C****D**

**Figure 2.22 – Analysis of the main and sub-branches of a portion of LGMD 2 neuron.** (A) Measuring the length of the main branch and the smaller sub-branches of the LGMD 2 neuron, *blue*, in Amira using a 3D tool measurement. (B) Showing the measurement results without the reconstruction. (C) Labelling the sub-branches on the reconstruction to identify location of synapses for synapse density measurements. (D) Reconstructions of two TmA neurons, *purple* and *orange*, that synapse onto one of the sub-branches of the LGMD 2 neuron, to determine which branch the synapses occur on.

During the segmentation and reconstruction process incomplete arbours of TmA neurons were noted. These were defined to be at either end of the dataset or to have been partially reconstructed, because their branches were only partially identifiable during segmentation. This could be due to the slice thickness and resolution of the images being too large to be able to identify the finer processes. Examples of the incomplete neurons can be found in Figure 2.23. Much of the analysis was performed on all neurons, including incomplete and completely reconstructed arbours of the TmA neurons to reduce bias, such as the analysis on synapse density. However, the network analysis was primarily performed only on the completely reconstructed arbours and analysis including the incomplete arbours is highlighted.

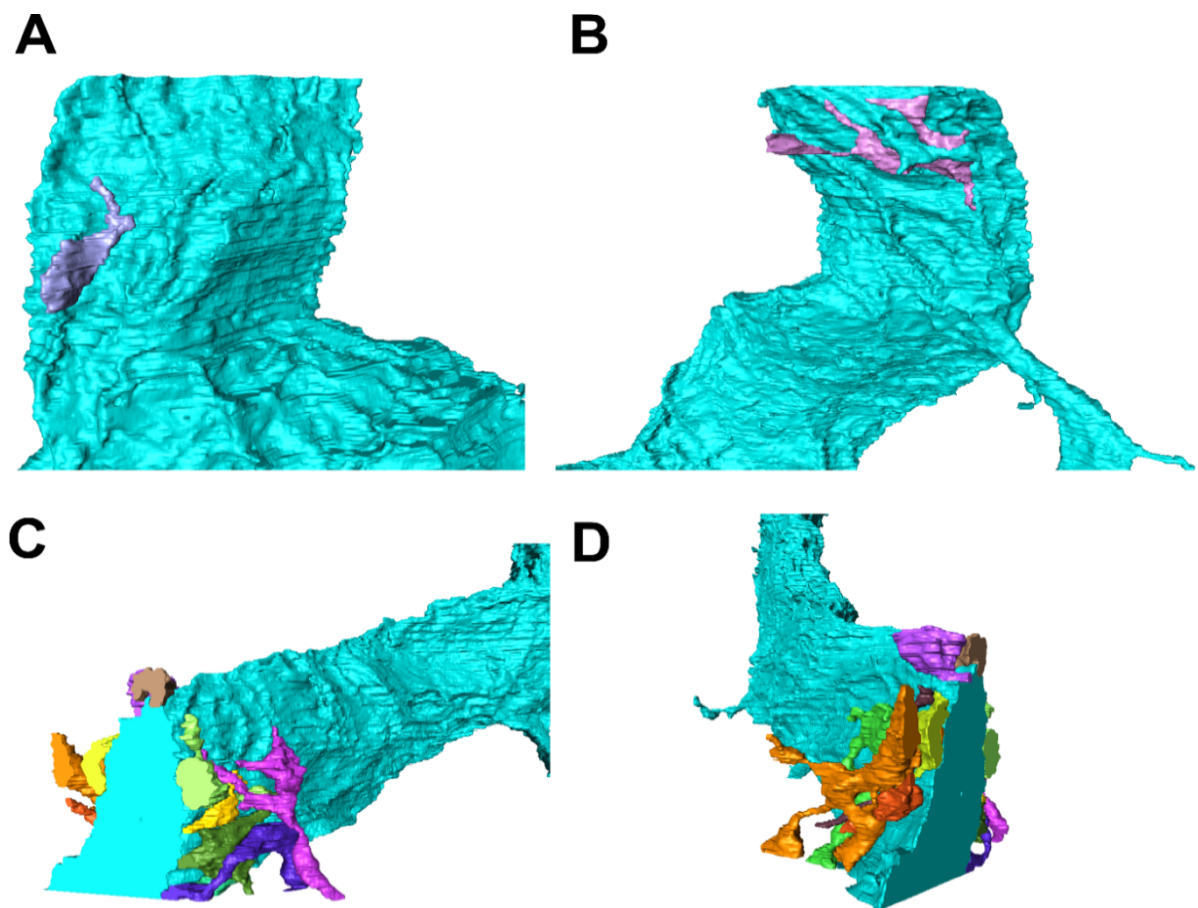


**Figure 2.23 – Reconstructions of incomplete arbours of TmA neurons.** (A) and (B) show an example of a TmA neurons, *light pink* and *light purple*, which are only partially reconstructed. (C) and (D) are examples of incomplete TmA neurons, *multi-coloured*, that occur at the end of the dataset, both are the same dataset in different views.

#### *2.4.4. Statistical Analysis*

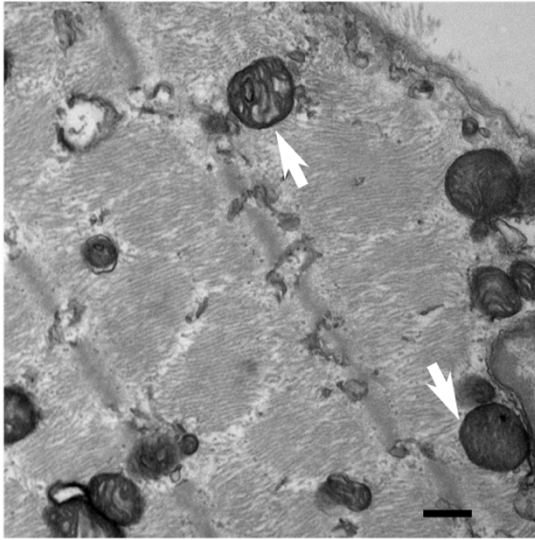
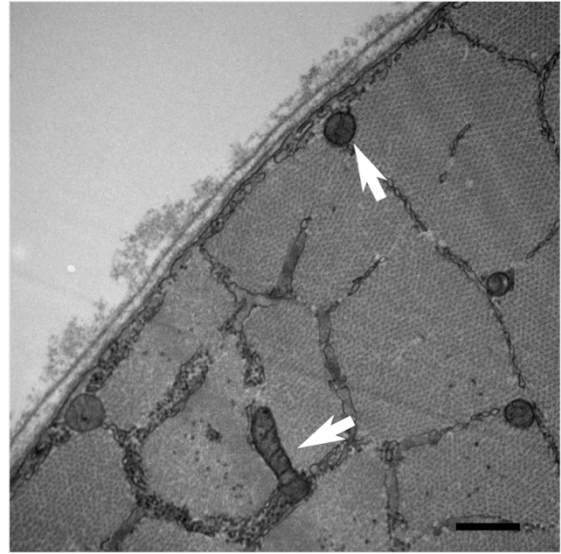
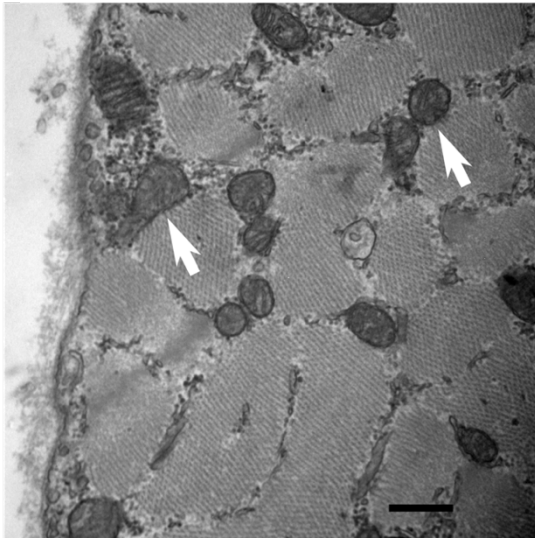
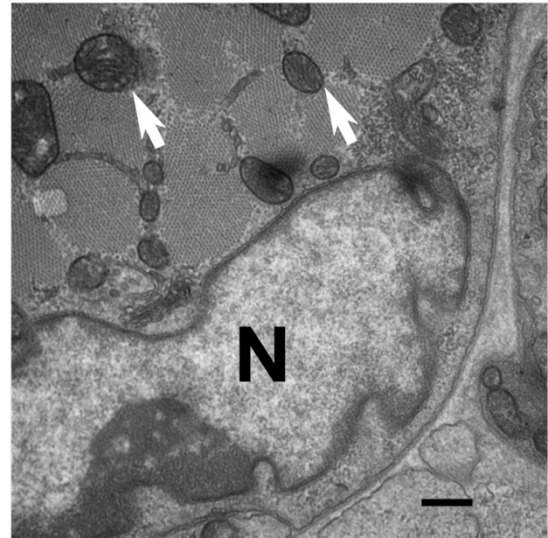
During the segmentation and reconstruction TmA neurons were labelled along with synapses and neighbouring TmA neurons. This information was compiled into a spreadsheet, with information on location, such as slice numbers and branch identification, such as main or sub-branch as well as specific LGMD 2 neuron branch identity. From this, a nodes list was developed, where 1 node is a TmA neuron and the 2<sup>nd</sup> node the neighbour. This was used to create connectomes in MATLAB. Other analysis was performed on the information in the spreadsheet. All graph production was performed in Microsoft Excel. The statistical analysis performed, included Mann-Whitney U test (for hub v non-hub) and Kruskal-Wallis with post-hoc Bonferroni test (branch innervation). All statistical analysis was performed in SPSS.

The dataset can be accessed at <https://doi.org/10.5281/zenodo.1434744>.

## **2.5. Optimised Procedure for Segmentation, Reconstruction and Analysis of Guinea Pig Skeletal Muscle**

### *2.5.1. Identification of Skeletal Muscle Cell Components*

The health of the cell and mitochondria was checked using TEM to obtain high magnification and high-resolution images of mitochondria, examples of these are seen in Figure 2.24. Once collected, all the datasets went through the same processing steps. This consisted of opening the datasets in Fiji and the contrast was normalised and enhanced when needed, Figure 2.25(A) and (B). The images were then converted into a .tif format from the .dm3 collected and opened in MIB for segmentation. From the datasets the nuclei and mitochondria could be identified, as well as other structures found surrounding the muscle cells.

**A****B****C****D**

**Figure 2.24 – Examples of high resolution TEM images of mitochondria from analysed samples.** (A) Adult Soleus, 19000x (B) Adult Psoas, 25000x (C) Foetal day 60-64 Soleus, 25000x (D) Foetal Day 60-64 Psoas, 19000x. Mitochondria are labelled with white arrows and a Nucleus with N. Scale bar 500nm.



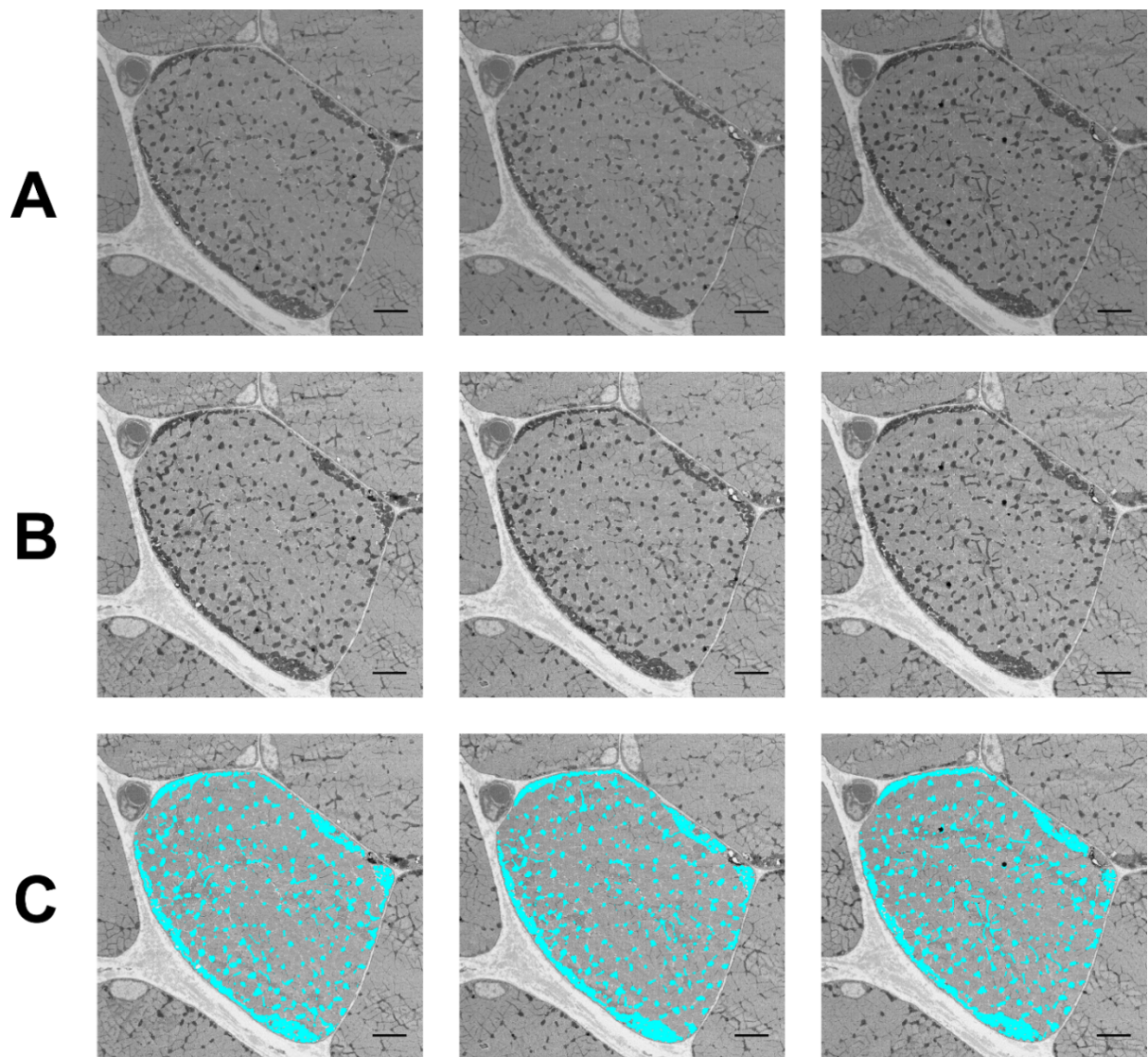


**Figure 2.25 – Steps of image processing from raw images to segmentations.**

(A) Raw images of slice number 1, 10 and 20 from a larger dataset (~250 sections) of the adult guinea pig soleus muscle in transverse. (B) The same slices that have been processed using ImageJ (Fiji). For all datasets collected the contrast was normalised across the dataset and then increased. (C) The processed images were used for segmentation, example of mitochondria (*light blue*) is shown. Scale bars 5 $\mu$ m, images 5000 x 5000 pixels and 10nm resolution.

### *2.5.2. Segmentation and Reconstruction of Nuclei*

The nuclei were segmented using semi-automatic methods, specifically the watershed brush and interpolation; and the cell using the watershed brush and interpolation. For the segmentation of the nuclei, 50 sections from one of the polar ends of the nucleus was reconstructed. The cell was reconstructed in both cases for the same 50 sections that corresponded to nuclei that had been segmented. Example of reconstructed nuclei is seen in Figure 2.26.

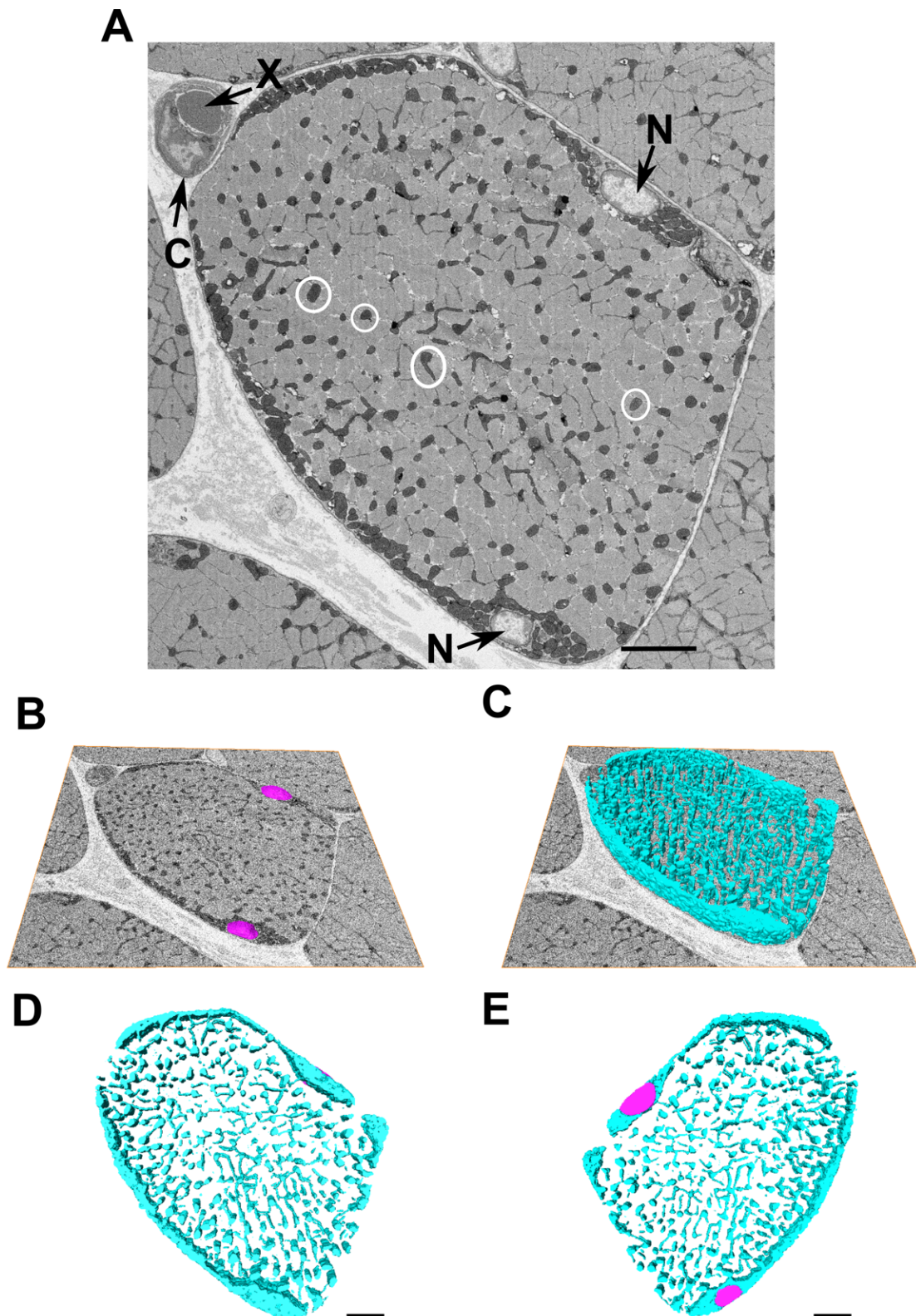


**Figure 2.26 – Example of segmentation of mitochondria and nuclei from 50 sections.** (A) Single section of adult guinea pig soleus muscle, showing muscle cell in transverse in the centre with two nuclei labelled, *N*, mitochondria, *circled*, capillary, *C*, and a red blood cell, *X*. (B) and (C) show 3D reconstructions of the two nuclei, *magenta*, and mitochondria, *light blue*, respectively both with orthoslice. Reconstructions without orthoslice shown (D) and flipped (E). Scale bars 5µm, image size 5000 x 5000 pixels and 10nm resolution. Video: <https://doi.org/10.6084/m9.figshare.7140380.v3>



### 2.5.3. Segmentation and Reconstruction of Mitochondrial Network

The mitochondrial network was segmented using a combination of manual and thresholding tools. First the cell was selected using the manual brush tool and interpolation, the selection was then added to the mask layer. When the 'mask only' was ticked in MIB, the segmentation was only performed in the masked area. The thresholding tool was then used to select the mitochondria within the cell or masked area. This was also used for segmenting the area of IMF mitochondria over 200 sections.

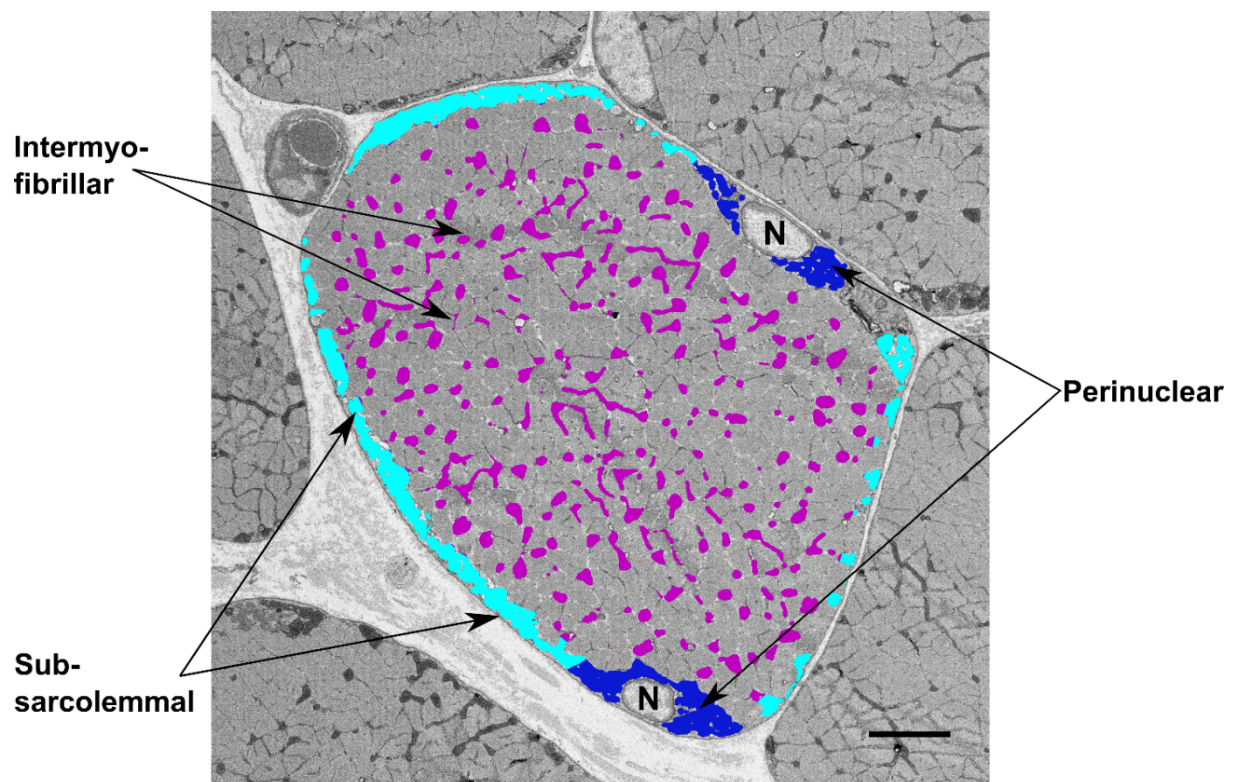
From the reconstructions various measurements were made in Amira. Mitochondria, from the whole cell, were segmented over 50, 75 and 100 sections and their volume measured. The results were compared to determine the pragmatic number of sections needed to take to get a representative value relative to estimates of cell volume, Table 2.4. Nuclei were removed from the analysis to ensure that calculations were based only on the volume of the cell that could be occupied by mitochondria. This indicated that estimates of the percentage of cell volume occupied by mitochondria were similar when using 50, 75 or 100 sections of data. Therefore, in all subsequent work, to analyse the mitochondrial network data from 50 sections of the dataset were segmented, as well as any nuclei that were present in those first sections. The cell boundaries/volume was reconstructed in both cases for the same 50 sections that corresponded to mitochondria that had been segmented.

**Table 2.4 – Mitochondrial Volume Test Results.** Mitochondria were segmented over 50, 75 and 100 sections. Volume measurements were made on each dataset and compared to determine the minimum number of sections required for a representative value based on the homogenous nature of the muscle and mitochondrial network.

Dataset	No. of slices	Mitochondrial Volume, $\mu\text{m}^3$	Cell Volume, $\mu\text{m}^3$	Percentage, %
<b>Adult Psoas</b>	100	310.21	1969.00	15.75
	75	234.64	1490.58	15.74
	50	156.13	990.92	15.76
<b>fetal day 60-64 Psoas</b>	100	70.00	800.62	8.74
	75	54.91	601.11	9.13
	50	37.41	398.70	9.38

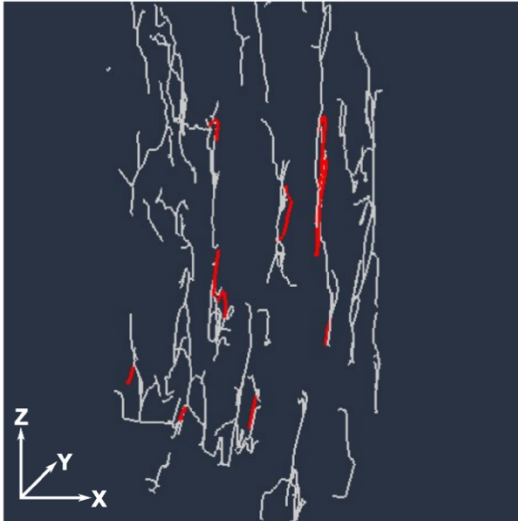
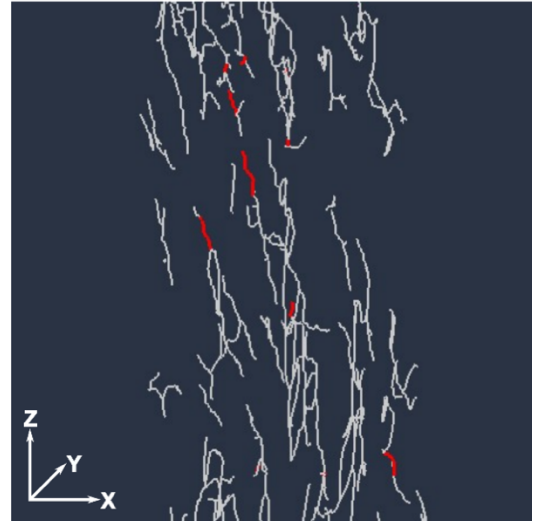
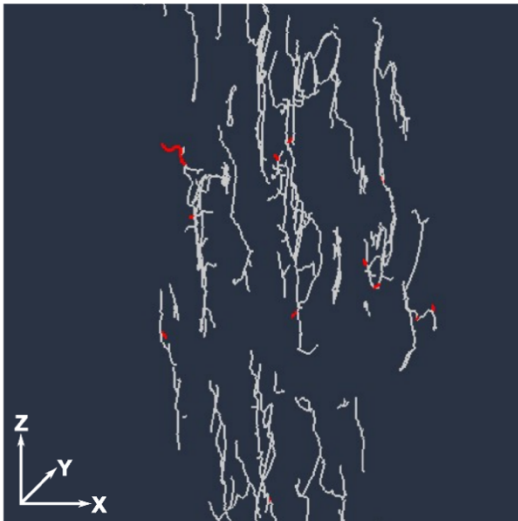
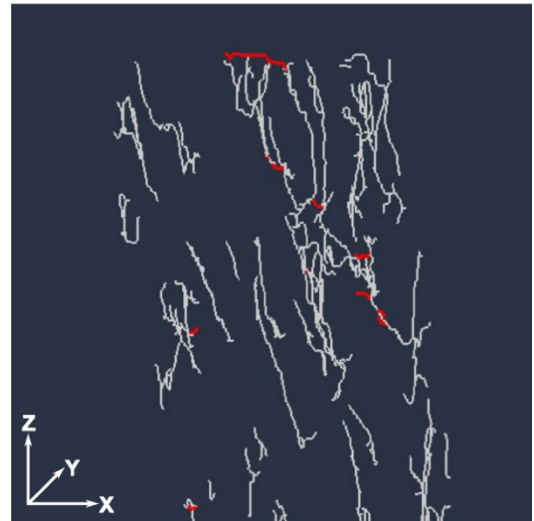
From these testing results a difference can already be seen between the fetal and adult mitochondrial volume, the biological contextualisation of the data is given in Results section 3.2.2 (pg142) and Discussion section 4.2.2 (pg193).

This segmented portion was divided up into IMF, SS and Peri-nuclear (PN) based on location, Figure 2.27. The SS mitochondria were defined as being between the cell boundary and the first layer of sarcomere. Sometimes these SS mitochondria extended towards the centre of the cell but, if the majority of the mitochondrion was between the sarcolemma and sarcomere, it was defined as being SS. The PN mitochondria were segmented in a similar way, but instead of the sarcolemma it was the nuclei that defined the boundary. So that any mitochondrion located in the area around the nuclei and between the nuclei and sarcomeres or sarcolemma was designated as PN. The remaining mitochondria were labelled as IMF. This was performed on the network segmentation and the individual mitochondrion segmentation.



**Figure 2.27 – Labelled single section of intermyofibrillar, subsarcolemmal and perinuclear mitochondria.** Single section from adult soleus muscle in transverse with the mitochondria divided into subsarcolemmal (SS), *light blue*, intermyofibrillar (IMF), *purple*, and perinuclear (PN), *dark blue*, with nuclei labelled, *N*. Scale bar 5µm.

For mitochondrial network analysis a portion of IMF mitochondria was reconstructed over 200 sections, as described above. The model files were opened in Amira and the surfaces generated. The 'Auto-skeleton' function was applied to the .am file to create a skeletonised version of the reconstruction. From the skeleton, angle measurements could be made to determine which segments or portions of the skeleton or branches extend along the transverse plane. Via a process of elimination, the angle  $50^{\circ}$  was chosen as the representative angle for segments branching along the XY axis with smallest rate of error, shown in Figure 2.28. All segments with an angle greater than 50 degrees was counted as a branch and proportion of segments  $>50$  and  $<50$  was obtained. The larger reconstructions would sometimes have more segments than true to the reconstruction. When this occurred, the model was eroded by a small factor in MIB in order to maintain the morphology of the network but reduce the rate of error during skeletonisation.

**A****B****C****D**

**Figure 2.28 – Angle measurement of skeletonised mitochondrial network.**

Reconstructed portion of IMF mitochondrial network from a foetal day 50-54 soleus cell skeletonised in Amira. Each image shows highlighted portion of the skeleton at certain angle measurements, (A) 0-9° (B) 20-29° (C) 50-59° (D) 70-89°.

#### *2.5.4. Segmentation and Reconstruction of Individual Mitochondria*

To analyse whole individual mitochondria, a method for randomly selecting mitochondria was implemented. A grid, with 1 to 5 $\mu$ m squares, was placed on all 250 slices and a number randomly generated between 50 and 200, corresponding to a chosen slice number. The size of the datasets used in this analysis were 250 sections but to ensure the maximum number of whole mitochondria could be segmented, the slice number was chosen between 50 and 200. On the randomly generated slice number every mitochondrion that crossed the grid lines was followed through the dataset, Figure 2.29. The individual mitochondrion had to be followed and segmented manually and only the mitochondria that started and ended within the dataset (250 sections) were segmented.

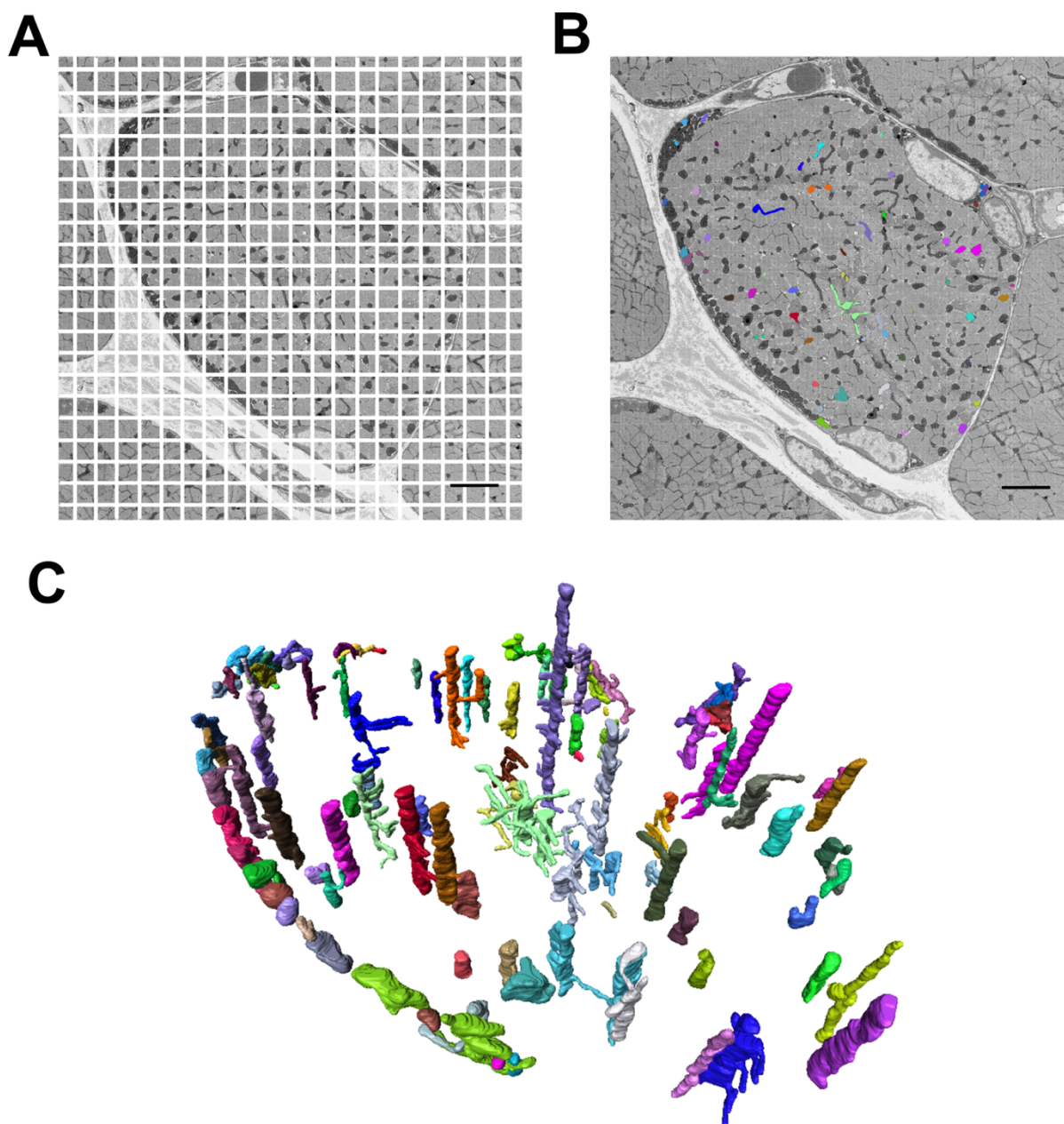


**Figure 2.29 – Random selection of mitochondria for analysis of individual whole mitochondria.** (A) Example of single section from adult guinea pig soleus muscle with bold grid in white superimposed on the image. (B) The chosen section, from random number generation, and grid showing segmentation of individual whole mitochondria that intersect with the grid lines. (C) 3D reconstruction of the individual mitochondria, multi-coloured, from the example dataset. Scale bar 5 $\mu$ m, image size 5000 x 5000 pixels and 10nm resolution. Video: <https://doi.org/10.6084/m9.figshare.7140713.v3>

#### *2.5.5. Statistical Analysis*

All statistical analysis and graphs were produced in Microsoft Excel and MATLAB. Throughout the results the mean and standard deviation is presented in brackets, as (mean  $\pm$  standard deviation). A one-way Anova was performed across the groups with post-hoc Bonferroni test to test between the groups, and paired T-test was used when needed, for example for comparison between the two muscles. All statistical analysis was performed in SPSS. The results from one-way Anova test, performed for age group comparison, is presented in text and the post-hoc Bonferroni or T-Test is shown on the graphs.

All of the raw datasets have been made available online, links to access the datasets and parameters are shown in Table 2.5. Links to videos of the reconstructions are stated in associated figure legends.

**Table 2.5 – Access links to skeletal muscle datasets.** Links to all of the datasets analysed in this project with the parameters for each dataset.

Age	Tissue Type	Code	nm/ pixel	No. of Slices	X & Y, pixels	Z, nm	Access Link
Adult	Psoas	163 Cell 1	10	250	4000	70	<a href="https://doi.org/10.5281/zenodo.1434998">https://doi.org/10.5281/zenodo.1434998</a>
		165 Cell 1	18	250	3000	70	<a href="https://doi.org/10.5281/zenodo.1434998">https://doi.org/10.5281/zenodo.1434998</a>
		165 Cell 2	19	250	3000	70	<a href="https://doi.org/10.5281/zenodo.1434998">https://doi.org/10.5281/zenodo.1434998</a>
		165 Cell 3	19	250	3000	70	<a href="https://doi.org/10.5281/zenodo.1434998">https://doi.org/10.5281/zenodo.1434998</a>
		166 Cell 1 and 2	11	250	5000	70	<a href="https://doi.org/10.5281/zenodo.1434998">https://doi.org/10.5281/zenodo.1434998</a>
		166 Cell 3	11	250	5000	70	<a href="https://doi.org/10.5281/zenodo.1434998">https://doi.org/10.5281/zenodo.1434998</a>
Adult	Soleus	162 Cell 1	22	250	3000	70	<a href="https://doi.org/10.5281/zenodo.1435432">https://doi.org/10.5281/zenodo.1435432</a>
		162 Cell 2	28	250	3000	70	<a href="https://doi.org/10.5281/zenodo.1435432">https://doi.org/10.5281/zenodo.1435432</a>
		164 Cell 1	10	250	5000	70	<a href="https://doi.org/10.5281/zenodo.1435432">https://doi.org/10.5281/zenodo.1435432</a>
		164 Cell 2	10	250	5000	70	<a href="https://doi.org/10.5281/zenodo.1435432">https://doi.org/10.5281/zenodo.1435432</a>
		166 Cell 1	8	300	5000	70	<a href="https://doi.org/10.5281/zenodo.1435432">https://doi.org/10.5281/zenodo.1435432</a>



		166					<a href="https://doi.org/10.5281/zenodo.1435432">https://doi.org/10.5281/zenodo.1435432</a>
		Cell 2	8	300	5000	70	
<b>Foetal</b>	<b>Day</b>	275					
		Pup 1					<a href="https://doi.org/10.5281/zenodo.1435532">https://doi.org/10.5281/zenodo.1435532</a>
		Cell 1,2	13	385	3000	70	
		and 3					
<b>60-64</b>		275					
		Pup 2					<a href="https://doi.org/10.5281/zenodo.1435532">https://doi.org/10.5281/zenodo.1435532</a>
		Cell 1	15	288	3500	70	
		and 2					
		275					
		Pup 3	9	311	2000	70	<a href="https://doi.org/10.5281/zenodo.1435532">https://doi.org/10.5281/zenodo.1435532</a>
		Cell 1					
		275					
		Pup 3	8	291	5000	70	<a href="https://doi.org/10.5281/zenodo.1435532">https://doi.org/10.5281/zenodo.1435532</a>
		Cell 2					
<b>Foetal</b>	<b>Day</b>	275					
		Pup 1	9	270	3000	70	<a href="https://doi.org/10.5281/zenodo.1435536">https://doi.org/10.5281/zenodo.1435536</a>
		Cell 1					
<b>60-64</b>		275					
		Pup 1	9	272	3000	70	<a href="https://doi.org/10.5281/zenodo.1435536">https://doi.org/10.5281/zenodo.1435536</a>
		Cell 2					
		275					
		Pup 2	8	300	3000	70	<a href="https://doi.org/10.5281/zenodo.1435536">https://doi.org/10.5281/zenodo.1435536</a>
		Cell 1					
		275					
		Pup 2	8	402	4000	70	<a href="https://doi.org/10.5281/zenodo.1435536">https://doi.org/10.5281/zenodo.1435536</a>
		Cell 2					

		275					<a href="https://doi.org/10.5281/zenodo.1435536">https://doi.org/10.5281/zenodo.1435536</a>
		Pup 3	8	296	3500	70	
		Cell 1					
		275					<a href="https://doi.org/10.5281/zenodo.1435536">https://doi.org/10.5281/zenodo.1435536</a>
		Pup 3	8	268	4000	70	
		Cell 2					
<b>Foetal</b>		521					<a href="https://doi.org/10.5281/zenodo.1435581">https://doi.org/10.5281/zenodo.1435581</a>
<b>Day</b>	Psoas	Pup 1	7	290	3000	70	
<b>55-59</b>		Cell 1					
		521					<a href="https://doi.org/10.5281/zenodo.1435581">https://doi.org/10.5281/zenodo.1435581</a>
		Pup 1	07	290	3000	70	
		Cell 2					
		521					<a href="https://doi.org/10.5281/zenodo.1435581">https://doi.org/10.5281/zenodo.1435581</a>
		Pup 4	9	250	2000	70	
		Cell 1					
		521					<a href="https://doi.org/10.5281/zenodo.1435581">https://doi.org/10.5281/zenodo.1435581</a>
		Pup 4	9	250	2000	70	
		Cell 2					
		521					<a href="https://doi.org/10.5281/zenodo.1435581">https://doi.org/10.5281/zenodo.1435581</a>
		Pup 4	9	250	2000	70	
		Cell 3					
		523					<a href="https://doi.org/10.5281/zenodo.1435581">https://doi.org/10.5281/zenodo.1435581</a>
		Pup 4	8	297	3000	70	
		Cell 1					
<b>Foetal</b>		523					<a href="https://doi.org/10.5281/zenodo.1435584">https://doi.org/10.5281/zenodo.1435584</a>
<b>Day</b>	Soleus	Pup 2	8	422	3000	70	
<b>55-59</b>		Cell 1					

		523					<a href="https://doi.org/10.5281/zenodo.1435584">https://doi.org/10.5281/zenodo.1435584</a>
		Pup 2	8	259	3000	70	
		Cell 2					
		523					<a href="https://doi.org/10.5281/zenodo.1435584">https://doi.org/10.5281/zenodo.1435584</a>
		Pup 3	9	321	3000	70	
		Cell 1					
		523					<a href="https://doi.org/10.5281/zenodo.1435584">https://doi.org/10.5281/zenodo.1435584</a>
		Pup 3	9	319	3000	70	
		Cell 2					
		523					<a href="https://doi.org/10.5281/zenodo.1435584">https://doi.org/10.5281/zenodo.1435584</a>
		Pup 5	8	269	3000	70	
		Cell 1					
		523					<a href="https://doi.org/10.5281/zenodo.1435584">https://doi.org/10.5281/zenodo.1435584</a>
		Pup 4	8	269	3000	70	
		Cell 2					
<b>Foetal</b>		522					<a href="https://doi.org/10.5281/zenodo.1435725">https://doi.org/10.5281/zenodo.1435725</a>
<b>Day</b>	Psoas	Pup 1	8	300	2500	70	
<b>50-54</b>		Cell 1					
		522					<a href="https://doi.org/10.5281/zenodo.1435725">https://doi.org/10.5281/zenodo.1435725</a>
		Pup 1	8	300	2500	70	
		Cell 2					
		522					<a href="https://doi.org/10.5281/zenodo.1435725">https://doi.org/10.5281/zenodo.1435725</a>
		Pup 2	8	299	3500	70	
		Cell 1					
		522					<a href="https://doi.org/10.5281/zenodo.1435725">https://doi.org/10.5281/zenodo.1435725</a>
		Pup 2	8	300	3500	70	
		Cell 2					

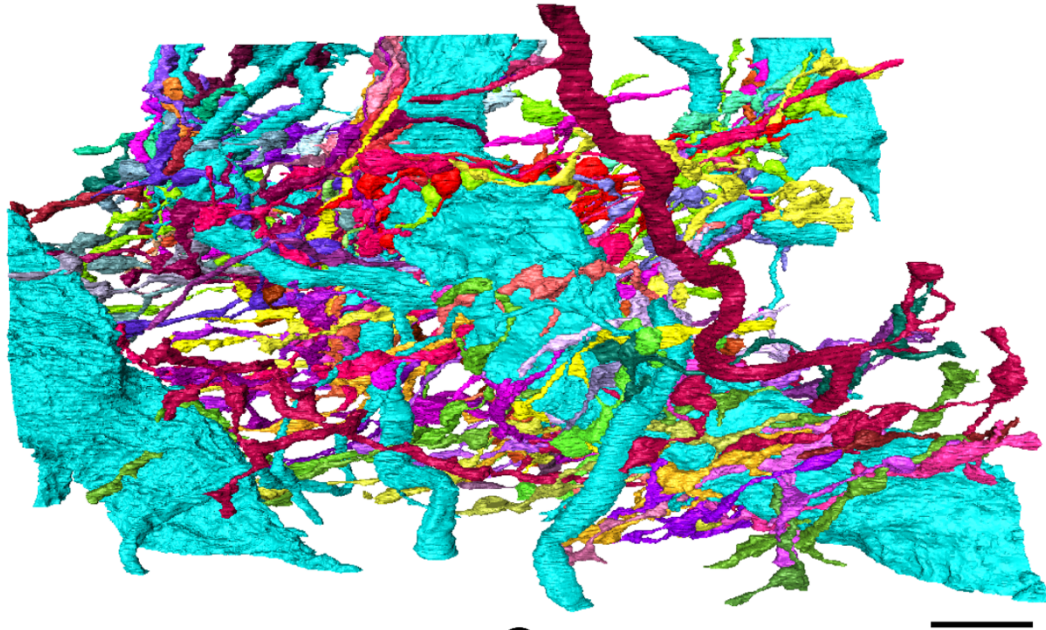
		522					<a href="https://doi.org/10.5281/zenodo.1435725">https://doi.org/10.5281/zenodo.1435725</a>
		Pup 3	8	300	3000	70	
		Cell 1					<a href="https://doi.org/10.5281/zenodo.1435725">https://doi.org/10.5281/zenodo.1435725</a>
		522					<a href="https://doi.org/10.5281/zenodo.1435725">https://doi.org/10.5281/zenodo.1435725</a>
		Pup 3	8	300	3000	70	
		cell 2					<a href="https://doi.org/10.5281/zenodo.1435725">https://doi.org/10.5281/zenodo.1435725</a>
<b>Foetal</b>		522					<a href="https://doi.org/10.5281/zenodo.1435729">https://doi.org/10.5281/zenodo.1435729</a>
<b>Day</b>	Soleus	Pup 1	8	300	3000	70	
<b>50-54</b>		Cell 1					<a href="https://doi.org/10.5281/zenodo.1435729">https://doi.org/10.5281/zenodo.1435729</a>
		522					<a href="https://doi.org/10.5281/zenodo.1435729">https://doi.org/10.5281/zenodo.1435729</a>
		Pup 1	8	298	2000	70	
		Cell 2					<a href="https://doi.org/10.5281/zenodo.1435729">https://doi.org/10.5281/zenodo.1435729</a>
		522					<a href="https://doi.org/10.5281/zenodo.1435729">https://doi.org/10.5281/zenodo.1435729</a>
		Pup 2	8	307	3000	70	
		Cell 1					<a href="https://doi.org/10.5281/zenodo.1435729">https://doi.org/10.5281/zenodo.1435729</a>
		522					<a href="https://doi.org/10.5281/zenodo.1435729">https://doi.org/10.5281/zenodo.1435729</a>
		Pup 2	8	247	2500	70	
		Cell 2					<a href="https://doi.org/10.5281/zenodo.1435729">https://doi.org/10.5281/zenodo.1435729</a>
		522					<a href="https://doi.org/10.5281/zenodo.1435729">https://doi.org/10.5281/zenodo.1435729</a>
		Pup 3	8	300	2000	70	
		Cell 1					<a href="https://doi.org/10.5281/zenodo.1435729">https://doi.org/10.5281/zenodo.1435729</a>
		522					<a href="https://doi.org/10.5281/zenodo.1435729">https://doi.org/10.5281/zenodo.1435729</a>
		Pup 3	8	287	2500	70	
		Cell 2					<a href="https://doi.org/10.5281/zenodo.1435729">https://doi.org/10.5281/zenodo.1435729</a>

## Chapter 3. Results

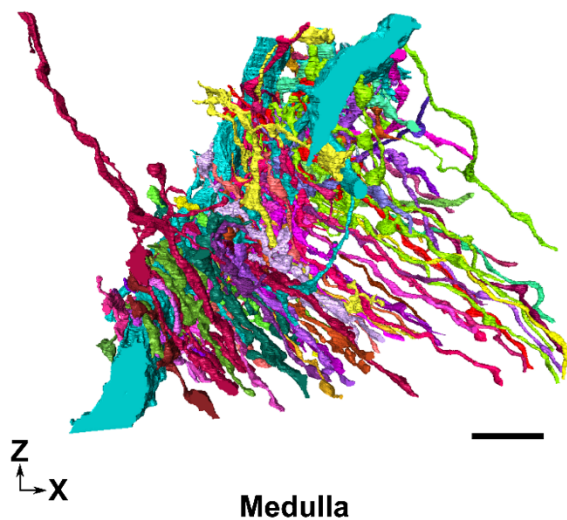
### 3.1. Locust Results

#### 3.1.1. Reconstructions

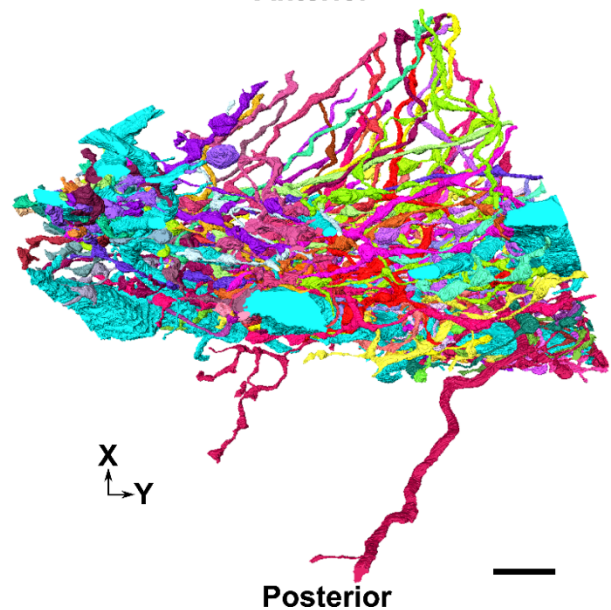
From the SBF-SEM dataset collected a length of  $\sim 47.11\mu\text{m}$  of a branch of the LGMD 2 neuron was reconstructed as well as any TmA neurons found to synapse onto the branch. In total 360 synapses were found to occur onto the LGMD 2 neuron branches and the TmA neurons associated with all were reconstructed, shown in Figure 3.1. The segmentation of the LGMD 2 neuron, TmA neurons and synapses took roughly 9 months, average 6hrs a day and 5 days a week. The average diameter of this branch of the LGMD 2 neuron was found to be  $12\mu\text{m}$ , calculated by taking a diameter measure every 10 sections, making it one of medium diameter. The TmA neurons were followed through the dataset allowing for a full reconstruction of them. This branch of the LGMD 2 neuron was termed the primary branch (\* in Figure 3.1). The TmA neurons also synapsed on subsequent neighbouring branches of the LGMD 2 neuron that were not traced to the large primary branch analysed and were therefore called secondary branches. These secondary branches were also reconstructed, a total of 9 more branches. The synaptic partners of the TmA neurons were also mapped for 7 of the 9 secondary LGMD 2 neuron branches. In total 216 TmA neurons were followed. For 92 of the TmA neurons, the complete terminal arbour was reconstructed (as described in the methods), referred to as complete neurons from now on. Including all the 10 branches, 1171 synapses onto the LGMD 2 neuron were found, with synaptic partners labelled for all. The TmA neurons first pass through the medulla, then cross in the second optic chiasm into the outer lobula region (OLO) of the optic lobe Rosner et al. (2017), to synapse upon the LGMD 2 neuron, Figure 3.1. From the reconstructions it can be seen that the TmA neurons synapse upon the LGMD 2 neuron in an organised manner. All TmA neurons, except two, follow a similar angular path, as shown in the reconstructions. The TmA neurons appear to have distinct regions of the LGMD 2 neuron where they terminate. This is indicative of a conserved retinotopic mapping present from the facets of the eye, with one facet associated with one TmA neuron, which in turn synapses with a single portion or area of the LGMD 2 neuron. Due to limited field of view, it cannot be determined from this dataset whether the TmA neurons found here also synapse upon the LGMD 1 neuron.

**A****B**

Protocerebrum

**C**

Anterior



Medulla

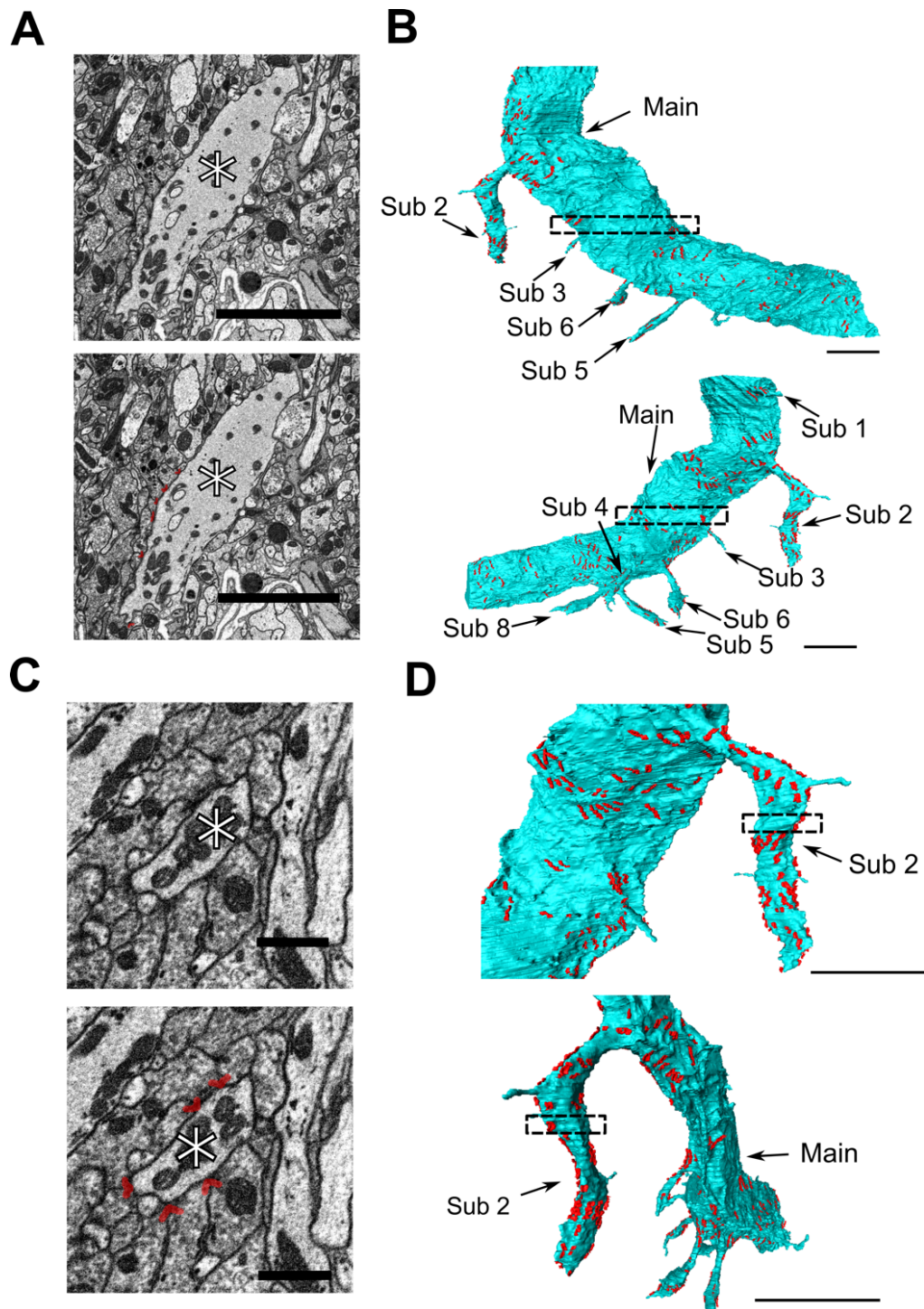
Posterior

**Figure 3.1 – Overview of reconstructed LGMD 2 neuron branches and TmA neuron segmentations.** (A) Shows the reconstructions of the LGMD 2 neuron branches reconstructed, *light blue*. As well as all 92 TmA neurons, *multi-coloured*, that were found to synapse onto the primarily analysed branch, (\*). (B) and (C) show the reconstructions with reference to the orientation of the neurons within the optic lobe, including the protocerebrum and medulla and anterior and posterior direction of the lobula. Scale bars are 5µm. Video: <https://doi.org/10.6084/m9.figshare.7172432>

### *3.1.2. Synapse Distribution Across the LGMD 2 Neuron Branch*

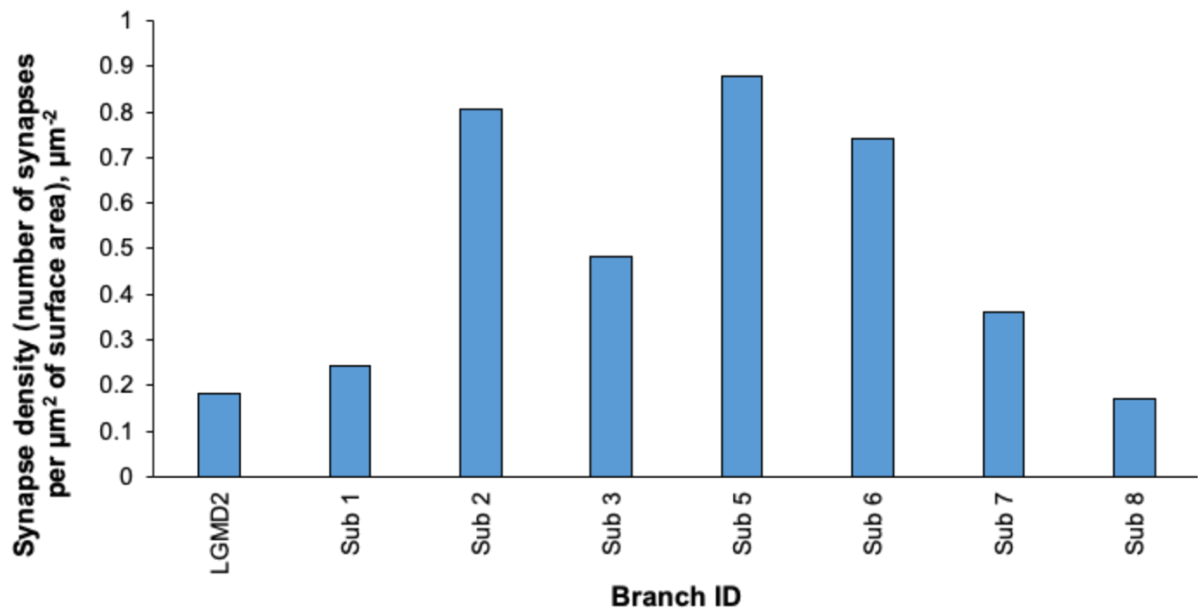
The location of the synapses made by TmA neurons on one of the LGMD 2 branches (primary branch), encompassing a main larger branch and smaller processes or sub-branches, extending from the main branch, were reconstructed (examples and reconstructions shown in Figure 3.2). The majority of the synapses were found on the larger branch, 245 (68%), with 115 (32%) on the smaller branches. However, the synapses were denser on the smaller processes, with a higher concentration of synapses over a smaller area and very few gaps between synapses. Along the larger main branch there were regions where there were no or few synapses present. When the synapse number by surface area was measured there was a higher density of synapses seen on the majority of the smaller branches (Figure 3.3). The large branch has an average of 0.18 synapses per  $1\mu\text{m}^2$ , whereas the smaller branches have an average 0.52 synapses per  $1\mu\text{m}^2$ , numbers ranging in the smaller branches from 0.17 to 0.81 synapses per  $1\mu\text{m}^2$ .





**Figure 3.2 – Distribution of synapses along larger and smaller branches of a portion of the LGMD 2 neuron.** (A) Shows cropped area of a slice from the dataset, with the second image showing the segmented synapses, *red*, surrounding the larger (main) branch of the LGMD 2, marked with a star. (B) Shows the reconstructions of the synapse segmentations, *red*, on the main branch, *blue*. The area the section was taken from is indicated by a box and two views are shown. (C) Cropped area from a single slice focusing on a sub-branch of the LGMD 2 (star). The second image shows the segmentation of the synapse around the smaller branch, *red*. (D) Example of reconstructions of the synapses, *red*, on one of the sub-branches. The area the section was taken from is indicated by a box and two views are shown. Scale bar for (A), (B) and (D) is 5 μm for (C) scale bar is 1 μm. Video: <https://doi.org/10.6084/m9.figshare.7172435>

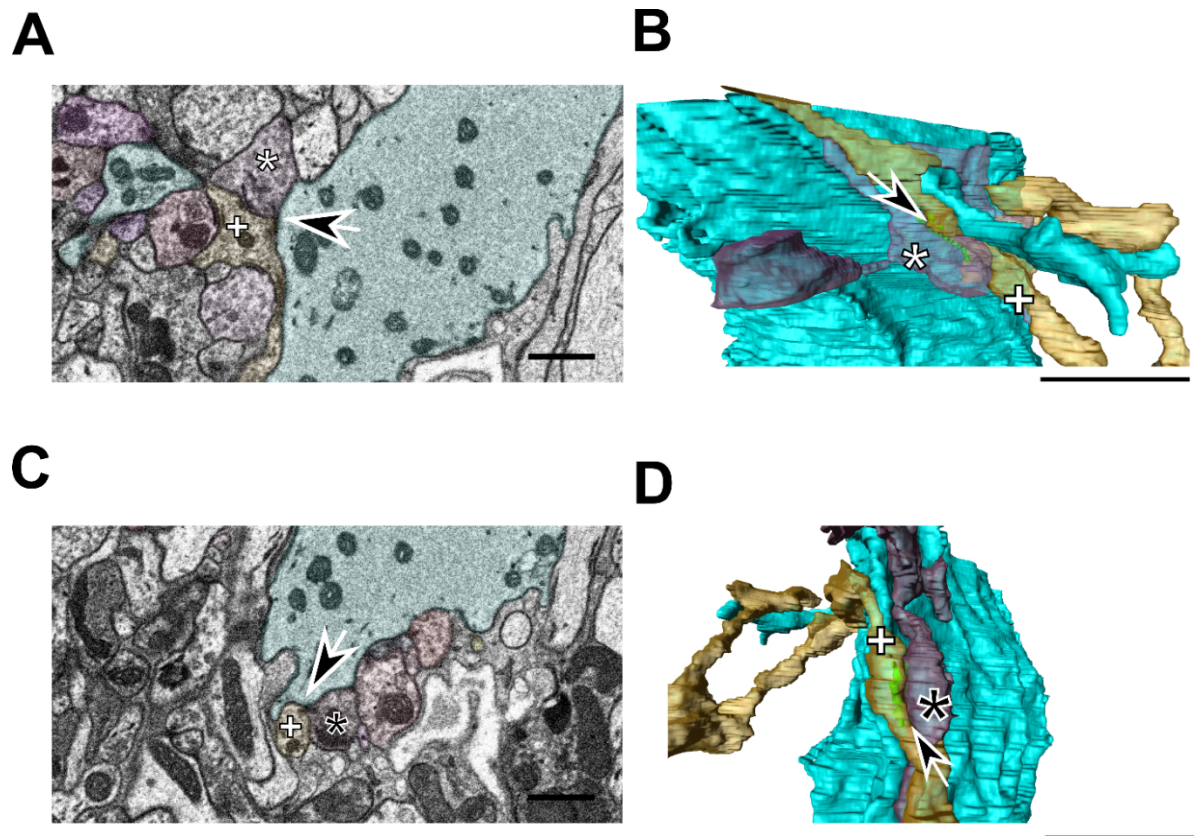




**Figure 3.3 – Results from distribution of synapses along larger and smaller branches.** Results of synaptic density (number of synapses per  $\mu\text{m}^2$  of surface area) of the main branch of the LGMD 2 neuron and the sub-branches originating from the main branch.

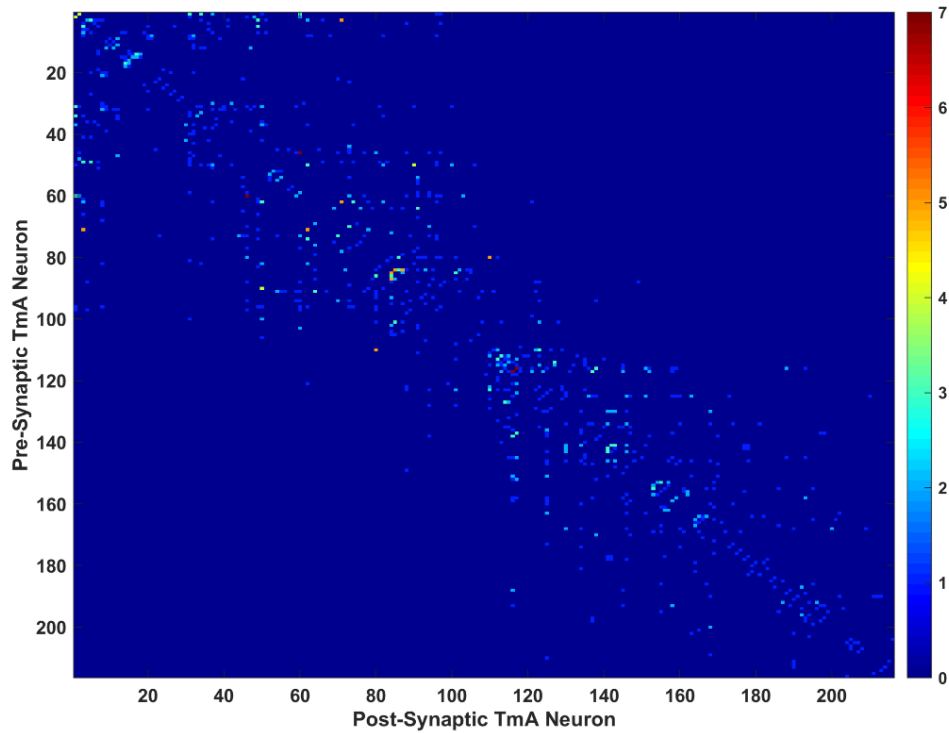
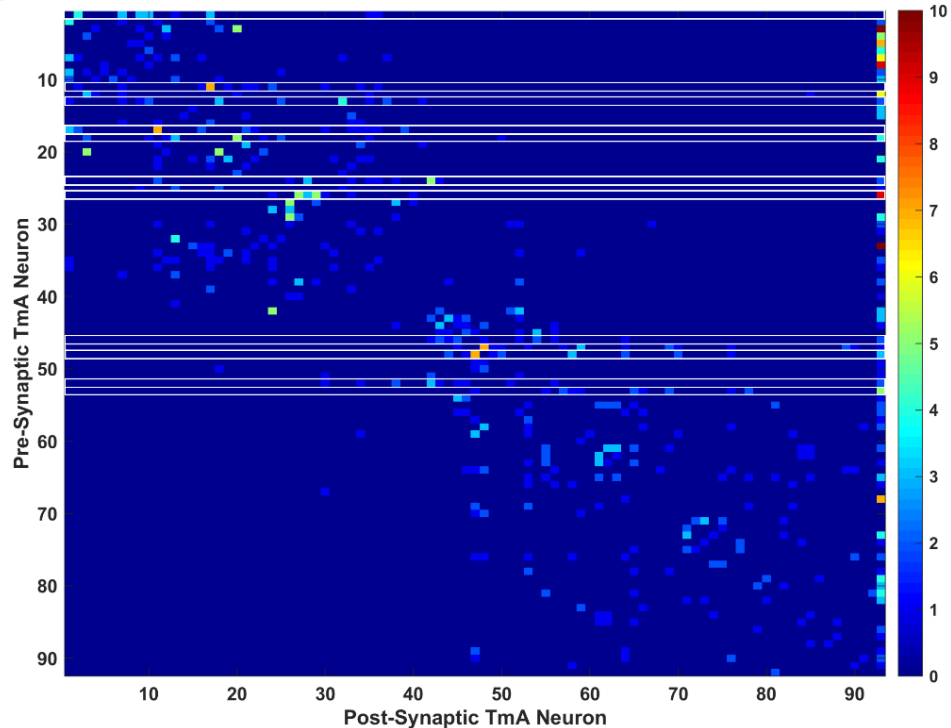
### 3.1.3. Connectivity in Z Direction

As detailed in the methods the final TmA neuron labels at each synapse were a combination of partially reconstructed neurons and TmA neurons whose terminal arbour was completely reconstructed. The analysis into the connectivity of the TmA neuron and LGMD 2 neuron branches was performed solely on the completely TmA arbours (with some exceptions for the connectome diagrams). As the TmA neurons were followed through the dataset information on the synapsing partners of the TmA neurons and the network of the TmA neurons was compiled. A single TmA can form a reciprocal synapse with another TmA neuron once or multiple times and potentially with different partners. An example of this is seen in Figure 3.4, showing how a single TmA neuron can synapse twice onto the LGMD 2 but in the second case with a different TmA neuron partner.



**Figure 3.4 – Formation of TmA neuron network via different synaptic partners.** (A) Example of synapse between two TmA neurons, *orange* (+) and *light pink* (white \*), onto the LGMD 2 neuron, *blue*. (B) The reconstruction of the TmA neurons at the synapse, green presynaptic density indicated by arrow. (C) The same TmA neuron, *orange* (+), with a different synaptic partner, *dark pink* (black \*), both synapsing onto the LGMD 2. (D) The reconstruction of the synapse, green presynaptic density indicated by black arrow. Scale bar on orthoslice is 1  $\mu\text{m}$  and on 3D model is 5  $\mu\text{m}$ . Video: <https://doi.org/10.6084/m9.figshare.7172441.v2>

The connectomes shown in Figure 3.5 map the synaptic partners of the TmA neurons and how many times that particular connection is made, indicated by the colour. The label of the neuron is spatial, with the lower numbers indicating a TmA neuron at the beginning of the dataset, thus further away from the medulla, compared to the neurons with a higher number label at the end of the dataset, closer to the medulla. The connectome diagram of the complete TmA neurons, show that they primarily synapse within a certain area of the dataset with nearby TmA neurons. This results in a network of connected TmA neurons over the LGMD 2 neuron branches. The individual TmA neurons have overlapping regions of connectivity but are still limited to a portion of the dataset, such that no TmA neuron from the beginning of the dataset synapses with a TmA neuron from the end of the dataset. Some TmA neuron to TmA neuron connections occur only once, but the majority of the TmA neuron to TmA neuron connections occur twice or three times, with a small proportion occurring upwards and including 7 times, as indicated by the colour code in the connectomes, Figure 3.5. A number of TmA neurons were also noted at having a high number of synapses, compared to others (indicated with white lines in Figure 3.5 (B)). To assess this and the connectivity further the total number of synapses, number of synaptic partners and the frequency of connections with the same partner was analysed.

**A****B**

**Figure 3.5 – Connectomes of TmA neuron v TmA neuron.** (A) Connectome of all TmA neurons onto TmA neurons  $N=216$ , synapse  $n = 1171$ . (B) Connectome of only the 92 completely reconstructed neurons  $N=92$ , synapse  $n = 837$ . In this plot TmA neuron 93 is the sum of all the partial neurons identified. For both connectomes the colour of each square, denoted in the heat-scale on the figure, indicates the number of times that a specific pre and post TmA neuron connection occurs. TmA neurons making a large number of synapses are delineated in white.

The frequency of TmA neuron partners and the total number of synapses is shown in Figure 3.6. The majority of the 92 TmA neurons with completely reconstructed arbours synapse between three and 10 times onto the LGMD 2 neuron, with a range from 1 to 26 times and a median of 8. As not all the synapses from a TmA neuron are with different partners, the number of synaptic partners was quantified, only taking into account the completely reconstructed terminal arbours of the TmA neurons. As shown in Figure 3.7, the highest number of the TmA neurons have at least 2 different synaptic partners, with the median of different partners being 4. The range extended from 1 to 13 partners. The number of synapses made with the same partner also varies, from the TmA neurons that only have one neighbour (9), three only synapse once, while the others synapse multiple times with the same partner. This led onto the next analysis, where the number of times a TmA neuron synapsed with the same partner was plotted. The graph in Figure 3.8 shows the frequency of times a neuron synapses with the same partner. The majority of the neurons synapse 2 to 3 times with the same neighbour. The range was from 1 to 7, with two pairs of neurons found to synapse with each other 7 times.

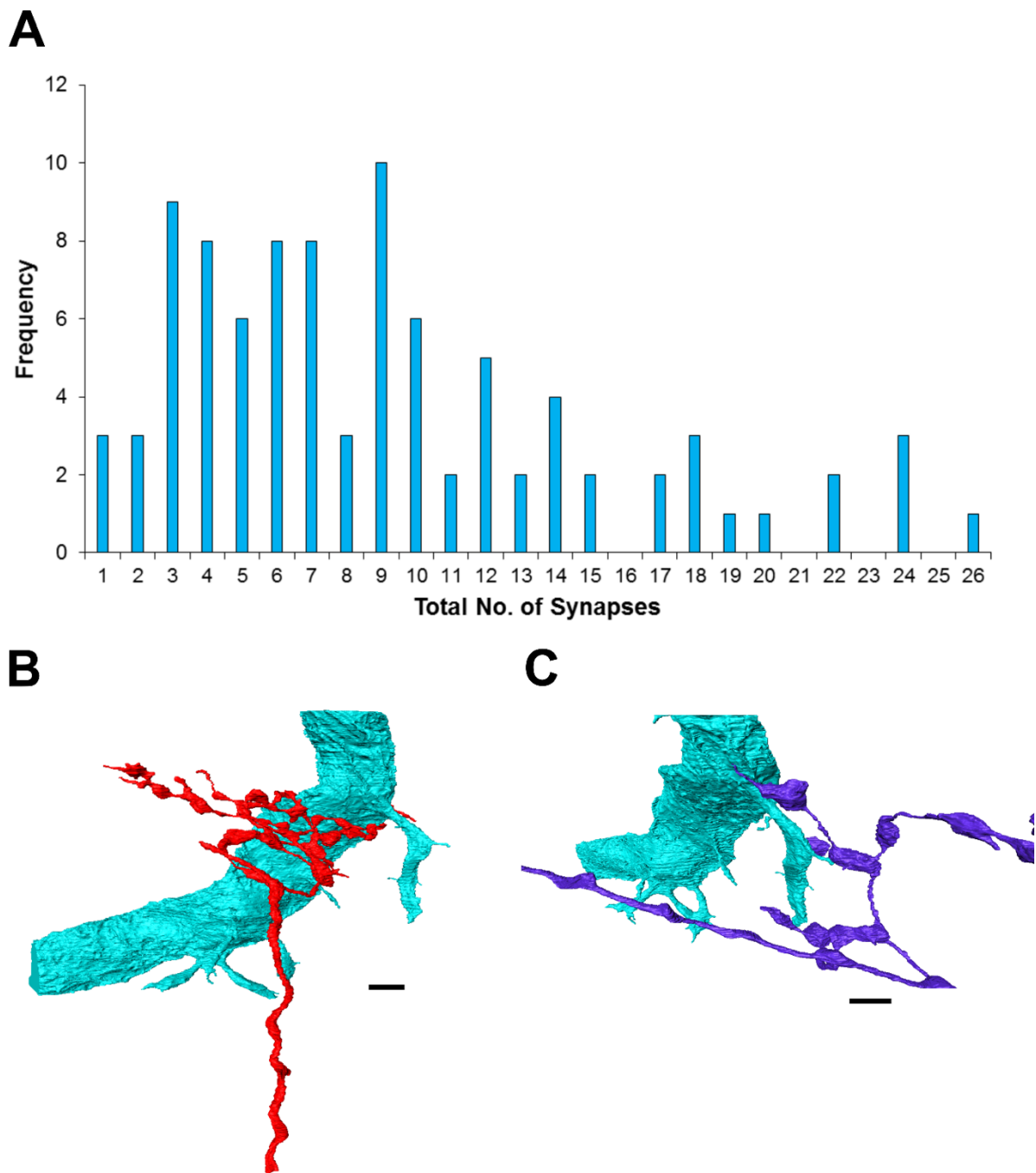


**Figure 3.6 –Total number of synapses from individual TmA neurons.** (A) Graph showing the frequency of TmA neurons that synapse between 1 and 26 times. Median = 8, IQR (25<sup>th</sup>) = 5, IQR (75<sup>th</sup>) = 12, Range = 1-26. (B) Reconstruction of the TmA neuron which synapses the highest number of times onto the LGMD 2 neuron (26). (C) Example of a TmA neuron, which only synapses once onto the LGMD 2 neuron branch. Scale bars 5µm. Video: <https://doi.org/10.6084/m9.figshare.7172450.v2>

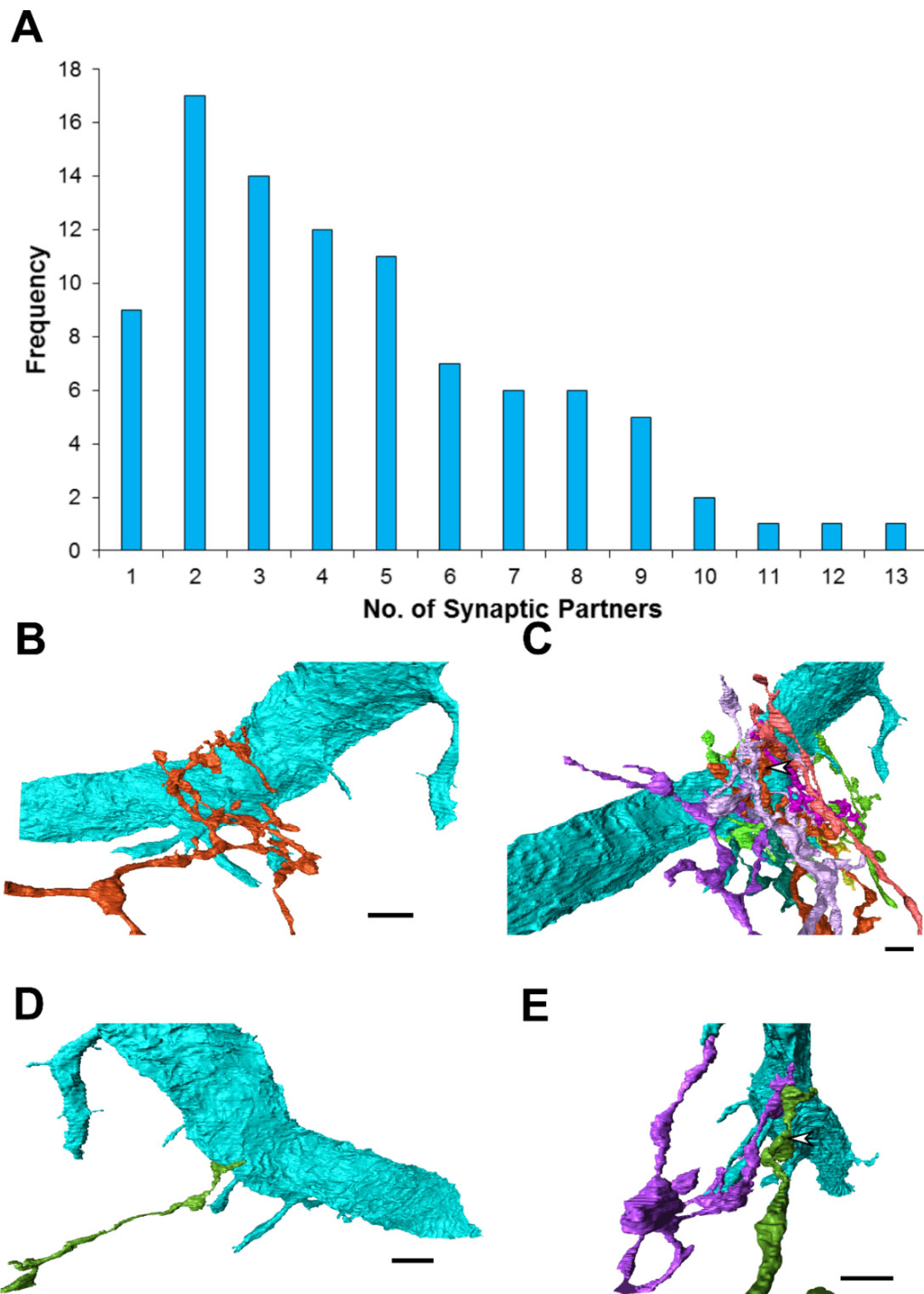


**Figure 3.7 –Number of synaptic partners found for individual TmA neurons.** (A) Graph of the frequency of unique connections made by individual TmA neurons that is the number of different synaptic partners (TmA neurons can synapse with same partner multiple times). (B) Example of TmA neuron known to have a high number of multiple synaptic partners. (C) Reconstructions of the same neuron, labelled with *arrow*, with some of the synaptic partners (5 out of 12 partners shown). (D) Example of a neuron with only one other synaptic partner and same neuron is shown, labelled with *arrow*, with the single partner in (E). Median = 4, IQR (25<sup>th</sup>) = 2, IQR (75<sup>th</sup>) = 5, Range = 1-13. Video: <https://doi.org/10.6084/m9.figshare.7172453.v2>

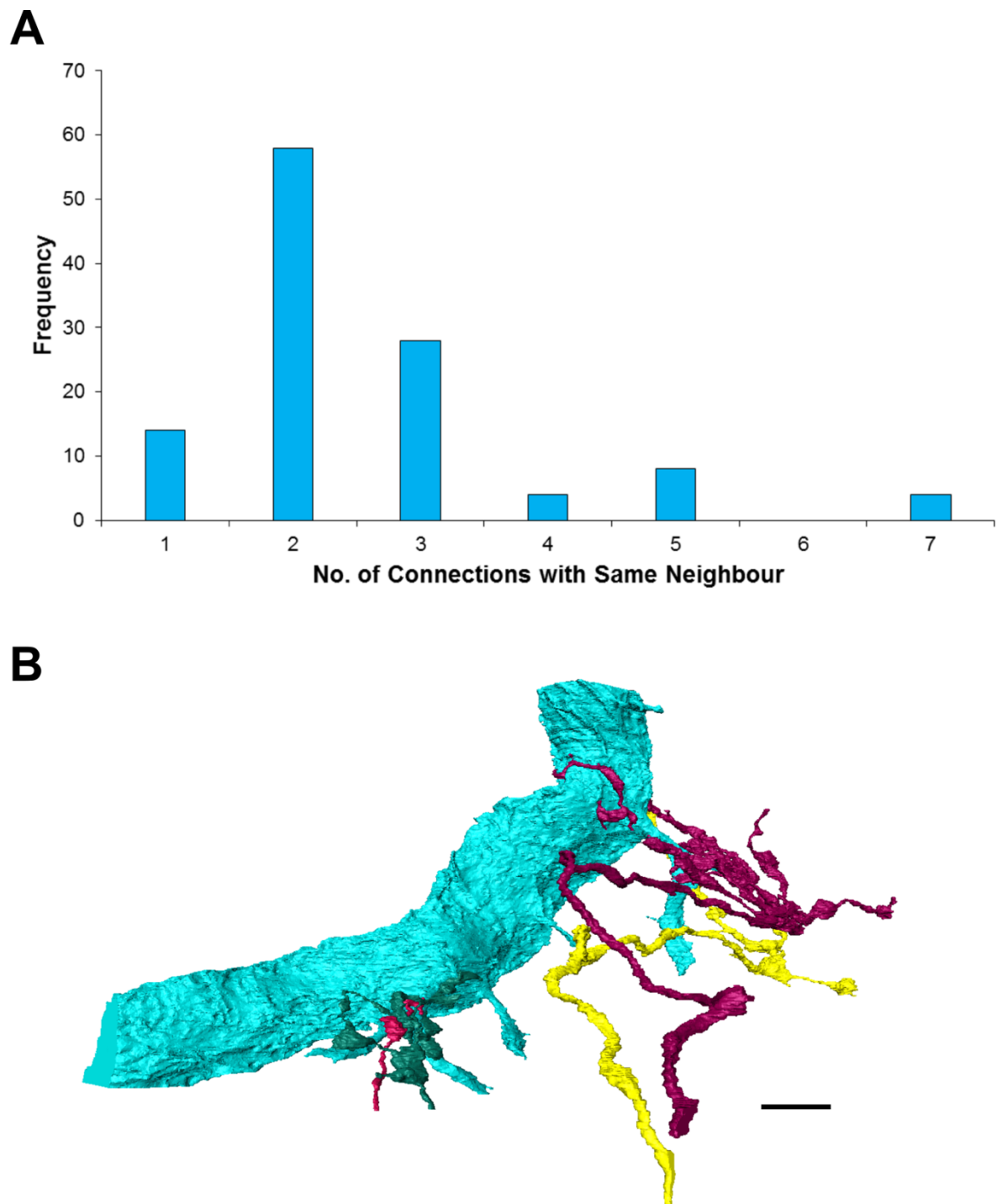


**Figure 3.8 – Frequency of TmA neurons synapsing with the same partner.** (A) Shows the results of analysing the number of times a TmA neuron synapses with the same partner and frequency of TmA neurons that share the same number. (B) Shows reconstruction of two pairs of TmA neurons that synapse with each other on only 2 occasions. Median = 2, IQR (25)=2, IQR(75)=3, Range = 1-7. Scale bar 5µm. Video: <https://doi.org/10.6084/m9.figshare.7172462.v2>



A schematic of the network to highlight these concepts was drawn, shown in Figure 3.9. Starting from a TmA neuron (149) that synapsed only once with another TmA neuron (88), the synaptic partners of this TmA neuron (88) was then added (TmA neuron 123) and so forth, including those connections found between slice 270 and slice 350 of the reconstruction. The diagram shows how the TmA neurons have a specific region in which they contact the LGMD 2 neuron and interact with other TmA neurons. These areas overlap, with TmA neurons having varied total numbers of synapses and synaptic partners. As found from the earlier results a small population of TmA neurons stood out by having a high number of synapses and also high number of synaptic partners, TmA neuron 115 and 123 for example, labelled with asterisks in Figure 3.9.

**Figure 3.9 – Schematic of a portion of the network of TmA neurons synapsing onto the LGMD 2 neuron.** The diagram shows a small portion of the pattern of synapsing TmA neurons synapsing on the LGMD 2 neuron (~80 slices). Each coloured line represents a different segmented neuron, colour matching the segmentation and reconstruction colour, only a portion of the synaptic partners for the neurons are also shown and only a small number of the synapses that occur within the region shown are presented. This map includes TmA neurons with both fully and partially reconstructed arbors. TmA neurons with high number of synapses are marked (\*).

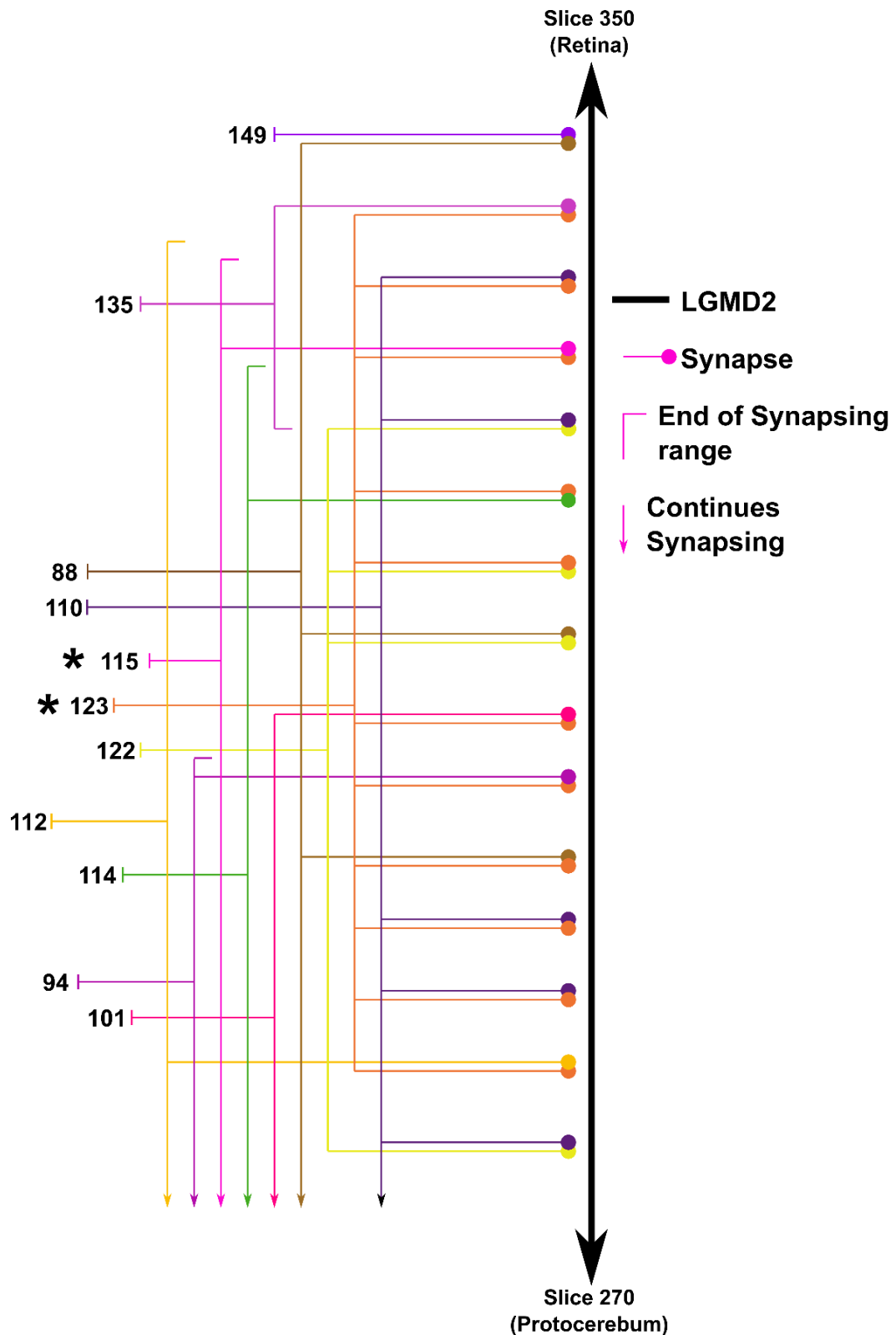


**Figure 3.9 – Schematic of a portion of the network of TmA neurons synapsing onto the LGMD 2 neuron.** The diagram shows a small portion of the pattern of synapsing TmA neurons synapsing on the LGMD 2 neuron (~80 slices). Each coloured line represents a different segmented neuron, colour matching the segmentation and reconstruction colour, only a portion of the synaptic partners for the neurons are also shown and only a small number of the synapses that occur within the region shown are presented. This map includes TmA neurons with both fully and partially reconstructed arbors. TmA neurons with high number of synapses are marked (\*).

To determine whether there were two groups of neurons, the total number of synapses was plotted against the number of postsynaptic partners, seen in Figure 3.10(A). There was a positive correlation between total number of synapses and number of unique connections ( $p=2.67E-36$ ) found. From this relationship, a connectivity index was calculated:

$$\text{Connectivity Index} = \frac{\text{Total Number of Synapses (n)} \times \text{Number of Unique partners (N)}}{100}$$

100

When this index was plotted against the total number of synapses (Figure 3.10(B)) a positive correlation was shown and formation of two groupings is seen. When the connectivity index is plotted alone the distinction between two groups is larger (Figure 3.10(C)). From these graphs, a cut-off was decided based on a connectivity index of 1 (shown as a black line on the graph 3.10(C)). In total 12 neurons were found to have a higher connectivity index than 1 and named 'hub neurons'. These neurons synapse a minimum of 12 times and up to 26 times (mean= 18) onto the LGMD 2 branches and have from 7 to 13 unique partners (mean= 10). The connectivity index distribution of the hub and non-hub neurons is plotted in Figure 3.11(A), indicating a highly connective sub-group of TmA neurons.

The synaptic distance and range were also measured for all neurons so as to compare between the two groups. The synaptic distance was calculated by cumulating the number of sections the TmA neuron made synaptic contact with the LGMD 2 neuron. The synaptic range is the distance, determined by number of slices, between the slice at which the TmA neuron first synapses to the last slice at which it synapses, irrespective of whether it was synapsing or not synapsing. For both measures there was significant difference found between the hub and non-hub neurons (Figure 3.11(B) and (C)). For the distance and range, the hub neurons were found to have a mean of 6.14 $\mu\text{m}$  and 10.41 $\mu\text{m}$  and the non-hub mean of 2.75 $\mu\text{m}$  and 4.72 $\mu\text{m}$ , respectively. The hub neurons had a larger synaptic range and synapsed for longer along the LGMD 2 neuron branches.

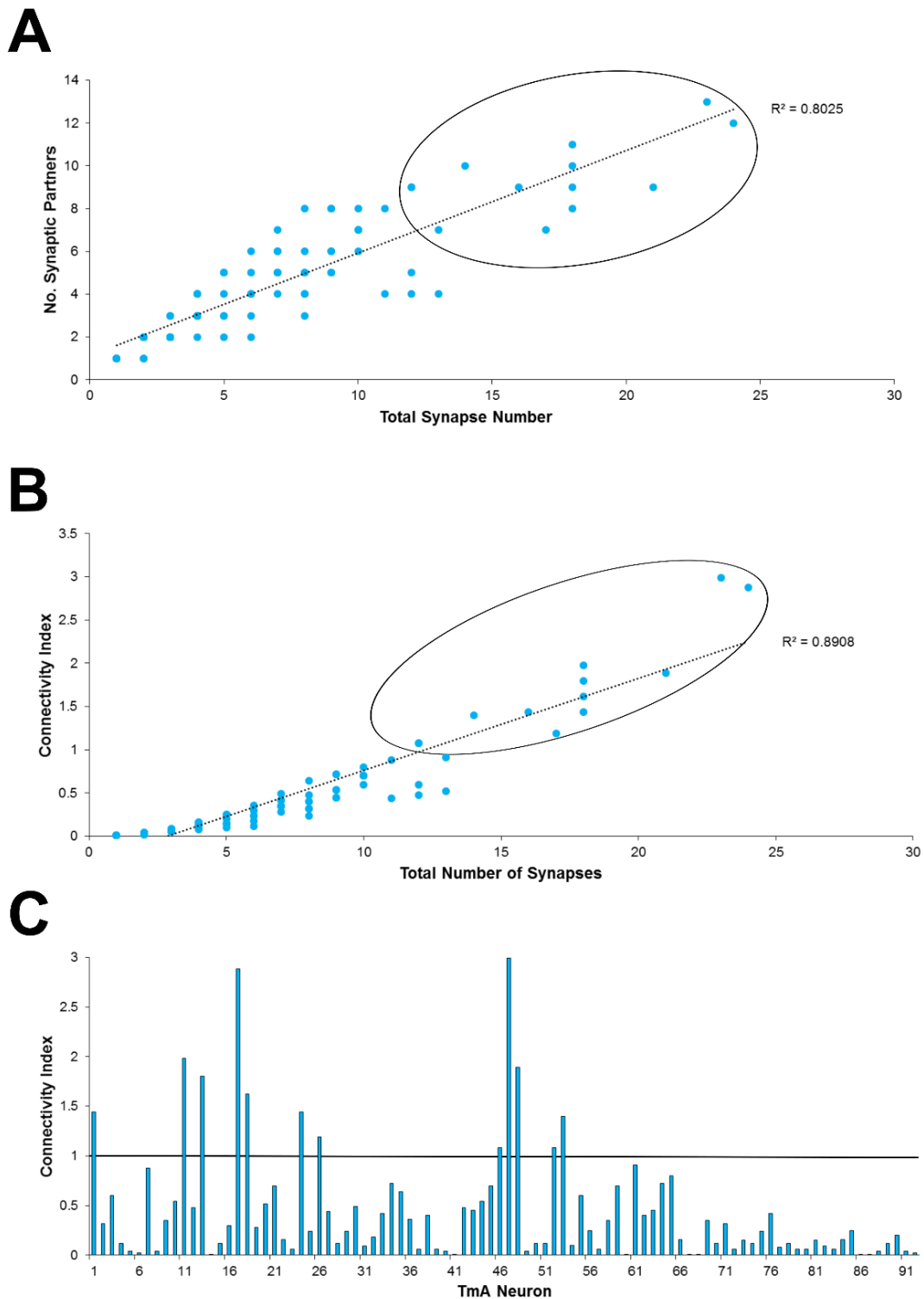


**Figure 3.10 – Analysis of total number of synaptic connections against number of unique connections for each of the TmA Neurons.** (A) Shows the results from mapping the total number of synapses against the number of unique partners for each of the complete TmA neurons,  $n=92$ . The  $R^2$  value is also shown on the graph alongside the plotted line. (B) Is the connectivity index (Connectivity Index = (Total Number of Synapses x Number of Unique partners)/100) plotted against the total number of synapses. (C) Is each TmA neuron and respective connectivity index. A line is drawn at connectivity index of 1 to denote the cut off for the so-called hub neurons that have a connectivity index above 1. These neurons are marked with an ellipse in (A) and (B)

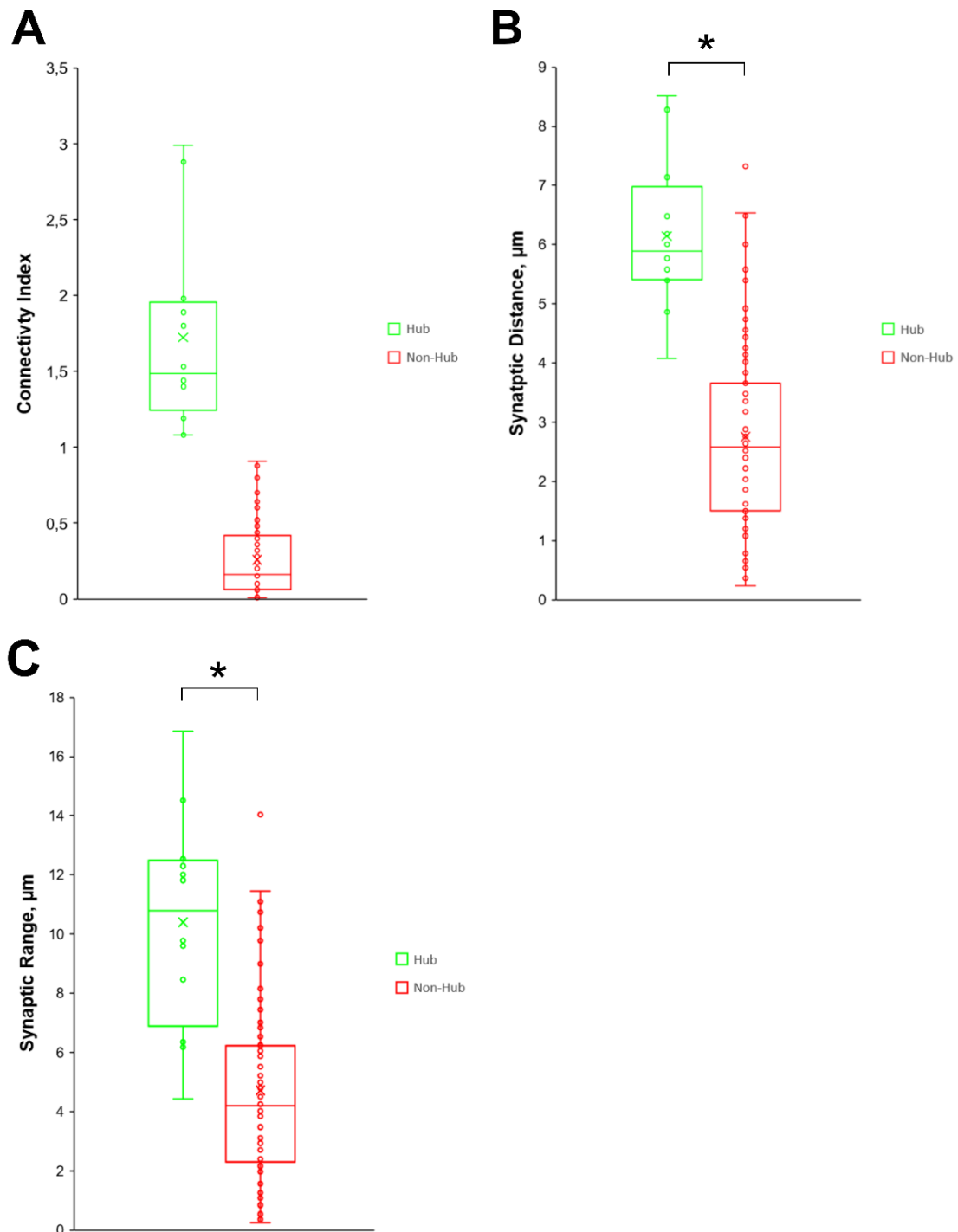


**Figure 3.11 – Comparison of ‘hub’ and non-hub neurons.** (A) The connectivity index for the hub and non-hub neurons. Hub median = 1.49, IQR(25<sup>th</sup>) = 1.35, IQR(75<sup>th</sup>) = 1.91 and range = 1.08-2.99. For non-hub, median = 0.16, IQR(25<sup>th</sup>) = 0.06, IQR(75<sup>th</sup>) = 0.42, and range 0.01-0.91. (B) Comparison of synaptic distance, measure of synaptic contact with the LGMD 2. For the hubs, median=5.88, IQD(25)=5.45, IQD(75)=6.65, range 4.1-8.52 and non-hub, median=2.58, IQR(25)=1.5, IWR(75)=3.66, range=0.24-7.32, (\*)  $p < 0.05$ . (C) Comparison of the synaptic range, distance from first synapse to last synapse. The hub median=10.8, IQR(25)=7.94, IQR(75)=12.36, range=4.44-16.86 and non-hub median=4.2, IQR(25)=2.37, IQR(75)=6.2, range=0.24-14.16. (\*)  $p < 0.05$ . The mean of each group is also plotted on the graphs (X) and the data points (O) and for all the Hub neurons are shown in green (n=12) and the non-hub neurons in red (n=80).

The reconstructions of the hub neurons are shown in Figure 3.12. They appear more complex than non-hubs, as shown in Figure 3.12(A) and (B). The hub neurons were also found to be situated around branches of the LGMD 2 neuron, with all neurons synapsing onto the primary branch as well as the secondary branches of this reconstructed portion of the LGMD 2 neuron (Figure 3.12(C)).

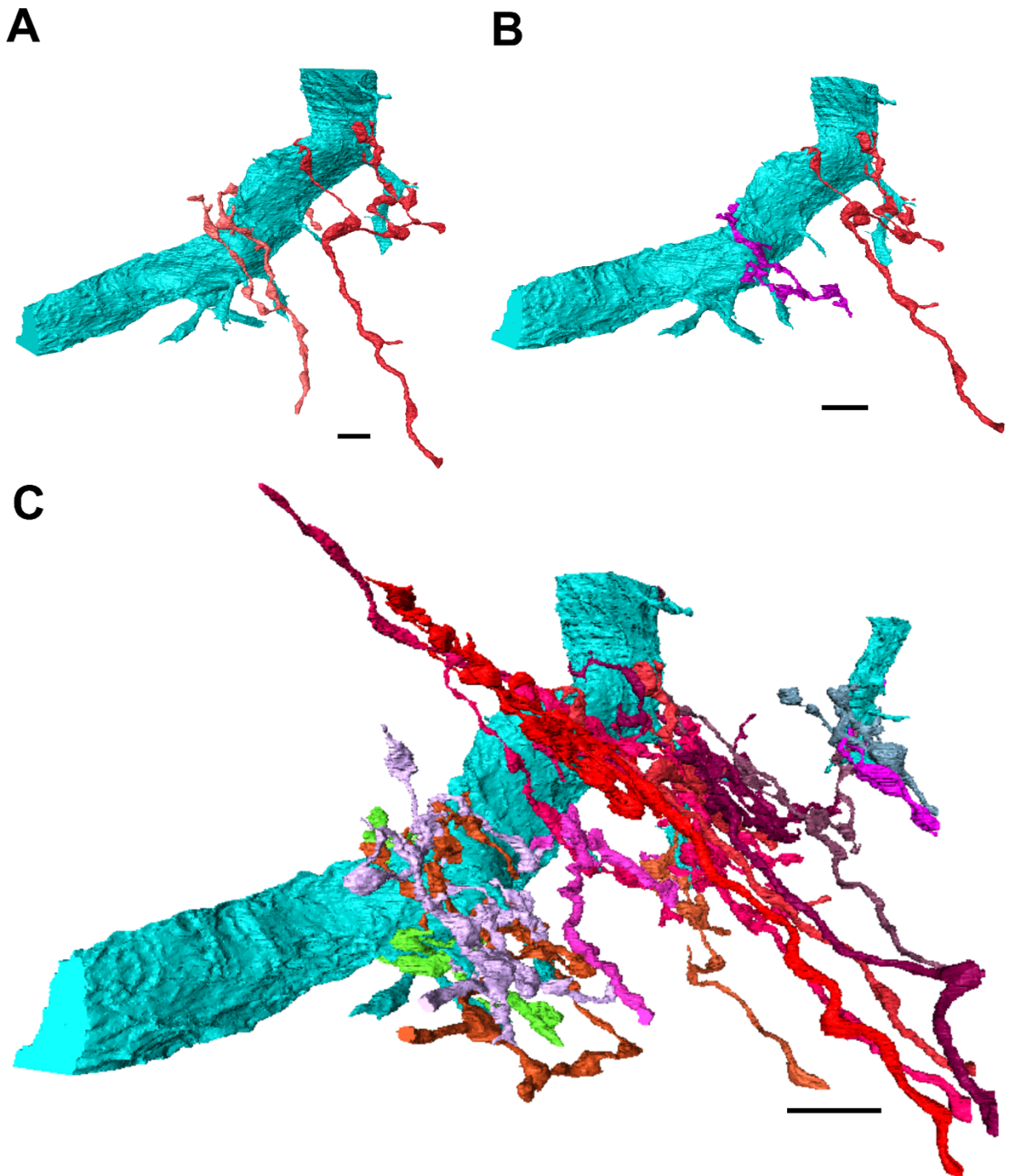


**Figure 3.12 – Reconstructions of the ‘hub’ neurons.** (A) and (B) Show examples of a hub (red) and 2 non-hub neurons (purple and orange), with different complexities. (C) Shows the reconstructions of all of the ‘hub’ neurons (multi-coloured),  $n=12$ , and the LGMD 2 neuron branches (light blue). All scale bars 5µm. Video: <https://doi.org/10.6084/m9.figshare.7172465.v2>



#### *3.1.4. Connectivity in X and Y Direction*

A small portion of TmA neurons followed from the main LGMD 2 neuron branch were found to synapse upon neighbouring branches of the LGMD 2 neuron as well. Representative example reconstruction of those TmA neurons and their post-synaptic LGMD 2 neuron branches can be seen in the reconstructions in Figure 3.13(A-G). By following and mapping the TmA neurons and the branches they synapse upon, three types of synaptic distribution across the LGMD 2 neuron were proposed. Firstly, TmA neurons could synapse upon one branch solely, secondly, they could synapse primarily on a single branch with a small proportion of synapses on another branch and lastly, they could synapse evenly across multiple branches. This is shown in a schematic in Figure 3.13(H). This would also give an indication of the connectivity that occurs in the X and Y direction, across the branches of the LGMD 2 neuron.

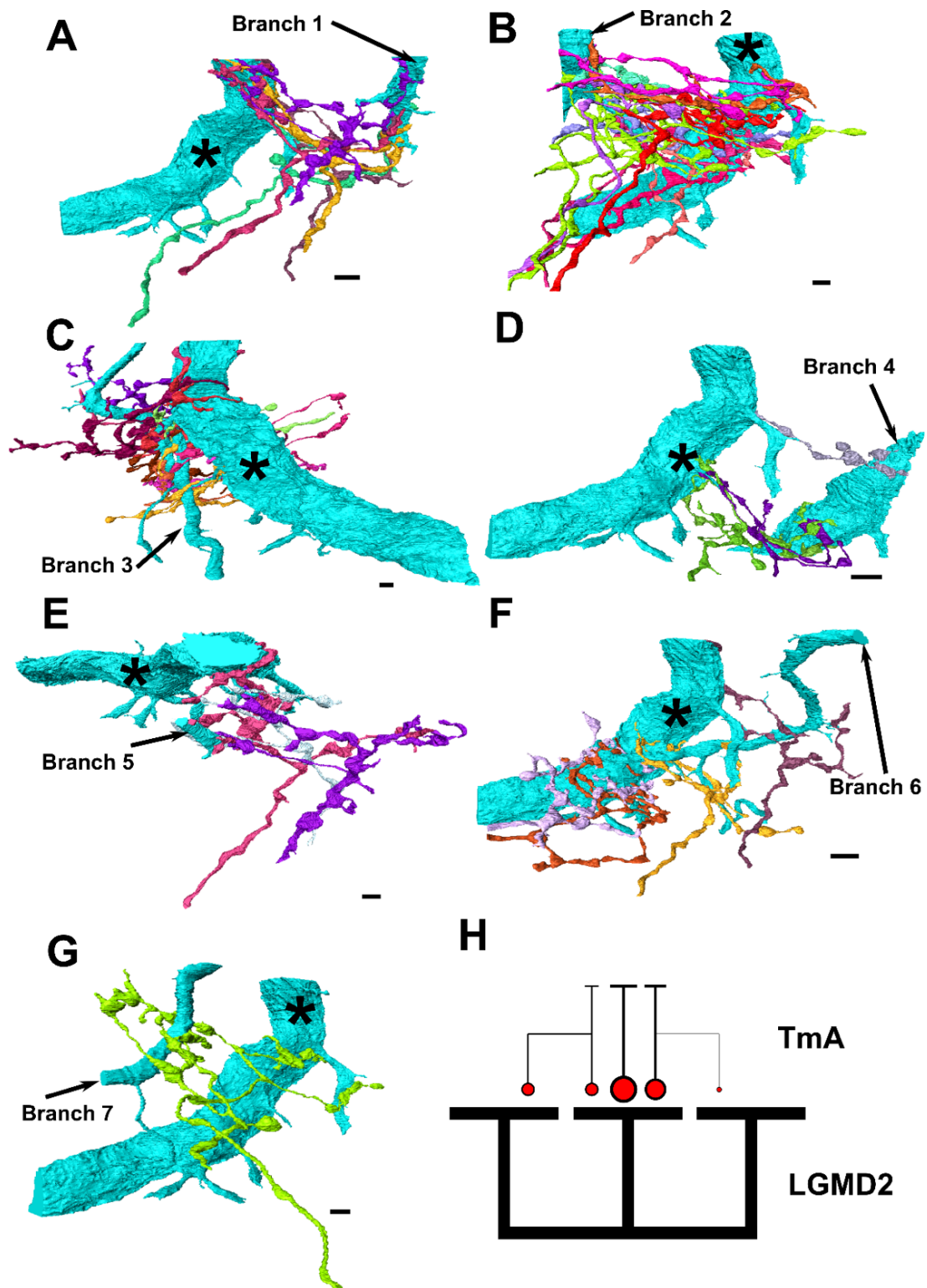


**Figure 3.13 – Synapse distribution on multiple branches of the LGMD 2 neuron.** (A) – (G) All show reconstructions of the main LGMD 2 neuron branch analysed with other branches, that are connected via TmA neurons, *multi-coloured*. (H) Schematic of the pattern of synapse distribution found between neighbouring branches. Some TmA neurons will synapse onto a single branch of the LGMD 2 neuron only (middle), others synapse primarily onto one branch with a small number onto another branch (right) and the last group were found to synapse onto two separate branches equally (left). All scale bars 5 $\mu$ m. Video: <https://doi.org/10.6084/m9.figshare.7172438>

The TmA neurons and the post-synaptic LGMD 2 neuron branch were mapped in a connectome diagram, shown in Figure 3.14. The diagram shows each of the LGMD 2 neuron branches the TmA neuron synapse and how many times that specific connection is made, indicating the distribution of the synapses of the TmA neurons across the dendritic branches of the LGMD 2 neuron. From the analysis of the complete TmA neurons against LGMD 2 neuron branch (Figure 3.14(B)), it was determined that only a small proportion of TmA neurons synapse across multiple branches. From the connectome it was determined that within the TmA neurons that synapse on more than 1 branch a small number synapse on more than 2 branches. The frequency of TmA neurons that synapse on multiple branches was determined and is shown in Figure 3.15A. The majority of neurons showed specificity and synapsed primarily on one branch of the LGMD 2 (60%), with a proportion synapsing onto 2 branches (32%) and very few synapsing onto 3 or 4 branches (total of 8%). A total of 37 TmA neurons were found to synapse onto multiple branches. The distribution of these synapses was analysed and is shown in Figure 3.15(B). Branch 1, 2, 3, and 4 in the figure are not always the same branch but are dependent on the individual TmA neuron, the branch with the highest proportion of synapses is labelled as branch 1 and so on. From this analysis it was determined that of those that synapse onto multiple branches there is a preference to a single branch, all primarily synapse onto one branch and have fewer synapses on another. This indicates that from the proposed distribution patterns, the first and second are true. The TmA neurons will synapse solely onto a single branch but of those that do synapse across multiple branches there is still a single branch of preference.

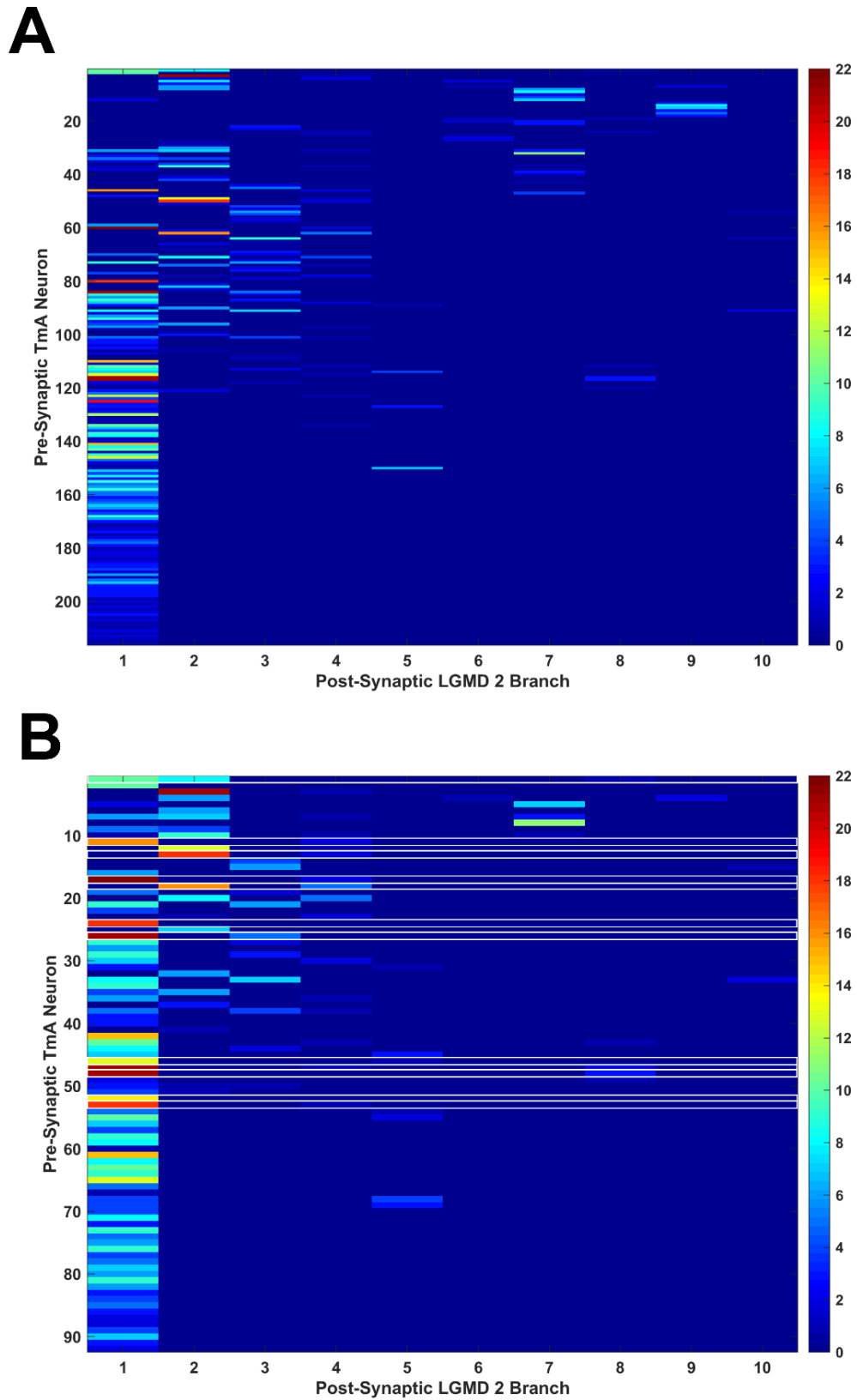


**Figure 3.14 – Connectome of TmA neuron V LGMD 2 neuron branches.** (A) Connectome of all TmAs onto separate branches of the LGMD 2 neuron, labelled 1-10, TmA neuron N=216, synapse n = 1171. (B) Connectome of only the whole reconstructed TmA neurons onto the LGMD 2 neuron branches, N=92, synapse n = 837. The colour of each square indicates the number of times that specific connection occurs, denoted in the figure legend on both connectomes. The hub neurons are highlighted in white.

When the hub neurons were isolated for the frequency distribution histogram, the majority were shown to synapse across multiple branches, with only 2 hub neurons (from 12) synapsing onto a single branch only (Figure 3.15(C)), whereas the vast majority of the non-hub neurons synapsed onto one branch only (Figure 3.15(C)), further evidence for the highly connective nature of the hub neurons. This confirms that the hub neurons innervate a larger portion of the LGMD 2 neuron than the non-hub neurons, both along the branches and across the branches of the LGMD 2 neuron. The graph in Figure 3.15(B) also shows that a small number of neurons, not identified as hub neurons also synapse onto multiple LGMD 2 neuron branches. However, when the incomplete TmA neurons were removed for any synapse, they had with a complete TmA neuron, they were referred to as unknown synaptic partners for the analysis. As the incomplete neurons could be portions of the same neuron and the identity is not known. The synapses with at least 1 unknown partner were not included in the connectivity analysis, detailed above. Although it does suggest that there could be more hub neurons present.

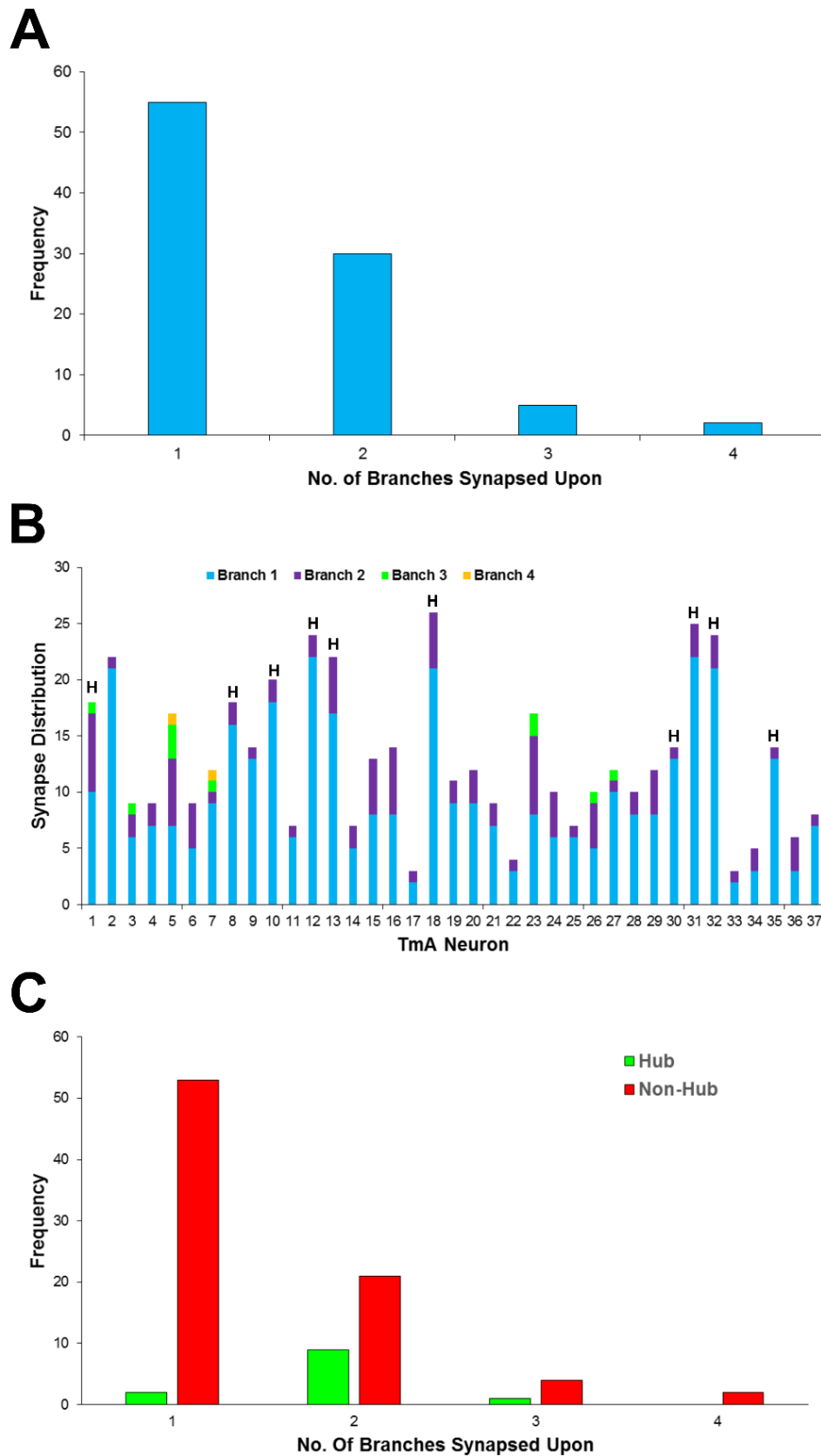


**Figure 3.15– Analyses of branch frequency and distribution.** (A) Shows the frequency or number of neurons that innervate 1, 2, 3 or 4 unassociated branches of the LGMD 2 neuron. (B) Shows the synapse distribution on each branch for the TmA neurons that synapse upon 2 or more branches of the LGMD 2 neuron. The hub neurons are labelled (H). (C) The comparison of the distribution between the hub (green, n=12) and non-hub (red, n=80).

The neurons that innervate multiple branches were compared with those that only synapse upon a single branch, shown in Figure 3.16. Significance was found for the number of total synapses by a TmA neuron between those that synapse onto one branch and those that synapse onto multiple branches (1 branch v 2 branches,  $p \leq 0.05$ , 1 branch v 3 branches,  $p \leq 0.05$ ), Figure 3.16(A). Significance was also found between the group synapsing onto one branch compared to those that synapse onto 2 branches for connectivity index ( $p \leq 0.05$ ) but not for the other groups, Figure 3.16(B). However, no significance was found between groups of TmA neurons that perform multiple innervations on different branches. The TmA neurons can also be further divided into a group based on whether they synapse onto one branch or onto multiple.

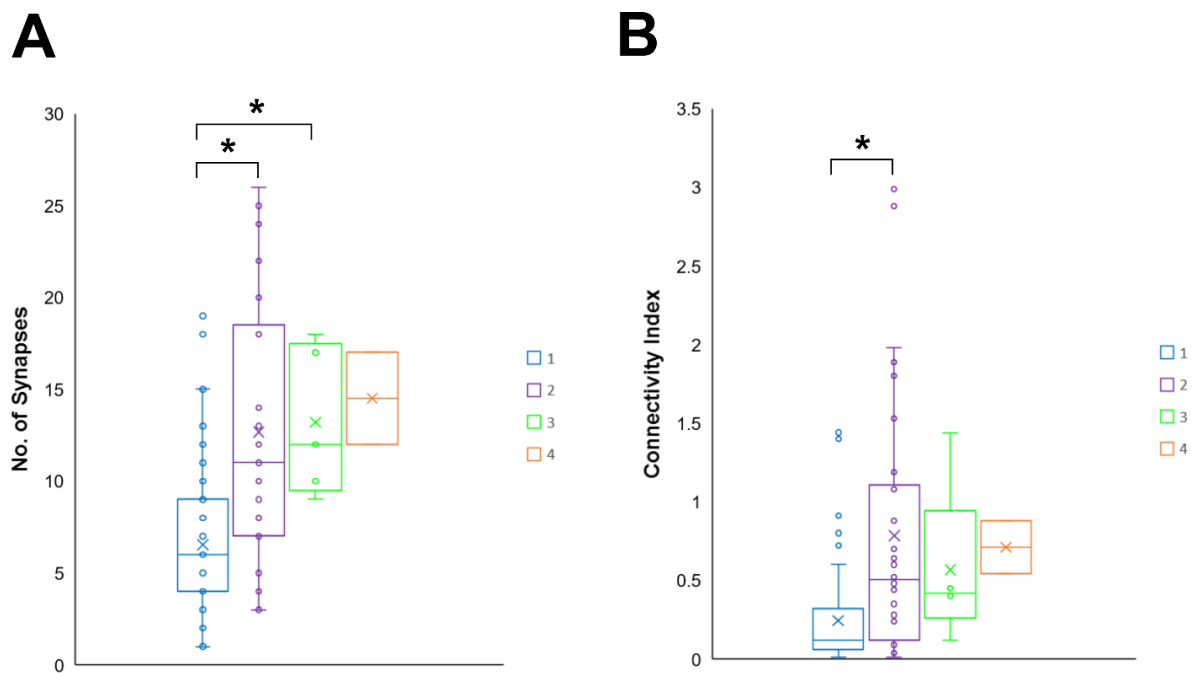


**Figure 3.16 – Comparison of TmA neurons that innervate a single branch of the LGMD 2 neuron with those that innervate multiple branches.** (A) Is a boxplot of the number of synapses for TmA neurons that synapse onto a single branch (blue), two branches (purple), three branches (green) and four branches (orange). (B) Is a box plot of the connectivity index of the four groups of TmA neurons. In both graphs the mean is shown as a cross on the box plots.

Overall, the analysis shows the existence of a connected TmA neuron network in both directions, along and across the LGMD 2 neuron branches. This network is shown in the diagram in Figure 3.17. Each line on the diagram represents a synapse by the connected neurons onto the LGMD 2 neuron, with the type of line indicating which branch this particular connection occurred upon. All of the connections occurring on the main branch are shown plus a small proportion of synapses that occurred on the secondary branches shown. The diagram primarily shows the connections arising from the primary branch of analysis, with a small number of TmA neurons that do not synapse upon the primary branch but are defined as hub neurons from earlier analysis. The hub neurons are highlighted by having red connections to their synaptic partner. The secondary connections from these partners are in orange, the next layer in yellow and those furthest from the hub neurons have green connections. Almost all TmA neurons are either directly connected to a hub neuron or are within a single synapse distance from one, via a shared synaptic partner. The TmA neurons furthest away are at the end of the dataset and it is likely that they would be close to further hubs or could be hubs themselves. The majority of the hubs ( $n=10$ ) were found to synapse upon the main branch of focus in the dataset. The other hubs were found to primarily synapse with another branch within the dataset. The hub neurons also stretch across multiple branches but each of the hubs had a single branch of the LGMD 2 neuron they mainly synapse upon. These hubs are vital to ensure that the TmA neuron network is connected. This is shown when the hub neurons are removed from the network diagram, seen in Figure 3.18. Without the hubs the network is not connected as a whole, with smaller 'islands' of TmA neurons connected with one another instead. A small number of TmA neurons ( $n=8$ ) only synapse with the hub neurons and are no longer connected within the network, circled in the diagram.



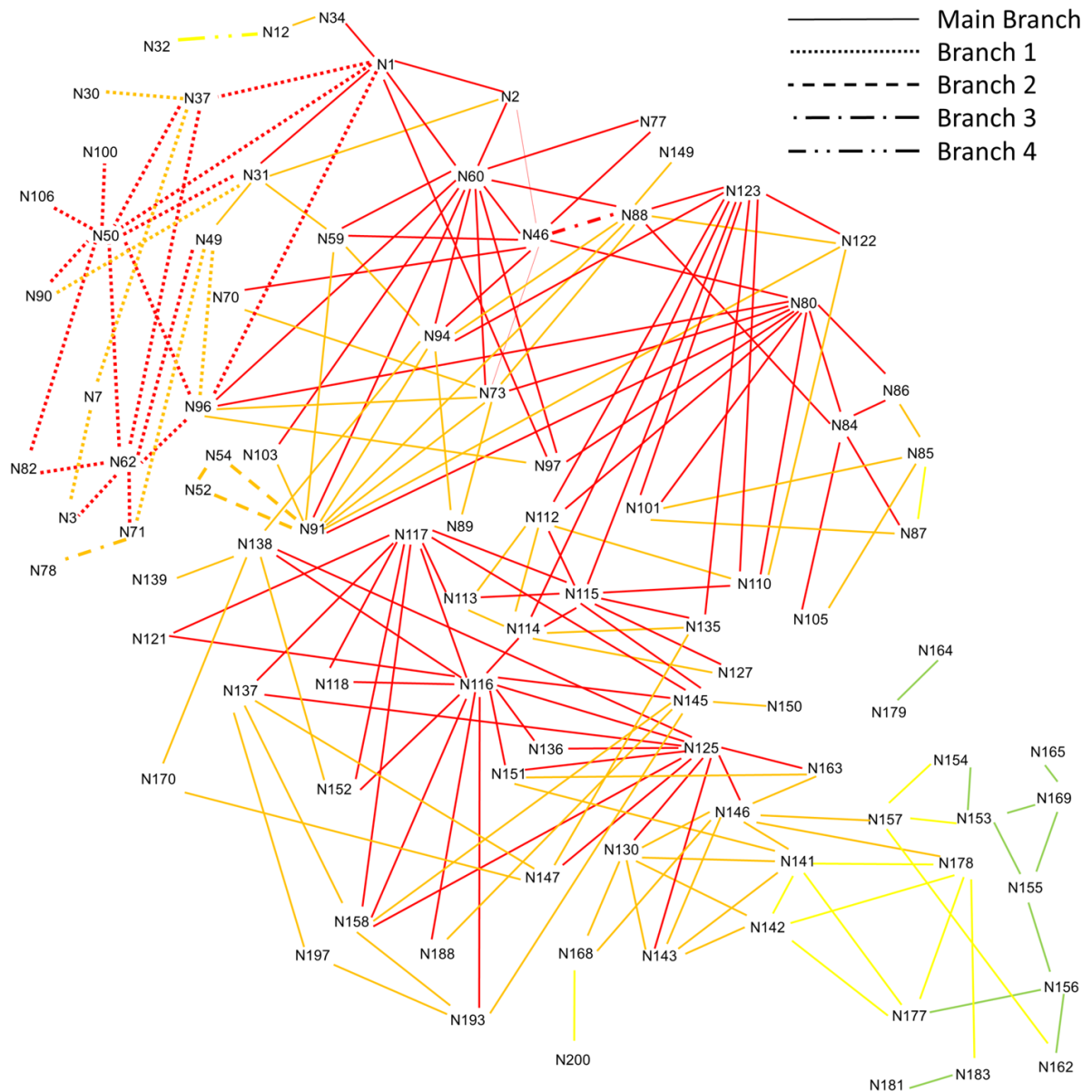


**Figure 3.17 – TmA neuron network diagram.** The diagram represents the TmA neuron network, each line denotes a synapse, which two TmA neuron neighbours form. The type of line indicates the second post-synaptic target, the LGMD 2 neuron branch where that connection occurs. The colour of the line denotes the distance from a hub neuron that connection is. The direct connections to a hub are red, the next connections on are orange, the next yellow, and the furthest are in green.



### 3.1.5. Summary

In summary, each TmA neuron has two synaptic partners, a second TmA neuron and the LGMD 2 neuron, which occur simultaneously within the lobula. This mapping of synapses is organised and reflects the retinotopy preserved from the eye down to the branches of the LGMD 2 neuron. This had been previously found in the LGMD 1 but yet to proven to be the same onto the LGMD 2 neuron. The TmA neurons will synapse multiple times with the LGMD 2 neuron and with the same or multiple TmA neuron synaptic partners. The synaptic area of the TmA neurons overlap and via shared synaptic partners a dense highly connected network has been found. This network not only spreads down the LGMD 2 neuron but also across multiple branches, connecting the neighbouring LGMD 2 neuron branches via the TmA neuron network. Within this network the existence of a small group of highly connective TmA neurons, hub neurons, has been found vital to ensure the network is connected. The results from the reconstructions and subsequent analysis show that the TmA neurons form an interconnected network, via formation of reciprocal synapses at a specific location of the LGMD 2 neuron. This organization of this network will impact on the integration of the signal across the LGMD 2 neuron. This is further discussed in Chapter 4.1 (pg180).

## **3.2. Muscle Results**

### *3.2.1. Reconstructions*

A total of 48 individual cells were imaged over 250-300 70nm thick sections. From this the mitochondrial network was segmented for every cell for 50 sections, for volume analysis and over 200 sections for the analysis on branching. A total of 2350 individual mitochondrion were segmented manually. From the datasets 56 nuclei were also partially reconstructed. Along with mitochondria and nuclei the cell was also segmented to be used in volume and density analysis of the mitochondria and nuclei. In total, the analysis of the skeletal muscle data took roughly 10 months, working for 6hrs a day, 5 days a week.

### 3.2.2. Mitochondrial Network Analysis

Over development the mitochondrial network will grow in conjunction with the size of the cell. So that as the muscle cells increase in size the mitochondrial network will as well, maintaining a ratio between network and cell volume.

As detailed in the methods section, the mitochondrial network was segmented from a partial volume of the whole dataset (50 sections), along with the corresponding cell volume. Any nuclei present within the volume were segmented and their contribution subtracted from the total cell volume. This was done to estimate the volume of mitochondria per cell they could potentially occupy.

Figures 3.19 and 3.20 show examples of the reconstructions of the network at the 4 age groups studied. From the reconstructions for both muscle types, it can be surmised that there is a change in the mitochondrial network from fetal to adult. The volume of mitochondria occupancy of the psoas or soleus cells in the two earliest fetal age groups (day 50-54 and day 55-59) appears less than in the older fetal group (day 60-64) and the adult group. Overall, for both muscle types, the adult mitochondrial network appears denser, and potentially more complex, than all of the fetal age groups.

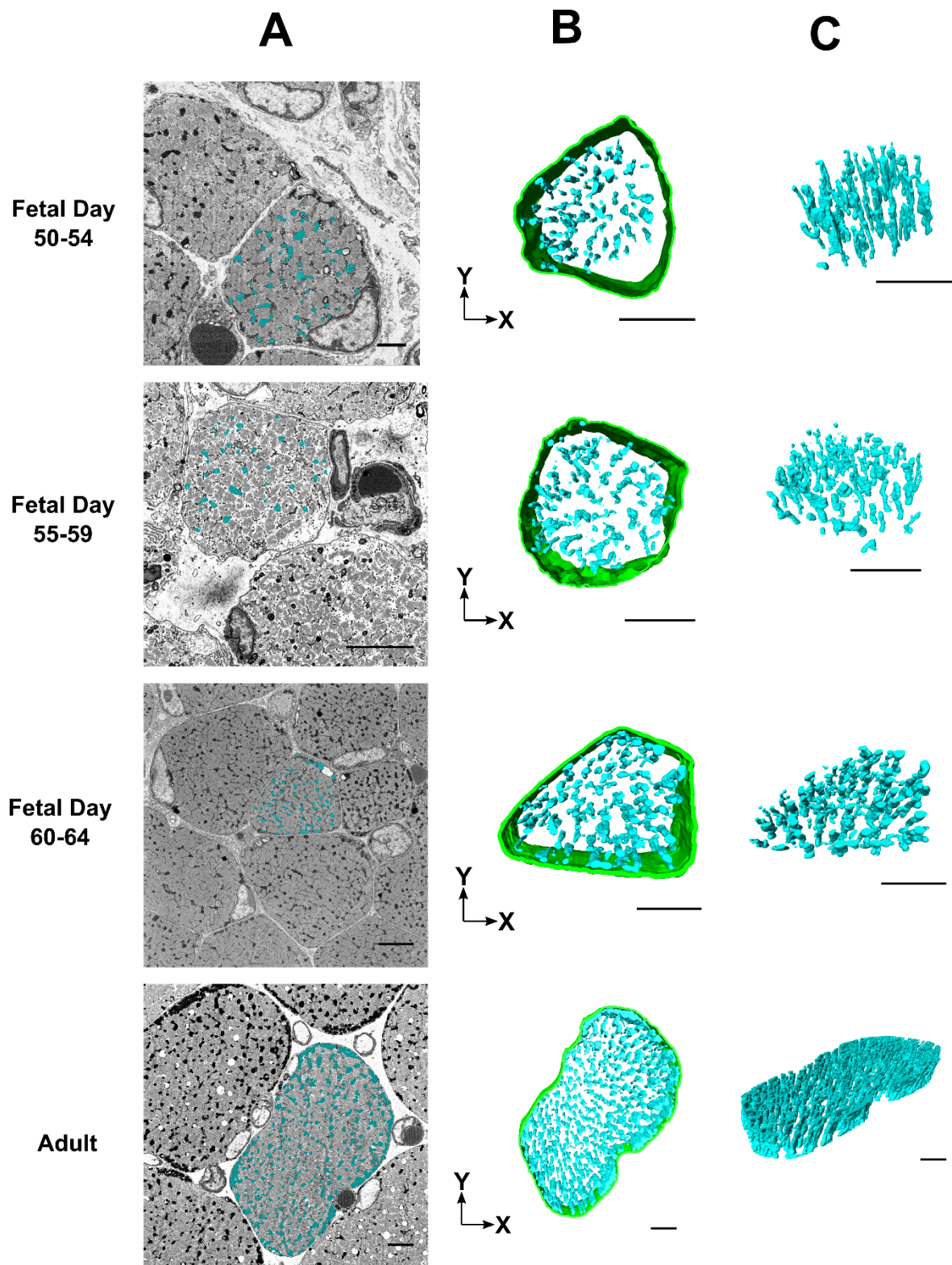


**Figure 3.19 – Examples of total mitochondria segmented from 50 sections of psoas.** (A) Single section from psoas muscle with mitochondria segmented, *light blue*. (B) Shows the reconstructions of the example shown in the single sections, with the segmented mitochondria, *light blue*, and the cell boundary, *green*. (C) The model of only the mitochondria at an angle. Scale bars 5 $\mu$ m for adult, fetal Day 60-64, and fetal day 55-59 and 1 $\mu$ m for fetal day 50-54 on the orthoslice, all scale bars on the 3D models are 5 $\mu$ m. Video: <https://doi.org/10.6084/m9.figshare.7165591.v2>



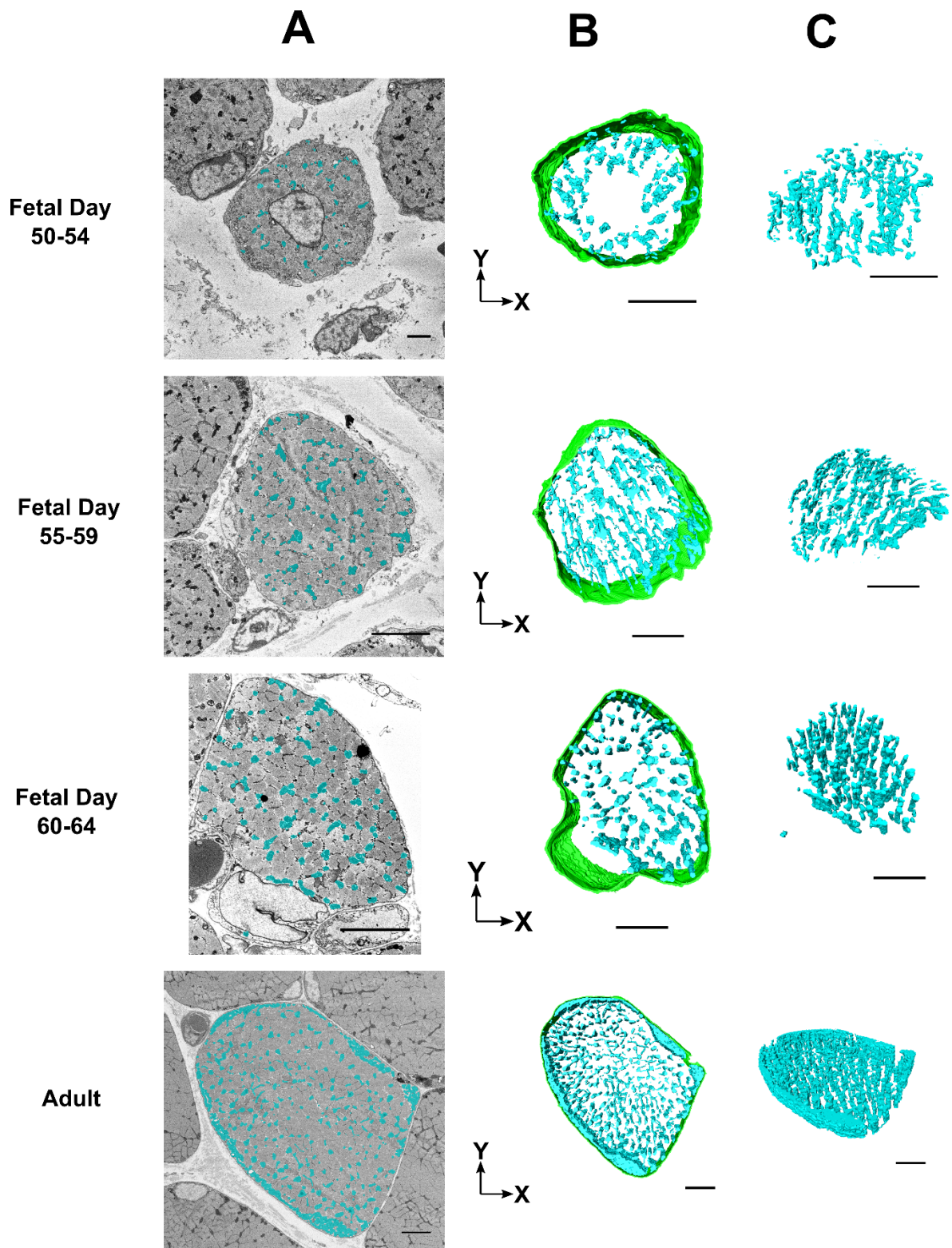


**Figure 3.20 – Examples of total mitochondria segmented from 50 sections of soleus.** (A) Single section from soleus muscle with mitochondria segmented, *light blue*. (B) Shows the reconstructions of the example shown in the single sections, with the segmented mitochondria, *light blue*, and the cell boundary, *green*. (C) The model of only the mitochondria at an angle. Scale bars 5µm for adult, fetal Day 60-64, and fetal day 55-59 and 1µm for fetal day 50-54 on the orthoslice, all scale bars on the 3D models are 5µm. Video: <https://doi.org/10.6084/m9.figshare.7166006.v2>

This is corroborated in the results shown in Figure 3.21. The percentage of the reconstructed volume occupied by mitochondria was calculated to compensate for the range of cell size present between the groups. For both muscle types there are significant differences found between the age groups ( $p \leq 0.05$  for both psoas and soleus). Upon further analysis significance was found between the day 50-54 (mitochondrial volume of  $5.6 \pm 1.8\%$  of cell volume for psoas and  $5.8 \pm 1.8\%$  for soleus), 55-59 ( $4.7 \pm 1.6\%$  and  $7.1 \pm 1.3\%$ ) fetal age groups and the fetal day 60-64 ( $13.1 \pm 6\%$  and  $12.8 \pm 3.3\%$ ) group for psoas and soleus and between day 50-54 and adult ( $11 \pm 4.7\%$ ) group for the soleus only.

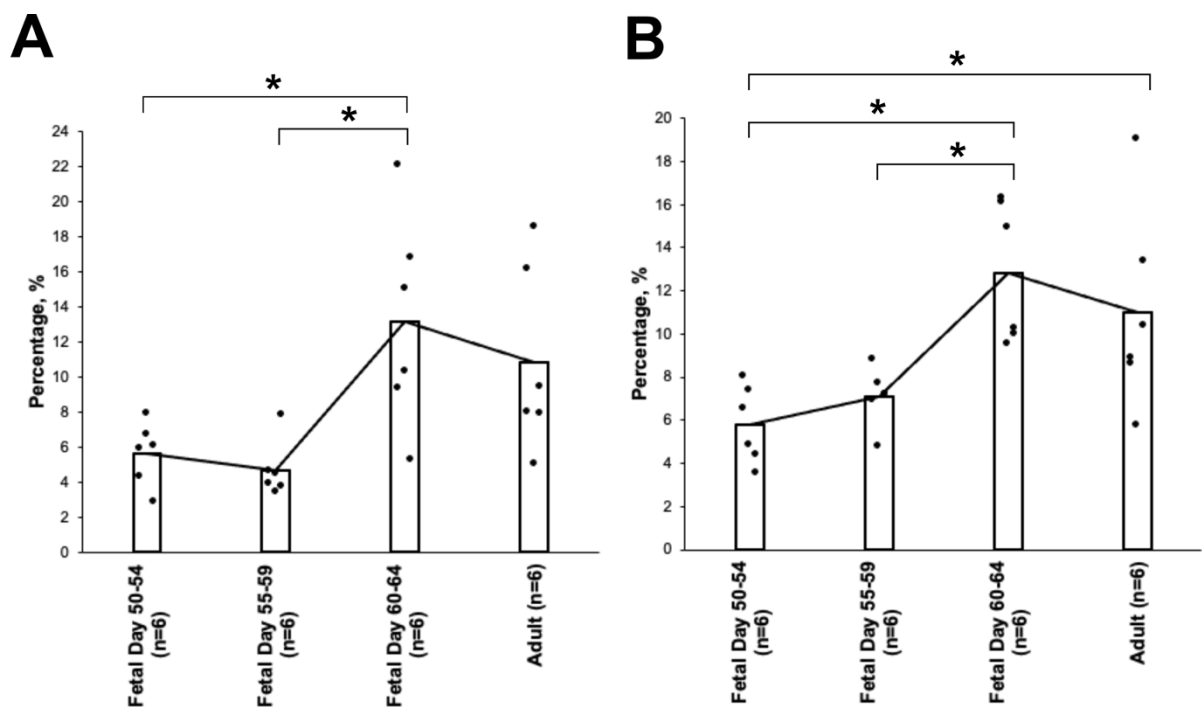


**Figure 3.21 – Results of percentage of portion of cell volume occupied by mitochondria.** (A) And (B) show the percentage of the reconstructed cell volume from 50 sections, of a larger dataset (~250 sections), occupied by mitochondria for the psoas and soleus, respectively. Each point is a result from a single cell, the mean is denoted by the bar and significance is (\*)  $p \leq 0.05$ .



This is further highlighted when the volume of the cell is shown, in Figure 3.22. The associated cell volume used for the mitochondrial density calculation shows significance only between the fetal and adult groups for psoas and soleus ( $p \leq 0.05$ ). Cell size does not show significance over fetal development for both muscles (day 50-54 is  $276.3 \pm 107.6 \mu\text{m}^3$  and  $310.6 \pm 113.1 \mu\text{m}^3$ , fetal day 55-59 is  $917.8 \pm 5113.8 \mu\text{m}^3$  and  $384.6 \pm 160.4 \mu\text{m}^3$  and fetal day 60-64 is  $836.5 \pm 365.4 \mu\text{m}^3$  and  $773.8 \pm 498.1 \mu\text{m}^3$  for soleus and psoas respectively) but there is a large increase between these groups and the adults ( $4058.1 \pm 1517.2 \mu\text{m}^3$  and  $2249.3 \pm 1631.1 \mu\text{m}^3$ ) for soleus and psoas, respectively.

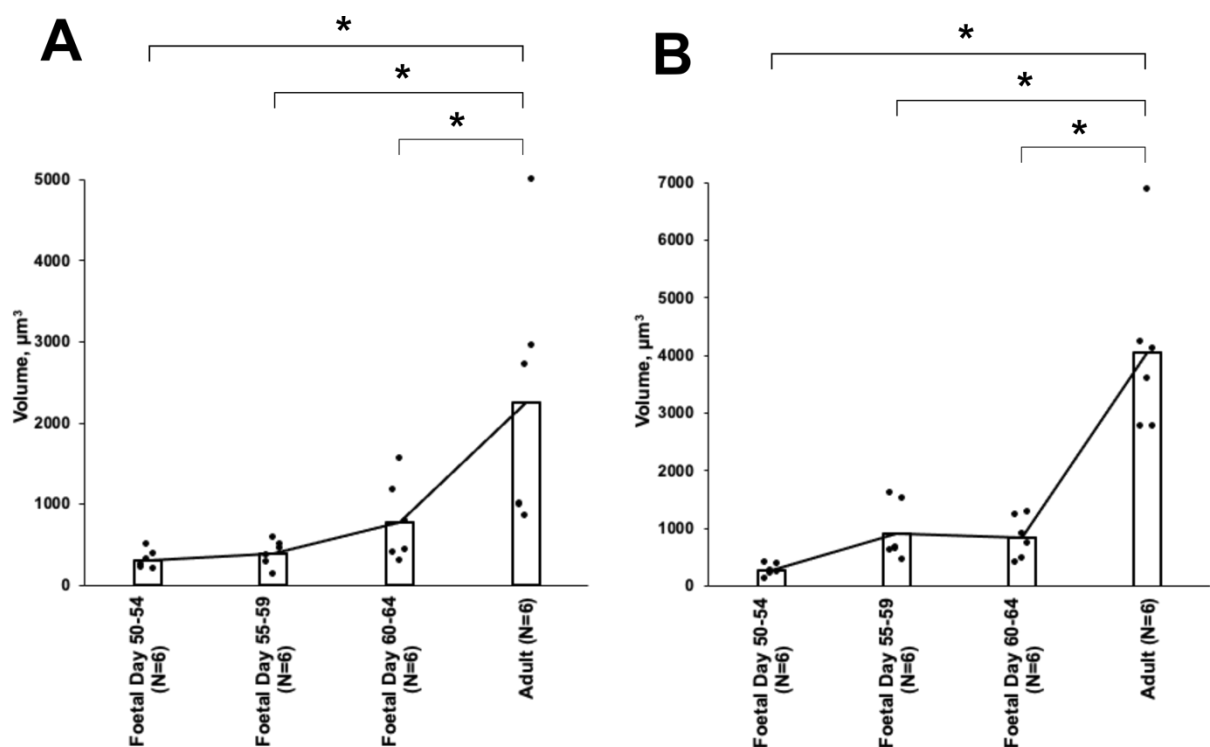


**Figure 3.22 – Results of portion of cell volume.** (A) And (B) show the portion of cell volume, same as used for mitochondrial density calculation, from 50 sections. Each point is a result from a single cell, the mean is denoted by the bar and significance is (\*)  $p \leq 0.05$ .

Mitochondria can be divided into three distinct locations within the cell, subsarcolemmal (SS), intermyofibrillary (IMF) and perinuclear (PN), shown in Methods Figure 2.26. The proportions of mitochondria within each of these locations changes over development. The reconstructions seen in Figures 3.23 and 3.24 show how the percentage of the mitochondrial network in each of these areas differs between the age groups. One of the noticeable differences is an increase in mitochondria present sub-sarcolemmally between each fetal group up to the adult for both muscle types. For this analysis only datasets containing nuclei in the reconstructed volumes were analysed.

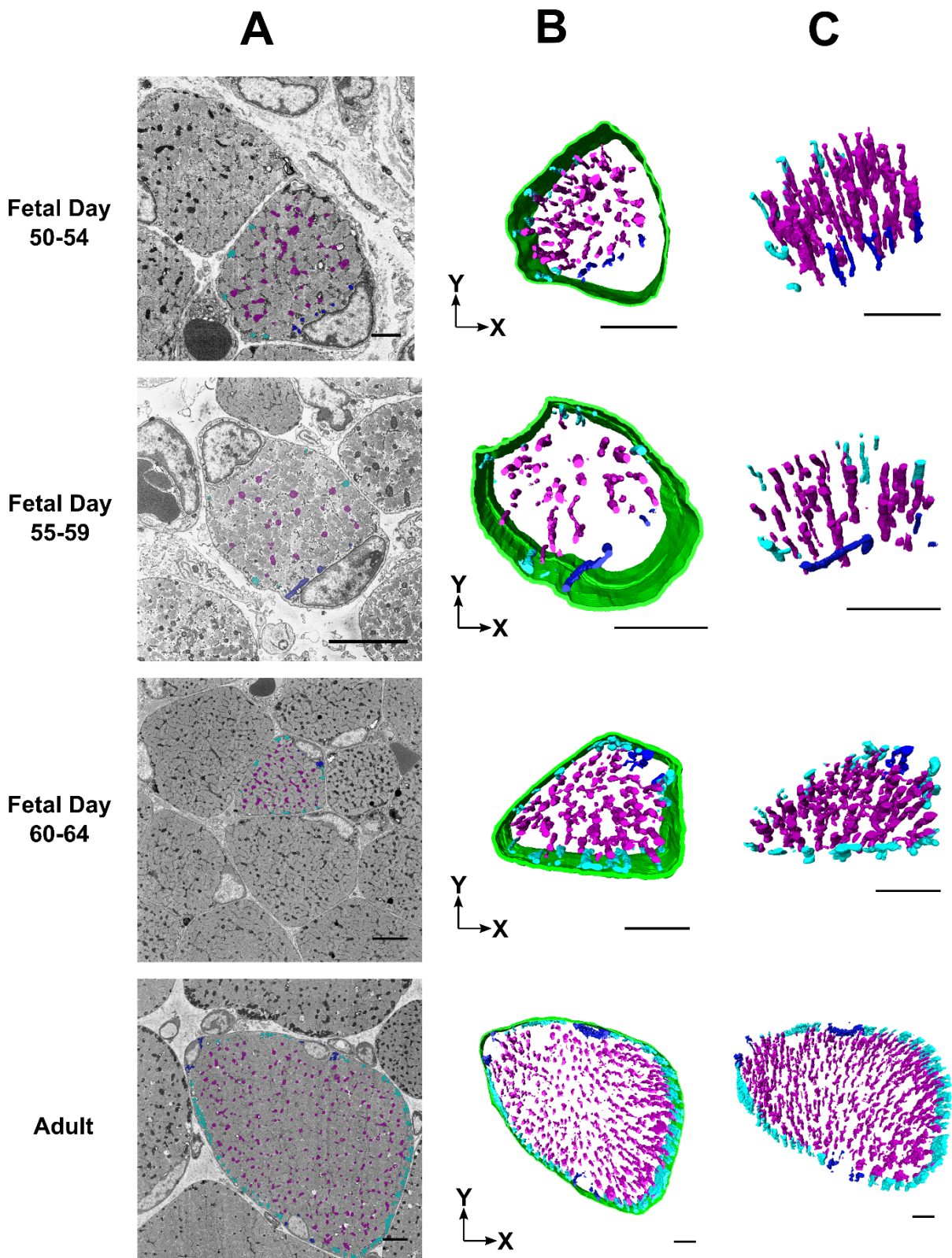


**Figure 3.23 – Examples of mitochondrial segmentation and reconstructions divided by location for psoas.** (A) Examples of a single section from each of the age groups from the psoas muscle. The segmentation of mitochondria is divided into locations SS, *light blue*, IMF, *purple*, and PN (when present), *dark blue*. (B) The subsequent reconstructions of the 50 sections of segmented mitochondria with cell boundary, *green*, and (C) show the same reconstructions without cell boundary and different orientation. Scale bars 5µm for adult, fetal Day 60-64, and fetal day 55-59 and 1µm for fetal day 50-54 on the orthoslice, all scale bars on the 3D models are 5µm. Video: <https://doi.org/10.6084/m9.figshare.7166093>

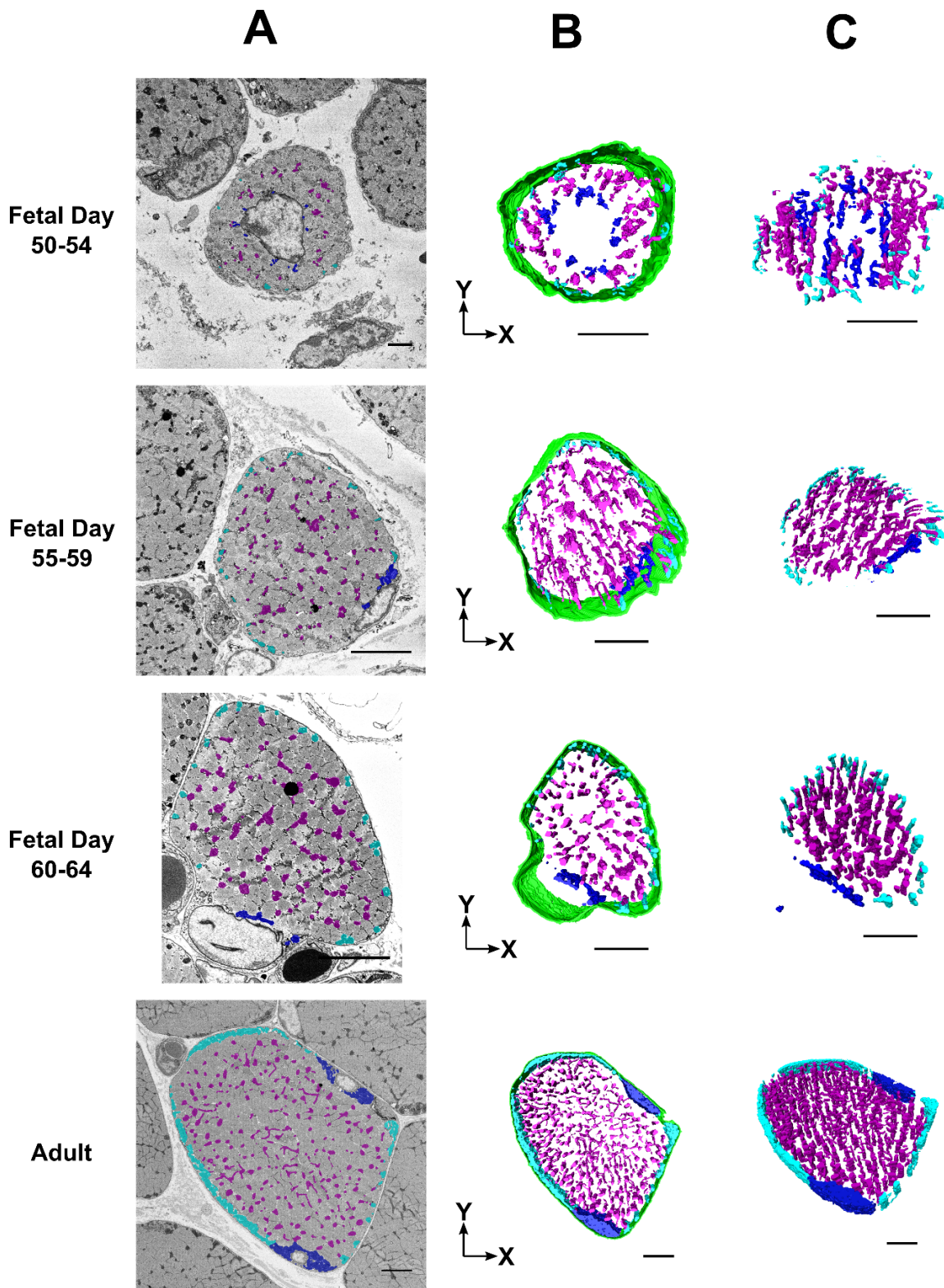


**Figure 3.24 - Examples of mitochondrial segmentation and reconstructions divided by location for soleus.** (A) Examples of a single section from each of the age groups from the soleus muscle. The segmentation of mitochondria is divided into locations SS, *light blue*, IMF, *purple*, and PN (when present), *dark blue*. (B) The subsequent reconstructions of the 50 sections of segmented mitochondria with cell boundary, *green*, and (C) show the same reconstructions without cell boundary and different orientation. Scale bars 5µm for adult, fetal Day 60-64, and fetal day 55-59 and 1µm for fetal day 50-54 on the orthoslice, all scale bars on the 3D models are 5µm. Video: <https://doi.org/10.6084/m9.figshare.7166096.v2>

The volumes of IMF located mitochondria shows a large increase from the fetal groups to the adult in both the psoas ( $15.6 \pm 11.5 \mu\text{m}^3$ ,  $13.5 \pm 9.0 \mu\text{m}^3$ ,  $86.3 \pm 78.2 \mu\text{m}^3$  and  $163.2 \pm 126.2 \mu\text{m}^3$  for day 50-54, 55-59, 60-64 and adult,  $p \leq 0.05$ ) and soleus ( $11.1 \pm 6.3 \mu\text{m}^3$ ,  $58.2 \pm 47.6 \mu\text{m}^3$ ,  $70.7 \pm 40.4 \mu\text{m}^3$  and  $272.5 \pm 88.2 \mu\text{m}^3$  for day 50-54, 55-59, 60-64 and adult,  $p \leq 0.05$ ). This is the same for the mitochondria located at the SS for psoas ( $1.03 \pm 0.5 \mu\text{m}^3$ ,  $1.6 \pm 0.8 \mu\text{m}^3$ ,  $18.7 \pm 18.6 \mu\text{m}^3$  and  $74.3 \pm 65.7 \mu\text{m}^3$  for day 50-54, 55-59, 60-64 and adult,  $p \leq 0.05$ ) and soleus ( $1.4 \pm 1.0 \mu\text{m}^3$ ,  $6.0 \pm 2.5 \mu\text{m}^3$ ,  $19.5 \pm 10.3 \mu\text{m}^3$  and  $106.2 \pm 51.1 \mu\text{m}^3$  for day 50-54, 55-59, 60-64 and adult,  $p \leq 0.05$ ). There was no significance found within the group for PN located mitochondria in the psoas ( $0.5 \pm 0.7 \mu\text{m}^3$ ,  $1.7 \pm 2.0 \mu\text{m}^3$ ,  $6.5 \pm 10.2 \mu\text{m}^3$  and  $6.7 \pm 8.9 \mu\text{m}^3$  for day 50-54, 55-59, 60-64 and adult) but there was in the soleus ( $1.3 \pm 1.3 \mu\text{m}^3$ ,  $2.6 \pm 2.6 \mu\text{m}^3$ ,  $8.4 \pm 6.0 \mu\text{m}^3$  and  $38.6 \pm 41.1 \mu\text{m}^3$  for day 50-54, 55-59, 60-64 and adult,  $p \leq 0.05$ ). These are shown in Figure 3.25(A-C) and 3.26(A-C).

To determine the proportion of mitochondria at each location the percentage of total volume at each location was calculated. This is shown in Figure 3.25(D) and 3.26(D) for the psoas and soleus respectively. Both muscles have a similar ratio of mitochondria in each of the locations for all age groups. The highest proportion of mitochondria are located in the IMF. The IMF percentage decreases from fetal day 50-54 to adult for the psoas ( $87.6 \pm 6.4\%$ ,  $80.6 \pm 12.3\%$ ,  $79 \pm 5.9\%$  and  $68.1 \pm 6.1\%$  for day 50-54, 55-59, 60-64 and adult,  $p \leq 0.05$ ) and soleus ( $79.4 \pm 9.8\%$ ,  $82.9 \pm 8.0\%$ ,  $70.2 \pm 7.6\%$  and  $66.8 \pm 8.3\%$ , for fetal day 50-54, 55-59, 60-64 and adult,  $p \leq 0.05$ ). Significance was found between fetal day 50-54 and adult for both psoas and soleus, indicated on graph. In contrast there is an increase in percentage of mitochondria located SS for psoas ( $9.6 \pm 6.8\%$ ,  $9.9 \pm 3.5\%$ ,  $16.6 \pm 7.6\%$  and  $27.9 \pm 5.6$ , for fetal day 50-54, 55-59, 60-64 and adult, respectively,  $p \leq 0.05$ ) and soleus ( $10 \pm 3.6\%$ ,  $12.5 \pm 6.3\%$ ,  $21.3 \pm 8.8\%$  and  $25.6 \pm 7.6\%$  for fetal day 50-54, 55-59, 60-64 and adult,  $p \leq 0.05$ ). Significance was specifically found between the fetal day 50-54 and adult groups for both psoas and soleus, for the proportion of IMF and SS mitochondria. There were no differences in the percentage of mitochondria in a perinuclear location during development of either muscle tissue.



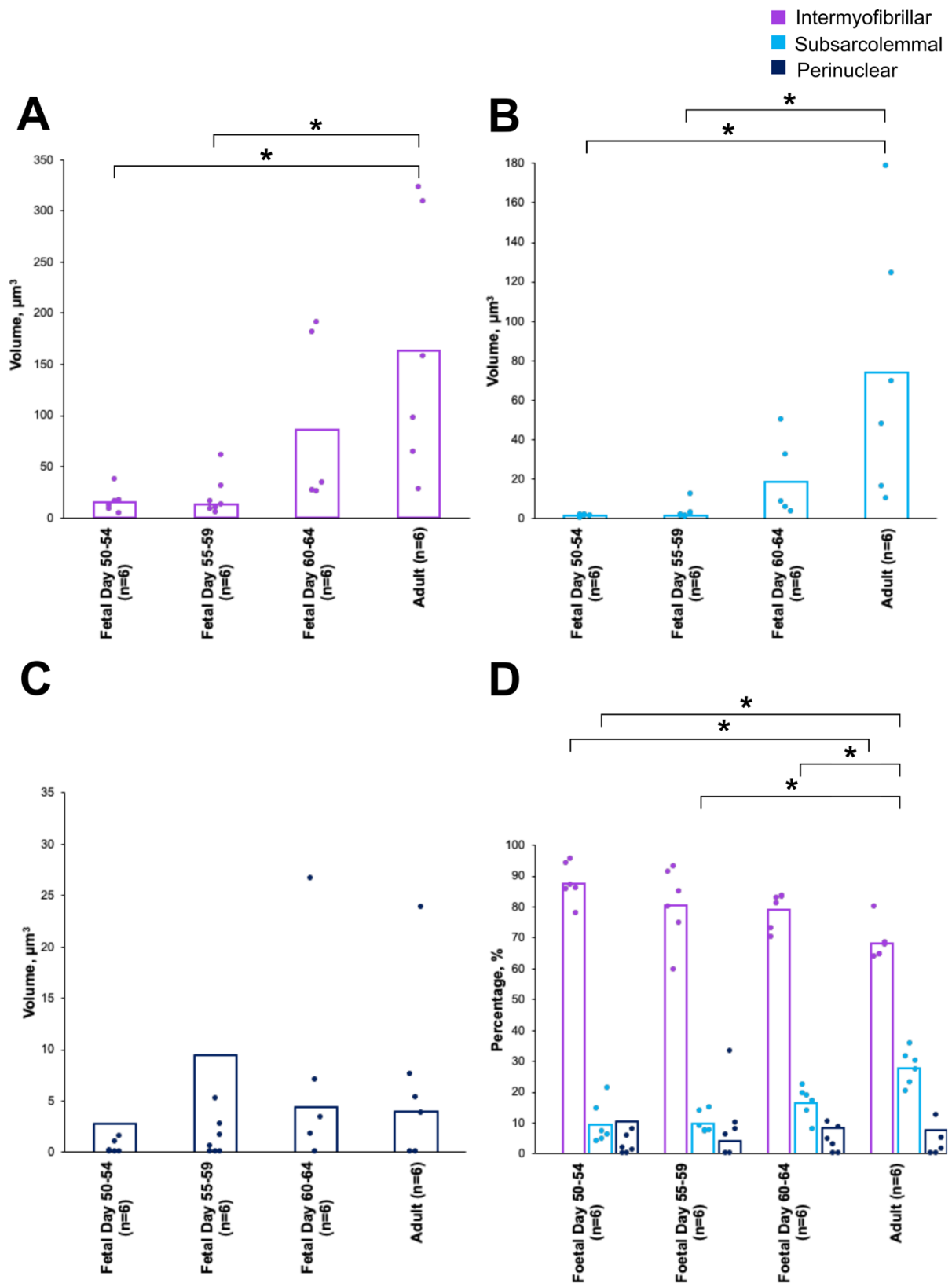


**Figure 3.25 – Results of the mitochondrial volume for each location and age group in the psoas.** (A), (B) and (C) show the volume results for the IMF, SS and PN locations respectively for the reconstructed mitochondrial volume (50 sections). (D) shows the percentage of the mitochondria volume at each of the locations between the age groups. Only cells with nuclei present in the reconstructions were analysed, signified by individual points, the mean is shown as a bar chart and significance is (\*)  $p \leq 0.05$ .

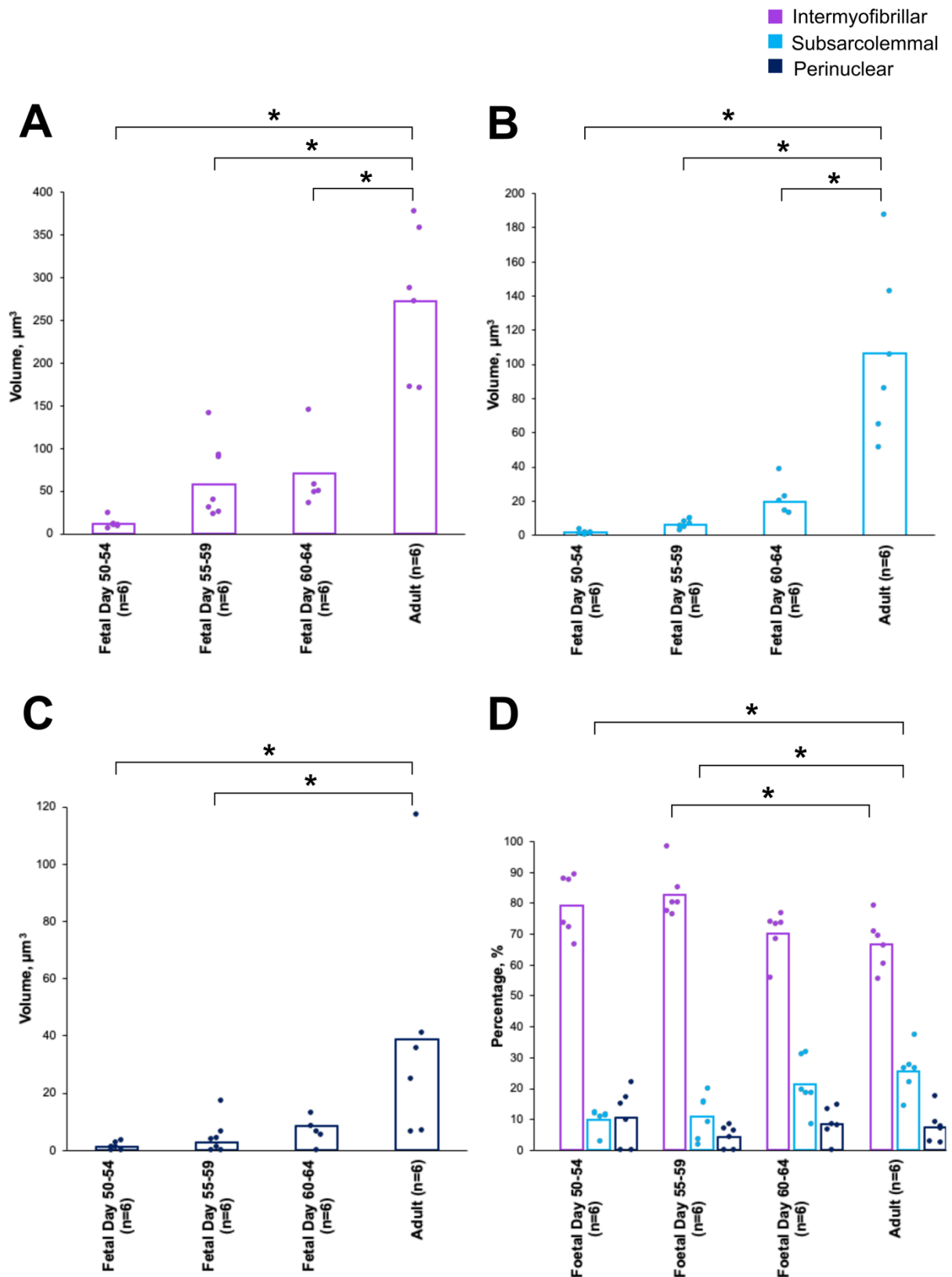


**Figure 3.26 – Results of the mitochondrial volume for each location and age group in the soleus.** (A), (B) and (C) show the volume results for the IMF, SS and PN locations respectively for the reconstructed mitochondrial volume (50 sections). (D) shows the percentage of the mitochondria volume at each of the locations between the age groups. Only cells with nuclei present in the reconstructions were analysed, signified by individual points, the mean is shown as a bar chart and significance is (\*)  $p \leq 0.05$ .

The complexity of the mitochondrial network is important for function of the cell. How the network changes over development are unknown. As such a portion of IMF mitochondria was segmented over 200 sections, reconstructed and analysed for evidence of network complexity via an assessment of branching, as described in the methods. Figure 3.27 shows the results from the branching analysis as a percentage of segments above the threshold degree. In the comparison between psoas and soleus, the only significance found was between the adult psoas and soleus. There was significantly less branching in adult psoas ( $5.8 \pm 3.2\%$ ) than the soleus ( $29.3 \pm 15.1\%$ ), as shown on the graph. For the comparison across development groups, the soleus muscle showed no change in mitochondrial branching. However, in the psoas muscle there was a significant drop in the percentage of branching in the adult ( $p \leq 0.05$ ), specifically between the adult ( $5.8 \pm 3.2\%$ ,  $0.06 \pm 0.04$ ) and each fetal group (day 60-64 ( $27.0 \pm 8.7\%$ ,  $0.39 \pm 0.17$ ), day 55-59 ( $28.5 \pm 16.8\%$ ,  $0.51 \pm 0.48$ ) and day 50-54 ( $29.6 \pm 9.1\%$ ,  $0.44 \pm 0.2$ )), as indicated on the graph. The differences in the complexity of the adult fibres in the psoas and soleus can be seen in the 3D reconstructions, shown in Figure 3.28.



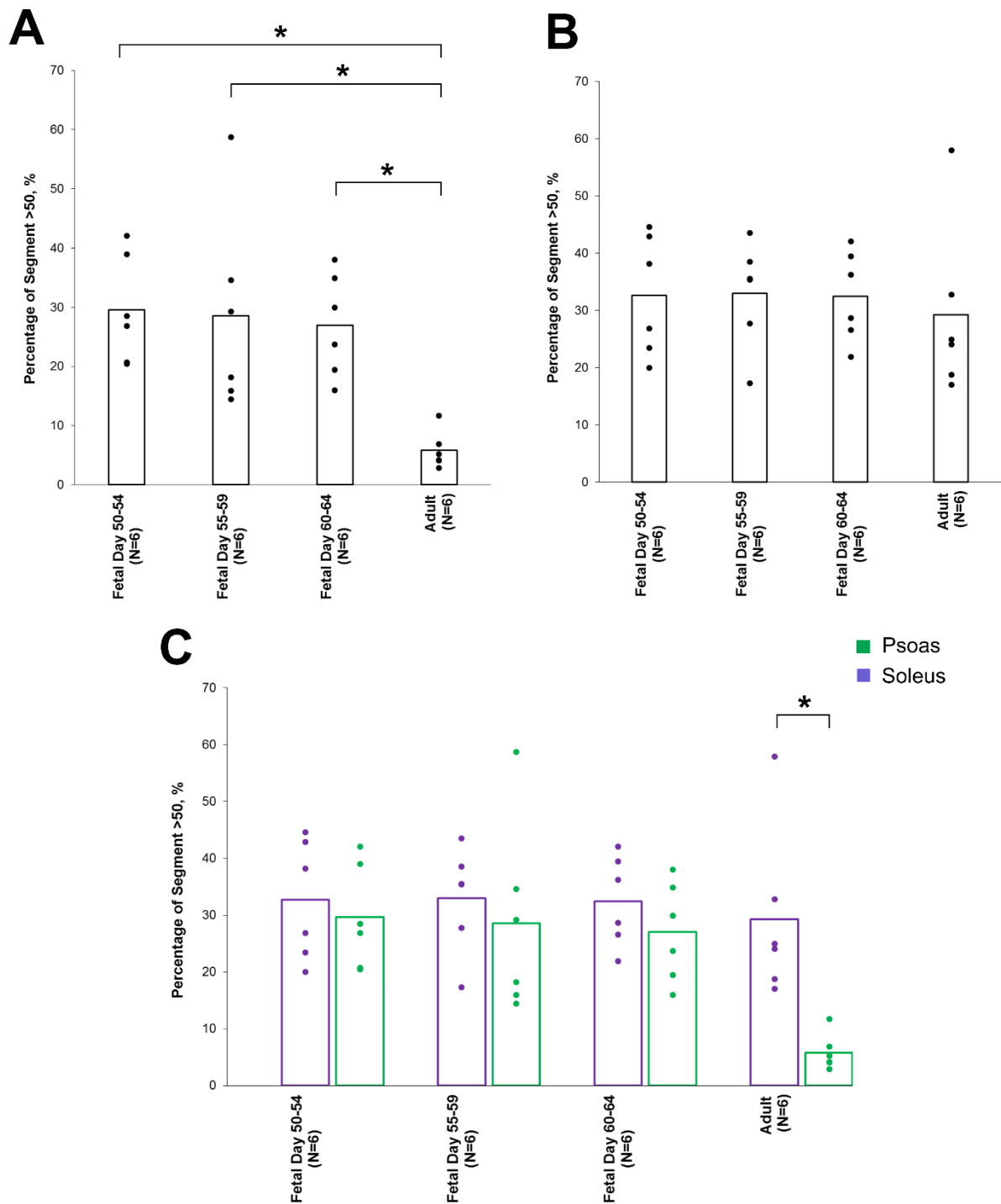


**Figure 3.27 – Branching analysis of mitochondrial network by percentage of segments >50 degrees.** (A) and (B) show the results of percentage of segments of reconstructed mitochondria network >50° for each age groups for the psoas and soleus, respectively, (\*)  $p \leq 0.05$ . (C) Is the comparison between the two muscle types for each group, (\*)  $p \leq 0.05$ .

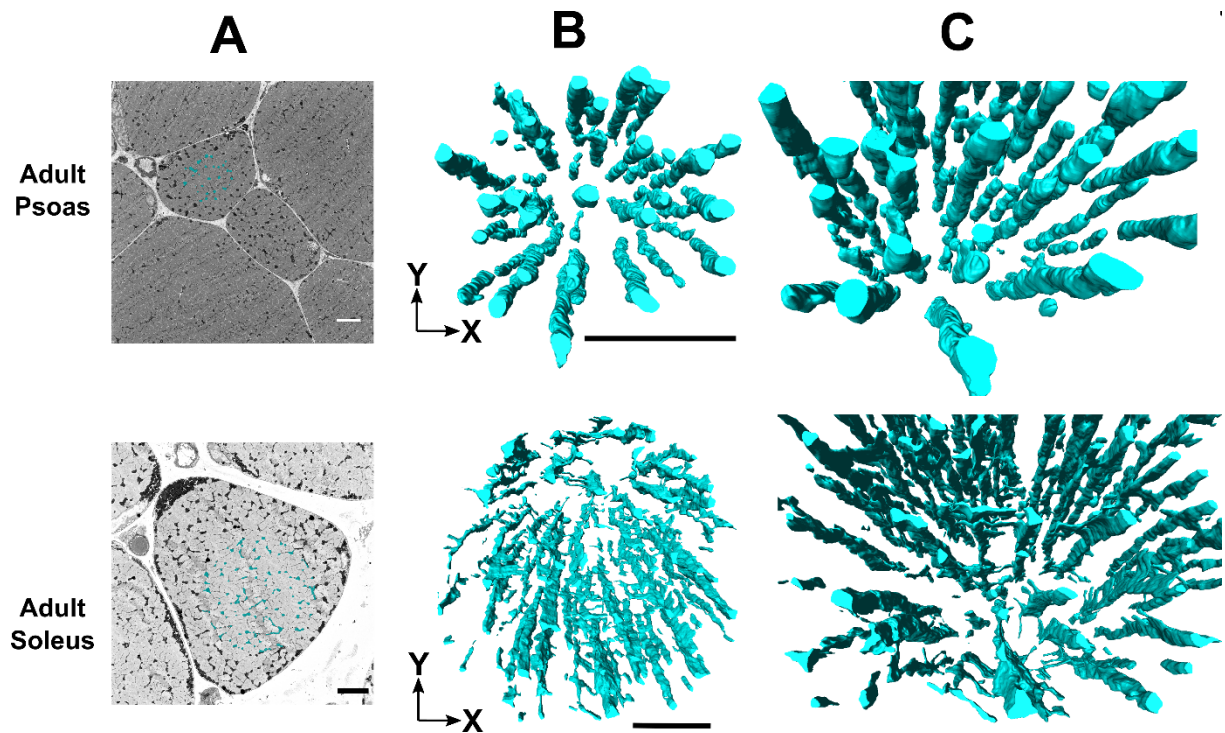


**Figure 3.28 –Reconstructions of mitochondrial network from adult psoas and soleus cells.** (A) Single section from adult psoas and soleus muscle with mitochondria segmented, *light blue*. (B) And (C) Shows the reconstructions of the example shown in the single sections, with the segmented mitochondria, *light blue* at different orientations. Scale bars 5μm. Video: <https://doi.org/10.6084/m9.figshare.11973753.v1>

### 3.2.3. Individual Mitochondria Analysis

As described in the methods, individual whole mitochondria were segmented and analysed via random selection from the same datasets used for the mitochondrial network analysis. This allowed for average size as well as morphology of individual mitochondria to be determined. Determining rate of individual growth in mitochondria will indicate whether it is the number of mitochondria or size that increases the mitochondrial volume during development. The volume and surface area were extracted from each analysed mitochondrion, and average values for mitochondrial surface area and volume obtained for each cell analysed, the results are shown in Figure 3.29. There is an increase in mean surface area and volume of the mitochondria in psoas and soleus ( $p \leq 0.05$ ). Specifically, there is significance found in the psoas between all fetal groups and the adult for surface area ( $2.6 \pm 1.4 \mu\text{m}^2$  for fetal day 50-54,  $5.4 \pm 2.2 \mu\text{m}^2$  fetal day 55-59,  $5.9 \pm 1.6 \mu\text{m}^2$  fetal day 60-64 and adult  $9.4 \pm 2.7 \mu\text{m}^2$ ). For the volume significance is found between the adult group ( $1.1 \pm 0.3 \mu\text{m}^3$ ) and fetal day 50-54 ( $0.2 \pm 0.1 \mu\text{m}^3$ ) and day 55-59 ( $0.4 \pm 0.2 \mu\text{m}^3$ ) and between day 60-64 ( $0.7 \pm 0.3 \mu\text{m}^3$ ) and fetal day 50-54. The soleus has significance, in both surface area and volume, between fetal day 50-54 ( $2.3 \pm 0.5 \mu\text{m}^2$ ,  $0.2 \pm 0.04 \mu\text{m}^3$ ), day 55-59 ( $3.3 \pm 0.9 \mu\text{m}^2$ ,  $0.22 \pm 0.04 \mu\text{m}^3$ ), day 60-64 ( $5.2 \pm 2.2 \mu\text{m}^2$ ,  $0.5 \pm 0.3 \mu\text{m}^3$ ) and the adult group ( $9.8 \pm 3.9 \mu\text{m}^2$ ,  $1.2 \pm 0.6 \mu\text{m}^3$ ).

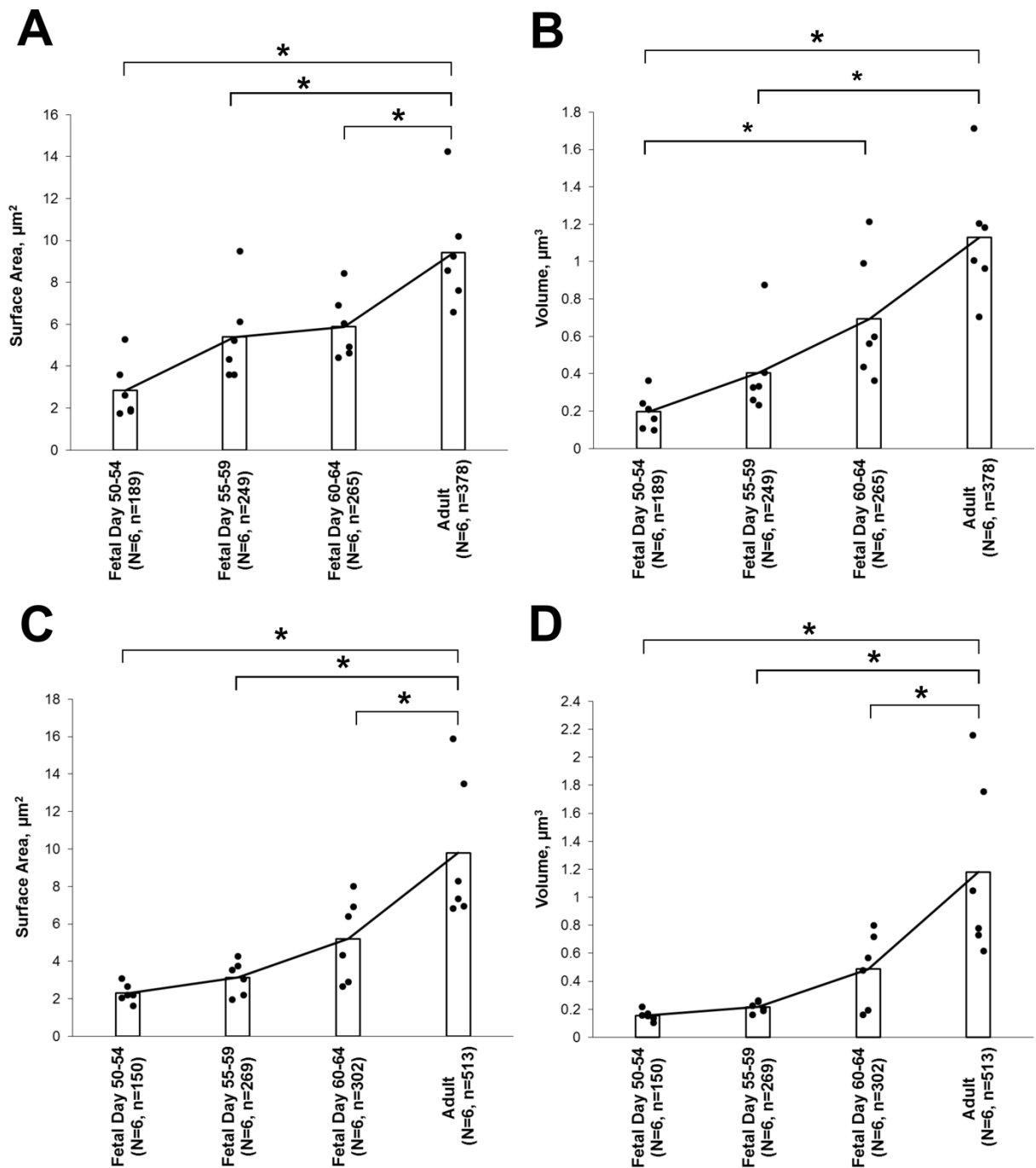


**Figure 3.29 – Surface area and volume of individual whole mitochondria.** (A) Show the results for the surface area and (B) the volume for the psoas muscle. (C) and (D) are the results for the soleus muscle. Each point represents the average measurement of the individual mitochondria (n) for each cell (N) and the overall mean for the cell is represented by the bar. Significance is denoted as (\*)  $P \leq 0.05$ .

During the segmentation of individual mitochondria, the location of the mitochondria was also noted. The mitochondria were divided by location and a similar analysis as above was performed comparing the mitochondria based upon location. No significant difference was seen in the comparison of volume and surface area, Figure 3.30, between the mitochondria at the different locations for both the psoas and soleus. For all, except the psoas PN, there was significance found ( $p \leq 0.05$ ) for the size of the mitochondria between the age groups, as detailed above.

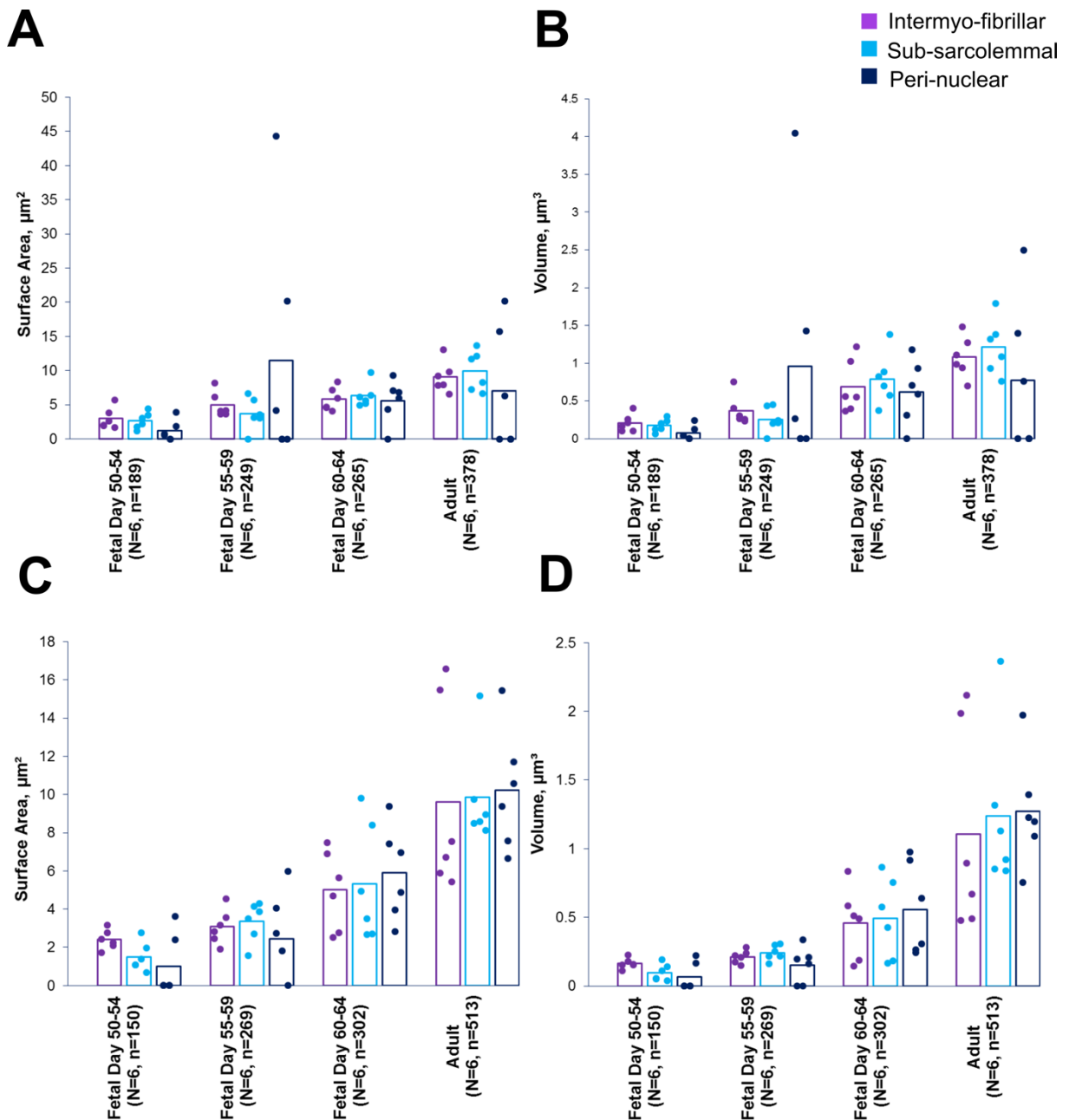


**Figure 3.30 – Results of volume and surface area of whole mitochondria for psoas and soleus divided by location.** (A) And (B) results of volume and surface area for the individual mitochondria for psoas (C) And (D) are the results for the soleus muscle. Each point on all graphs is the average of the individual mitochondrion (n) from each cell (N), only including cells containing nuclei and the average is represented by a bar.

The individual mitochondria were analysed further using a classification system based upon the morphology of the models. Through qualitative analysis it was found that a mitochondrion could be divided into three categories based on the overall shape of the mitochondrion, Figure 3.31. By analysing thousands of whole individual mitochondria, three terms were decided upon to describe the shape, these are 'column', 'spheroid' and 'irregular'. In transverse orientation the 'column' shaped mitochondria stretch over a number of sections and are longer than they are wide. 'Spheroid' shaped mitochondria are as long as they are wide and appear round and shaped like a ball. Any mitochondrion not found to fall into either of these two categories was described as being 'irregular'.

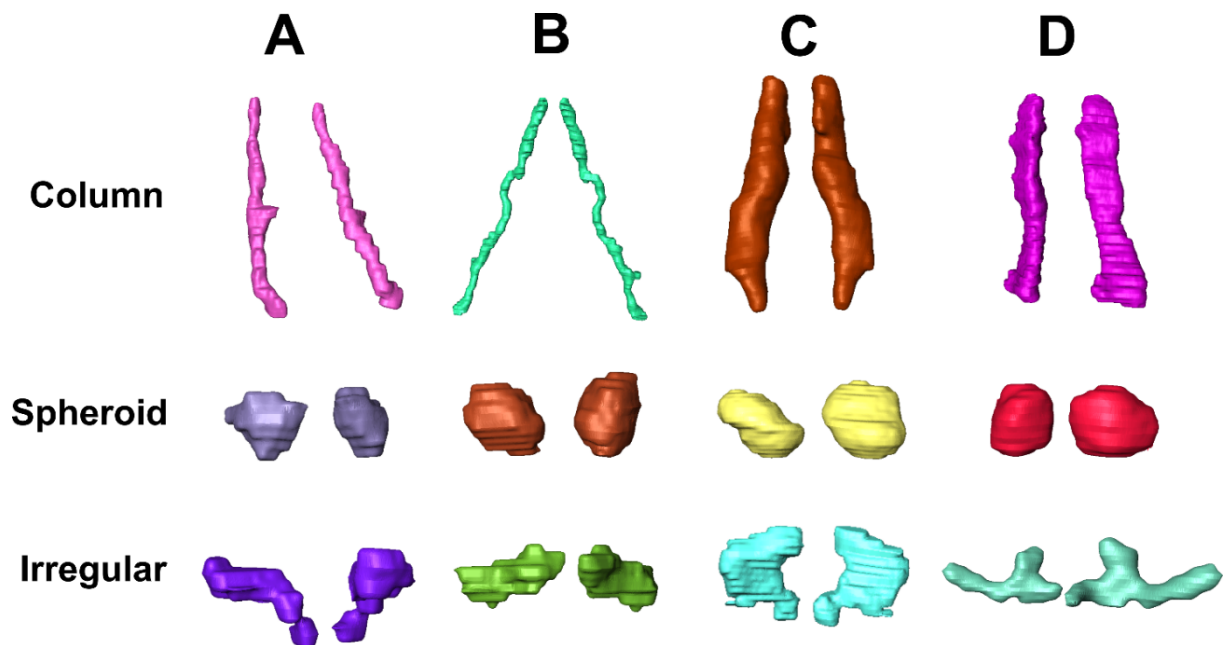


**Figure 3.31 – Examples of shapes of mitochondria found.** 3D reconstructions of individual whole mitochondria from each of the age groups, fetal day 50-54 (A), fetal day 55-59 (B), fetal day 60-64 (C) and adult (D) for each of the shapes are shown. The column shape is characterised by extending over multiple sections, in transverse orientation, and having greater length than width. Spheroid mitochondria are round, will have a similar width and length. Mitochondria that have an overall shape that does not fall into either of these two categories are classified as irregular. Video: <https://doi.org/10.6084/m9.figshare.7159775.v2>

The results of the shape analysis for the psoas and soleus can be seen in Figure 3.32. Both the psoas and soleus were found to have different proportions of the three shapes for all age groups ( $p \leq 0.05$ ). The primary shape seen in the psoas muscle is the columnar shape, as seen in the fetal day 55-59 ( $86.1 \pm 9.5\%$ ), 60-64 ( $65.3 \pm 16.1\%$ ) and adult ( $68.6 \pm 15.2\%$ ) age groups. This is significantly higher than the percentage of irregular shaped mitochondria found in fetal day 55-59 ( $13.3 \pm 8.9\%$ ), fetal day 60-64 ( $31.3 \pm 12.1\%$ ) and adult ( $29.3 \pm 14.9\%$ ). The spheroid shaped mitochondria formed the lowest proportion in each group of psoas muscle (fetal day 55-59,  $0.3 \pm 0.8\%$ ; day 60-64,  $3.4 \pm 4.6\%$ ; adult,  $1.3 \pm 1.4\%$ ). In contrast in the soleus muscle, there was no significant difference found between the percentage of column and irregular shaped mitochondria for fetal day 50-54 (column  $50.7 \pm 31\%$ , irregular  $45 \pm 30.3\%$ ), fetal day 55-59 ( $38.7 \pm 28.1\%$ ,  $52.7 \pm 17.4\%$ ) and adult ( $42.2 \pm 23.2\%$ ,  $50.8 \pm 20.7\%$ ). The spheroid shaped mitochondria again formed the lowest proportion in each group (fetal day 50-54  $4.3 \pm 2.8\%$ , fetal day 55-59,  $8.7 \pm 13.2\%$ ; day 60-64,  $5.4 \pm 7\%$ ; adult,  $7 \pm 5.5\%$ ).



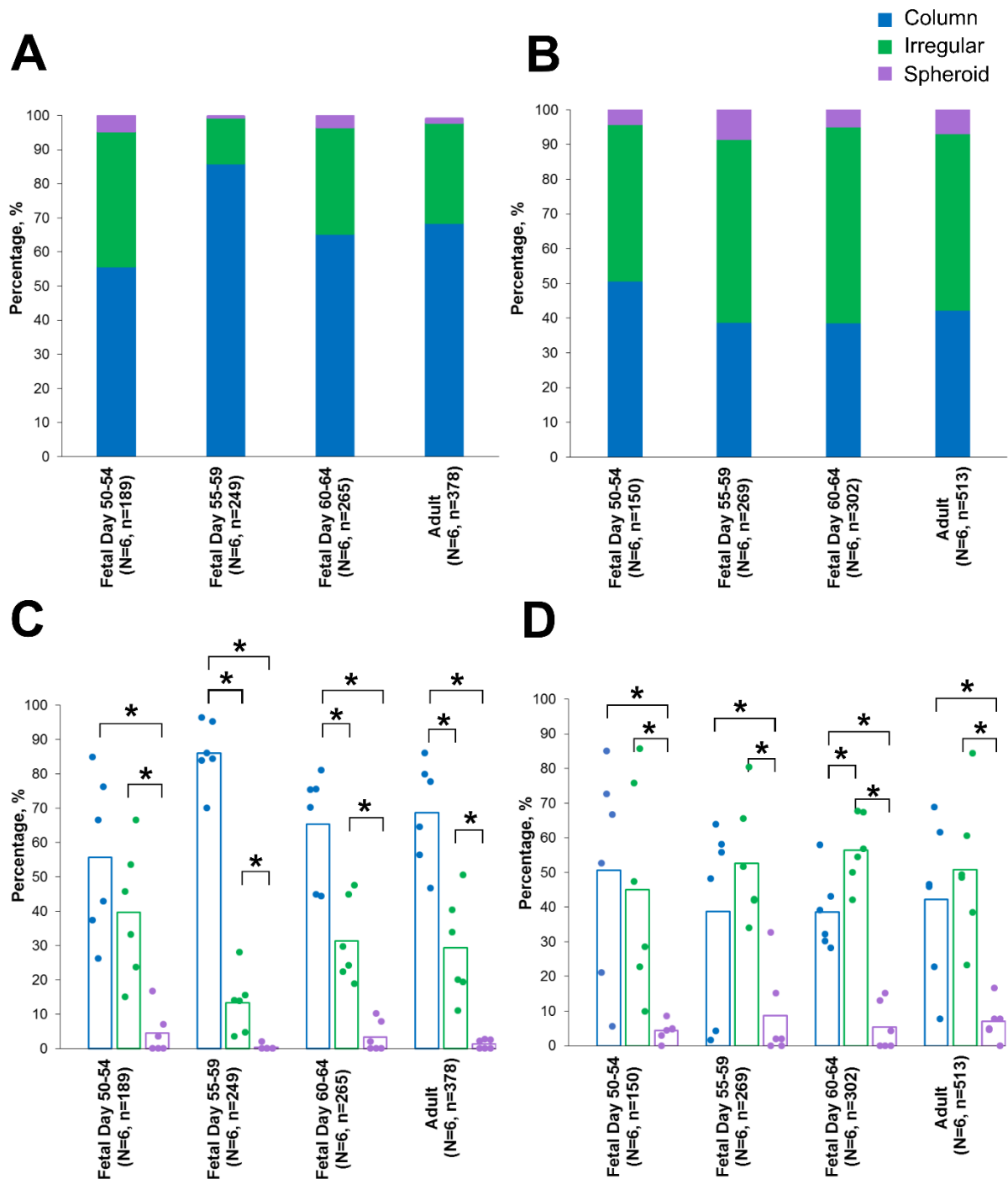


**Figure 3.32 – Results from analysis of central shapes for individual mitochondria for psoas and soleus.** (A) And (B) show percentage of each central shape present at each of the age groups for psoas and soleus respectively. (C) Shows results from comparison between the central shape proportion for each age group for the psoas and (D) for the soleus. Each point represents the average measurement of the individual mitochondria (n) for each cell (N) and the overall mean for the cell is represented by the bar. Significance is denoted as (\*)  $p \leq 0.05$ .

For ease of comparison between the psoas and soleus muscles data is re-presented in Figure 3.33. This indicates for age group fetal day 55-59, day 60-64 and adult, that there is a higher proportion of columnar shaped mitochondria present in the psoas muscle than in the soleus ( $p \leq 0.05$ ). In contrast, there is a higher proportion of irregular shaped mitochondria for fetal day 55-59, 60-64 and adult age groups in the soleus muscle than in the psoas ( $p \leq 0.05$ ).

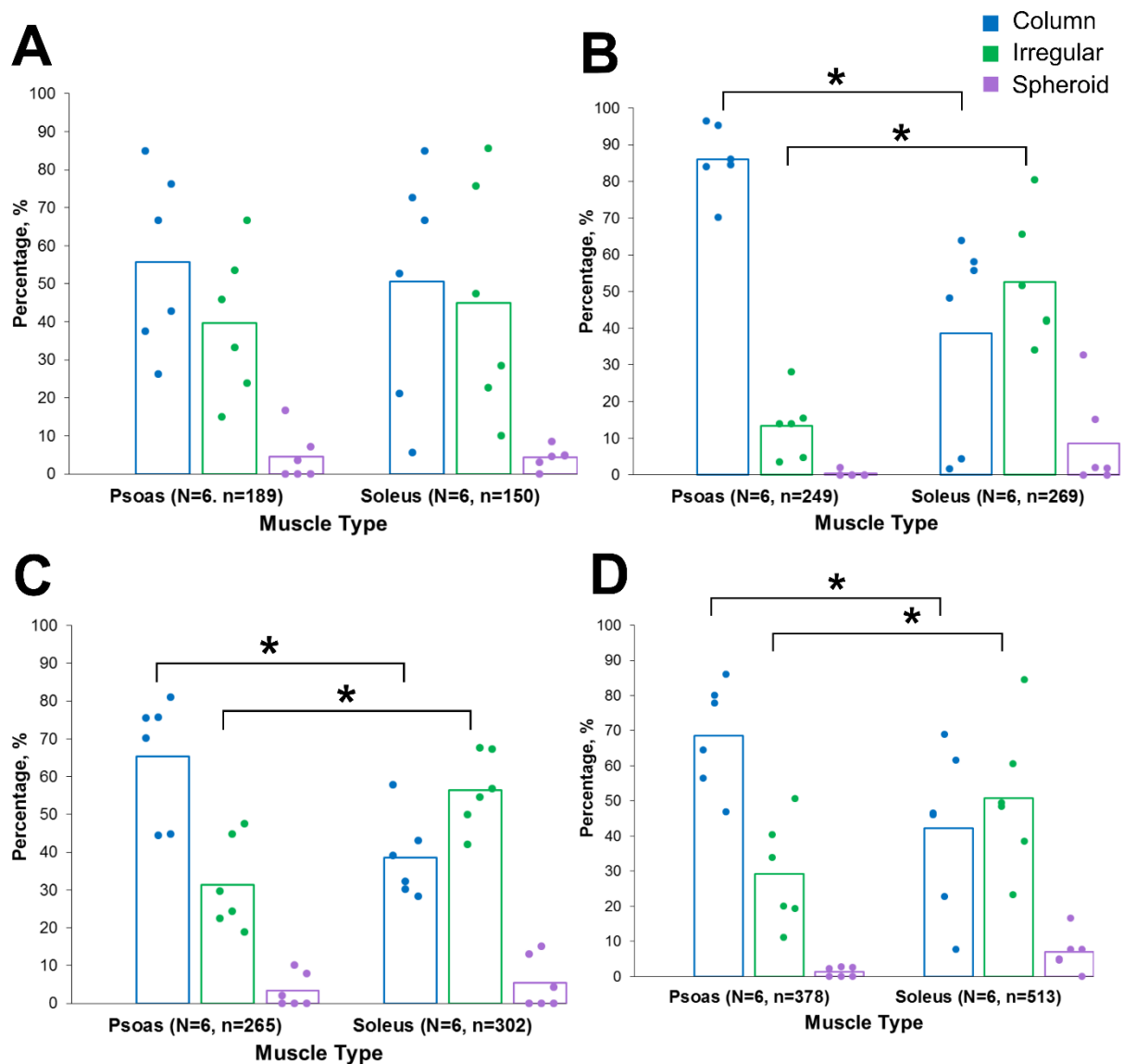


**Figure 3.33 – Comparison of central shape analysis between psoas and soleus for all age groups.** The results comparing the percentages of each central shape found in the psoas and soleus are shown for the fetal day 50-54 (A) fetal day 55-59 (B), fetal day 60-64 (C) and adult (D). Each point represents the average measurement of the individual mitochondria (n) for each cell (N) and the average of the cell averages is represented by the bar. Significance is denoted as (\*)  $p \leq 0.05$ .

The shape analysis for the psoas and soleus was also divided based on location, shown in Figure 3.34 and 3.35. The results from the adult show a significant difference between the percentage of mitochondria located at the IMF between columnar ( $75.9 \pm 8.5\%$ ) and irregular ( $21.9 \pm 8.8\%$ ). However, the mitochondria located SS had a similar proportion of columnar ( $52.2 \pm 23.9\%$ ) and irregular ( $46.6 \pm 22.3\%$ ). In comparison, the soleus does not have any significant difference in the adult at the IMF location for columnar ( $52.3 \pm 28.8\%$ ) and irregular ( $42.2 \pm 25\%$ ) or at the SS location for columnar ( $32.4 \pm 20.5\%$ ) and irregular ( $55.8 \pm 27.4\%$ ). Similar results are seen at the fetal day 50-54, 55-59 and 60-64 age groups, with similar proportion of each of the shapes seen in each of the locations. However, there is wide variation present for all age groups at all locations.

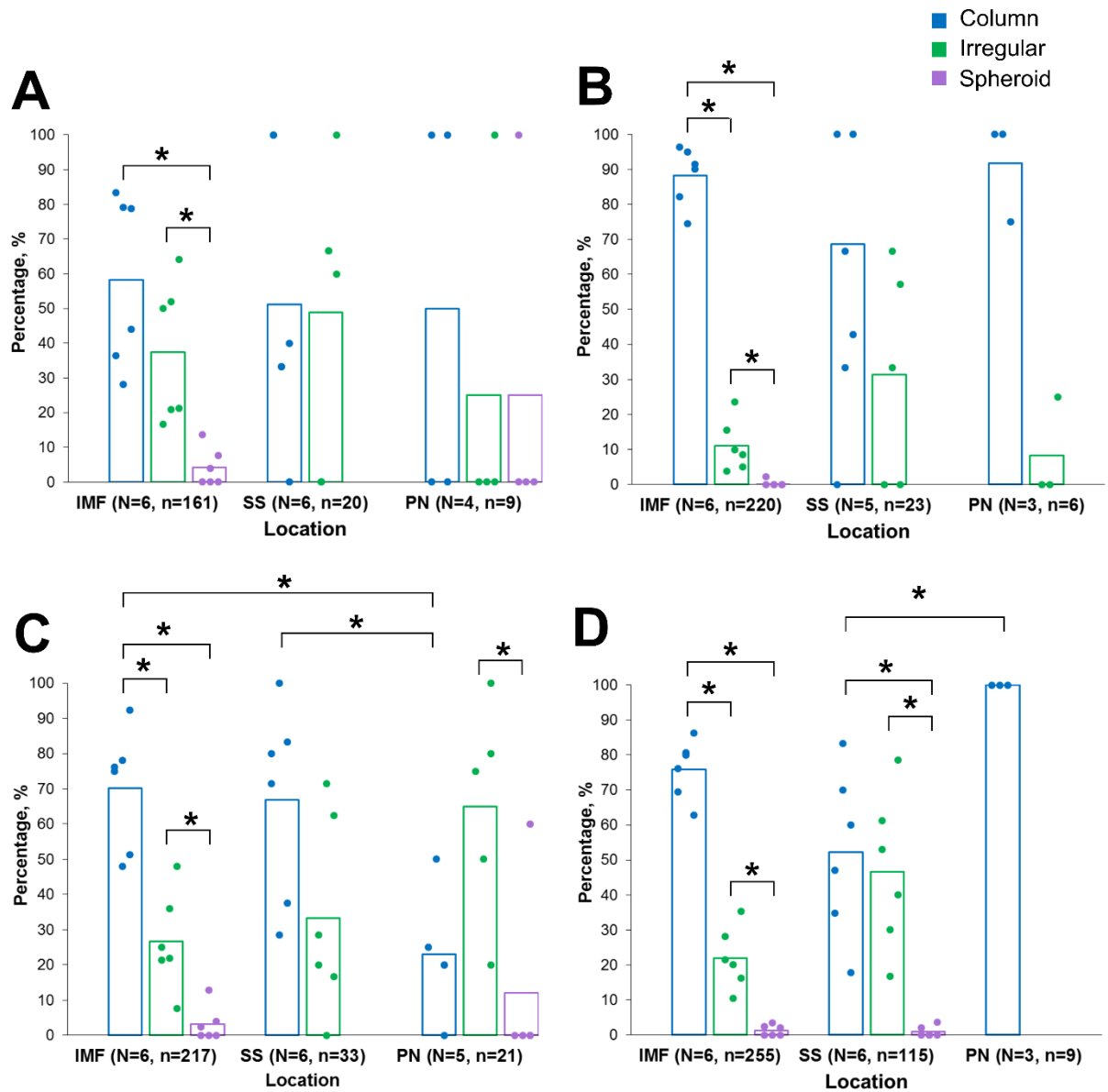


**Figure 3.34 – Percentage of central shapes divided by location for psoas muscle.** (A) Results for fetal day 50-54. (B) Results for fetal day 55-59 (C) Results for fetal day 60-64 and (D) Results for adult. Each data point represents the average pf the mitochondrion (n) from the cells (N) analysed and the overall average by the bar. Significance is denoted as (\*)  $p \leq 0.05$ .

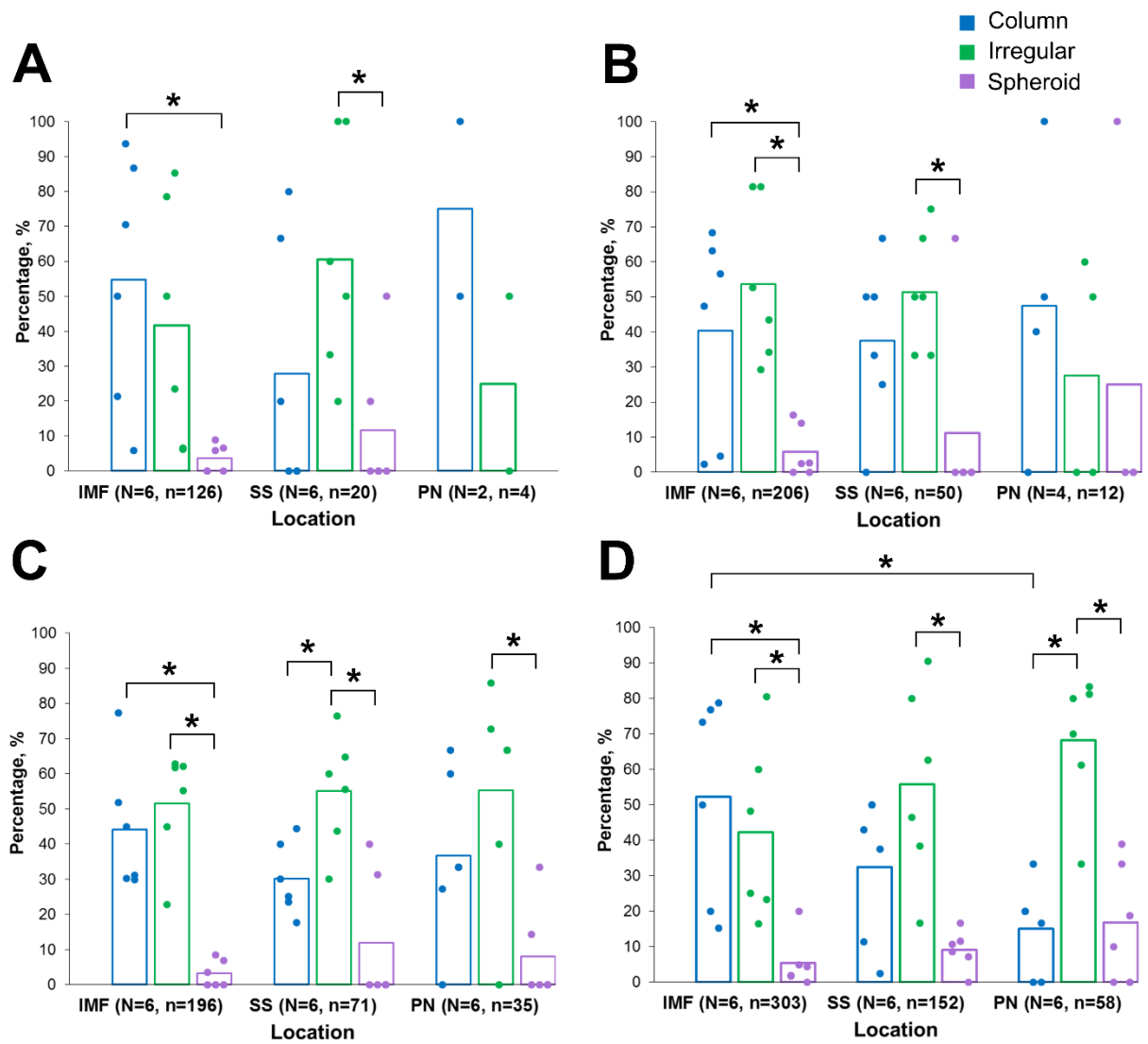


**Figure 3.35 – Percentage of central shapes divided by location for soleus muscle.** (A) Results for fetal day 50-54. (B) Results for fetal day 55-59 (C) Results for fetal day 60-64 and (D) Results for adult. Each data point represents the average pf the mitochondrion (n) from the cells (N) analysed and the overall average by the bar. Significance is denoted as (\*)  $p \leq 0.05$ .

The results for the branching analysis for psoas and soleus individual mitochondria are shown in Figure 3.36 and the results from the comparison between the two muscles is shown in Figure 3.37. Although, no significance was found in the one-way Anova when comparing the age groups for both the psoas (and soleus), there is a slight increase in mitochondria that are non-branching from fetal day 50-54 group to the adult group for the psoas. A further test (paired T-test) showed significance between branching and non-branching percentages for only day 55-59 for the psoas and day 50-54 for the soleus (shown on the graph). When the psoas and soleus are compared directly, significance is found in the fetal day 55-59 and 60-64 age groups and the adult group is very close ( $p=0.057$ ).

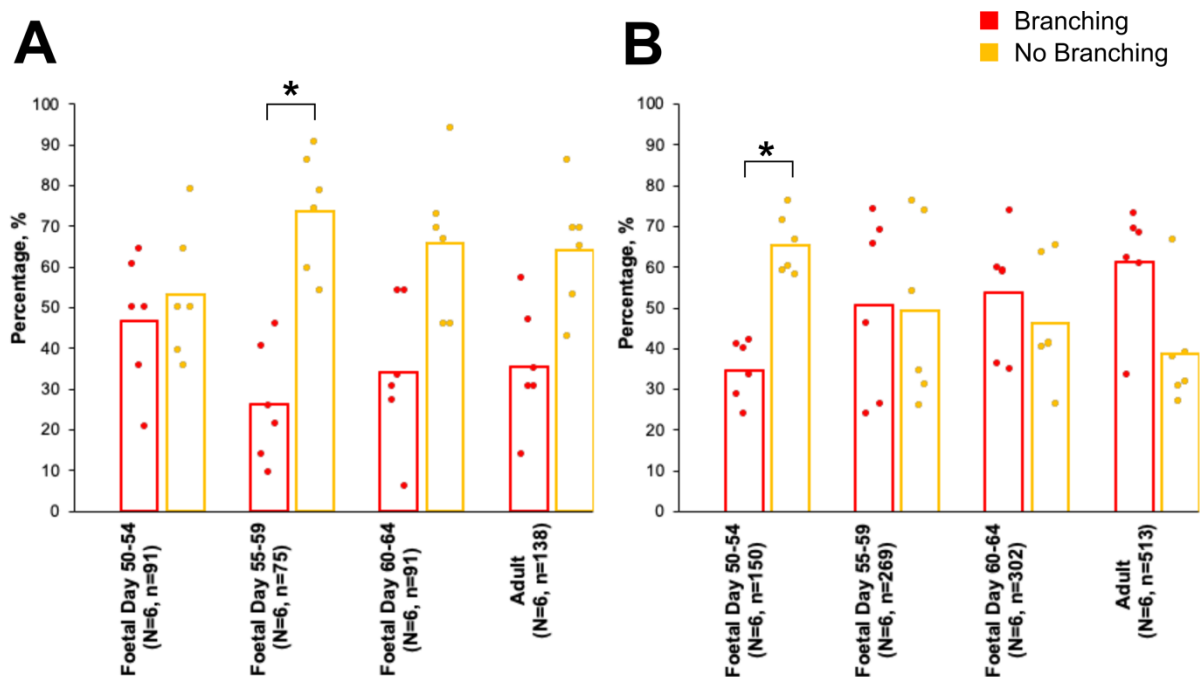


**Figure 3.36 – Results of the percentage of branching and non-branching mitochondria for psoas and soleus.** (A) Comparison between percentage of branching and non-branching mitochondria in the psoas and (B) soleus. Each point represents the average measurement of the individual mitochondria (n) for each cell (N) and the overall mean for the cell is represented by the bar. Significance is denoted as (\*)  $p \leq 0.05$ .

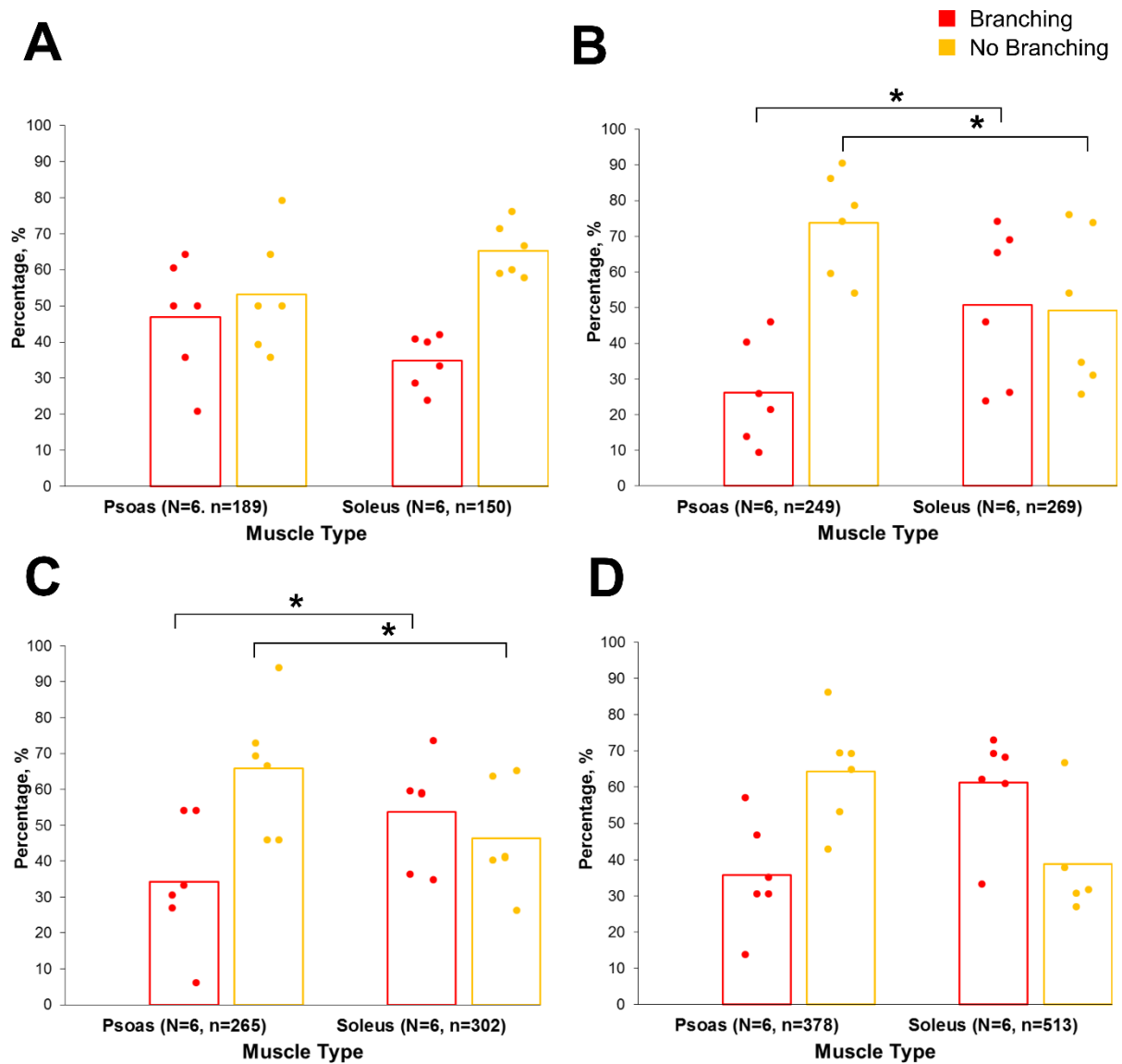


**Figure 3.37 – Comparison of the percentage of branching and non-branching mitochondria between the psoas and soleus muscle.** The psoas and soleus are shown for the fetal day 50-54 (A), fetal day 55-59 (B), fetal day 60-64 (C) and adult (D). Each point represents the average measurement of the individual mitochondria (n) for each cell (N) and the overall mean for the cell is represented by the bar. Significance is denoted as (\*)  $p \leq 0.05$ .



Results of the branching versus non-branching divided by location is shown for psoas, Figure 3.38, and soleus, Figure 3.39. In the adult psoas there is a significant difference between the branching and non-branching within the IMF. For the other age groups, significance was only found in fetal day 55-59 between the PN located mitochondria and the IMF and SS mitochondria. In the soleus, there is little difference between the proportion of branching and non-branching at the different locations for fetal day 55-59, 60-64 and adult age groups. Significance was found in the 50-54 age group when comparing the IMF and SS with the PN mitochondria, but the number of PN mitochondria analysed is far lower than for IMF or SS, and within the IMF and SS groups.

Overall, each location for both the psoas and soleus shares similar results, with only a few significant differences found for each shape and branching at each locations. For both muscles, only a few PN mitochondria were found, limiting the results for that location and the comparison between the PN to the IMF and SS mitochondria.

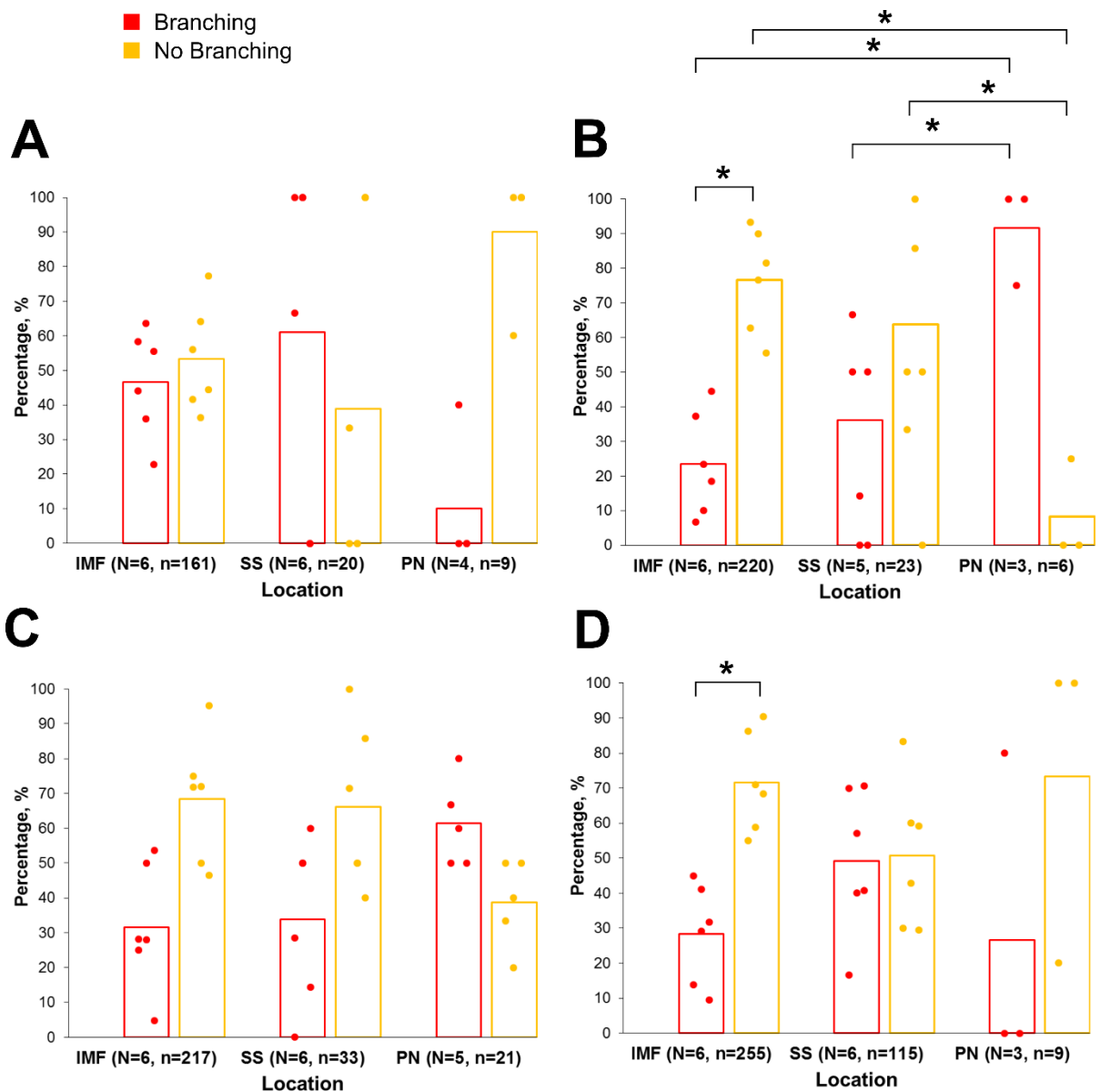


**Figure 3.38 – Percentage of branching and non-branching mitochondria divided by location for psoas muscle.** (A) Results for fetal day 50-54. (B) Results for fetal day 55-59 (C) Results for fetal day 60-64 and (D) Results for adult. Each data point represents the average pf the mitochondrion (n) from the cells (N) analysed and the overall average by the bar. Significance is denoted as (\*)  $p \leq 0.05$ .

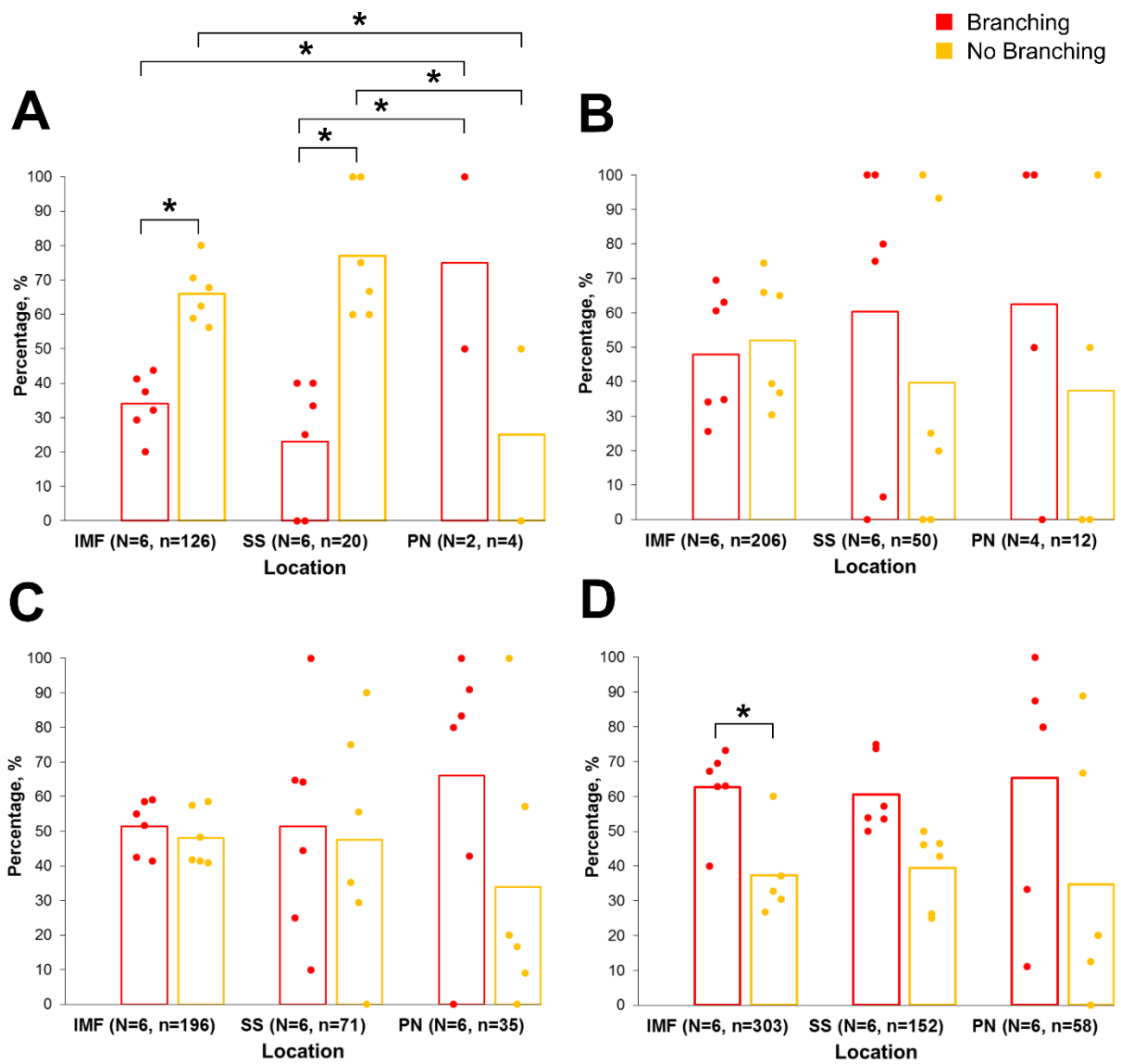


**Figure 3.39 – Percentage of branching and non-branching mitochondria divided by location for soleus muscle.** (A) Results for fetal day 50-54. (B) Results for fetal day 55-59 (C) Results for fetal day 60-64 and (D) Results for adult. Each data point represents the average pf the mitochondrion (n) from the cells (N) analysed and the overall average by the bar. Significance is denoted as (\*)  $p \leq 0.05$ .

#### 3.2.4. *Nuclei Analysis*

Not all of the SBF-SEM datasets contained a nucleus or a complete nucleus.

However, on occasions whole cell nuclei could be reconstructed (see Figures 3.40 and 3.41 for examples at each biological grouping for each muscle type). Therefore, for the quantitative analysis, the nuclei were partially reconstructed along with the corresponding cell volume to ensure consistent representation across all datasets.

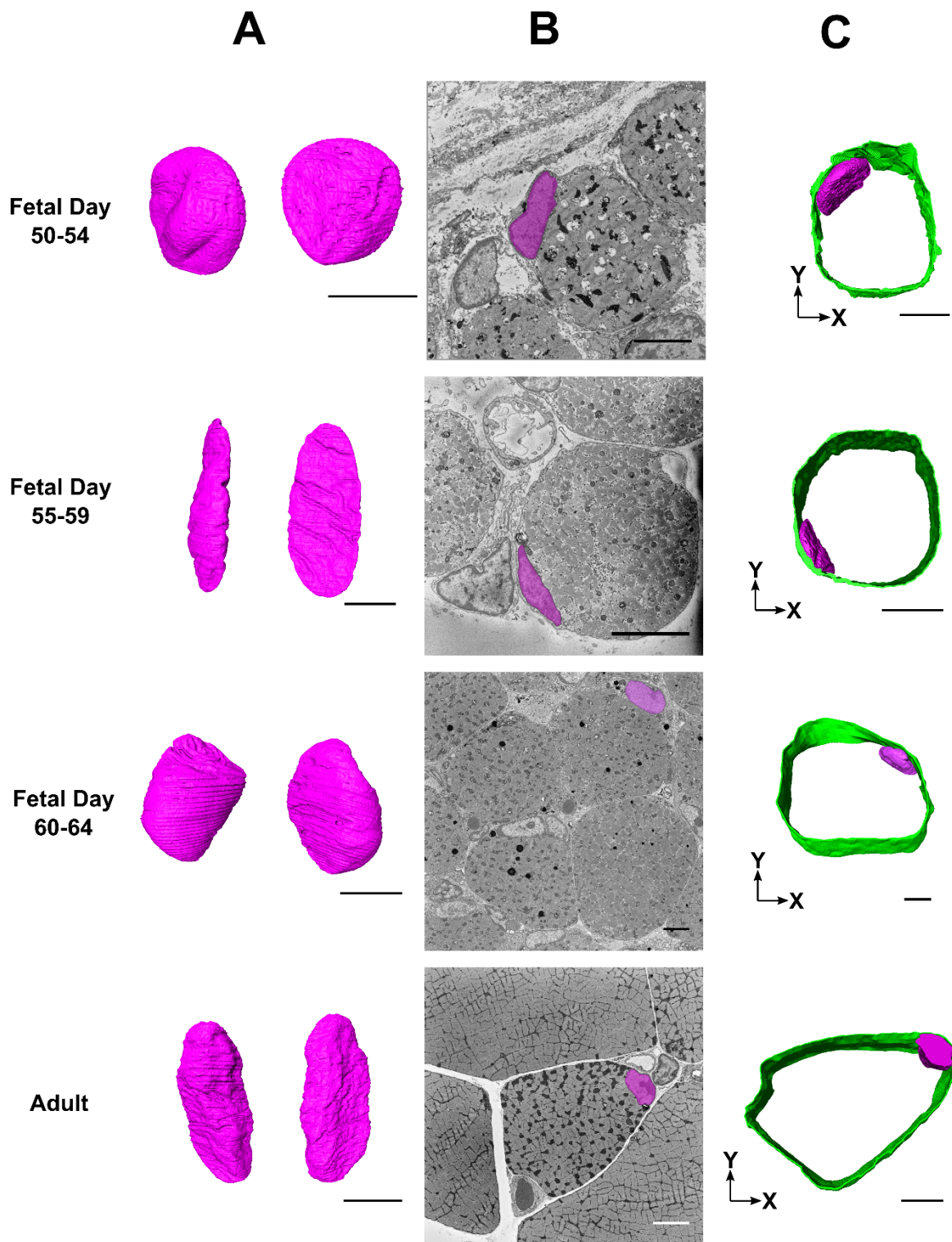


**Figure 3.40 – Examples of whole and partially reconstructed nuclei for psoas muscle for each age group.** (A) Examples of reconstructions of entire nuclei at two different orientations from each of the age groups. (B) Single sections showing segmentation of the nuclei that were partially segmented, reconstructed (50 sections) and analysed, in *magenta*. (C) Shows the subsequent reconstructions of the partial nuclei, *magenta*, and cell boundary, *green*. Scale bar 5 $\mu$ m. Video: <https://doi.org/10.6084/m9.figshare.7166357.v2>

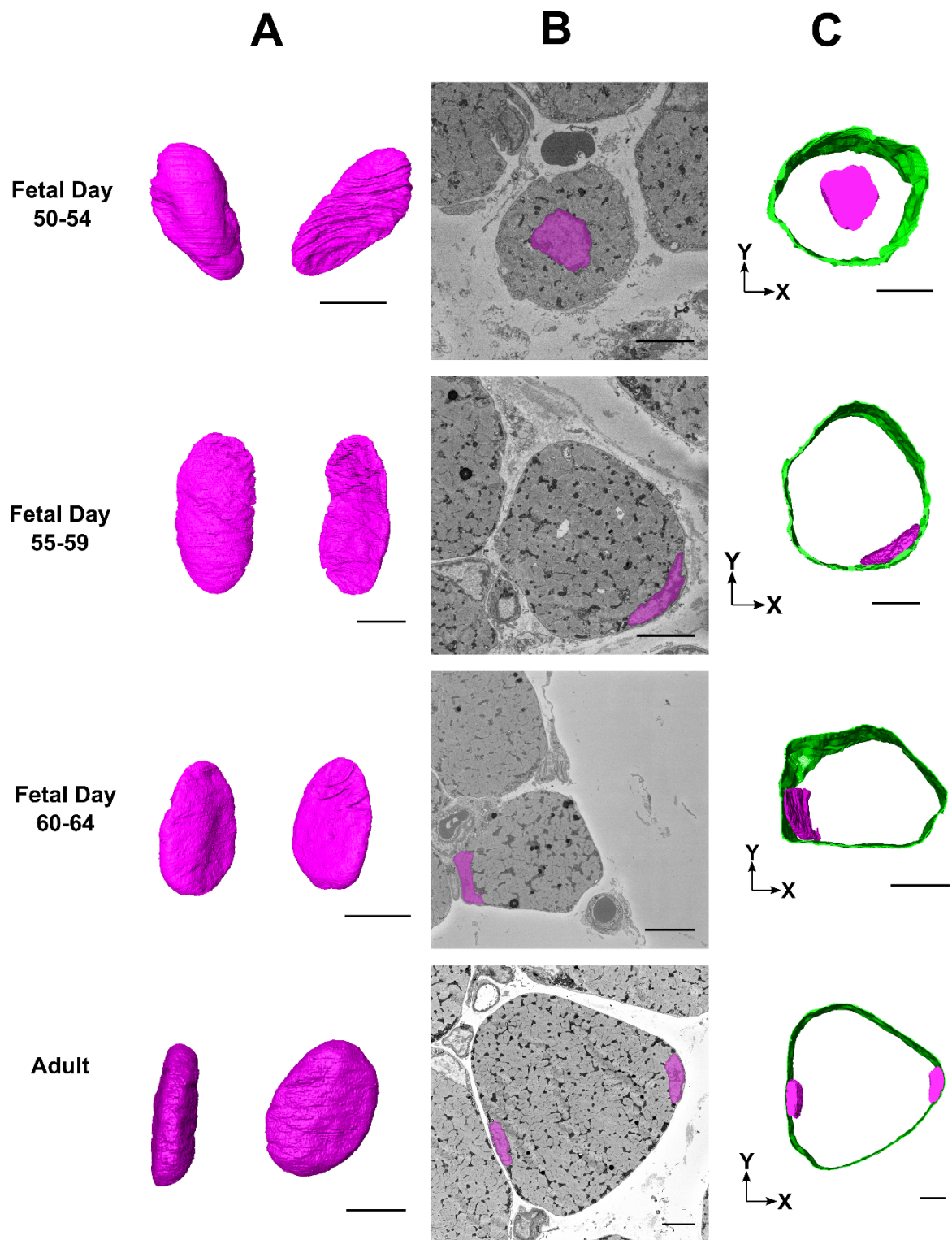


**Figure 3.41 – Examples of whole and partially reconstructed nuclei for soleus muscle for each age group.** (A) Examples of reconstructions of entire nuclei at two different orientations from each of the age groups. (B) Single sections showing segmentation of the nuclei that were partially segmented, reconstructed (50 sections) and analysed, in *magenta*. (C) Shows the subsequent reconstructions of the partial nuclei, *magenta*, and cell boundary, *green*. Scale bar 5µm. Video: <https://doi.org/10.6084/m9.figshare.7166363.v2>

The results indicate that the volume of each individual nucleus is not significantly different between the age groups for either psoas or soleus, Figure 3.42(A) and (B). In the psoas, the volume is similar for the fetal day 50-54 ( $31.7 \pm 6.4 \mu\text{m}^3$ ), day 55-59 ( $30.7 \pm 17.4 \mu\text{m}^3$ ), day 60-64 ( $41.8 \pm 10.6 \mu\text{m}^3$ ) and adult ( $39.2 \pm 20.9 \mu\text{m}^3$ ). Similar results were also seen in the soleus between the fetal day 50-54 ( $23.6 \pm 14 \mu\text{m}^3$ ), day 55-59 ( $27.9 \pm 6.2 \mu\text{m}^3$ ), day 60-64 ( $36.4 \pm 20.6 \mu\text{m}^3$ ) and adult ( $34.7 \pm 12.2 \mu\text{m}^3$ ). However, due to the increase in cell size with development, the nucleus volume was also expressed as a percentage of the reconstructed cell volume (same 50 sections), Figure 3.42(C) and (D). The psoas results show a decrease in cell volume occupied by nuclei volume from fetal day 50-54 ( $10.4 \pm 2.9\%$ ), day 55-59 ( $6.5 \pm 3\%$ ), day 60-64 ( $4.6 \pm 1.5\%$ ) to adult ( $1.9 \pm 1.2\%$ ). The same is seen in the soleus with the percentage decreasing between fetal day 50-54 ( $9.4 \pm 5.4\%$ ), day 55-59 ( $3.3 \pm 2\%$ ), and day 60-64 ( $3.8 \pm 1.8\%$ ) to adult ( $1 \pm 0.43\%$ ). For both muscles this was found to be significant ( $p \leq 0.05$ ). With further post hoc testing, significance was found between fetal day 50-54 and day 60-64 and the adult group, and fetal day 55-59 and the adult group for the psoas. For the soleus significance was found between fetal day 50-54 and all of the other age groups.

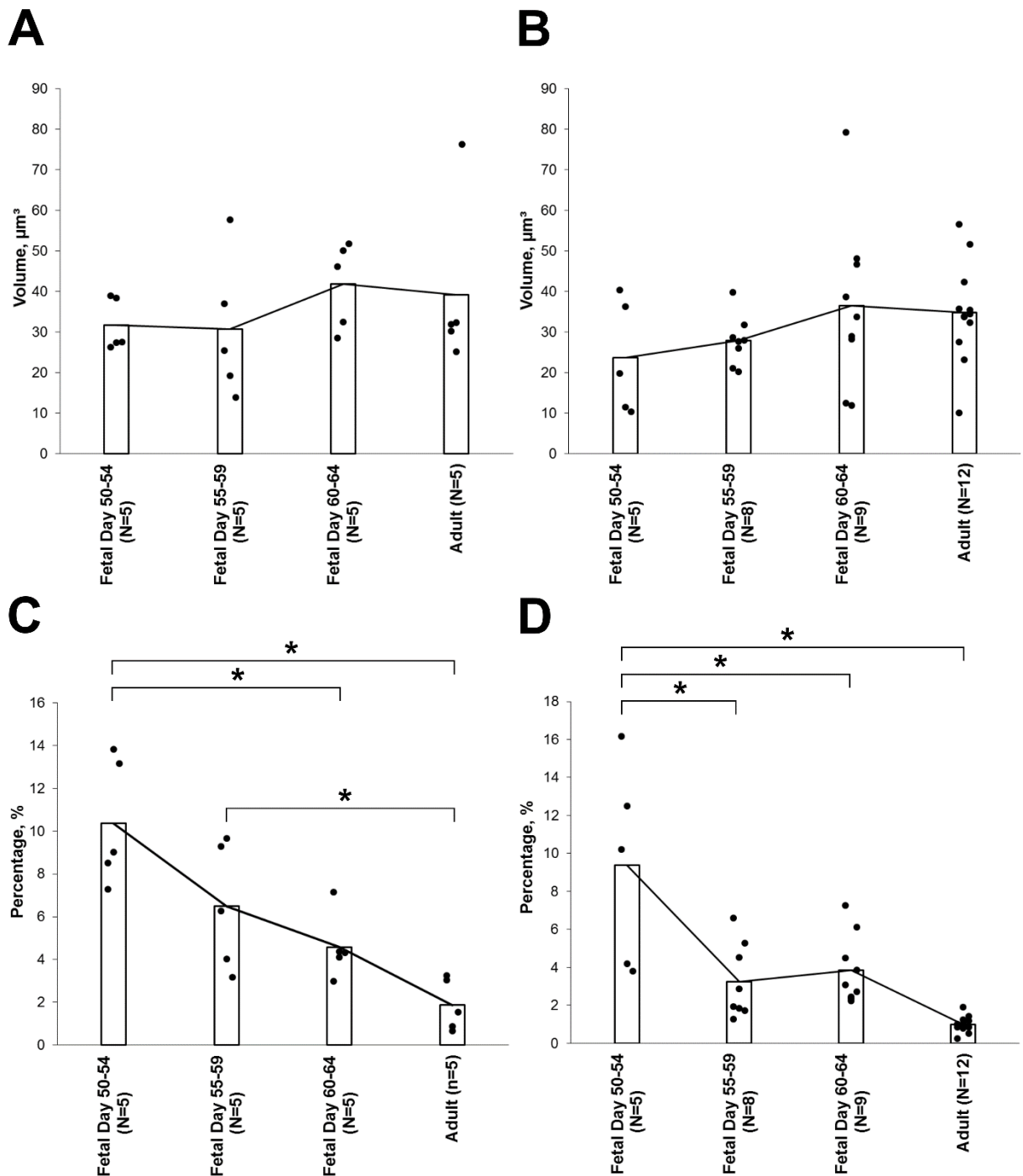


**Figure 3.42 – Volume and percentage results of partially reconstructed nuclei for psoas and soleus for all age groups.** (A) Shows the volume of partially reconstructed nuclei (50 sections) for each of the age groups for the psoas and (B) for the soleus. Each data point represents a single nucleus reconstructed, with bar indicating the average volume of nuclei for each age group. The percentage of cell volume taken up by single nuclear volume, both partially reconstructed (50 sections) is shown for the psoas (C) and soleus (D). Each data point is a single nucleus, the average is indicated by the bar and the significance denoted by (\*)  $p \leq 0.05$ .



### 3.2.5. *Summary*

Overall, the results show that the development of the guinea pig skeletal muscle mitochondrial network occurs in stages between foetus (mid- to late gestation) and adult. There is an increase in size and number of mitochondria, preceding cell growth, and by late gestation, the mitochondrial network occupies a similar area of the cell as that seen in the adult. Indicating that by late fetal gestation the ratio between mitochondria volume and cell size is determined. Distinct morphologies of mitochondria were found in both skeletal muscles examined and across all age groups. From this a morphological classification was developed so as to quantify the shapes found for analysis. Branching of mitochondria is indicative of the rate of fusion and fission and will differ based on functional requirements of the individual muscle fibre. As such it was analysed in a portion of the mitochondrial network and in the individual mitochondria reconstructions. Overall, from this analysis, it was found that the differences in branching are only seen in the adult fibres and not in the fetal age groups. These are all important factors to know to be able to understand the development of the mitochondrial network, as a whole and in individual mitochondria. As well as mitochondria a second important organelles were also analysed, the nucleus. The analysis of the nuclei during the fetal stages, and when compared of the adult fibres, shows that the nuclei maintain a similar volume during fetal gestation and is similar to adults. Conversely the cell volume increases, and due to this the percentage of cell volume occupied by the nucleus decreases from the earliest fetal group and into the adult group. As with the mitochondria results, this analysis indicates stages in the development of the muscle fibre associated with the nuclei. All of this, mitochondria and nuclei results, are further discussed in the Chapter 4.2 (pg192).

## **Chapter 4. Discussion**

In this project SBF-SEM has been used to study morphological features of two distinct biological tissues, the locust lobula and guinea pig skeletal muscle. From this novel information was found for both tissue types. The following discussion summarizes the findings and speculates on potential biological impact or function, as well as discussing the application of SBF-SEM to tackle two different types of experiments and tissue types.

## 4.1. Locust

### 4.1.1. Summary

A branch of the LGMD 2 neuron was identified, based upon its location (Leitinger and Simmons, 2000, Rind et al., 2016), subsequently imaged and analysed within an area of the lobula, 48 by 48 by 30 $\mu\text{m}^2$  (x by y by z). This is the first time such a detailed analysis of the LGMD 2 neuron branches have been performed. In particular it is the first time the complete arborisation of each TmA neuron as it synapses with the LGMD 2 neuron has been revealed, along with the path neighbouring TmA neurons synapsing with the LGMD 2 neuron take through the lobula. All the synapses along the length of specific LGMD 2 neuron branches were noted and the TmA neurons followed and reconstructed through the whole dataset. From this the following conclusions were made. The TmA neurons synapse upon the LGMD 2 neuron branches in an organised manner, each covering a certain area of the LGMD 2 neuron. This ensures that there is retinotopic mapping onto the LGMD 2, that preserves the mapping according to the position of its input facet in the locust eye. Each TmA neuron has two post-synaptic targets, another TmA neuron and the LGMD 2 neuron. The paired reciprocal synapses between TmA neurons and the LGMD 2 neuron occur back-to-back with one another and share a common synaptic cleft. Because of these reciprocal synapses with other TmA neurons, onto the LGMD 2, the TmA neurons form a network over the LGMD 2 neuron branches. Each TmA neuron has been shown to synapse upon the LGMD 2 neuron within a certain volume and mainly on a single branch. The TmA neurons found to synapse onto multiple branches, no more than 4, were shown to have a primary branch on which they synapse. The majority of TmA neurons form connections with multiple other TmA neurons, often more than once, and synapse multiple times onto the LGMD 2 neuron. Within the neurons a small proportion were found to have a higher number of synapses and synaptic partners and cover a larger portion of the LGMD 2 neuron, when compared to the other TmA neurons. These neurons were termed hub neurons and are highly connected and vital for ensuring that the network is fully connected. Without these hub neurons, non-connected islands of TmA neurons form and some lose their only synaptic partner. The hub neurons and their associated connectivity are a new find, within the TmA neuron to LGMD 2 neuron system. A summary of this is seen in the Figure 4.1.

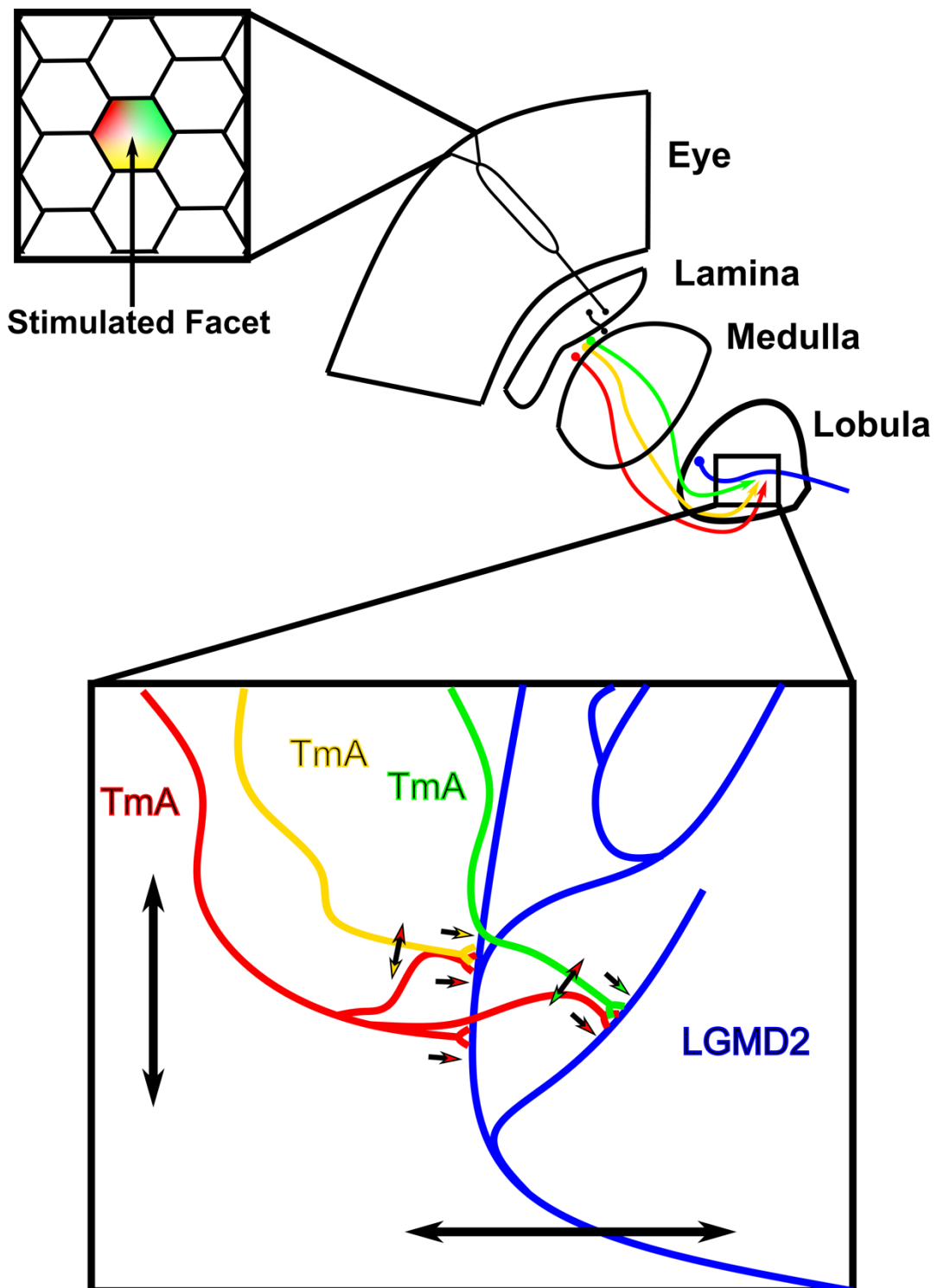


**Figure 4.1 – Summary diagram of TmA interaction onto the LGMD 2 neuron.** The schematic shows how from a single stimulated facet an area of the LGMD 2 neuron can be stimulated. The colour of the facet (*red, green and yellow*) is the same as the TmA neurons associated with it. TmA neurons, originating from the medulla (*red, yellow and green*) travel into the Lobula and synapse upon the LGMD 2 neuron branches (*blue*). There is an example of a hub neuron (*red*), showing how they synapse multiple times onto multiple branches of the LGMD 2 neuron. The direction of synapsing is indicated by the coloured, each TmA neuron has two post synaptic targets, the LGMD 2 neuron and a second TmA neuron. By mapping these connections an idea of the network in the Z direction (up-down black arrow) and in the X and Y direction (left-right black arrow) was determined.

#### *4.1.2. Synaptic Density*

The results of the analysis of synaptic density over the LGMD 2 neuron branches is consistent with previous work on other neurons within the locust nervous system (Killmann et al., 1999, Watson and Burrows, 1985) and the LGMD 1 neuron (Rind and Simmons, 1998, Rind et al., 2016) and LGMD 2 (Rind et al., 2016). The highest density found in this dataset is not yet at the mean found in previous studies (Rind et al., 2016). However, the branch and sub-branches analysed here are from a thicker portion of the LGMD 2 neuron closer to the protocerebrum and the beginning portion of the synaptic area of the LGMD 2 neuron. The synaptic density was higher on the smaller sub-branches extending from the branch analysed, as expected based on what is known. As found here the synaptic density increases on the thinner processes of the LGMD neurons closest to the medulla.

#### 4.1.3. *The TmA Neuron Network*

Previous studies followed the TmA neurons but not over the same distance as performed here. By reconstructing the full length of a TmA neuron's arborisation, where possible, the identity of TmA network pairs at the synapses onto the LGMD 2 neuron was found. By following the TmA neurons through the dataset, originating from synapses onto the LGMD 2 neuron, identifying the TmA neuron pairs has allowed for quantification and analysis of the TmA neuron connections, both to other TmA neurons and the LGMD 2 neuron. The complete TmA neurons, as defined by tracing throughout the dataset and consisting of all the terminals of the TmA neurons, were found to form a complex network over a series of branches of the LGMD 2, not previously shown structurally before. The identification of a TmA neuron network and of hub TmA neurons are new observations and are currently unique to the LGMD 2 neuron. Their implications for connectivity have been shown here for the first time. This connectivity may be crucial to detect looming stimuli, because with looming stimuli, image edges can move out over the eye in many directions simultaneously. The detail necessary to reveal this organisation was only possible using long series of consecutive sections. No alternative methods, apart from consecutive ssEM, could have revealed such a connectivity network maintained by hub neurons, and it has not been seen elsewhere in the animal kingdom.

There is known to be a retinotopic map preserved from the facets of the locust eye, through the TmA neurons and onto the LGMD 1 neuron branches (Rowell et al., 1977, Rind and Bramwell, 1996, Rind and Simmons, 1998, Krapp and Gabbiani, 2005, Peron et al., 2009, Rind et al., 2016, Zhu and Gabbiani, 2016), with a facet being associated with a TmA neuron and a specific portion of the LGMD 1 neuron. However, it was not known whether TmA neurons synapsing upon the LGMD 2 neuron also maintained retinotopy from the eye and how fine any retinotopy may be. The organised nature of the network found and seen within the reconstruction supports the preservation of the retinotopic map from the facet onto the branches of the LGMD 2 neuron. Using this principle and results from previous studies (Rind et al, 2016) allows for estimations on the nature of the facet to TmA neuron relationship. Previous estimations suggest that the number of synapses on the LGMD 2 neuron per facet is at maximum 23 and the maximum number estimated for TmA neuron synapses is 42 (6 synaptic partners up to 7 times) (Rind et al, 2016). From this it was suggested that TmA neurons from a facet will interact with up to 6 TmA neurons associated with the neighbouring facets. In comparison, the results from this study for

total number of synapses per TmA neuron the median number is 7, with 5 unique synaptic partners meaning they synapse with the same partner at least twice (the upper range extends up to 26 for total synapse number and up to 13 for synaptic partners). This coincides with the previous results, which found TmA neurons synapsing onto the LGMD 2 to have up to 6 different synaptic partners (Rind et al., 2016). In Rind et al, (2016), by dividing the scaled total number of synapses by the number of facets, it was calculated that each facet is associated with an estimated 23 synapses upon the LGMD 2 neuron. Combining this with the findings from the dataset analysed here, that each TmA neuron has an average of 8 synapses, it suggests that up to three TmA neurons are linked with a single facet. These TmA neurons will most likely interact primarily within the facet, with some interaction with the neighbouring facets, this is shown in Figure 4.1.

Although, as shown in the results, a sub-type of TmA neuron is distinct in that it synapses above the average number of times and with a high number of different synaptic partners, termed hub neurons. The small group has a median of 18 synapses and up to 9 synaptic partners, whereas the non-hub TmA neurons have 5 synapses and 4 synaptic partners. Both the hub and non-hub TmA neurons extend past their own facet and interact with TmA neurons associated with neighbouring facets, but the hub neurons extend much further than the majority of TmA neurons. This relationship between neighbouring facets gives rise to possible scenarios in regard to, distribution of TmA neuron. Firstly, that for each facet there is an associated hub neuron and 2 non-hub neurons, with the two non-hub neurons synapsing mainly within their facet, the majority of synapses outside the facet made by the hub neuron. The other possibility is that only a proportion of facets are associated with a hub neuron and a small number of non-hub neurons. The remaining facets would only have non-hub neurons, with an equal share of synaptic activity. This is the most likely option suggested by the results here. A large number of facets are represented in this dataset, by the large number of TmA neurons present. However, there are only a small number of hub neurons, and the majority of the non-hub neurons have equal weighting, meaning they synapse the same number of times onto the LGMD 2 neuron and have the same number of synaptic partners. These hub neurons were also found to be highly connected in the X and Y direction. The majority of the hub neurons synapse on more than 1 branch of the LGMD 2 neuron. It is known from calcium imaging during localized visual activation that the

TmA neurons upon the LGMD 1 neuron map the retina in two directions, both along the dendrites and across neighbouring dendrites (Zhu and Gabbiani, 2016, Jones and Gabbiani, 2012, Fotowat and Gabbiani, 2011, Jones and Gabbiani, 2010). In the current study a small proportion of the TmA neurons were found to synapse onto other LGMD 2 neuron branches, when followed through the dataset, shown in Figure 4.1. Thus, a single TmA neuron, associated with a facet, has the potential to not only synapse onto one LGMD 2 neuron branch but onto multiple branches. The majority of the neurons synapse onto a single branch so there is a possibility that the TmA neurons that synapse onto multiple branches are a sub type of TmA neuron. The network observed in the Z direction from the primary branch is also observed across the other branches and there is an additional network that links the branches via the TmA neuron to TmA neuron interaction.

Recent studies using calcium and fluorescence imaging have shown that when a single facet is stimulated there is excitation onto multiple non-associated branches (Zhu and Gabbiani, 2016). In the same study they presented overlapping areas of excitation along the LGMD 1 neuron, when neighbouring but distinct facets were illuminated. This suggests that TmA neurons from one facet potentially cover a larger area and associate with TmA neurons outside their respective facet. This agrees with the structural evidence shown in previous studies and presented here. The calcium imaging (Zhu and Gabbiani, 2016) was performed on the LGMD 1 neuron and the structural evidence presented here is from the LGMD 2 neuron, so this means that in both the LGMD 1 neuron and in the LGMD 2 neuron, TmA neurons can have an influence on the excitation pattern of their neighbours.

Both LGMD neurons function similarly, albeit with different preferences, the LGMD 2 neuron to dark objects. Any differences would be seen at the medulla level, where the ON and OFF circuitry is thought to differ between the two neurons (Gerd Leitinger, personal communication). The other differences between the LGMD 1 neuron and LGMD 2 neuron is the action of inhibition, the LGMD 1 neuron has a direct inhibitory GABAergic input onto the dendritic sub-fields B and C, whereas it is thought that in the LGMD 2 neuron inhibitory GABAergic neurons may synapse upon the TmA neurons instead (Rind et al 2016).

Overall, the hub neurons are highly connected within the TmA neuron network. They are located around areas of branching along the LGMD 2 neuron volume, areas which have high synaptic density, such as near or around small processes. As



mentioned, they are required for the network to be fully connected. The majority of the non-hub neurons are connected to a hub neuron directly, or indirectly via shared TmA neuron partner. It is these hub neurons that would cause the overlap in excitation and the wider spread of excitation, down a branch and across multiple branches

Knowing the structure of the TmA neuron network and the patterning of synapses onto the LGMD 2 neuron is needed to understand the function of the network. The structural analysis has revealed the presence of the hub neurons. Previously it was thought that all TmA neurons had a shared weight in the integration of the signal onto the LGMD neuron branches (Rind and Bramwell, 1996). However, the hub neurons have a higher proportion of synapses within the TmA neurons, suggesting that not all TmAs are equal. The impact of this functionally requires further investigation but some assumptions can be made based on what is known already about the network. It is known that the TmA neurons are excitatory upon the LGMD 2 neurons, but the interaction between TmAs neuron is debated.

Based on structural evidence and calcium imaging studies (detailed above) when a facet is stimulated the area of the LGMD neuron excited extends past the area covered by the facet, both in up-down (along a branch) and right-left (across branches). This spread of the excitation is most likely caused by the action of hub neurons and their lateral connectivity onto neighbouring TmA neurons. If every facet has an associated hub, regardless of which facet is stimulated the resulting spread of excitation would be the same. A stimulation of multiple facets associated with hub neurons would result in a larger driving force. As more facets are stimulated the LGMD neurons will reach the threshold, with the minimum number of facets required. The overlapping and extensive coverage by the hub neurons will extend the signal across the dendritic field. So that once the number of facets needed for signal propagation has been reached the LGMD neuron is close to the threshold, easily excitable and the progression of the signal is rapid. If there were facets that do not have a hub TmA neurons, the resulting stimulation would be lessened and would require number of facets to be stimulated to produce the downstream signal.

However, as hub neurons are interspersed throughout the network in an organised way, ensuring that each TmA neuron is connected either directly to a hub, the most common, or via a shared synaptic partner. The majority of the TmA neurons were

found to be directly connected to a hub, indicating that the stimulation may extend further as a result.

The nature of the interaction between the TmA neurons is debated and it not known whether it is inhibitory or excitatory. It is known that there is a form of cross communication between the partnering TmA neurons at a synapse (Rind and Simmons, 1998, Rind et al., 2016, Zhu et al., 2018). Inhibition was proposed in the model of the LGMD 1 neuron (Rind and Bramwell, 1996), and is now thought to sharpen the signal in response to stimuli rather than stop the signal (Rind et al., 2016). Although still under debate, a recent publication provides evidence for the presence of excitatory acetylcholinergic receptors on the TmA neurons (Zhu et al., 2018), but does not provide evidence against the presence of inhibition occurring but suggests it is weak.

This connectivity between TmA neurons could be a modulation system to control signal propagation. Without enough of the hub neurons stimulated, excitation of the non-hub TmA neurons would not be strong enough to generate a propagating signal in the LGMD 2 neuron. For this, enough facets would need to be stimulated to ensure a hub neuron is stimulated. As facets are stimulated the TmA neurons become excited and at the same time potential inhibition occurs between the same neurons. If a large number of the TmA neurons, including hub neurons, are excited then the signal will be propagated at the LGMD 2 neuron level. However, if not enough hub neurons are stimulated, the inhibition across the TmA neuron network will overcome the excitation from TmA neuron to LGMD 2 neuron. The hub neurons connect with a larger number of TmA neurons and would inhibit the excitation of the TmA neurons of neighbouring facets. However, if these neighbouring facets are also stimulated, as a looming object covers more of the eye field, this would overcome the inhibition received from the hub neurons.

In contrast, if the TmA neuron to TmA neuron connection was excitatory, and a lateral inhibition between the TmA neurons happened further upstream in the medulla, then the excitation of hub neurons would help increase the signal so that the LGMD 2 neuron is able to distinguish between approaching and passing objects more quickly. This would help to explain how the collision detection network is rapid and allows for a quick response as soon as the stimulus reaches a threshold angular size (covers enough of the facets). The LGMD 2 neuron will be partially excited by the action of the TmA neuron network, causing a spread of excitation in all directions

via the reciprocal TmA neuron to TmA neuron synapses. Leading the LGMD 2 neuron into an easily excitable state, so that as soon as the threshold is reached it causes a signal resulting in a rapid response.

Regardless of whether the TmA neuron to TmA neuron interaction is inhibitory or excitatory, for the threshold to be met at the LGMD 2 neuron level, the action of excitation has to be stronger and faster than that of the rate of inhibition. Inhibition alone between the TmA neurons may not be enough to do this. The LGMD 1 neuron has a specific dendritic field that receives inhibitory inputs directly and the LGMD 2 neuron indirectly, via action upon the TmA neurons and not the LGMD 2 neuron branches. As the LGMD 1 neuron and LGMD 2 neuron each have several mechanisms for inhibition understanding these require further experimental and modelling work and is discussed in Chapter 4.1.5. Future Work (pg190)

#### *4.1.4. Conclusion*

Overall, the structural analysis of the LGMD 2 neuron performed here supports results from previous studies of the TmA neuron inputs onto the LGMD neurons. Understanding the network that forms, due to the reciprocal nature of the synapses in the locust and other insects, is of importance. The presence of excitation (and or inhibition) adds complexity to the computation of the signal, prior to synapsing onto the LGMD neurons. The results from this structural study of the TmA neurons also shows why this type of analysis is important and needed. By being able to elucidate the organisation of the network, it is possible to understand how the signal is integrated across the dendritic field and also the computation that the TmA neurons undergo. This is of particular interest as the majority of studies mentioned use calcium imaging, which is a coarse form of imaging and lacks high specificity.

This type of experiment is novel, in that it has only been performed on the LGMD 1 neuron. Previous work on the LGMD 2 neuron using SBF-SEM is also limited in the size of the dataset analysed (Rind et al., 2016) and for this dataset a different analysis approach was applied. By following the TmA neurons throughout the dataset the pattern of their synapsing onto the LGMD 2 neuron and their respective partners could be mapped, and various insights have been gained based upon the results of this analysis. The identification of a TmA neuron network and hub TmA neurons are new findings, currently unique to the LGMD 2 neuron. Their connectivity may be crucial for the collision avoidance pathways in the locust. Only 3D-EM imaging methods allow for the 3D imaging at high resolution required to reveal the organisation of neurons and the connectivity network maintained by hub neurons. This has yet to be shown in other species.

#### 4.1.5. Future Work

There are a number of possibilities for the distribution of these neurons that requires further analysis. These hub neurons could either be placed throughout the dendritic field of the LGMD 2 neuron at equal distances along the dendrites or concentrated in areas of thinner processes. However, in this portion of the dataset where the LGMD 2 is still relatively large in comparison to the thinner neurites closer to the medulla, it cannot be determined by which of these conditions the 'hub' neurons are organised. Further work is required into the 'hub' neurons, to not only determine their spatial organisation but whether they are a real sub-type of the TmA neuron and not due to the spatial sampling limitations of the technique (discussed in the main discussion).

A lot more information can be garnered from the dataset collected. The analysis performed could be continued, focusing on the other branches of the LGMD 2 neuron and their afferent neurons. The other branches are only briefly analysed in this study and by repeating the analysis could test whether the pattern seen is replicated on multiple branches. A similar analysis should also be repeated on thinner branches closer to the medulla. The distribution of synapses is thought to increase as the branches get thinner (Rind et al., 2016). The next step would be to determine the circuitry of the afferent neurons at the thinner branches, to see whether the pattern found here is maintained over the branches or changes. This could be important for understanding the integration of the signal and the speed at which it occurs. To determine whether the patterning differs in the thinner branches closer to the origin of the afferent neurons from the medulla.

Differences between the inputs to the LGMD 1 and LGMD 2 neurons may only be observable in the medulla region. In other insects the ON and OFF signals are transmitted via separate motion detecting neurons (Joesch et al., 2010, Takemura et al., 2011, Shinomiya et al., 2019) The LGMD 2 neuron has a preference towards darker objects, via the OFF path from the eye. Both the ON and OFF paths will connect with TmA neurons, directly or potentially indirectly. However, once the TmA neurons are stimulated they follow the same path through the chiasm and into the lobula, regardless of whether it is connected with the ON or OFF paths within the medulla. This means that within the lobula there may be minimal difference in the TmA neuron interaction between the two LGMD neurons. Widening this type of study to include the medulla would answer this question. Such as attempting to image from the medulla and into the lobula within the same dataset using SBF-SEM.

Other types of neurons that can be identified in the dataset are inhibitory neurons. The inhibitory GABAergic neurons in the locust can be identified by a darker cytoplasm and pleiomorphic vesicles (Rind and Simmons, 1998). Although the resolution in the dataset is not high enough to visualise the shape of the vesicles in the pre-synaptic neurons. The action of GABAergic inhibition is unknown in the LGMD 2 neuron. As mentioned, in the LGMD 1 there are inhibitory inputs onto the sub-fields of the dendritic tree (Rind and Bramwell, 1996, Gabbiani et al., 2005) but the LGMD 2 neuron dendritic tree differs in structure and does not have these sub-fields (Simmons and Rind, 1997, Rind et al., 2016). The inhibition onto the LGMD 2 neuron must then occur either directly onto the afferents, to stop the signal, or onto the LGMD 2 neuron, to reduce excitation. Preliminary analysis of the GABAergic neurons within the dataset has been performed. What was found was evidence of GABAergic neurons partnering with an afferent neuron to synapse onto the LGMD 2 neuron directly or to synapse onto the afferent neurons themselves. The presence of these two forms of potential GABAergic inhibition would impact onto the signal integration.

Currently only a portion of the dataset has been analysed so far in regard to the location and structure of the inhibitory neurons that can be identified. The combination of labelling and other imaging methods would also be beneficial for studying the inhibitory neurons further. One such method would be through immunolabelling of receptors present in the neurons, in this case GABA receptors. Immunogold labelling has been routinely used in EM studies (Hainfield and Powell, 2000). However, it is not yet widely used in combination with 3D-EM techniques and as such would require extensive testing and optimisation to combine immunogold labelling with SBF-SEM. In principle the GABAergic receptors could be labelled with Nanogold particles, either pre or post embedding on slices of the sample. It would then undergo an altered EM staining protocol, to allow for visualisation of both the labelling and tissue on the SBF-SEM. With this the inhibitory neurons and synapses would be mapped and further understanding on the role of the inhibitory network specific to the LGMD 2 neuron. Once developed, this type of method could be replicated to study other receptors within the lobula, such as the acetylcholine receptors present on the TmA neurons and the LGMD neurons.

## **4.2. Skeletal Muscle**

### *4.2.1. Summary*

The principal aim of these experiments was to examine the nature of, and any differences in, mitochondrial volume, sub-cellular localisations and morphology during guinea pig skeletal muscle (psoas and soleus) development between fetal and adult age groups. The underlying perspective was that any changes noted may reflect the changes in muscle function occurring during the establishment of a mature contractile phenotype in adulthood. To do so SBF-SEM datasets were taken of psoas and soleus muscle cells, in transverse orientation, at 3 different time points in fetal gestation and from adult guinea pig. Datasets for 48 individual cells were collected, for between 250 to 300 sections, resulting in around 220GB worth of raw data.

From the datasets the following observations were made. The mitochondrial density increases during fetal development, and by the late fetal stage the density is similar to that found in the adult group, even though the volume of the cell does not differ greatly between the fetal age groups. The mitochondrial network branching was also analysed. Differences were only found between the adult psoas and soleus groups and not the fetal groups. Size and morphology of each identified mitochondrion were analysed. There was an increase in surface area and volume across the fetal groups with the late fetal group similar to the adult for both muscles. From the reconstructions three distinct morphologies were found across all age groups and in both muscles, termed columnar, irregular and spheroidal. The branching of the whole mitochondria was also analysed. Again, the only difference was found between the psoas and soleus in the adult group. The location of the mitochondria was also mapped. An increase in the proportion of SS located mitochondria was seen between the fetal groups and the adult psoas and soleus. Although the location was found not to impact the size and morphology of the mitochondria.

On a number of occasion nuclei were also found in the datasets collected, due to the multi nucleated nature of skeletal muscle cells. As such, analysis of the nuclei over development was also performed. It was found that volume of the nucleus does not differ greatly between the fetal groups and the adult group for both muscles, even as cell size increases (increasing the ratio of cell to nuclei volume as the muscle cells mature).

#### *4.2.2. Mitochondrial Volume, Surface Area and Location*

During development, the volume of a muscle cell and mitochondrial network will increase. Due to their importance in the homeostasis of metabolically active cells, such as skeletal muscle, the total mitochondrial volume should increase in parallel with cell growth. However, during gestation the relationship between mitochondria and cell growth is non-linear. As fetal age increases the density of mitochondria per cell volume increases and then stabilises between late fetus and adult. Although an increase in cell volume is only seen between the late fetal stage and adult groups. This occurs even as the volume and surface area of the individual mitochondria show an increase over development for both muscles, with a sharp increase between fetal day 60+ and adult.

When the results from the mitochondrial density and individual size of mitochondria are combined, the developmental pattern of the mitochondrial network can be determined. Prior to late gestation (day 60-64) there is a steady growth in mitochondrial size and an increase in mitochondrial density. However, the increase in individual mitochondria size from day 55-59 to day 60-64 does not account for the sharp increase in mitochondrial density between the same age groups. This suggests there could be an increase in proliferation of mitochondria, so that increased mitochondrial number rather than size contributes to the increased mitochondrial density in the later stages of fetal development. As there are no studies looking at mitochondria size or number over development, it would be of interest to determine if this is the case, using light microscopy methods that can image and track mitochondria in live cells.

Thus, development of the mitochondrial network appears to undergo a shift between days 55-59 and 60-64, being well-developed and similar to the adult by this later stage in gestation. This could be explained by a change in activity of the fetal guinea pigs. Movement of guinea pig pups in utero increases up until around day 60 gestation. At this point there is a reduction in activity due to the development of sleeping behaviours, more time spent in rest and lack of room in the amniotic sac (van Kan et al., 2009). At birth, guinea pig pups have a well-developed muscular and nervous system, with the in utero development being akin to human gestation (Dyson et al., 2012).

When the mitochondrial density was assessed by location, it was found that a higher proportion was found sub-sarcolemmal in the adult than in the fetal groups. As there



was no significant difference found between the location and surface area and volume for the individual mitochondria across all age groups, it suggests that the increase in percentage is due to an increase in number of mitochondria located SS, not by an increase in their size. It is uncertain as to why there is an increase in mitochondria in the SS as the muscle develops. One possibility is that the increase in size and number of mitochondria occurs in the middle of the cell, forcing the mitochondria to the periphery to occupy the free space as biogenesis of larger mitochondria increases. It is unknown whether the increase in size of individual mitochondria is due to fusion of mitochondria already present or the biogenesis of larger mitochondria. This could only be determined by tracking the development of individual mitochondria in vitro.

#### 4.2.3. *Branching and Shape Analysis of Mitochondria*

From the earlier SBF-SEM experiments different morphologies of individual mitochondria has been noted. One question that arises is what changes in morphology and complexity, if any, occur over development within the two different muscle types? The qualitative analysis of the morphology devised in this study is the first to do so thoroughly based on 3D-EM data. There have been previous studies highlighting changes in human muscle focusing on known morphological changes due to stress or in the cases of disease, donut-shaped mitochondria, and nanotunnel formations (Vincent et al., 2019, Vincent et al., 2017, Vincent et al., 2016). The shape analysis presented in this work on guinea pig skeletal muscle indicates the presence of common mitochondrial morphologies across muscle type and age.

The results show that the majority of the mitochondria for both the psoas and soleus fall into the column or irregular categories. There is also the consideration of how mitochondrial shape or branching may change with development. For the psoas there was no significance found in fetal day 50-54 in the percentage of column or irregular. Then for fetal day 55-59 and day 60-64 there was a higher percentage of column mitochondria than irregular, similar to the results seen in the adult group. Therefore, in the mature psoas muscle column mitochondria is the predominant shape type. In contrast, in the soleus muscle there was no significance found in either fetal day 50-54, day 55-59, day 60-64 or adult between the percentages of column and irregular shaped mitochondria. Although there was a slight majority in irregular shaped mitochondria. Thus, changes in mitochondrial shape are noted during psoas muscle development that are not apparent in soleus muscle.

In comparing the two skeletal muscle types in adulthood, it was found that the psoas had a higher amount of column shaped mitochondria than the soleus, and the soleus a higher amount of irregular and spheroid shaped mitochondria. For all age groups the spheroid shaped mitochondria made up the smallest proportion of the mitochondrion. The full biological meaning of these tissue type-specific proportions of mitochondrial shape remains to be resolved. Although these simple spheroidal mitochondria have been found more in cases of disease (Vincent et al., 2019).

From the shape analysis there was no difference seen between the IMF and SS locations in the soleus for all age groups. For the psoas a difference was noted between the IMF and SS locations for the adult and none of the other age groups. The IMF had a higher percentage of column shaped mitochondria and the SS had a

higher percentage of irregular shaped mitochondria. There was only a small number of mitochondria segmented that were located at the PN so the results for that location are varied and explains why there was a number of differences found between the PN mitochondria and the other locations. Due to differences metabolically the mitochondria can be treated as sub-populations, it is posited that they develop separately but through the process of fusion and fission the two populations integrate and connect (Hood and Iqbal, 2013, Picard et al., 2013, Dahl et al., 2015). There is also evidence found in the results here to suggest that the two sub-populations develop separately from one another.

The branching of the mitochondrial network and of individual mitochondria was analysed. From the network analysis, the soleus shows a similar percentage of branching (protrusions extending off from a single mitochondrion) for all age groups and the psoas across each fetal group. However, the cells from adult psoas have a significantly smaller percentage of mitochondrial segments above the threshold, suggestive of reduced branching and less complexity. For the individual mitochondria, the psoas has a higher percentage of non-branching mitochondria from fetal age day 55-59 to adult. Whereas the soleus at fetal day 50-54 has a higher proportion of non-branching, which switches to branching by the adult group. Again, there are no studies that have measured the rate of fusion and fission in mammalian skeletal muscle over development, so as to determine whether the shift in branching is due to alterations in the balance between fusion and fission.

As shown in the results mitochondria are malleable and the complexity and shape of the mitochondrion is dictated by the action of fusion and fission and the balance between these two processes. A balance is maintained to ensure a steady state of morphology, mtDNA and metabolic mixing and bioenergetic functions and organelle number (Griparic and van der Bliek, 2001). An imbalance has been noted to lead to shifts in morphology and impacts cell vitality (Palmer et al., 2011). Fission is the division of the organelle, and, if unregulated, leads to heterogeneous distribution of mtDNA, variations in ATP production, an increase in the presence of the reactive oxygen species and an increase in the likelihood of apoptosis (Parone et al., 2008). It also removes old or damaged mitochondria, by dividing the organelles into small enough portions to undergo mitophagy by lysosomes (Kim et al., 2007). Fusion aids in maintaining a homogenous population. There is a large amount of information regarding the dysfunction of fusion and fission related to disease and in studies

discovering the regulatory mechanism of fusion and fission. However, there is very limited studies on the role of fusion and fission over development.

The shape of the mitochondria will have a direct impact on the function of the organelle. The limitation in this study and in previous is that the 3D data presented here is not combined with functional tests. Previous functional studies are limited as they do not image the mitochondria in 3D to map the mitochondrial network shape or at the resolution to determine the shape of individual mitochondria. However, a recent review paper has compiled evidence from various studies to suggest potential functional impacts. Elongated mitochondria have an increased surface area which facilitates interaction with the environment (Glancy et al., 2020). Elongation of mitochondria was found in proliferating fibroblasts (Yao et al., 2019) and in skeletal muscle cells in aged mice (Leduc-Gaudet et al., 2015). Elongated mitochondria also have an increase in oxidative capacity and can protect cells against cell death (Gomes et al., 2011). On the other hand, more compact mitochondria might have a more optimal volume for internal functional capacity. On the other hand, more compact mitochondria are found in quiescent cells (Yao et al., 2019) and the action of fission, required for mitochondria to shift from elongated to compact, is needed for apoptotic signalling (Youle and Karbowski, 2005). Highly branched mitochondria have a larger surface area, resulting in a better exchange of calcium and other ions and metabolites, and an increase in interaction with their environment and long-distance communication (Bleck et al., 2018, Glancy et al., 2020) although it comes at a large cost of removal.

How this relates to the results found in this study are as follows. The adult psoas muscle fibres had a higher proportion of elongated mitochondria, columnar shaped, compared to the soleus, which allows for a greater interaction with other organelles within the cell and the environment. Whereas the more compact mitochondria found in the adult soleus would have a higher volume for internal functional capacity. The soleus fibres were found to have a higher amount of branching than the psoas, which counteracts the deficit from having a higher proportion of compact mitochondria. Both elongated and branching mitochondria allow for communication over long distance and between the mitochondria and their surrounding environment. This long-distance communication is vital for muscle cells, regardless of fibre type, for uniform contractions to occur. As to why the two muscle types favour one potential mechanism for ensuring communication throughout the cell is not known.

Fusion and fission are driven by the requirements of the muscle, directly related to function. This is in turn related to the fibre type. Thus, the shapes and complexity of the mitochondria discussed above will be directly related to the fibre type and the functional requirements of the muscle. Using parameters from previous studies and the results found here an attempt at identifying fibre type in the fetal and adult cells analysed has been made.

For the fetal age groups the results are similar between the two muscles from the earlier to late gestation stages. This coincides with evidence from studies of expression during gestation in mice and rats. Prior to embryo day 16 (in mice and rats), the muscle fibres (including soleus, extensor digitorum longus, anterior tibial muscles and the myotome found in embryos) in these mammals express both proteins associated with primary fibres (Myosin Heavy Chain *-neo* and *-emb*), as well as fast and slow isoforms (Condon et al., 1990a, Lyons, 1990, Narusawa et al., 1987, Niro et al., 2010, Wang et al., 2015). Later in development there is a loss of slow myosin expression, coinciding with the beginning of neural innervation (Lyons, 1990). Thus, differentiation of the muscle fibres only starts to occur close to birth (Zhang et al., 1987, Condon et al., 1990a, Condon et al., 1990b, Lyons et al., 1990, Narusawa et al., 1987, Niro et al., 2010, Wang et al., 2015, Schiaffino and Reggiani, 2011). Therefore, for the fetal age group no specific fibre type for any of the cells analysed was found.

From previous imaging studies, slow twitch fibres appear to be abundant in mitochondria and these mitochondria have been shown to have a high degree of branching (Kayar et al., 1988, Ogata and Yamasaki, 1997, Picard et al., 2012, Fujioka et al., 2013, Mishra et al., 2015, Bleck et al., 2018). From previous fibre type identification (Peter et al., 1972, Gollnick et al., 1974, Soukup et al., 2002) the cells analysed from the soleus muscle are most likely to be slow twitch fibres. The higher proportion of branching in the network and individual mitochondria found in this study coincide with results from previous studies on slow twitch muscle mitochondria morphology. All this evidence suggests that it is highly probable that the cells analysed from the soleus are slow twitch.

On the other hand, the fast twitch fibres are less dense in mitochondria, have a lower percentage of branching (Ogata and Yamasaki, 1997, Picard et al., 2012, Mishra et al., 2015) and are more string-like, extending through the muscle fibre (Fujioka et al., 2013). The psoas muscle is more complicated due to the combination of fibre type

shown previously (Johnson et al., 1973, Parkkola et al., 1993, Arbanas et al., 2009). Although when the results are compared to the soleus, lower complexity and smaller number of branching mitochondria are found. In alignment with fibre morphology from past studies the results are indicative of primarily fast twitch fibres.

An overall summary of the differences found between the adult muscle types and potentially in relation to their fibre type is shown in Table 4.1. However, the muscle fibres can be homogenous or heterogeneous (Bottinelli et al., 1994, DeNardi et al., 1993, Gorza, 1990, Schiaffino et al., 1988, Bagust et al., 1974, Peter et al., 1972, Schiaffino et al., 1989, Burke et al., 1971). This makes the fibre type highly specific to each muscle and thus makes it difficult to determine the fibre type of the muscle without combining different studies.

**Table 4.1 – Overview of results of mitochondrial complexity and morphology compared to previous studies.** Details results from fibre typing percentages in the psoas and soleus muscles and morphological differences found between fibre types. Alongside the results from the morphological analysis performed in this study. \* (Peter et al., 1972, Gollnick et al., 1974, Soukup et al., 2002), \*\* (Johnson et al., 1973, Parkkola et al., 1993, Arbanas et al., 2009), \*\*\* (Ogata and Yamasaki, 1997, Picard et al., 2012, Mishra et al., 2015), \*\*\*\*(Kayar et al., 1988, Ogata and Yamasaki, 1997, Picard et al., 2013, Mishra et al., 2015, Bleck et al., 2018), \*\*\*\*\* (Fujioka et al., 2013).

<b>Muscle</b>	<b>% Oxidative</b>	<b>% Glycolytic</b>	<b>Branching (lit)</b>	<b>Shape (lit)</b>	<b>Branching Network</b>	<b>Branching Individual</b>	<b>Morphology – Columnar</b>	<b>Morphology – Spheroid</b>	<b>Morphology – Irregular</b>
<b>Psoas</b>	~50% *	~50% *	Simple ***	Elongated, string-like *****	~8%	~35%	~70%	~1%	~29%
<b>Soleus</b>	~90% **	~10% **	Complex ****		~30%	~60%	~40%	~7%	~51%

However, without functional studies, the full impact of these shapes on the function of mitochondria and even on the cell remains unknown. Currently, there have been minimal studies that focus on the shape of individual mitochondria and impact on function of the mitochondria themselves and the overall impact on muscle tissue specifically. Within the studies that have the main imaging methods used have been light microscopy or TEM, which do not provide the detail in 3D that can be gained through use of SBF-SEM. That being said there has been an increase in the use of 3D-EM techniques to study individual mitochondria shape (Vincent et al., 2016, Vincent et al., 2017, Bleck et al., 2018, Vincent et al., 2019). The development and improvements in combining other techniques, such as anti-body labelling, with EM (discussed further in Chapter 4.2.6. Future Work, pg205), will increase the output of information from such 3D-EM studies as this.



#### 4.2.4. Nuclei Analysis

An important step in nucleus development is the migration of the nucleus to the periphery. Nuclei are found primarily in the centre of the muscle cell early on in muscle formation (Capers, 1960, Cadot et al., 2015, Folker and Baylies, 2013, Roman et al., 2017, Roman and Gomes, 2017, Rosen and Baylies, 2017, Roman et al., 2018). Then the nuclei migrate to the periphery, which was previously debated, with recent research suggesting it is the crosslinking of myofibrils during development that forces the nuclei to the periphery (Rosen and Baylies, 2017, Roman et al., 2018). Without this movement of the nuclei to the periphery the muscle function can be impaired, as seen in central nuclear myopathies (Jungbluth et al., 2008, Jungbluth and Gautel, 2014). Although what is not known is at what stage in development this occurs. In the datasets collected there were some examples of centrally located nuclei found in the day 55-59 (two examples) and day 50-54 (one example) for both muscle types. However, for all other cells the nuclei were located at the periphery, suggesting that all of the nuclei have re-localised to the periphery by day 59 gestation. Although there are numerous studies on the positioning of nuclei, there are few studies that have shown the time points at which the nuclei move to the periphery during development, but it can be assumed to occur very early in myogenesis based on studies into chick embryos, day 13 of a 21 day gestation (Capers, 1960).

The results from the nuclear volumes show that also by day 50 the nuclei are a similar size to that seen in later fetal and adults, including both peripheral and centrally located nuclei. This suggests that the nuclei, which originate from the fusion of myoblasts (Shenkman et al., 2010, Roman and Gomes, 2017), do not increase in size over development but are already at the required size. Indeed, when the volume of each individual nucleus is calculated as a percentage of cell volume there is a significant decrease from the earliest fetal to the later fetal and adult groups. This is due to the increase in cell size that occurs during this time. However, these calculations are based upon estimating the volume of one nucleus per cell (due to pragmatic issues around the area of image data to be segmented and quantified). It has not factored in the potential increase in total nuclei numbers, as post-natal growth, induced hypertrophy (exercise) and repair can increase the number of myonuclei by fusion of satellite cells or myoblasts (Shenkman et al., 2010). Thus, although the percentage volume of the cell in which a single nucleus occupies decreases, the percentage of the cell occupied by total nuclear volume may not.

Further analysis could be performed on earlier fetal datasets and taking more samples from the day 50 age group. This could help to determine the percentage of nuclei that are centrally versus peripherally located and potentially provide a timeline in the migration of the nuclei to the periphery in the guinea pig. This could be repeated in a variety of animal models of disease, either during gestation or comparison of myopathies.

#### 4.2.5. Conclusion

Overall, this study found that over development not only do the size of the mitochondria increase but also the number. An increase in proliferation of new mitochondria was found from the early to the late fetal age groups and the ratio of cell to mitochondrial network volume was found to be set by the latest fetal age group for both the psoas and soleus muscle. Although two different muscle types with varying fibre type proportion were used, many features of mitochondrial network development were similar including mitochondrial volume changes, and sub-cellular location proportions during skeletal muscle maturation. From a qualitative analysis three distinct morphologies of mitochondria have been found, columnar, spheroidal and irregular. Although these morphologies have been suggested previously, this is the first instance that a qualitative classification system has been devised. There were very few differences seen between the fetal age groups in regard to morphological analysis for both the psoas and soleus. The largest difference in morphology was seen in the comparisons between the psoas and soleus, especially in the adult. This is indicative of the morphology of the mitochondria being driven by fibre differentiation, which does occur during fetal development but is primarily seen in very late fetal and during post-natal development.

This type of analysis has not been performed before on the nuclei and mitochondria in skeletal muscle over development. This was only made possible through the use of SBF-SEM, which provides both the necessary resolution but also the 3D capabilities to reconstruct a mitochondrion, the mitochondrial network, the nuclei and the whole cell from a single dataset. The study presents a method of analysing the structure of skeletal muscle organelles and provides a novel way to classify the morphology of mitochondria and determine complexity of the network. It has the potential to be applied to other experimental settings using SBF-SEM or in combination with other methods, as discussed in future work below.

#### 4.2.6. Future Work

The next step would be to combine a method of fibre type identification with SBF-SEM. The results are indicative of a specific fibre type (in the adult only) however further experiments would be needed to verify this. This could be achieved by combining known methods for fibre typing, for example immunohistochemistry and light microscopy (Barnard et al., 1971, Peter et al., 1972), antibody labelling and gene expression (Moore et al., 1984, Zhang et al., 1987, Condon et al., 1990a, Schiaffino and Reggiani, 2011, Wang et al., 2015), with SBF-SEM in parallel.

Analysis of earlier fetal groups will help establish the timeline of the nuclei migrating from the centre to the periphery of the skeletal muscle fibres. In the data currently collected there are examples of centrally located nuclei in both the psoas and soleus. However, the proportion of centrally located nuclei in the fetal day 50-54 datasets is not known and reimaging and quantification is required. Instead, the focus of the data collection will be on ensuring that nuclei are present and attempting to image whole nuclei. This type of analysis could be repeated on all of the other age groups and also in aged adults, proposed to have a higher number of centralised nuclei (Valdez et al., 2010). This would require imaging tissue block faces at lower magnification, and for greater depths which, of course, has knock-on considerations for volume of data storage and subsequent analysis.

Collection of data from neo-natal guinea pigs would also inform us of trajectories of skeletal muscle development, and mitochondrial and nuclear morphology changes associated with this, to adulthood. Research suggests that the period shortly after birth is important for fibre type specification (in mice and rats) (Moore et al., 1984, Narusawa et al., 1987). Collection and analysis of data from aged adult guinea pigs would also be of importance. Research shows that this balance of fusion and fission is affected in aged adults (Wyckelsma et al., 2017), which would affect mitochondrial network morphology. Other factors that affect mitochondria morphology, such as exercise, fasting and other stressors (Holloszy, 1967, Bizeau et al., 1998, Holloszy, 2008), could also be explored and may benefit from this type of structural analysis at high resolution.

The morphological analysis presented here could be applied to muscular diseases that may affect the morphology and function of the mitochondria and cells.

Mitochondria from patients with mitochondrial diseases have been shown to present with distinct shapes (Vincent et al., 2016), which may benefit from applying the

classification system presented here. Another disease that would benefit from SBF-SEM analysis is Duchenne muscular dystrophy (DMD), which affects the structure of skeletal muscle cells. From previous studies it is known that the nuclei are mis-localised in *MDX* mice and are not distributed equally (Totsuka et al., 1998, Terada et al., 2010, Iyer et al., 2017). Samples from *MDX* and control mice have been collected, processed for SBF-SEM but only viewed on TEM for preliminary results. From the samples a high number of centrally located nuclei were found, as well as changes in the appearance of the mitochondria. SBF-SEM would determine whether there are any structural differences in the 3D structure of the nuclei and the shape of the mitochondrial network and individual mitochondria between the control and *MDX* mice.

### **4.3. Consideration of the Utility of SBF-SEM for the Study of Neuron and Skeletal Muscle Biology**

#### *4.3.1. Summary*

The extensive application here of SBF-SEM to the study of two distinct sets of biological tissues and questions has allowed for the discovery of previously unknown concepts in skeletal muscle development and neuronal networks in the Locust. These experiments present novel methods for analysis of mitochondria and for the first time present a connectomic-type analysis applied to the locust visual system. In doing so a large amount of raw data was collected for both experimental projects and all of this, plus segmented and 3D reconstructed datasets, have been made available online for people to access, analyse and use as they wish.

#### 4.3.2. 3D-Electron Microscopy (Microscopy)

The limitation of the locust data collected using SBF-SEM is that the sample is lost during the in-situ sectioning. By sectioning the entire cross-section of the optic lobe with the ATUMtome, multiple areas can be imaged, either using mSEM or SEM. In theory the entire lobula region could be imaged from beginning to end, this would allow for the full reconstruction of the TmA neuron and LGMD neuron connectome.

In regard to the skeletal muscle data, the amount of resin surrounding the individual cells limits the capability of the imaging. A large amount of resin requires a higher amount of nitrogen in the chamber to compensate and reduce charging. This has been counteracted by the development of the Focal Point Injector (Deerinck et al., 2018). This injects a small amount of nitrogen close to the surface of the block after the block is cut and during the imaging cycles, allowing for the chamber to remain at high vacuum, maximising resolution available

Advances in SBF-SEM imaging have been dramatic in the last decade. The current project used Zeiss Sigma with Gatan 3View, the latest model as of 2015 when this project started, for obtaining images of high-quality resolution for a variety of experimental purposes. The technological options have continued to increase since then and there are a variety of SBF-SEM microscope manufacturer options available (including the Merlin, Sigma and Gemini from Zeiss and the Teneo VolumeScope from Thermofisher) each with different capabilities. The most notable development in recent 3D-EM techniques is the creation of the mSEM (Eberle et al., 2015, Pereira et al., 2016). It has a single strong electron beam that is split into multiple beams, up to 91 parallel beams, and each of these beams can scan an area of a section simultaneously. Out of all the 3D-EM techniques so far described this has the highest throughput of data acquisition, imaging an area of 1cm<sup>2</sup> at 4nm resolution in under 3 hours (<https://www.zeiss.com/microscopy/int/products/scanning-electron-microscopes/multisem.html>).

#### 4.3.3. Analysis

Like many other biology experimental approaches, the manual and computational analyses of the large volumes of data collected from 3D-EM techniques still remains a bottleneck. The analysis is often the most time-consuming portion of the experiments. The segmentation of the neural dataset took roughly 9 months, average 6hrs a day and 5 days a week. The analysis of the skeletal muscle data took roughly 10 months, again 6hrs a day 5 days a week. For both experiments a range of tools were used from manual brush and semi-automatic methods, like interpolation and thresholding. For this reason, there has been an increase in finding ways to reduce the time it takes to analyse the data produced.

Computer-based machine learning is the current focus of computational scientists in analysing EM data. Training a program to recognise multiple feature types from different tissues would reduce time spent analysing data but this process takes time to build a library of training data. There have been researchers working to develop automated segmentation, often involving machine learning (Kasthuri et al., 2015, Kaynig et al., 2015, Beier et al., 2017, Krasowski et al., 2018). On the other hand, this is currently limited to neuronal EM datasets and also requires computing experience. The next step would be to make automated workflows accessible to those with a range of computing knowledge and also applicable to a broad range of datasets (e.g., different biological specimens, structures and dataset resolutions). Researchers may analyse a variety of tissue types, therefore an automated segmentation tool or program that can be applied to multiple types of data would be beneficial. In theory the best program or tool would be able to identify different structures and individual cells, based upon computer-based learning, and segment the structures of choice for all sections in the data. This is a major challenge that will require multi-lab iterative collaboration.

Another option, which also assists, if given appropriate training, with experimental rigour, is to increase the number of people performing the analysis. This has been the case for many connectomic studies (Helmstaedter et al., 2013), where students are trained on analysing the data with a particular purpose. Alternatively, there is also an increase in 'citizen science' projects, where members of the public can aid in the segmentation of a dataset or in computer training to improve automated workflows (example: <https://www.zooniverse.org/projects/h-spiers/etch-a-cell>). However, for



both cases an expert is required to oversee and check the work produced to ensure accuracy of segmentation.

Everything above is helped by the deposition of experimental raw data in open access repositories, the granting of permission to semi-accessible repositories or providing data upon request. However currently the availability of the data that is analysed and presented in publications is limited. As indicated in the literature review table in the introduction (Appendix 1), only 21 publications have made their data accessible online, from a total of 238 publications using SBF-SEM. The majority of publications show either the segmented data or reconstructions in video form, sometimes with small portions of the raw or processed data in video form. Although there has been a drive to increase the accessibility of data related to EM and for other types of experimental studies. This has been aided by the funders making it mandatory to make all data available (BBSRC) and easier deposition and linking of data to publications (EMPIAR or Zenodo). As previously indicated, all of the raw data analysed here have been made accessible online for download, which is around 16GB of neural data and total of over 200GB of skeletal muscle data.

#### *4.3.4. Conclusion and Future Work*

The two experiments overall achieved success using SBF-SEM, with novel information regarding structure found from the analysis of the locust and the skeletal muscle data. The network of TmA neurons synapsing upon the LGMD 2 neuron in the locust had never been studied previously to the extent shown here. The discovery of a potential sub-group of highly connected TmA neurons is entirely novel and only made possible with SBF-SEM. For the skeletal muscle study, it is the first time a classification system for mitochondria shape in skeletal muscle has been devised. This was only made possible with the resolution and 3D imaging able to be performed with SBF-SEM.

However, both studies share a limitation and is one found in a lot of research involving SBF-SEM. This limitation is that in some tissues the identity of the cell can sometimes be difficult to determine, unless there are specific structural markers or only a single cell is being imaged. For the locust the identification of inhibitory cells can be done visually within the EM dataset however identification via labelling methods would aid in this. This could also apply to identification of other receptors at the synapses between the TmA neuron and LGMD neurons. For skeletal muscle the fibre type of the cells analysed can only be assumed based on structural evidence in the adult cells and could not be determined from the data collected of the fetal cells. Being able to stain the muscle cells to determine fibre type and image prior to imaging with SBF-SEM or combine so that the labelling can be visualised in the SBF-SEM. Such a technique is described as Correlative light microscopy and electron microscopy (CLEM) would aid in answering this question and many more.

Although a combination of molecular labelling, and EM has been performed for a number of years, such as immunogold labelling with TEM (Vandré and Burry, 1992, Burry et al., 1992, Hainfield and Powell, 2000), there has been an increase in the need to combine such methods with the 3D-EM techniques. Currently alterations to the labelling and staining methods, CLEM has been made possible (Ou et al., 2015, Shu et al., 2011). There are now a number of examples using fluorescence and light microscopy followed by 3D-EM acquisition (Bolasco et al., 2018, Booth et al., 2019, Shami et al., 2016, Drawitsch et al., 2018, Maclachlan et al., 2018, Hoover et al., 2017). Immunogold labelling has difficulties with penetrating through samples and other staining methods used for light microscopy will impact on the EM staining and alter the contrast. However, these methods are currently limited. Use of fluorescence

combined with EM is still novel and as with all these methods will improve in the future.

Although the usage of 3D-EM, in particular SBF-SEM, is constantly growing and improving. However, access to 3D-EM techniques is still limited, due to cost and access to machinery, and as such is still relatively unknown outside of specific research areas, such as connectomics. The largest limitation to the technique currently is the data analysis. The size and amount of data produced has increased greatly as the technique improves but the segmentation and analysis still rely on user input and the automated methods are not routinely available for novices. That being said there are still examples of large amounts of data being analysed with the aid of citizen science or students, so the daunting nature of the analysis should not limit the majority of experiments. As mentioned previously, all the data collected here has been made available online. Hopefully as the users of SBF-SEM and other 3D-EM techniques grows the amount of data available online to be used by others will increase. The hope for the future is to be able to have a library of segmentation scenarios appropriate to tissues from different animal models.

Overall 3D-EM, the experiments described here have illustrated benefits in using SBF-SEM for the quantitative and qualitative study of neural and muscle tissues. The technique can be applied to a range of biological circumstances to answer a variety of experimental questions. An additional aspect of this project is that all of the data collected has been made available online for further analysis by others or to be used to answer other questions.

## Chapter 5. References

- Abdollahzadeh, A., Belevich, I., Jokitalo, E., Tohka, J. & Sierra, A. 2019. Automated 3d Axonal Morphometry of White Matter. *Sci Rep*, 9, 6084.
- Abmayr, S. M. & Pavlath, G. K. 2012. Myoblast Fusion: Lessons from Flies and Mice. *Development*, 139, 641-56.
- Agbulut, O., Noirez, P., Beaumont, F. & Butler-Browne, G. 2003. Myosin Heavy Chain Isoforms in Postnatal Muscle Development of Mice. *Biology of the Cell*, 95, 399-406.
- Agrawal, S. A., Burgoyne, T., Eblimit, A., Bellingham, J., Parfitt, D. A., Lane, A., Nichols, R., Asomugha, C., Hayes, M. J., Munro, P. M., Xu, M., Wang, K., Futter, C. E., Li, Y., Chen, R. & Cheetham, M. E. 2017. Reep6 Deficiency Leads to Retinal Degeneration through Disruption of Er Homeostasis and Protein Trafficking. *Hum Mol Genet*, 26, 2667-2677.
- Allen, D. L., Monke, S. R., Talmadge, R. J., Roy, R. R. & Edgerton, V. R. 1995. Plasticity of Myonuclear Number in Hypertrophied and Atrophied Mammalian Skeletal Muscle Fibers. *J Appl Physiol* (1985), 78, 1969-76.
- Allen, D. L., Roy, R. R. & Edgerton, V. R. 1999. Myonuclear Domains in Muscle Adaptation and Disease. *Muscle Nerve*.
- Alvarez, J., Saudino, G., Musteata, V., Madhavan, P., Genovese, A., Behzad, A. R., Sougrat, R., Boi, C., Peinemann, K. V. & Nunes, S. P. 2019. 3d Analysis of Ordered Porous Polymeric Particles Using Complementary Electron Microscopy Methods. *Sci Rep*, 9, 13987.
- Anderson, E. J. & Neufer, P. D. 2006. Type II Skeletal Myofibers Possess Unique Properties That Potentiate Mitochondrial H<sub>2</sub>O<sub>2</sub> Generation. *Am J Physiol Cell Physiol*, 290, C844-51.
- Andersson-Cedergren, E. 1959. Ultrastructure of Motor End Plate and Sarcoplasmic Components of Mouse Skeletal Muscle Fiber as Revealed by Three-Dimensional Reconstructions from Serial Sections. *Journal of Ultrastructure Research*, 2, 5-191.
- Andres, B., Koethe, U., Kroeger, T., Helmstaedter, M., Briggman, K. L., Denk, W. & Hamprecht, F. A. 2012. 3d Segmentation of Sbfsem Images of Neuropil by a Graphical Model over Supervoxel Boundaries. *Med Image Anal*, 16, 796-805.
- Anttonen, T., Belevich, I., Kirjavainen, A., Laos, M., Brakebusch, C., Jokitalo, E. & Pirvola, U. 2014. How to Bury the Dead: Elimination of Apoptotic Hair Cells from the Hearing Organ of the Mouse. *J Assoc Res Otolaryngol*, 15, 975-92.
- Anttonen, T., Kirjavainen, A., Belevich, I., Laos, M., Richardson, W. D., Jokitalo, E., Brakebusch, C. & Pirvola, U. 2012. Cdc42-Dependent Structural Development of Auditory Supporting Cells Is Required for Wound Healing at Adulthood. *Sci Rep*, 2, 978.
- Appleby, T. R. & Manookin, M. B. 2020. Selectivity to Approaching Motion in Retinal Inputs to the Dorsal Visual Pathway. *eLife*, 9, e51144.
- Arbanas, J., Klasan, G. S., Nikolic, M., Jerkovic, R., Miljanovic, I. & Malnar, D. 2009. Fibre Type Composition of the Human Psoas Major Muscle with Regard to the Level of Its Origin. *J Anat*, 215, 636-41.
- Arkill, K. P., Qvortrup, K., Starborg, T., Mantell, J. M., Knupp, C., Michel, C. C., Harper, S. J., Salmon, A. H., Squire, J. M., Bates, D. O. & Neal, C. R. 2014. Resolution of the Three Dimensional Structure of Components of the Glomerular Filtration Barrier. *BMC Nephrol*, 15, 24.
- Armer, H. E., Mariggi, G., Png, K. M., Genoud, C., Monteith, A. G., Bushby, A. J., Gerhardt, H. & Collinson, L. M. 2009. Imaging Transient Blood Vessel Fusion

- Events in Zebrafish by Correlative Volume Electron Microscopy. *PLoS One*, 4, e7716.
- Attiger, J., Boos, A. & Klisch, K. 2018. Morphological Characterization of Basally Located Uninucleate Trophoblast Cells as Precursors of Bovine Binucleate Trophoblast Giant Cells. *Cells Tissues Organs*, 205, 151-163.
- Babai, F., Musevi-Aghdam, J., Schurch, W., Royal, A. & Gabbiani, G. 1990. Coexpression of A-Sarcomeric Actin, A-Smooth Muscle Actin and Desmin During Myogenesis in Rat and Mouse Embryos I. Skeletal Muscle. *Differentiation*, 44, 132-142.
- Bagust, J., Lewis, D. M. & Lucks, J. C. 1974. Post-Tetanic Effects in Motor Units of Fast and Slow Twitch Muscle of the Cat. *J Physiol*, 237, 115-121.
- Bakeeva, L. E., Chentsov, Y. S. & Skulachev, V. P. 1978. Mitochondrial Framework (Reticulum Mitochondriale) in Rat Diaphragm Muscle. *Biochim Biophys Acta*, 501, 349-369.
- Barnard, R., Edgerton, V., Furukawa, T. & Peter, J. 1971. Histochemical, Biochemical, and Contractile Properties of Red, White, and Intermediate Fibers. *American Journal of Physiology-Legacy Content*, 220, 410-414.
- Bartlett, K. & Eaton, S. 2004. Mitochondrial Beta-Oxidation. *Eur J Biochem*, 271, 462-9.
- Baughman, J. M., Perocchi, F., Girgis, H. S., Plovanich, M., Belcher-Timme, C. A., Sancak, Y., Bao, X. R., Strittmatter, L., Goldberger, O., Bogorad, R. L., Koteliensky, V. & Mootha, V. K. 2011. Integrative Genomics Identifies Mcu as an Essential Component of the Mitochondrial Calcium Uniporter. *Nature*, 476, 341-5.
- Beier, T., Pape, C., Rahaman, N., Prange, T., Berg, S., Bock, D. D., Cardona, A., Knott, G. W., Plaza, S. M., Scheffer, L. K., Koethe, U., Kreshuk, A. & Hamprecht, F. A. 2017. Multicut Brings Automated Neurite Segmentation Closer to Human Performance. *Nat Methods*, 14, 101-102.
- Belevich, I., Joensuu, M., Kumar, D., Vihinen, H. & Jokitalo, E. 2016. Microscopy Image Browser: A Platform for Segmentation and Analysis of Multidimensional Datasets. *PLoS Biol*, 14, e1002340.
- Bellesi, M., De Vivo, L., Chini, M., Gilli, F., Tononi, G. & Cirelli, C. 2017. Sleep Loss Promotes Astrocytic Phagocytosis and Microglial Activation in Mouse Cerebral Cortex. *J Neurosci*, 37, 5263-5273.
- Bellesi, M., De Vivo, L., Tononi, G. & Cirelli, C. 2015. Effects of Sleep and Wake on Astrocytes: Clues from Molecular and Ultrastructural Studies. *BMC Biol*, 13, 66.
- Berman, S. B., Pineda, F. J. & Hardwick, J. M. 2008. Mitochondrial Fission and Fusion Dynamics: The Long and Short of It. *Cell Death Differ*, 15, 1147-52.
- Berning, M., Boergens, K. M. & Helmstaedter, M. 2015. Segem: Efficient Image Analysis for High-Resolution Connectomics. *Neuron*, 87, 1193-1206.
- Biazik, J., Vihinen, H., Anwar, T., Jokitalo, E. & Eskelinen, E. L. 2015a. The Versatile Electron Microscope: An Ultrastructural Overview of Autophagy. *Methods*, 75, 44-53.
- Biazik, J., Ylä-Anttila, P., Vihinen, H., Jokitalo, E. & Eskelinen, E. L. 2015b. Ultrastructural Relationship of the Phagophore with Surrounding Organelles. *Autophagy*, 11, 439-51.
- Bizeau, M. E., Willis, W. T. & Hazel, J. R. 1998. Differential Responses to Endurance Training in Subsarcolemmal and Intermyoibrillar Mitochondria. *American Journal of Physiology*

- Bleck, C. K. E., Kim, Y., Willingham, T. B. & Glancy, B. 2018. Subcellular Connectomic Analyses of Energy Networks in Striated Muscle. *Nature Communications*, 9, 5111.
- Bleckert, A., Zhang, C., Turner, M. H., Koren, D., Berson, D. M., Park, S. J. H., Demb, J. B., Rieke, F., Wei, W. & Wong, R. O. 2018. Gaba Release Selectively Regulates Synapse Development at Distinct Inputs on Direction-Selective Retinal Ganglion Cells. *Proceedings of the National Academy of Sciences*, 201803490.
- Blumer, C., Vivien, C., Genoud, C., Perez-Alvarez, A., Wiegert, J. S., Vetter, T. & Oertner, T. G. 2015. Automated Analysis of Spine Dynamics on Live Ca1 Pyramidal Cells. *Med Image Anal*, 19, 87-97.
- Boergens, K. M., Berning, M., Bocklisch, T., Bräunlein, D., Drawitsch, F., Frohnhofen, J., Herold, T., Otto, P., Rzepka, N., Werkmeister, T., Werner, D., Wiese, G., Wissler, H. & Helmstaedter, M. 2017. Webknossos: Efficient Online 3d Data Annotation for Connectomics. *Nature Methods*, 14, 691-694.
- Boergens, K. M., Kapfer, C., Helmstaedter, M., Denk, W. & Borst, A. 2018. Full Reconstruction of Large Lobula Plate Tangential Cells in Drosophila from a 3d Em Dataset. *PLOS ONE*, 13, e0207828.
- Bohórquez, D., Haque, F., Medicetty, S. & Liddle, R. A. 2015. Correlative Confocal and 3d Electron Microscopy of a Specific Sensory Cell. *J Vis Exp*, e52918.
- Bohórquez, D. V., Samsa, L. A., Roholt, A., Medicetty, S., Chandra, R. & Liddle, R. A. 2014. An Enteroendocrine Cell-Enteric Glia Connection Revealed by 3d Electron Microscopy. *PLoS One*, 9, e89881.
- Bolasco, G., Weinhard, L., Boissonnet, T., Neujahr, R. & Gross, C. T. 2018. Three-Dimensional Nanostructure of an Intact Microglia Cell. *Front Neuroanat*, 12, 105.
- Bone, C. R. & Starr, D. A. 2016. Nuclear Migration Events Throughout Development. *J Cell Sci*, 129, 1951-61.
- Booth, D. G., Beckett, A. J., Molina, O., Samejima, I., Masumoto, H., Kouprina, N., Larionov, V., Prior, I. A. & Earnshaw, W. C. 2016. 3d-Clem Reveals That a Major Portion of Mitotic Chromosomes Is Not Chromatin. *Mol Cell*, 64, 790-802.
- Booth, D. G., Beckett, A. J., Prior, I. A. & Meijer, D. 2019. Superclem: An Accessible Correlative Light and Electron Microscopy Approach for Investigation of Neurons and Glia in Vitro. *Biol Open*, 8.
- Borrett, S. & Hughes, L. 2016. Reporting Methods for Processing and Analysis of Data from Serial Block Face Scanning Electron Microscopy. *J Microsc*, 263, 3-9.
- Bottinelli, R., Betto, R., Schiaffino, S. & Reggiani, C. 1994. Maximum Shortening Velocity and Coexistence of Myosin Heavy Chain Isoforms in Single Skinned Fast Fibres of Rat Skeletal Muscle. *Journal of Muscle Research and Cell Motility*, 15.
- Bouwer, J. C., Deerinck, T. J., Bushong, E., Astakhov, V., Ramachandra, R., Peltier, S. T. & Ellisman, M. H. 2017. Deceleration of Probe Beam by Stage Bias Potential Improves Resolution of Serial Block-Face Scanning Electron Microscopic Images. *Advanced Structural and Chemical Imaging*, 2.
- Brama, E., Peddie, C. J., Wilkes, G., Gu, Y., Collinson, L. M. & Jones, M. L. 2016. Ultralm and Minilm: Locator Tools for Smart Tracking of Fluorescent Cells in Correlative Light and Electron Microscopy. *Wellcome Open Res*, 1, 26.
- Bråten, T. 1978. High Resolution Scanning Electron Microscopy in Biology: Artefacts Caused by the Nature and Mode of Application of the Coating Material. *Journal of Microscopy*, 113, 53-59.

- Breidenbach, A. P., Aschbacher-Smith, L., Lu, Y., Dymont, N. A., Liu, C. F., Liu, H., Wylie, C., Rao, M., Shearn, J. T., Rowe, D. W., Kadler, K. E., Jiang, R. & Butler, D. L. 2015. Ablating Hedgehog Signaling in Tenocytes During Development Impairs Biomechanics and Matrix Organization of the Adult Murine Patellar Tendon Enthesis. *J Orthop Res*, 33, 1142-51.
- Briggman, K. L., Helmstaedter, M. & Denk, W. 2011. Wiring Specificity in the Direction-Selectivity Circuit of the Retina. *Nature*, 471, 183-8.
- Bruusgaard, J. C., Liestøl, K., Ekmark, M., Kollstad, K. & Gundersen, K. 2003. Number and Spatial Distribution of Nuclei in the Muscle Fibres of Normal Mice Studied in Vivo. *J Physiol*, 551, 467-78.
- Bruusgaard, J. C., Liestøl, K. & Gundersen, K. 2006. Distribution of Myonuclei and Microtubules in Live Muscle Fibers of Young, Middle-Aged, and Old Mice. *J Appl Physiol (1985)*, 100, 2024-30.
- Buchacker, T., Mühlfeld, C., Wrede, C., Wagner, W. L., Beare, R., McCormick, M. & Grothausmann, R. 2019. Assessment of the Alveolar Capillary Network in the Postnatal Mouse Lung in 3d Using Serial Block-Face Scanning Electron Microscopy. *Front Physiol*, 10, 1357.
- Buckingham, M., Bajard, L., Chang, T., Daubas, P., Hadchouel, J., Meilhac, S., Montarras, D., Rocancourt, D. & Relaix, F. 2003. The Formation of Skeletal Muscle: From Somite to Limb. *J Anat*, 202, 59-68.
- Burke, R. E., Levine, D. N., Zajac Iii, F. E., Tsairis, P. & Engel, W. K. 1971. Mammalian Motor Units: Physiological-Histochemical Correlation in Three Types in Cat Gastrocnemius. *Science*, 174.
- Burry, R. W., Vandr , D. D. & Hayes, D. M. 1992. Silver Enhancement of Gold Antibody Probes in Pre-Embedding Electron Microscopic Immunocytochemistry. 40, 1849-1856.
- Bushong, E. A., Johnson, D. D., Kim, K.-Y., Terada, M., Hatori, M., Peltier, S. T., Panda, S., Merkle, A. & Ellisman, M. H. 2014. X-Ray Microscopy as an Approach to Increasing Accuracy and Efficiency of Serial Block-Face Imaging for Correlated Light and Electron Microscopy of Biological Specimens. *Microscopy and Microanalysis*, 21, 231-238.
- B sse, S., H rnschemeyer, T. & Fischer, C. 2016. Three-Dimensional Reconstruction on Cell Level: Case Study Elucidates the Ultrastructure of the Spinning Apparatus of Embia Sp. (Insecta: Embioptera). *R Soc Open Sci*, 3, 160563.
- Butler-Browne, G. & Whalen, R. G. 1984. Myosin Isozyme Transitions Occurring During the Postnatal Development of the Rat Soleus Muscle. *Dev Biol*.
- Cabez n, I., Aug , E., Bosch, M., Beckett, A. J., Prior, I. A., Pelegr , C. & Vilaplana, J. 2017. Serial Block-Face Scanning Electron Microscopy Applied to Study the Trafficking of 8d3-Coated Gold Nanoparticles at the Blood-Brain Barrier. *Histochem Cell Biol*, 148, 3-12.
- Cadot, B., Gache, V. & Gomes, E. R. 2015. Moving and Positioning the Nucleus in Skeletal Muscle - One Step at a Time. *Nucleus*, 6, 373-81.
- Cadot, B., Gache, V., Vasyutina, E., Falcone, S., Birchmeier, C. & Gomes, E. R. 2012. Nuclear Movement During Myotube Formation Is Microtubule and Dynein Dependent and Is Regulated by Cdc42, Par6 and Par3. *EMBO Rep*, 13, 741-9.
- Cali, C., Agus, M., Kare, K., Boges, D. J., Lehvaslaiho, H., Hadwiger, M. & Magistretti, P. J. 2019. 3d Cellular Reconstruction of Cortical Glia and Parenchymal Morphometric Analysis from Serial Block-Face Electron Microscopy of Juvenile Rat. *Prog Neurobiol*, 101696.

- Capers, C. R. 1960. Multinucleation of Skeletal Muscle in Vitro. *J Biophysic. and Biochem. Cytol.*, 7.
- Cardona, A., Saalfeld, S., Schindelin, J., Arganda-Carreras, I., Preibisch, S., Longair, M., Tomancak, P., Hartenstein, V. & Douglas, R. J. 2012. Trakem2 Software for Neural Circuit Reconstruction. *PLoS One*, 7, e38011.
- Cattini, P. A. & Davies, H. G. 1983. Kinetics of Lead Citrate Staining of Thin Sections for Electron Microscopy. *Stain Technology*, 58, 29-40.
- Cattini, P. A. & Davies, H. G. 1984. Observations on the Kinetics of Uranyl Acetate and Phosphotungstic Acid Staining of Chromatin in Thin Sections for Electron Microscopy. *Stain Technology*, 59, 291-304.
- Cetina, K., Buenaposada, J. M. & Baumela, L. 2018. Multi-Class Segmentation of Neuronal Structures in Electron Microscopy Images. *BMC Bioinformatics*, 19.
- Chai, H., Diaz-Castro, B., Shigetomi, E., Monte, E., Ochteau, J. C., Yu, X., Cohn, W., Rajendran, P. S., Vondriska, T. M., Whitelegge, J. P., Coppola, G. & Khakh, B. S. 2017. Neural Circuit-Specialized Astrocytes: Transcriptomic, Proteomic, Morphological, and Functional Evidence. *Neuron*, 95, 531-549 e9.
- Chapman, M. A., Zhang, J., Banerjee, I., Guo, L. T., Zhang, Z., Shelton, G. D., Ouyang, K., Lieber, R. L. & Chen, J. 2014. Disruption of Both Nesprin 1 and Desmin Results in Nuclear Anchorage Defects and Fibrosis in Skeletal Muscle. *Hum Mol Genet*, 23, 5879-92.
- Charles, J. P., Cappellari, O., Spence, A. J., Hutchinson, J. R. & Wells, D. J. 2016. Musculoskeletal Geometry, Muscle Architecture and Functional Specialisations of the Mouse Hindlimb. *PLoS One*, 11, e0147669.
- Chavan, V., Willis, J., Walker, S. K., Clark, H. R., Liu, X., Fox, M. A., Srivastava, S. & Mukherjee, K. 2015. Central Presynaptic Terminals Are Enriched in Atp but the Majority Lack Mitochondria. *PLoS One*, 10, e0125185.
- Cheek, D. 1985. The Control of Cell Mass and Replication. The DNA Unit - a Personal 20-Year Study. *Early Human Development*, 12, 211-239.
- Cheek, D. B., Holt, A. B., Hill, D. E. & Talbert, J. L. 1971. Skeletal Muscle Cell Mass and Growth: The Concept of the Deoxyribonucleic Acid Unit. *Pediatric Research*, 5, 312.
- Chen, B., Guizar-Sicairos, M., Xiong, G., Shemilt, L., Diaz, A., Nutter, J., Burdet, N., Huo, S., Mancuso, J., Monteith, A., Vergeer, F., Burgess, A. & Robinson, I. 2013. Three-Dimensional Structure Analysis and Percolation Properties of a Barrier Marine Coating. *Sci Rep*, 3, 1177.
- Chen, B., Yusuf, M., Hashimoto, T., Estandarte, A. K., Thompson, G. & Robinson, I. 2017. Three-Dimensional Positioning and Structure of Chromosomes in a Human Prophase Nucleus. *Sci Adv*, 3, e1602231.
- Chklovskii, D. B., Vitaladevuni, S. & Scheffer, L. K. 2010. Semi-Automated Reconstruction of Neural Circuits Using Electron Microscopy. *Current Opinion in Neurobiology*, 20, 667-675.
- Chuang, J. Z., Hsu, Y. C. & Sung, C. H. 2015. Ultrastructural Visualization of Trans-Ciliary Rhodopsin Cargoes in Mammalian Rods. *Cilia*, 4, 4.
- Chung, G. H. C., Domart, M.-C., Peddie, C., Mantell, J., Mclaverty, K., Arabiotorre, A., Hodgson, L., Byrne, R. D., Verkade, P., Arkill, K., Collinson, L. M. & Larijani, B. 2018. Acute Depletion of Diacylglycerol from the Cis-Golgi Affects Localized Nuclear Envelope Morphology During Mitosis. *Journal of Lipid Research*, 59, 1402-1413.
- Chung, K. F., Seiffert, J., Chen, S., Theodorou, I. G., Goode, A. E., Leo, B. F., Mcgilvery, C. M., Hussain, F., Wiegman, C., Rossios, C., Zhu, J., Gong, J., Tariq, F., Yufit, V., Monteith, A. J., Hashimoto, T., Skepper, J. N., Ryan, M. P., Zhang, J., Tetley, T. D. & Porter, A. E. 2017. Inactivation, Clearance, and



- Functional Effects of Lung-Instilled Short and Long Silver Nanowires in Rats. *ACS Nano*, 11, 2652-2664.
- Clarke, N. I. & Royle, S. J. 2018. Chapter 2 - Correlating Light Microscopy with Serial Block Face Scanning Electron Microscopy to Study Mitotic Spindle Architecture. In: MAIATO, H. & SCHUH, M. (eds.) *Methods in Cell Biology*. Academic Press.
- Cocks, E., Taggart, M., Rind, F. C. & White, K. 2018. A Guide to Analysis and Reconstruction of Serial Block Face Scanning Electron Microscopy Data. *J Microsc*, 270, 217-234.
- Collin, C., Hauser, F., De Valdivia, E. G., Li, S., Reisenberger, J., Carlsen, E. M. M., Khan, Z., Hansen, N. Ø., Puhm, F., Søndergaard, L., Niemiec, J., Heninger, M., Ren, G. R. & Grimmlikhuijzen, C. J. P. 2013. Two Types of Muscarinic Acetylcholine Receptors in Drosophila and Other Arthropods. *Cellular and Molecular Life Sciences*, 70, 3231-3242.
- Colman, M. A., Pinali, C., Trafford, A. W., Zhang, H. & Kitmitto, A. 2017. A Computational Model of Spatio-Temporal Cardiac Intracellular Calcium Handling with Realistic Structure and Spatial Flux Distribution from Sarcoplasmic Reticulum and T-Tubule Reconstructions. *PLoS Comput Biol*, 13, e1005714.
- Condon, K., Silberstein, L., Blau, H. M. & Thompson, W. J. 1990a. Development of Muscle Fiber Types in the Prenatal Rat Hindlimb. *Dev Biol*, 138, 256-274.
- Condon, K., Silberstein, L., Blau, H. M. & Thompson, W. J. 1990b. Differentiation of Fiber Types in Aneural Musculature of the Prenatal Rat Hindlimb. *Dev Biol*, 138, 275-295.
- Courson, J. A., Smith, I., Do, T., Landry, P. T., Hargrave, A., Behzad, A. R., Hanlon, S. D., Rumbaut, R. E., Smith, C. W. & Burns, A. R. 2019. Serial Block-Face Scanning Electron Microscopy Reveals Neuronal-Epithelial Cell Fusion in the Mouse Cornea. *PLoS One*, 14, e0224434.
- Crescenzo, R., Bianco, F., Mazzoli, A., Giacco, A., Liverini, G. & Lossa, S. 2014. Alterations in Proton Leak, Oxidative Status and Uncoupling Protein 3 Content in Skeletal Muscle Subsarcolemmal and Intermysofibrillar Mitochondria in Old Rats. *BMC Geriatrics*, 14.
- D'albis, A., Chanoine, C., Janmot, C., Mira, J.-C. & Couteaux, R. 1990. Muscle-Specific Response to Thyroid Hormone of Myosin Isoform Transitions During Rat Postnatal Development. *European Journal of Biochemistry*, 193.
- D'albis, A., Couteaux, R., Janmot, C. & Roulet, A. 1989. Specific Programs of Myosin Expression in the Postnatal Development of Rat Muscle. *European Journal of Biochemistry*, 183.
- D'alessandro, M., Hnia, K., Gache, V., Koch, C., Gavriilidis, C., Rodriguez, D., Nicot, A. S., Romero, N. B., Schwab, Y., Gomes, E., Labouesse, M. & Laporte, J. 2015. Amphiphysin 2 Orchestrates Nucleus Positioning and Shape by Linking the Nuclear Envelope to the Actin and Microtubule Cytoskeleton. *Dev Cell*, 35, 186-98.
- Dahl, R., Larsen, S., Dohlmann, T. L., Qvortrup, K., Helge, J. W., Dela, F. & Prats, C. 2015. Three-Dimensional Reconstruction of the Human Skeletal Muscle Mitochondrial Network as a Tool to Assess Mitochondrial Content and Structural Organization. *Acta Physiol (Oxf)*, 213, 145-55.
- Daum, J. M., Keles, O., Holwerda, S. J., Kohler, H., Rijli, F. M., Stadler, M. & Roska, B. 2017. The Formation of the Light-Sensing Compartment of Cone Photoreceptors Coincides with a Transcriptional Switch. *Elife*, 6.

- De Stefani, D., Raffaello, A., Teardo, E., Szabò, I. & Rizzuto, R. 2011. A Forty-Kilodalton Protein of the Inner Membrane Is the Mitochondrial Calcium Uniporter. *Nature*, 476, 336-40.
- De Vivo, L., Nagai, H., De Wispelaere, N., Spano, G. M., Marshall, W., Bellesi, M., Nemec, K. M., Schiereck, S. S., Nagai, M., Tononi, G. & Cirelli, C. 2019. Evidence for Sleep-Dependent Synaptic Renormalization in Mouse Pups. *Sleep*, 42.
- Deerinck, T. J., Bushong, E., Thor, A. & Ellisman, M. 2010. *Ncmir Methods for 3d Em: A New Protocol for Preparation of Biological Specimens for Serial Block Face Scanning Electron Microscopy*.
- Deerinck, T. J., Shone, T. M., Bushong, E. A., Ramachandra, R., Peltier, S. T. & Ellisman, M. H. 2018. High-Performance Serial Block-Face Sem of Nonconductive Biological Samples Enabled by Focal Gas Injection-Based Charge Compensation. *J Microsc*, 270, 142-149.
- Denardi, C., Ausoni, S., Moretti, P., Gorza, L., Velleca, M., Buckingham, M. & Schiaffino, S. 1993. Type 2x-Myosin Heavy Chain Is Coded by a Muscle Fiber Type-Specific and Developmentally Regulated Gene. *Journal of Cell Biology*, 123.
- Denk, W. & Horstmann, H. 2004. Serial Block-Face Scanning Electron Microscopy to Reconstruct Three-Dimensional Tissue Nanostructure. *PLoS Biol*, 2, e329.
- Dettmer, J., Ursache, R., Campilho, A., Miyashima, S., Belevich, I., O'regan, S., Mullendore, D. L., Yadav, S. R., Lanz, C., Beverina, L., Papagni, A., Schneeberger, K., Weigel, D., Stierhof, Y. D., Moritz, T., Knoblauch, M., Jokitalo, E. & Helariutta, Y. 2014. Choline Transporter-Like1 Is Required for Sieve Plate Development to Mediate Long-Distance Cell-to-Cell Communication. *Nat Commun*, 5, 4276.
- Ding, H., Smith, R. G., Poleg-Polsky, A., Diamond, J. S. & Briggman, K. L. 2016. Species-Specific Wiring for Direction Selectivity in the Mammalian Retina. *Nature*, 535, 105-110.
- Dorkenwald, S., Schubert, P. J., Killinger, M. F., Urban, G., Mikula, S., Svara, F. & Kornfeld, J. 2017. Automated Synaptic Connectivity Inference for Volume Electron Microscopy. *Nat Methods*, 14, 435-442.
- Dow, E., Siletti, K. & Hudspeth, A. J. 2015. Cellular Projections from Sensory Hair Cells Form Polarity-Specific Scaffolds During Synaptogenesis. *Genes Dev*, 29, 1087-1094.
- Draper, M. H. & Hodge, A. J. 1949. Studies on Muscle with the Electron Microscope. *Australian Journal of Experimental Biology and Medical Science*, 27, 465-504.
- Drawitsch, F., Karimi, A., Boergens, K. M. & Helmstaedter, M. 2018. Fluoem, Virtual Labeling of Axons in Three-Dimensional Electron Microscopy Data for Long-Range Connectomics. *Elife*, 7.
- Duchen, M. R. 1992. Ca<sup>2+</sup>-Dependent Changes in the Mitochondrial Energetics in Single Dissociated Mouse Sensory Neurons. *Biochem J*, 283, 41-50.
- Dyson, R. M., Palliser, H. K., Kelleher, M. A., Hirst, J. J. & Wright, I. M. R. 2012. The Guinea Pig as an Animal Model for Studying Perinatal Changes in Microvascular Function. *Pediatric Research*, 71, 20-24.
- Dziasko, M. A., Armer, H. E., Levis, H. J., Shortt, A. J., Tuft, S. & Daniels, J. T. 2014. Localisation of Epithelial Cells Capable of Holoclone Formation in Vitro and Direct Interaction with Stromal Cells in the Native Human Limbal Crypt. *PLoS One*, 9, e94283.
- Eberle, A. L., Mikula, S., Schalek, R., Lichtman, J., Knothe Tate, M. L. & Zeidler, D. 2015. High-Resolution, High-Throughput Imaging with a Multibeam Scanning Electron Microscope. *J Microsc*, 259, 114-20.

- Endo, M. 1964. Entry of a Dye into the Sarcotubular System of Muscle. *Nature*, 202, 1115.
- Endo, M. 1966. Entry of Fluorescent Dyes into the Sarcotubular System of the Frog Muscle. *J Physiol*, 185, 224-238.
- Erdström, L., Hultman, E., Sahlin, K. & Sjöholm, H. 1982. The Contents of High-Energy Phosphates in Different Fibre Types in Skeletal Muscles from Rat, Guinea-Pig and Man. *J Physiol*, 332, 47-58.
- Eustaquio, T., Wang, C., Dugard, C. K., George, N. I., Liu, F., Slikker, W., Paule, M. G., Howard, P. C. & Paredes, A. M. 2018. Electron Microscopy Techniques Employed to Explore Mitochondrial Defects in the Developing Rat Brain Following Ketamine Treatment. *Experimental Cell Research*.
- Falcone, S., Roman, W., Hnia, K., Gache, V., Didier, N., Laine, J., Auradé, F., Marty, I., Nishino, I., Charlet-Berguerand, N., Romero, N. B., Marazzi, G., Sassoon, D., Laporte, J. & Gomes, E. R. 2014. N-Wasp Is Required for Amphiphysin-2/Bin1-Dependent Nuclear Positioning and Triad Organization in Skeletal Muscle and Is Involved in the Pathophysiology of Centronuclear Myopathy. *EMBO Mol Med*, 6, 1455-75.
- Fawcett, D. W. & Bloom, W. 1994. *A Textbook of Histology*, New York, Chapman & Hall.
- Feeney, M., Kittelmann, M., Menassa, R., Hawes, C. & Frigerio, L. 2018. Protein Storage Vacuoles Originate from Remodeled Preexisting Vacuoles in *Arabidopsis thaliana*1[Open]. *Plant Physiology*, 177, 241-254.
- Feierbach, B., Piccinotti, S., Bisher, M., Denk, W. & Enquist, L. W. 2006. Alpha-Herpesvirus Infection Induces the Formation of Nuclear Actin Filaments. *PLoS Pathog*, 2, e85.
- Feng, T., Paterson, B. D., Webb, R. & Johnston, S. D. 2016. Three-Dimensional Reconstruction of Black Tiger Prawn (*Penaeus Monodon*) Spermatozoa Using Serial Block-Face Scanning Electron Microscopy. *J Morphol*, 277, 565-74.
- Fiorotto, M. 2012. The Making of a Muscle. *Biochem (Lond)*, 34, 4-11.
- Fischbach, F., Nedelcu, J., Leopold, P., Zhan, J., Clarner, T., Nellessen, L., Beißel, C., Van Heuvel, Y., Goswami, A., Weis, J., Denecke, B., Schmitz, C., Hochstrasser, T., Nyamoya, S., Victor, M., Beyer, C. & Kipp, M. 2019. Cuprizone-Induced Graded Oligodendrocyte Vulnerability Is Regulated by the Transcription Factor DNA Damage-Inducible Transcript 3. *Glia*, 67, 263-276.
- Fladby, T. & Jansen, J. K. S. 1990. Development of Homogeneous Fast and Slow Motor Units in the Neonatal Mouse Soleus Muscle. *Development*, 109.
- Folker, E. S. & Baylies, M. K. 2013. Nuclear Positioning in Muscle Development and Disease. *Front Physiol*, 4, 363.
- Forte, M., Gold, B. G., Marracci, G., Chaudhary, P., Basso, E., Honsen, D., Yu, X., Fowlkes, J., Rahder, M., Stem, K., Bernardi, P. & Bourdette, D. 2007. Cyclophilin D Inactivation Protects Axons in Experimental Autoimmune Encephalomyelitis, an Animal Model of Multiple Sclerosis. *PNAS*, 104, 7558-7563.
- Fotowat, H. & Gabbiani, F. 2011. Collision Detection as a Model for Sensory-Motor Integration. *Annu Rev Neurosci*, 34, 1-19.
- Franzini-Armstrong, C. & Porter, K. R. 1964. Sarcolemmal Invaginations Constituting the T System in Fish Muscle Fibers *J Cell Biol*, 22, 675-696.
- Fredericksen, M. A., Zhang, Y., Hazen, M. L., Loreto, R. G., Mangold, C. A., Chen, D. Z. & Hughes, D. P. 2017. Three-Dimensional Visualization and a Deep-Learning Model Reveal Complex Fungal Parasite Networks in Behaviorally Manipulated Ants. *Proc Natl Acad Sci U S A*, 114, 12590-12595.

- Friedman, P. L. & Ellisman, M. H. 1981. Enhanced Visualization of Peripheral Nerve and Sensory Receptors in the Scanning Electron Microscope Using Cryofracture and Osmium- Thiocarbohydrazide-Osmium Impregnation. *J Neurocytology*, 10, 111-131.
- Frontera, W. R. & Ochala, J. 2015. Skeletal Muscle: A Brief Review of Structure and Function. *Calcif Tissue Int*, 96, 183-95.
- Fujioka, H., Tandler, B., Haldar, S. M., Jain, M. K. & Hoppel, C. L. 2013. String Mitochondria in Mouse Soleus Muscle. *Microsc Res Tech*, 76, 237-41.
- Funke, J., Tschopp, F. D., Grisaitis, W., Sheridan, A., Singh, C., Saalfeld, S. & Turaga, S. C. 2018. Large Scale Image Segmentation with Structured Loss Based Deep Learning for Connectome Reconstruction. *IEEE Transactions on Pattern Analysis and Machine Intelligence*, 1-1.
- Furness, D. N. & Hackney, C. M. 1986. High-Resolution Scanning-Electron Microscopy of Stereocilia Using the Osmium-Thiocarbohydrazide Coating Technique. *Hearing Research*, 21, 243-249.
- Gabbiani, F., Cohen, I. & Laurent, G. 2005. Time-Dependent Activation of Feed-Forward Inhibition in a Looming-Sensitive Neuron. *J Neurophysiol*, 94, 2150-2161.
- Gabbiani, F., Krapp, H. G., Hatsopoulos, N., Mo, C. H., Koch, C. & Laurent, G. 2004. Multiplication and Stimulus Invariance in a Looming-Sensitive Neuron. *J Physiol Paris*, 98, 19-34.
- Gabbiani, F., Krapp, H. G., Koch, C. & Laurent, G. 2001a. Multiplicative Computation in a Visual Neuron Sensitive to Looming. *Nature*, 420, 320-324.
- Gabbiani, F., Laurent, G., Hatsopoulos, N. & Krapp, H. G. 1999. The Many Ways of Building Collision-Sensitive Neurons. *Trends in Neurosciences*, 22, 437-438.
- Gabbiani, F., Mo, C. H. & Laurent, G. 2001b. Invariance of Angular Threshold Computation in a Wide-Field Looming-Sensitive Neuron. *Journal of Neuroscience*, 21, 314-329.
- Galloway, C. A., Lee, H. & Yoon, Y. 2012. Mitochondrial Morphology-Emerging Role in Bioenergetics. *Free Radic Biol Med*, 53, 2218-28.
- Gambke, B., Lyons, G. E., Haselgrove, J., Kelly, A. M. & Rubinstein, N. A. 1983. Thyroidal and Neural Control of Myosin Transitions During Development of Rat Fast and Slow Muscles. *FEBS J*, 156.
- Gan, W. J., Zavortink, M., Ludick, C., Templin, R., Webb, R., Webb, R., Ma, W., Poronnik, P., Parton, R. G., Gaisano, H. Y., Shewan, A. M. & Thorn, P. 2017. Cell Polarity Defines Three Distinct Domains in Pancreatic Beta-Cells. *J Cell Sci*, 130, 143-151.
- Geissinger, H. D., Vriend, R. A., Meade, L. D., Ackerley, C. A. & Bhatnagar, M. K. 1983. Osmium-Thiocarbohydrazide-Osmium Versus Tannic Acid-Osmium Staining of Skeletal Muscle for Scanning Electron Microscopy and Correlative Microscopy. *Transactions of the American Microscopical Society*, 102, 390-398.
- Genoud, C., Titze, B., Graff-Meyer, A. & Friedrich, R. W. 2018. Fast Homogeneous En Bloc Staining of Large Tissue Samples for Volume Electron Microscopy. *Frontiers in Neuroanatomy*, 12.
- Giacci, M. K., Bartlett, C. A., Huynh, M., Kilburn, M. R., Dunlop, S. A. & Fitzgerald, M. 2018. Three Dimensional Electron Microscopy Reveals Changing Axonal and Myelin Morphology Along Normal and Partially Injured Optic Nerves. *Scientific Reports*, 8.
- Giarmarco, M. M., Cleghorn, W. M., Sloat, S. R., Hurley, J. B. & Brockerhoff, S. E. 2017. Mitochondria Maintain Distinct Ca<sup>2+</sup> Pools in Cone Photoreceptors. *J Neurosci*, 37, 2061-2072.

- Gillies, A. R., Bushong, E. A., Deerinck, T. J., Ellisman, M. H. & Lieber, R. L. 2014. Three-Dimensional Reconstruction of Skeletal Muscle Extracellular Matrix Ultrastructure. *Microsc Microanal*, 20, 1835-40.
- Gillies, A. R., Chapman, M. A., Bushong, E. A., Deerinck, T. J., Ellisman, M. H. & Lieber, R. L. 2017. High Resolution Three-Dimensional Reconstruction of Fibrotic Skeletal Muscle Extracellular Matrix. *J Physiol*, 595, 1159-1171.
- Giuly, R. J., Martone, M. E. & Ellisman, M. H. 2012. Method: Automatic Segmentation of Mitochondria Utilizing Patch Classification, Contour Pair Classification, and Automatically Seeded Level Sets. *BMC Bioinformatics*, 13, 29.
- Gjoni, E., Aguet, C., Sahlender, D. A., Knott, G. & Schneggenburger, R. 2018. Ultrastructural Basis of Strong Unitary Inhibition in a Binaural Neuron. *J Physiol*.
- Glancy, B., Kim, Y., Katti, P. & Willingham, T. B. 2020. The Functional Impact of Mitochondrial Structure across Subcellular Scales. *Front Physiol*, 11, 541040.
- Gluezn, E., Wheeler, R. J., Hughes, L. & Vaughan, S. 2015. Scanning and Three-Dimensional Electron Microscopy Methods for the Study of Trypanosoma Brucei and Leishmania Mexicana Flagella. *Methods Cell Biol*, 127, 509-42.
- Godwin, A. R. F., Starborg, T., Sherratt, M. J., Roseman, A. M. & Baldock, C. 2017. Defining the Hierarchical Organisation of Collagen Vi Microfibrils at Nanometre to Micrometre Length Scales. *Acta Biomater*, 52, 21-32.
- Godwin, A. R. F., Starborg, T., Smith, D. J., Sherratt, M. J., Roseman, A. M. & Baldock, C. 2018. Multiscale Imaging Reveals the Hierarchical Organization of Fibrillin Microfibrils. *Journal of Molecular Biology*, 430, 4142-4155.
- Gokhin, D. S., Ward, S. R., Bremner, S. N. & Lieber, R. L. 2008. Quantitative Analysis of Neonatal Skeletal Muscle Functional Improvement in the Mouse. *J Exp Biol*, 211, 837-43.
- Goldfischer, S., Kress, Y., Coltoff-Schiller, B. & Berman, J. 1981. Primary Fixation in Osmium-Potassium Ferrocyanide: The Staining of Glycogen, Glycoproteins, Elastin, an Intranuclear Reticular Structure, and Intercisternal Trabeculae. *J Histochem Cytochem*, 29, 1105-1111.
- Gollnick, P. D., Sjödin, B., Karlsson, J., Jansson, E. & Saltin, B. 1974. Human Soleus Muscle: A Comparison of Fiber Composition and Enzyme Activities with Other Leg Muscles. *Pflugers Arch*, 348, 247-255.
- Gomes, L. C., Di Benedetto, G. & Scorrano, L. 2011. During Autophagy Mitochondria Elongate, Are Spared from Degradation and Sustain Cell Viability. *Nat Cell Biol*, 13, 589-98.
- Gorza, L. 1990. Identification of a Novel Type 2 Fiber Population in Mammalian Skeletal Muscle by Combined Use of Histochemical Myosin Atpase and Anti-Myosin Monoclonal Antibodies. *Journal of Histochemistry & Cytochemistry*, 38, 257-265.
- Graves, L. P., Hughes, L. C., Irons, S. L., Possee, R. D. & King, L. A. 2019. In Cultured Cells the Baculovirus P10 Protein Forms Two Independent Intracellular Structures That Play Separate Roles in Occlusion Body Maturation and Their Release by Nuclear Disintegration. *PLOS Pathogens*, 15, e1007827.
- Graydon, C. W., Lieberman, E. E., Rho, N., Briggman, K. L., Singer, J. H. & Diamond, J. S. 2018. Synaptic Transfer between Rod and Cone Pathways Mediated by Aii Amacrine Cells in the Mouse Retina. *Current Biology*, 28, 2739-2751.e3.

- Grillo, F. W., Neves, G., Walker, A., Vizcay-Barrena, G., Fleck, R. A., Branco, T. & Burrone, J. 2018. A Distance-Dependent Distribution of Presynaptic Boutons Tunes Frequency-Dependent Dendritic Integration. *Neuron*, 99, 275-282 e3.
- Griparic, L. & Van Der Bliek, A. M. 2001. The Many Shapes of Mitochondrial Membranes. *Traffic*, 2, 235-244.
- Guérin, C. J., Kremer, A., Borghgraef, P. & Lippens, S. 2019. Targeted Studies Using Serial Block Face and Focused Ion Beam Scan Electron Microscopy. *J Vis Exp*.
- Gulati, J. 1976. Force-Velocity Characteristics for Calcium-Activated Mammalian Slow-Twitch and Fast-Twitch Skeletal Fibers from the Guinea Pig. *Proceedings of the National Academy of Sciences of the United States of America*, 73, 4693-4697.
- Gundersen, G. G. & Worman, H. J. 2013. Nuclear Positioning. *Cell*, 152, 1376-89.
- Guth, L. & Samaha, F. J. 1969. Qualitative Differences between Actomyosin ATPase of Slow and Fast Mammalian Muscle. *Experimental Neurology*, 25, 138-152.
- Haehn, D., Hoffer, J., Matejek, B., Suissa-Peleg, A., Al-Awami, A., Kamensky, L., Gonda, F., Meng, E., Zhang, W., Schalek, R., Wilson, A., Parag, T., Beyer, J., Kaynig, V., Jones, T., Tompkin, J., Hadwiger, M., Lichtman, J. & Pfister, H. 2017. Scalable Interactive Visualization for Connectomics. *Informatics*, 4.
- Hainfield, J. F. & Powell, R. D. 2000. New Frontiers in Gold Labeling. *Journal of Histochemistry & Cytochemistry*, 48, 471-480.
- Hall, C. E., Jakus, M. A. & Schmitt, F. O. 1946. An Investigation of Cross Striations and Myosin Filaments in Muscle. *Biological Bulletin*, 90, 32-50.
- Hall, Z. W. & Ralston, E. 1989. Nuclear Domains in Muscle Cells. *Cell*, 59, 771-772.
- Hämäläinen, N. & Pette, D. 1993. The Histochemical Profiles of Fast Fiber Types IId, IId, and IId in Skeletal Muscles of Mouse, Rat, and Rabbit. *Journal of Histochemistry & Cytochemistry*, 41, 733-743.
- Hammer, S., Carrillo, G. L., Govindaiah, G., Monavarfeshani, A., Bircher, J. S., Su, J., Guido, W. & Fox, M. A. 2014. Nuclei-Specific Differences in Nerve Terminal Distribution, Morphology, and Development in Mouse Visual Thalamus. *Neural Development*, 9.
- Hammer, S., Monavarfeshani, A., Lemon, T., Su, J. & Fox, M. A. 2015. Multiple Retinal Axons Converge onto Relay Cells in the Adult Mouse Thalamus. *Cell Rep*, 12, 1575-83.
- Han, B., Newbould, M., Batra, G., Cheesman, E., Craigie, R. J., Mohamed, Z., Rigby, L., Padidela, R., Skae, M., Mironov, A., Starborg, T., Kadler, K. E., Cosgrove, K. E., Banerjee, I. & Dunne, M. J. 2016. Enhanced Islet Cell Nucleomegaly Defines Diffuse Congenital Hyperinsulinism in Infancy but Not Other Forms of the Disease. *Am J Clin Pathol*, 145, 757-68.
- Hanlon, S. D., Behzad, A. R., Sakai, L. Y. & Burns, A. R. 2015. Corneal Stroma Microfibrils. *Exp Eye Res*, 132, 198-207.
- Harris, J. R. 2015. Transmission Electron Microscopy in Molecular Structural Biology: A Historical Survey. *Arch Biochem Biophys*, 581, 3-18.
- Harwood, R., Goodman, E., Gudmundsdottir, M., Huynh, M., Musulin, Q., Song, M. & Barbour, M. M. 2019. Cell and Chloroplast Anatomical Features Are Poorly Estimated from 2d Cross-Sections. *New Phytol*.
- Hashimoto, T., Thompson, G. E., Zhou, X. & Withers, P. J. 2016. 3d Imaging by Serial Block Face Scanning Electron Microscopy for Materials Science Using Ultramicrotomy. *Ultramicroscopy*, 163, 6-18.
- Hatsopoulos, N., Gabbiani, F. & Laurent, G. 1995. Elementary Computation of Object Approach by a Wide-Field Visual Neuron. *Science*, 270, 1000-1003.
- Hayat, M. A. 1981. *Fixation for Electron Microscopy*, New York, Academic Press.

- Hayat, M. A. 1986. Glutaraldehyde: Role in Electron Microscopy. *Micron and Microscopica Acta*, 17, 115-135.
- Hayes, M. J., Burgoyne, T., Wavre-Shapton, S. T., Tolmachova, T., Seabra, M. C. & Futter, C. E. 2019. Remodeling of the Basal Labyrinth of Retinal Pigment Epithelial Cells with Osmotic Challenge, Age, and Disease. *Invest Ophthalmol Vis Sci*, 60, 2515-2524.
- Hayworth, K. J., Morgan, J. L., Schalek, R., Berger, D. R., Hildebrand, D. G. & Lichtman, J. W. 2014. Imaging Atom Ultrathin Section Libraries with Wafermapper: A Multi-Scale Approach to Em Reconstruction of Neural Circuits. *Front Neural Circuits*, 8, 68.
- He, Q., Hsueh, M., Zhang, G., Joy, D. C. & Leapman, R. D. 2018. Biological Serial Block Face Scanning Electron Microscopy at Improved Z-Resolution Based on Monte Carlo Model. *Scientific Reports*, 8.
- Helmstaedter, M., Briggman, K. L. & Denk, W. 2011. High-Accuracy Neurite Reconstruction for High-Throughput Neuroanatomy. *Nat Neurosci*, 14, 1081-8.
- Helmstaedter, M., Briggman, K. L., Turaga, S. C., Jain, V., Seung, H. S. & Denk, W. 2013. Connectomic Reconstruction of the Inner Plexiform Layer in the Mouse Retina. *Nature*, 500, 168-74.
- Herms, A., Bosch, M., Ariotti, N., Reddy, B. J., Fajardo, A., Fernandez-Vidal, A., Alvarez-Guaita, A., Fernandez-Rojo, M. A., Rentero, C., Tebar, F., Enrich, C., Geli, M. I., Parton, R. G., Gross, S. P. & Pol, A. 2013. Cell-to-Cell Heterogeneity in Lipid Droplets Suggests a Mechanism to Reduce Lipotoxicity. *Curr Biol*, 23, 1489-96.
- Hildebrand, D. G. C., Cicconet, M., Torres, R. M., Choi, W., Quan, T. M., Moon, J., Wetzel, A. W., Scott Champion, A., Graham, B. J., Randlett, O., Plummer, G. S., Portugues, R., Bianco, I. H., Saalfeld, S., Baden, A. D., Lillanay, K., Burns, R., Vogelstein, J. T., Schier, A. F., Lee, W. A., Jeong, W. K., Lichtman, J. W. & Engert, F. 2017. Whole-Brain Serial-Section Electron Microscopy in Larval Zebrafish. *Nature*, 545, 345-349.
- Hill, A. V. 1949. The Abrupt Transition from Rest to Activity in Muscle. *Proceedings of the Royal Society of London. Series B - Biological Sciences*, 136, 399.
- Holcomb, P. S., Hoffpauir, B. K., Hoyson, M. C., Jackson, D. R., Deerinck, T. J., Marrs, G. S., Dehoff, M., Wu, J., Ellisman, M. H. & Spirou, G. A. 2013. Synaptic Inputs Compete During Rapid Formation of the Calyx of Held: A New Model System for Neural Development. *J Neurosci*, 33, 12954-69.
- Holloszy, J. O. 1967. Biochemical Adaptations in Muscle. *Journal of Biological Chemistry*, 242, 2278-2282.
- Holloszy, J. O. 2008. Regulation by Exercise of Skeletal Muscle Content of Mitochondria and Glut4. *Journal of Physiology and Pharmacology*, 59, 5-18.
- Hondow, N., Brown, M. R., Starborg, T., Monteith, A. G., Brydson, R., Summers, H. D., Rees, P. & Brown, A. 2016. Quantifying the Cellular Uptake of Semiconductor Quantum Dot Nanoparticles by Analytical Electron Microscopy. *J Microsc*, 261, 167-76.
- Hood, D. A. & Iqbal, S. 2013. Muscle Mitochondrial Ultrastructure: New Insights into Morphological Divergences. *J Appl Physiol* (1985), 114, 159-60.
- Hoover, B., Baena, V., Kaelberer, M. M., Getaneh, F., Chinchilla, S. & Bohórquez, D. V. 2017. The Intestinal Tuft Cell Nanostructure in 3d. *Sci Rep*, 7, 1652.
- Horstmann, H., Körber, C., Sätzler, K., Aydin, D. & Künner, T. 2012. Serial Section Scanning Electron Microscopy (S3em) on Silicon Wafers for Ultra-Structural Volume Imaging of Cells and Tissues. *PLoS One*, 7, e35172.
- Hua, Y., Laserstein, P. & Helmstaedter, M. 2015. Large-Volume En-Bloc Staining for Electron Microscopy-Based Connectomics. *Nat Commun*, 6, 7923.

- Hughes, L., Borrett, S., Towers, K., Starborg, T. & Vaughan, S. 2017. Patterns of Organelle Ontogeny through a Cell Cycle Revealed by Whole-Cell Reconstructions Using 3d Electron Microscopy. *J Cell Sci*, 130, 637-647.
- Hughes, L., Hawes, C., Monteith, S. & Vaughan, S. 2014. Serial Block Face Scanning Electron Microscopy--the Future of Cell Ultrastructure Imaging. *Protoplasma*, 251, 395-401.
- Hughes, L., Towers, K., Starborg, T., Gull, K. & Vaughan, S. 2013. A Cell-Body Groove Housing the New Flagellum Tip Suggests an Adaptation of Cellular Morphogenesis for Parasitism in the Bloodstream Form of Trypanosoma Brucei. *J Cell Sci*, 126, 5748-57.
- Hunter, D. R. & Haworth, R. A. 1979. The Ca<sup>2+</sup>-Induced Membrane Transition in Mitochondria. *Arch Biochem Biophys*, 195, 453-459.
- Hussain, A., Ghosh, S., Kalkhoran, S. B., Hausenloy, D. J., Hanssen, E. & Rajagopal, V. 2018. An Automated Workflow for Segmenting Single Adult Cardiac Cells from Large-Volume Serial Block-Face Scanning Electron Microscopy Data. *J Struct Biol*, 202, 275-285.
- Huxley, A. F. 1974. Muscular Contraction. *J Physiol*, 243, 1-43.
- Huxley, H. E. 1964. Evidence for Continuity between the Central Elements of the Triads and Extracellular Space in Frog Sartorius Muscle. *Nature*, 202, 1067.
- Huxley, H. E. 1967. Recent X-Ray Diffraction and Electron Microscope Studies of Striated Muscle. *J Gen Physiol*, 50.
- Ichimura, K., Kakuta, S., Kawasaki, Y., Miyaki, T., Nonami, T., Miyazaki, N., Nakao, T., Enomoto, S., Arai, S., Koike, M., Murata, K. & Sakai, T. 2017. Morphological Process of Podocyte Development Revealed by Block-Face Scanning Electron Microscopy. *J Cell Sci*, 130, 132-142.
- Ichimura, K., Miyazaki, N., Sadayama, S., Murata, K., Koike, M., Nakamura, K., Ohta, K. & Sakai, T. 2015. Three-Dimensional Architecture of Podocytes Revealed by Block-Face Scanning Electron Microscopy. *Sci Rep*, 5, 8993.
- Iyer, S. R., Shah, S. B., Valencia, A. P., Schneider, M. F., Hernández-Ochoa, E. O., Stains, J. P., Blemker, S. S. & Lovering, R. M. 2017. Altered Nuclear Dynamics in Mdx Myofibers. *J Appl Physiol (1985)*, 122, 470-481.
- Jakob, M., Hoffmann, A., Amodeo, S., Peitsch, C., Zuber, B. & Ochseneiter, T. 2016. Mitochondrial Growth During the Cell Cycle of Trypanosoma Brucei Bloodstream Forms. *Sci Rep*, 6, 36565.
- Jansen, I. M. & Fladby, T. 1990. The Perinatal Reorganization of the Innervation of Skeletal Muscle in Mammals. *Prog Neurobiol*, 34.
- Januszewski, M., Kornfeld, J., Li, P. H., Pope, A., Blakely, T., Lindsey, L., Maitin-Shepard, J., Tyka, M., Denk, W. & Jain, V. 2018. High-Precision Automated Reconstruction of Neurons with Flood-Filling Networks. *Nature Methods*, 15, 605.
- Jesior, J. C. 1989. Use of Low-Angle Diamond Knives Leads to Improved Ultrastructural Preservation of Ultrathin Sections. *Scanning Microscop Suppl*, 3, 147-153.
- Joesch, M., Mankus, D., Yamagata, M., Shahbazi, A., Schalek, R., Suissa-Peleg, A., Meister, M., Lichtman, J. W., Scheirer, W. J. & Sanes, J. R. 2016. Reconstruction of Genetically Identified Neurons Imaged by Serial-Section Electron Microscopy. *Elife*, 5.
- Joesch, M., Schnell, B., Raghu, S. V., Reiff, D. F. & Borst, A. 2010. On and Off Pathways in Drosophila Motion Vision. *Nature*, 468, 300-4.
- Johnson, M. A., Polgar, J., Weightman, D. & Appleton, D. 1973. Data on the Distribution of Fibre Types in Thirty-Six Human Muscles an Autopsy Study. *Journal of Neurological Sciences*, 18, 111-129.



- Jones, P. W. & Gabbiani, F. 2010. Synchronized Neural Input Shapes Stimulus Selectivity in a Collision-Detecting Neuron. *Curr Biol*, 20, 2052-7.
- Jones, P. W. & Gabbiani, F. 2012. Logarithmic Compression of Sensory Signals within the Dendritic Tree of a Collision-Sensitive Neuron. *J Neurosci*, 32, 4923-34.
- Jorstad, A., Nigro, B., Cali, C., Wawrzyniak, M., Fua, P. & Knott, G. 2015. Neuromorph: A Toolset for the Morphometric Analysis and Visualization of 3d Models Derived from Electron Microscopy Image Stacks. *Neuroinformatics*, 13, 83-92.
- Jouaville, L. S., Pinton, P., Bastianutto, C., Rutter, G. A. & Rizzuto, R. 1999. Regulation of Mitochondrial Atp Synthesis by Calcium: Evidence for a Long-Term Metabolic Priming. *PNAS*, 96, 13807-13812.
- Ju, W.-K., Shim, M. S., Kim, K.-Y., Park, T. L., Ahn, S., Edwards, G. & Weinreb, R. N. 2019. Inhibition of Camp/Pka Pathway Protects Optic Nerve Head Astrocytes against Oxidative Stress by Akt/Bax Phosphorylation-mediated Mfn1/2 Oligomerization. *Oxidative Medicine and Cellular Longevity*.
- Judge, S. J. & Rind, F. C. 1997. The Locust Dcmd, a Movement-Detecting Neurone Tightly Tuned to Collision Trajectories. *J Exp Biol*, 200, 2209-2216.
- Jungbluth, H. & Gautel, M. 2014. Pathogenic Mechanisms in Centronuclear Myopathies. *Front Aging Neurosci*, 6, 339.
- Jungbluth, H., Wallgren-Pettersson, C. & Laporte, J. 2008. Centronuclear (Myotubular) Myopathy. *Orphanet J Rare Dis*, 3, 26.
- Jungreuthmayer, C., Steppert, P., Sekot, G., Zankel, A., Reingruber, H., Zanghellini, J. & Jungbauer, A. 2015. The 3d Pore Structure and Fluid Dynamics Simulation of Macroporous Monoliths: High Permeability Due to Alternating Channel Width. *J Chromatogr A*, 1425, 141-9.
- Jurrus, E., Hardy, M., Tasdizen, T., Fletcher, P. T., Koshevoy, P., Chien, C. B., Denk, W. & Whitaker, R. 2009. Axon Tracking in Serial Block-Face Scanning Electron Microscopy. *Med Image Anal*, 13, 180-8.
- Kaiser, G., De Niz, M., Zuber, B., Burda, P. C., Kornmann, B., Heussler, V. T. & Stanway, R. R. 2016. High Resolution Microscopy Reveals an Unusual Architecture of the Plasmodium Berghei Endoplasmic Reticulum. *Mol Microbiol*, 102, 775-791.
- Kaji, T., Kakui, K., Miyazaki, N., Murata, K. & Palmer, A. R. 2016. Mesoscale Morphology at Nanoscale Resolution: Serial Block-Face Scanning Electron Microscopy Reveals Fine 3d Detail of a Novel Silk Spinneret System in a Tube-Building Tanaid Crustacean. *Front Zool*, 13, 14.
- Kalson, N. S., Starborg, T., Lu, Y., Mironov, A., Humphries, S. M., Holmes, D. F. & Kadler, K. E. 2013. Nonmuscle Myosin II Powered Transport of Newly Formed Collagen Fibrils at the Plasma Membrane. *Proc Natl Acad Sci U S A*, 110, E4743-52.
- Karnovsky, M. J. 1961. Simple Methods for "Staining with Lead" at High Ph in Electron Microscopy. *J Biophysic. and Biochem. Cytol.*, 11, 729-732.
- Karthik, S., Djukic, T., Kim, J.-D., Zuber, B., Makanya, A., Odriozola, A., Hlushchuk, R., Filipovic, N., Jin, S. W. & Djonov, V. 2018. Synergistic Interaction of Sprouting and Intussusceptive Angiogenesis During Zebrafish Caudal Vein Plexus Development. *Scientific Reports*, 8.
- Kasthuri, N., Hayworth, K. J., Berger, D. R., Schalek, R. L., Conchello, J. A., Knowles-Barley, S., Lee, D., Vazquez-Reina, A., Kaynig, V., Jones, T. R., Roberts, M., Morgan, J. L., Tapia, J. C., Seung, H. S., Roncal, W. G., Vogelstein, J. T., Burns, R., Sussman, D. L., Priebe, C. E., Pfister, H. &

- Lichtman, J. W. 2015. Saturated Reconstruction of a Volume of Neocortex. *Cell*, 162, 648-61.
- Kayar, S. R., Hoppeler, H., Mermoud, L. & E.R., W. 1988. Mitochondrial Size and Shape in Equine Skeletal Muscle: A Three-Dimensional Reconstruction Study. *The Anatomical Record*, 222, 333-339.
- Kaynig, V., Vazquez-Reina, A., Knowles-Barley, S., Roberts, M., Jones, T. R., Kasthuri, N., Miller, E., Lichtman, J. & Pfister, H. 2015. Large-Scale Automatic Reconstruction of Neuronal Processes from Electron Microscopy Images. *Med Image Anal*, 22, 77-88.
- Keefe, A. C., Lawson, J. A., Flygare, S. D., Fox, Z. D., Colasanto, M. P., Mathew, S. J., Yandell, M. & Kardon, G. 2015. Muscle Stem Cells Contribute to Myofibres in Sedentary Adult Mice. *Nat Commun*, 6, 7087.
- Keller, A., Ott, M.-O., Lamandé, N., Lucas, M., Gros, F., Buckingham, M. & Lazar, M. 1992. Activation of the Gene Encoding the Glycolytic Enzyme/3-Enolase During Early Myogenesis Precedes an Increased Expression During fetal Muscle Development. *Mech Dev*, 38, 41-54.
- Kerov, V., Laird, J. G., Joiner, M.-L., Knecht, S., Soh, D., Hagen, J., Gardner, S. H., Gutierrez, W., Yoshimatsu, T., Bhattarai, S., Puthussery, T., Artemyev, N. O., Drack, A. V., Wong, R. O., Baker, S. A. & Lee, A. 2018. A2δ-4 Is Required for the Molecular and Structural Organization of Rod and Cone Photoreceptor Synapses. *The Journal of Neuroscience*, 38, 6145-6160.
- Khadangi, A., Hanssen, E. & Rajagopal, V. 2019. Automated Segmentation of Cardiomyocyte Z-Disks from High-Throughput Scanning Electron Microscopy Data. *BMC Med Inform Decis Mak*, 19, 272.
- Killmann, F., Gras, H. & Schürmann, F. W. 1999. Types, Numbers and Distribution of Synapses on the Dendritic Tree of an Identified Visual Interneuron in the Brain of the Locust. *Cell Tissue Res.*, 296, 645-655.
- Kim, I., Rodriguez-Enriquez, S. & Lemasters, J. J. 2007. Selective Degradation of Mitochondria by Mitophagy. *Arch Biochem Biophys*, 462, 245-53.
- Kirichok, Y., Krapivinsky, G. & Clapham, D. E. 2004. The Mitochondrial Calcium Uniporter Is a Highly Selective Ion Channel. *Nature*, 427.
- Kittlmann, M., Hawes, C. & Hughes, L. 2016. Serial Block Face Scanning Electron Microscopy and the Reconstruction of Plant Cell Membrane Systems. *J Microsc*, 263, 200-11.
- Kleesattel, D., Crish, S. D. & Inman, D. M. 2015. Decreased Energy Capacity and Increased Autophagic Activity in Optic Nerve Axons with Defective Anterograde Transport. *Invest Ophthalmol Vis Sci*, 56, 8215-27.
- Knoll, M. & Ruska, E. 1932. Das Elektronenmikroskop. *EZ Physik*, 78, 318-339.
- Knott, G., Marchman, H., Wall, D. & Lich, B. 2008. Serial Section Scanning Electron Microscopy of Adult Brain Tissue Using Focused Ion Beam Milling. *J Neurosci*, 28, 2959-64.
- Knott, G., Rosset, S. & Cantoni, M. 2011. Focussed Ion Beam Milling and Scanning Electron Microscopy of Brain Tissue. *J Vis Exp*, e2588.
- Kornfeld, J., Benezra, S. E., Narayanan, R. T., Svara, F., Egger, R., Oberlaender, M., Denk, W. & Long, M. A. 2017. Em Connectomics Reveals Axonal Target Variation in a Sequence-Generating Network. *Elife*, 6.
- Koudouna, E., Young, R. D., Overby, D. R., Ueno, M., Kinoshita, S., Knupp, C. & Quantock, A. J. 2019. Ultrastructural Variability of the Juxtacanalicular Tissue Along the Inner Wall of Schlemm's Canal. *Mol Vis*, 25, 517-526.
- Krapp, H. G. & Gabbiani, F. 2005. Spatial Distribution of Inputs and Local Receptive Field Properties of a Wide-Field, Looming Sensitive Neuron. *J Neurophysiol*, 93, 2240-53.

- Krasowski, N. E., Beier, T., Knott, G. W., Köthe, U., Hamprecht, F. A. & Kreshuk, A. 2018. Neuron Segmentation with High-Level Biological Priors. *IEEE Trans Med Imaging*, 37, 829-839.
- Kremer, J. R., Mastronarde, D. N. & McIntosh, J. R. 1996. Computer Visualization of Three-Dimensional Image Data Using Imod. *Journal of Structural Biology*, 116, 71-76.
- Kreshuk, A., Walecki, R., Koethe, U., Gierthmuehlen, M., Plachta, D., Genoud, C., Haastert-Talini, K. & Hamprecht, F. A. 2015. Automated Tracing of Myelinated Axons and Detection of the Nodes of Ranvier in Serial Images of Peripheral Nerves. *J Microsc*, 259, 143-154.
- Kristen, M. H. & Stevens, K. 1988. Study of Dendritic Spines by Serial Electron Microscopy and Three-Dimensional Reconstructions. In: LASEK, R. J., BLACK, M. M. & LISS, A. R. (eds.) *Intrinsic Determinants of Neuronal Form and Function*. Cleveland, Ohio.
- Kuwajima, M., Mendenhall, J. M. & Harris, K. M. 2013a. Large-Volume Reconstruction of Brain Tissue from High-Resolution Serial Section Images Acquired by Sem-Based Scanning Transmission Electron Microscopy. *Methods Mol Biol*, 950, 253-73.
- Kuwajima, M., Mendenhall, J. M., Lindsey, L. F. & Harris, K. M. 2013b. Automated Transmission-Mode Scanning Electron Microscopy (Tsem) for Large Volume Analysis at Nanoscale Resolution. *PLoS One*, 8, e59573.
- Kuzirian, A. M. & Leighton, S. B. 1983. Oxygen Plasma Etching of Entire Block Faces Improves the Resolution and Usefulness of Serial Scanning Electron Microscopic Images. *Scan Electron Microsc*, 1877-85.
- Lafontant, P. J., Behzad, A. R., Brown, E., Landry, P., Hu, N. & Burns, A. R. 2013. Cardiac Myocyte Diversity and a Fibroblast Network in the Junctional Region of the Zebrafish Heart Revealed by Transmission and Serial Block-Face Scanning Electron Microscopy. *PLoS One*, 8, e72388.
- Lai, J., Su, Y., Swain, D. L., Huang, D., Getchevski, D. & Gong, H. 2019. The Role of Schlemm's Canal Endothelium Cellular Connectivity in Giant Vacuole Formation: A 3d Electron Microscopy Study. *Invest Ophthalmol Vis Sci*, 60, 1630-1643.
- Laif, Z. A., Noel, J. & Alejandro, R. 1988. A Simple Method of Staining Fresh and Cultured Islets. *Transplantation*, 45, 827-829.
- Lang, S., Drouvelis, P., Tafaj, E., Bastian, P. & Sakmann, B. 2011. Fast Extraction of Neuron Morphologies from Large-Scale Sbfsem Image Stacks. *J Comput Neurosci*, 31, 533-45.
- Le Corrionc, H., Lapied, B. & Hue, B. 1991. M2-Like Presynaptic Receptors Modulate Acetylcholine Release in the Cockroach (*Periplaneta Americana*) Central Nervous System. *J Insect Physiol*, 37, 647-652.
- Leduc-Gaudet, J.-P., Picard, M., Sgarioto, N., Auger, M.-J., Vallée, J., Robitaille, R., St-Pierre, D. H. & Gouspillou, G. 2015. Mitochondrial Morphology Is Altered in Atrophied Skeletal Muscle of Aged Mice. *Oncotarget*, 6.
- Leiss, F., Groh, C., Butcher, N. J., Meinertzhagen, I. A. & Tavosanis, G. 2009. Synaptic Organization in the Adult *Drosophila* Mushroom Body Calyx. *Journal of Comparative Neurology*, 517, 808-824.
- Leitinger, G. & Simmons, P. J. 2000. Cytochemical Evidence That Acetylcholine Is a Neurotransmitter of Neurons That Make Excitatory and Inhibitory Outputs in the Locust Ocellar Visual System. *Journal of Comparative Neurology*, 416, 345-355.

- Lenhart, R. L., Francis, C. A., Lenz, A. L. & Thelen, D. G. 2014. Empirical Evaluation of Gastrocnemius and Soleus Function During Walking. *J Biomech*, 47, 2969-74.
- Lewis, P. N., White, T. L., Young, R. D., Bell, J. S., Winlove, C. P. & Meek, K. M. 2016. Three-Dimensional Arrangement of Elastic Fibers in the Human Corneal Stroma. *Exp Eye Res*, 146, 43-53.
- Li, K., Li, Y., Shelton, J. M., Richardson, J. A., Spencer, E., Chen, Z. J., Wang, X. & Williams, R. S. 2000. Cytochrome C Deficiency Causes Embryonic Lethality and Attenuates Stress-Induced Apoptosis. *Cell*, 101, 389-399.
- Li, P., Nijhawan, D., Budihardjo, I., Srinivasula, S. M., Ahmad, M., Alnemri, E. S. & Wang, X. 1997. Cytochrome C and Dap-Dependent Formation of Apaf-1/Caspase-9 Complex Initiates an Apoptotic Protease Cascade. *Cell*, 91, 479-489.
- Li, Y.-Z., Li, C. J., Pinto, A. V. & Pardee, A. B. 1999. Release of Mitochondrial Cytochrome C in Both Apoptosis and Necrosis Induced by 8-Lapachone in Human Carcinoma Cells. *Molecular medicine*, 5, 232-239.
- Liang, C., Kerr, A., Qiu, Y., Cristofoli, F., Van Esch, H., Fox, M. A. & Mukherjee, K. 2017. Optic Nerve Hypoplasia Is a Pervasive Subcortical Pathology of Visual System in Neonates. *Invest Ophthalmol Vis Sci*, 58, 5485-5496.
- Lipke, E., Hörnschemeyer, T., Pakzad, A., Booth, C. R. & Michalik, P. 2014. Serial Block-Face Imaging and Its Potential for Reconstructing Diminutive Cell Systems: A Case Study from Arthropods. *Microsc Microanal*, 20, 946-55.
- Litman, R. B. & Barnett, R. J. 1972. The Mechanism of the Fixation of Tissue Components by Osmium Tetroxide Via Hydrogen Bonding. *J Ultrastructure Research*, 38, 63-86.
- Little, J. P., Safdar, A., Wilkin, G. P., Tarnopolsky, M. A. & Gibala, M. J. 2010. A Practical Model of Low-Volume High-Intensity Interval Training Induces Mitochondrial Biogenesis in Human Skeletal Muscle: Potential Mechanisms. *J Physiol*, 588, 1011-22.
- Liu, B., Blanch, A. J., Namvar, A., Carmo, O., Tiash, S., Andrew, D., Hanssen, E., Rajagopal, V., Dixon, M. W. A. & Tilley, L. 2019. Multimodal Analysis of Plasmodium Knowlesi-Infected Erythrocytes Reveals Large Invaginations, Swelling of the Host Cell, and Rheological Defects. *Cell Microbiol*, 21, e13005.
- Lyons, G. E. 1990. The Expression of Myosin Genes in Developing Skeletal Muscle in the Mouse Embryo. *The Journal of Cell Biology*, 111, 1465-1476.
- Lyons, G. E., Buckingham, M. & Mannherz, H. G. 1991. A-Actin Proteins and Gene Transcripts Are Colocalized in Embryonic Mouse Muscle. *Development*, 111, 451-454.
- Lyons, G. E., Ontell, M., Cox, R., Sassoon, D. & Buckingham, M. 1990. The Expression of Myosin Genes in Developing Skeletal Muscle in the Mouse Embryo. *Journal of Cell Biology*, 111, 1465-1476.
- Macke, J. H., Maack, N., Gupta, R., Denk, W., Schölkopf, B. & Borst, A. 2008. Contour-Propagation Algorithms for Semi-Automated Reconstruction of Neural Processes. *J Neurosci Methods*, 167, 349-57.
- MacLachlan, C., Sahlender, D. A., Hayashi, S., Molnár, Z. & Knott, G. 2018. Block Face Scanning Electron Microscopy of Fluorescently Labeled Axons without Using near Infra-Red Branding. *Frontiers in Neuroanatomy*, 12.
- Maechler, P., Carobbio, S. & Rubi, B. 2006. In Beta-Cells, Mitochondria Integrate and Generate Metabolic Signals Controlling Insulin Secretion. *Int J Biochem Cell Biol*, 38, 696-709.
- Majaneva, M., Remonen, I., Rintala, J. M., Belevich, I., Kremp, A., Setälä, O., Jokitalo, E. & Blomster, J. 2014. Rhinomonas Nottbecki N. Sp.

- (Cryptomonadales) and Molecular Phylogeny of the Family Pyrenomonadaceae. *J Eukaryot Microbiol*, 61, 480-92.
- Manhart, A., Windner, S., Baylies, M. & Mogilner, A. 2018. Mechanical Positioning of Multiple Nuclei in Muscle Cells. *PLoS Comput Biol*, 14, e1006208.
- Mantani, Y., Haruta, T., Nishida, M., Yokoyama, T., Hoshi, N. & Kitagawa, H. 2019. Three-Dimensional Analysis of Fibroblast-Like Cells in the Lamina Propria of the Rat Ileum Using Serial Block-Face Scanning Electron Microscopy. *The Journal of Veterinary Medical Science*.
- Martin, E. A., Woodruff, D., Rawson, R. L. & Williams, M. E. 2017. Examining Hippocampal Mossy Fiber Synapses by 3d Electron Microscopy in Wildtype and Kirrel3 Knockout Mice. *eNeuro*, 4.
- Matsumoto, M., Sawada, M., García-González, D., Herranz-Pérez, V., Ogino, T., Bang Nguyen, H., Quynh Thai, T., Narita, K., Kumamoto, N., Ugawa, S., Saito, Y., Takeda, S., Kaneko, N., Khodosevich, K., Monyer, H., García-Verdugo, J. M., Ohno, N. & Sawamoto, K. 2019. Dynamic Changes in Ultrastructure of the Primary Cilium in Migrating Neuroblasts in the Postnatal Brain. *The Journal of Neuroscience*, 39, 9967-9988.
- Mcbride, E. L., Rao, A., Zhang, G., Hoyne, J. D., Calco, G. N., Kuo, B. C., He, Q., Prince, A. A., Pokrovskaya, I. D., Storrie, B., Sousa, A. A., Aronova, M. A. & Leapman, R. D. 2018. Comparison of 3d Cellular Imaging Techniques Based on Scanned Electron Probes: Serial Block Face Sem Vs. Axial Bright-Field Stem Tomography. *J Struct Biol*, 202, 216-228.
- Mcdonald, K. 2007. Cryopreparation Methods for Electron Microscopy of Selected Model Systems. *Methods in Cell Biology*. Academic Press.
- Mcdonald, K. L. & Webb, R. I. 2011. Freeze Substitution in 3 Hours or Less. *J Microsc*, 243, 227-33.
- Mcglynn, S. E., Chadwick, G. L., O'Neill, A., Mackey, M., Thor, A., Deerinck, T. J., Ellisman, M. H. & Orphan, V. J. 2018. Subgroup Characteristics of Marine Methane-Oxidizing Anme-2 Archaea and Their Syntrophic Partners as Revealed by Integrated Multimodal Analytical Microscopy. *Applied and Environmental Microbiology*, 84.
- Meinertzhagen, I. A. & O'neil, S. D. 1991. Synaptic Organization of Columnar Elements in the Lamina of the Wild Type in *Drosophila Melanogaster*. *Journal of Comparative Neurology*, 305, 232-263.
- Melek, Z., Mayerich, D., Yuksel, C. & Keyser, J. 2006. Visualization of Fibrous and Thread-Like Data. *IEEE TRANSACTIONS ON VISUALIZATION AND COMPUTER GRAPHICS*, 12, 1165-1172.
- Melia, C. E., Peddie, C. J., De Jong, A. W. M., Snijder, E. J., Collinson, L. M., Koster, A. J., Van Der Schaar, H. M., Van Kuppeveld, F. J. M. & Bárcena, M. 2019. Origins of Enterovirus Replication Organelles Established by Whole-Cell Electron Microscopy. *mBio*, 10.
- Messina, G., Biressi, S., Monteverde, S., Magli, A., Cassano, M., Perani, L., Roncaglia, E., Tagliafico, E., Starnes, L., Campbell, C. E., Grossi, M., Goldhamer, D. J., Gronostajski, R. M. & Cossu, G. 2010. Nfix Regulates fetal-Specific Transcription in Developing Skeletal Muscle. *Cell*, 140, 554-66.
- Meyer, K., Ostrenko, O., Bourantas, G., Morales-Navarrete, H., Porat-Shliom, N., Segovia-Miranda, F., Nonaka, H., Ghaemi, A., Verbavatz, J. M., Brusch, L., Sbalzarini, I., Kalaidzidis, Y., Weigert, R. & Zerial, M. 2017. A Predictive 3d Multi-Scale Model of Biliary Fluid Dynamics in the Liver Lobule. *Cell Syst*.
- Mikula, S., Binding, J. & Denk, W. 2012. Staining and Embedding the Whole Mouse Brain for Electron Microscopy. *Nature Methods*, 9.

- Mikula, S. & Denk, W. 2015. High-Resolution Whole-Brain Staining for Electron Microscopic Circuit Reconstruction. *Nat Methods*, 12, 541-6.
- Mishra, P., Varuzhanyan, G., Pham, A. H. & Chan, D. C. 2015. Mitochondrial Dynamics Is a Distinguishing Feature of Skeletal Muscle Fiber Types and Regulates Organellar Compartmentalization. *Cell Metab*, 22, 1033-44.
- Mitra, K., Wunder, C., Roysam, B., Lin, G. & Lippincott-Schwartz, J. 2009. A Hyperfused Mitochondrial State Achieved at G1-S Regulates Cyclin E Buildup and Entry into S Phase. *Proc Natl Acad Sci U S A*, 106, 11960-5.
- Miyazaki, N., Esaki, M., Ogura, T. & Murata, K. 2014. Serial Block-Face Scanning Electron Microscopy for Three-Dimensional Analysis of Morphological Changes in Mitochondria Regulated by Cdc48p/P97 Atpase. *J Struct Biol*, 187, 187-193.
- Möbius, W. 2009. Cryopreparation of Biological Specimens for Immunoelectron Microscopy. *Ann Anat*, 191, 231-47.
- Mollica, M. P., Lionetti, L., Crescenzo, R., D'andrea, E., Ferraro, M., Liverini, G. & Iossa, S. 2006. Heterogeneous Bioenergetic Behaviour of Subsarcolemmal and Intermysofibrillar Mitochondria in Fed and Fasted Rats. *Cell Mol Life Sci*, 63, 358-66.
- Moore, S. E., Hurko, O. & Walsh, F. S. 1984. Immunocytochemical Analysis of Fibre Type Differentiation in Developing Skeletal Muscle. *Journal of Neuroimmunology*, 7, 137-149.
- Motskin, M., Müller, K. H., Genoud, C., Monteith, A. G. & Skepper, J. N. 2011. The Sequestration of Hydroxyapatite Nanoparticles by Human Monocyte-Macrophages in a Compartment That Allows Free Diffusion with the Extracellular Environment. *Biomaterials*, 32, 9470-82.
- Mukherjee, K., Clark, H. R., Chavan, V., Benson, E. K., Kidd, G. J. & Srivastava, S. 2016. Analysis of Brain Mitochondria Using Serial Block-Face Scanning Electron Microscopy. *J Vis Exp*.
- Mullner, T., Zankel, A., Mayrhofer, C., Reingruber, H., Höltzel, A., Lv, Y., Svec, F. & Tallarek, U. 2012. Reconstruction and Characterization of a Polymer-Based Monolithic Stationary Phase Using Serial Block-Face Scanning Electron Microscopy. *Langmuir*, 28, 16733-7.
- Mun, J. Y., Jeong, S. Y., Kim, J. H., Han, S. S. & Kim, I. H. 2011. A Low Fluence Q-Switched Nd:Yag Laser Modifies the 3d Structure of Melanocyte and Ultrastructure of Melanosome by Subcellular-Selective Photothermolysis. *J Electron Microscop (Tokyo)*, 60, 11-8.
- Murphy, M. & Kardon, G. 2011. Origin of Vertebrate Limb Muscle: The Role of Progenitor and Myoblast Populations. *Curr Top Dev Biol*, 96, 1-32.
- Mustafi, D., Kikano, S. & Palczewski, K. 2014. Serial Block Face-Scanning Electron Microscopy: A Method to Study Retinal Degenerative Phenotypes. *Curr Protoc Mouse Biol*, 4, 197-204.
- Mutha, N. V. R., Mohammed, W. K., Krasnogor, N., Tan, G. Y. A., Choo, S. W. & Jakubovics, N. S. 2018. Transcriptional Responses of Streptococcus Gordonii and Fusobacterium Nucleatum to Coaggregation. *Molecular Oral Microbiology*, 33, 450-464.
- Nakagawa, T., Shimizu, S., Watanabe, T., Yamaguchi, O., Otsu, K., Yamagata, H., Inohara, H., Kubo, T. & Tsujimoto, Y. 2005. Cyclophilin D-Dependent Mitochondrial Permeability Transition Regulates Some Necrotic but Not Apoptotic Cell Death. *Nature*, 434, 652-8.
- Nakao, A., Miyazaki, N., Ohira, K., Hagihara, H., Takagi, T., Usuda, N., Ishii, S., Murata, K. & Miyakawa, T. 2017. Immature Morphological Properties in

- Subcellular-Scale Structures in the Dentate Gyrus of Schnurri-2 Knockout Mice: A Model for Schizophrenia and Intellectual Disability. *Mol Brain*, 10, 60.
- Narusawa, M., Fitzsimons, R. B., Izumo, S., Nadal-Ginard, B., Rubinstein, N. A. & Kelly, A. M. 1987. Slow Myosin in Developing Rat Skeletal Muscle. *Journal of Cell Biology*, 104, 447-459.
- Navarro, P. P., Genoud, C., Castaño-Díez, D., Graff-Meyer, A., Lewis, A. J., De Gier, Y., Lauer, M. E., Britschgi, M., Bohrmann, B., Frank, S., Hench, J., Schweighauser, G., Rozemuller, A. J. M., Van De Berg, W. D. J., Stahlberg, H. & Shahmoradian, S. H. 2018. Cerebral Corpora Amylacea Are Dense Membranous Labyrinths Containing Structurally Preserved Cell Organelles. *Scientific Reports*, 8.
- Needham, D. M. 1926. Red and White Muscle. *Physiol Rev*, 6.
- Neuhaus, J., Schröppel, B., Dass, M., Zimmermann, H., Wolburg, H., Fallier-Becker, P., Gevaert, T., Burkhardt, C. J., Do, H. M. & Stolzenburg, J.-U. 2018. 3d-Electron Microscopic Characterization of Interstitial Cells in the Human Bladder Upper Lamina Propria. *Neurourology and Urodynamics*, 37, 89-98.
- Neves, R. C. & Reichert, H. 2015. Microanatomy and Development of the Dwarf Male of Symbion Pandora (Phylum Cyclophora): New Insights from Ultrastructural Investigation Based on Serial Section Electron Microscopy. *PLoS One*, 10, e0122364.
- Nguyen, H. B., Sui, Y., Thai, T. Q., Ikenaka, K., Oda, T. & Ohno, N. 2018. Decreased Number and Increased Volume with Mitochondrial Enlargement of Cerebellar Synaptic Terminals in a Mouse Model of Chronic Demyelination. *Medical Molecular Morphology*, 51, 208-216.
- Nguyen, H. B., Thai, T. Q., Saitoh, S., Wu, B., Saitoh, Y., Shimo, S., Fujitani, H., Otake, H. & Ohno, N. 2016. Conductive Resins Improve Charging and Resolution of Acquired Images in Electron Microscopic Volume Imaging. *Sci Rep*, 6, 23721.
- Niro, C., Demignon, J., Vincent, S., Liu, Y., Giordani, J., Sgarbi, N., Favier, M., Guillet-Deniau, I., Blais, A. & Maire, P. 2010. Six1 and Six4 Gene Expression Is Necessary to Activate the Fast-Type Muscle Gene Program in the Mouse Primary Myotome. *Dev Biol*, 338, 168-82.
- Nixon, F. M., Honnor, T. R., Clarke, N. I., Starling, G. P., Beckett, A. J., Johansen, A. M., Brettschneider, J. A., Prior, I. A. & Royle, S. J. 2017. Microtubule Organization within Mitotic Spindles Revealed by Serial Block Face Scanning Electron Microscopy and Image Analysis. *J Cell Sci*, 130, 1845-1855.
- Nkwe, D. O., Pelchen-Matthews, A., Burden, J. J., Collinson, L. M. & Marsh, M. 2016. The Intracellular Plasma Membrane-Connected Compartment in the Assembly of Hiv-1 in Human Macrophages. *BMC Biol*, 14, 50.
- Nowel, M. S. & Shelton, P. M. J. 1981. Golgi-Electron-Microscopical Study of the Structure and Development of the Lamina Ganglionaris of the Locust Optic Lobe. *Cell Tissue Res*, 216, 377-401.
- O'shea, M. & Rowell, C. H. F. 1975. Protection from Habituation by Lateral Inhibition. *Nature*, 254, 53.
- O'shea, M. & Rowell, C. H. F. 1976. The Neuronal Basis of a Sensory Analyser, the Acridid Movement Detector System II. Response Decrement, Convergence, and the
- Nature of the Excitatory Afferents to the Fan-Like Dendrites of the Lgmd. *J Exp Biol*, 65, 289-308.
- O'shea, M., Rowell, C. H. F. & Williams, J. D. 1974. The Anatomy of a Locust Visual Interneuron; the Descending Contralateral Movement Detector. *J Exp Biol*, 60, 1-12.

- O'shea, M. & Williams, J. D. 1974. The Anatomy and Output Connection of a Locust Visual Interneuron; the Lobular Giant Movement Detector (Lgmd) Neuron. *J Comp Physiol* 91, 257-266.
- Ogata, T. & Yamasaki, Y. 1997. Ultra-High-Resolution Scanning Electron Microscopy of Mitochondria and Sarcoplasmic Reticulum Arrangement in Human Red, White, and Intermediate Muscle Fibers. *The Anatomical Record*, 248, 214-233.
- Ordahl, C. P. & Le Douarin, N. M. 1992. Two Myogenic Lineages within the Developing Somite. *Development*, 114, 339-353.
- Osellame, L. D., Blacker, T. S. & Duchen, M. R. 2012. Cellular and Molecular Mechanisms of Mitochondrial Function. *Best Pract Res Clin Endocrinol Metab*, 26, 711-23.
- Ou, H. D., Deerinck, T. J., Bushong, E., Ellisman, M. H. & O'shea, C. C. 2015. Visualizing Viral Protein Structures in Cells Using Genetic Probes for Correlated Light and Electron Microscopy. *Methods*, 90, 39-48.
- Pain, C., Kriechbaumer, V., Kittelmann, M., Hawes, C. & Fricker, M. 2019. Quantitative Analysis of Plant Er Architecture and Dynamics. *Nature Communications*, 10.
- Palade, G. E. 1952. A Study of Fixation for Electron Microscopy. *J Exp Med*, 95, 285-298.
- Palaiologou, E., Goggin, P., Chatelet, D. S., Lofthouse, E. M., Torrens, C., Sengers, B. G., Cleal, J. K., Page, A. & Lewis, R. M. 2017. Serial Block-Face Scanning Electron Microscopy of Erythrocytes Protruding through the Human Placental Syncytiotrophoblast. *J Anat*.
- Pallotto, M., Watkins, P. V., Fubara, B., Singer, J. H. & Briggman, K. L. 2015. Extracellular Space Preservation Aids the Connectomic Analysis of Neural Circuits. *eLife*, 4, e08206.
- Palmer, C. S., Osellame, L. D., Stojanovski, D. & Ryan, M. T. 2011. The Regulation of Mitochondrial Morphology: Intricate Mechanisms and Dynamic Machinery. *Cell Signal*, 23, 1534-45.
- Parker, A. R., Palka, B. P., Purslow, C., Holden, S., Lewis, P. N. & Meek, K. M. 2019. Transparency in the Eye Region of an Ostracod Carapace ( Macrocypridina Castanea, Myodocopida). *Philosophical Transactions. Series A, Mathematical, Physical, and Engineering Sciences*, 377, 20180267.
- Parker, D. & Newland, P. L. 1995. Cholinergic Synaptic Transmission between Proprioceptive Afferents and a Hind Leg Motor Neuron in the Locust. *Journal of Neurophysiology*, 73, 586-594.
- Parkkola, R., Alanen, A., Kalimo, H., Lillsunde, I., Komu, M. & Kormano, M. 1993. Mr Relaxation Times and Fiber Type Predominance of the Psoas and Multifidus Muscle. *Acta Radiologica*, 34, 16-19.
- Parone, P. A., Da Cruz, S., Tondera, D., Mattenberger, Y., James, D. I., Maechler, P., Barja, F. & Martinou, J. C. 2008. Preventing Mitochondrial Fission Impairs Mitochondrial Function and Leads to Loss of Mitochondrial DNA. *PLoS One*, 3, e3257.
- Patterson, S. S., Bordt, A. S., Girresch, R. J., Linehan, C. M., Bauss, J., Yeo, E., Perez, D., Tseng, L., Navuluri, S., Harris, N. B., Matthews, C., Anderson, J. R., Kuchenbecker, J. A., Manookin, M. B., Ogilvie, J. M., Neitz, J. & Marshak, D. W. 2019. Wide-Field Amacrine Cell Inputs to on Parasol Ganglion Cells in Macaque Retina. *J Comp Neurol*.
- Pawley, J. 1997. The Development of Field-Emission Scanning Electron Microscopy for Imaging Biological Surfaces. *Scanning*, 19, 324-336.



- Pereira, A. F., Hageman, D. J., Garbowski, T., Riedesel, C., Knothe, U., Zeidler, D. & Knothe Tate, M. L. 2016. Creating High-Resolution Multiscale Maps of Human Tissue Using Multi-Beam Sem. *PLoS Comput Biol*, 12, e1005217.
- Perez, A. J., Seyedhosseini, M., Deerinck, T. J., Bushong, E. A., Panda, S., Tasdizen, T. & Ellisman, M. H. 2014. A Workflow for the Automatic Segmentation of Organelles in Electron Microscopy Image Stacks. *Front Neuroanat*, 8, 126.
- Peron, S. P., Jones, P. W. & Gabbiani, F. 2009. Precise Subcellular Input Retinotopy and Its Computational Consequences in an Identified Visual Interneuron. *Neuron*, 63, 830-42.
- Peter, J. B., Barnard, R. J., Edgerton, V. R., Gillespie, C. A. & Stempel, K. E. 1972. Metabolic Profiles of Three Fiber Types of Skeletal Muscle in Guinea Pigs and Rabbitst. *Biochemistry*, 11, 2627-2633.
- Pfeifer, C. R., Shomorony, A., Aronova, M. A., Zhang, G., Cai, T., Xu, H., Notkins, A. L. & Leapman, R. D. 2015. Quantitative Analysis of Mouse Pancreatic Islet Architecture by Serial Block-Face Sem. *J Struct Biol*, 189, 44-52.
- Picard, M., Csukly, K., Robillard, M. E., Godin, R., Ascah, A., Bourcier-Lucas, C. & Burelle, Y. 2008. Resistance to Ca<sup>2+</sup>-Induced Opening of the Permeability Transition Pore Differs in Mitochondria from Glycolytic and Oxidative Muscles. *Am J Physiol Regul Integr Comp Physiol*, 295, R659-68.
- Picard, M., Hepple, R. T. & Burelle, Y. 2012. Mitochondrial Functional Specialization in Glycolytic and Oxidative Muscle Fibers: Tailoring the Organelle for Optimal Function. *Am J Physiol Cell Physiol*, 302, C629-41.
- Picard, M., Taivassalo, T., Gouspillou, G. & Hepple, R. T. 2011. Mitochondria: Isolation, Structure and Function. *J Physiol*, 589, 4413-21.
- Picard, M., White, K. & Turnbull, D. M. 2013. Mitochondrial Morphology, Topology, and Membrane Interactions in Skeletal Muscle: A Quantitative Three-Dimensional Electron Microscopy Study. *J Appl Physiol (1985)*, 114, 161-71.
- Pinali, C., Bennett, H., Davenport, J. B., Trafford, A. W. & Kitmitto, A. 2013. Three-Dimensional Reconstruction of Cardiac Sarcoplasmic Reticulum Reveals a Continuous Network Linking Transverse-Tubules: This Organization Is Perturbed in Heart Failure. *Circ Res*, 113, 1219-30.
- Pinali, C., Bennett, H. J., Davenport, J. B., Caldwell, J. L., Starborg, T., Trafford, A. W. & Kitmitto, A. 2015. Three-Dimensional Structure of the Intercalated Disc Reveals Plicate Domain and Gap Junction Remodeling in Heart Failure. *Biophys J*, 108, 498-507.
- Pinali, C. & Kitmitto, A. 2014. Serial Block Face Scanning Electron Microscopy for the Study of Cardiac Muscle Ultrastructure at Nanoscale Resolutions. *J Mol Cell Cardiol*, 76, 1-11.
- Pinali, C., Malik, N., Davenport, J. B., Allan, L. J., Murfitt, L., Iqbal, M. M., Boyett, M. R., Wright, E. J., Walker, R., Zhang, Y., Dobryznski, H., Holt, C. M. & Kitmitto, A. 2017. Post-Myocardial Infarction T-Tubules Form Enlarged Branched Structures with Dysregulation of Junctophilin-2 and Bridging Integrator 1 (Bin-1). *J Am Heart Assoc*, 6.
- Pingel, J., Lu, Y., Starborg, T., Fredberg, U., Langberg, H., Nedergaard, A., Weis, M., Eyre, D., Kjaer, M. & Kadler, K. E. 2014. 3-D Ultrastructure and Collagen Composition of Healthy and Overloaded Human Tendon: Evidence of Tenocyte and Matrix Buckling. *J Anat*, 224, 548-55.
- Pipkin, J. E., Bushong, E. A., Ellisman, M. H. & Kristan Jr., W. B. 2018. Verifying, Challenging, and Discovering New Synapses among Fully Em-Reconstructed Neurons in the Leech Ganglion. *Frontiers in Neuroanatomy*, 12.

- Pipkin, J. E., Bushong, E. A., Ellisman, M. H. & Kristan, W. B., Jr. 2016. Patterns and Distribution of Presynaptic and Postsynaptic Elements within Serial Electron Microscopic Reconstructions of Neuronal Arbors from the Medicinal Leech *Hirudo Verbaria*. *J Comp Neurol*, 524, 3677-3695.
- Pisania, A., Weir, G. C., O'neil, J. J., Omer, A., Tchipashvili, V., Lei, J., Colton, C. K. & Bonner-Weir, S. 2010. Quantitative Analysis of Cell Composition and Purity of Human Pancreatic Islet Preparations. *Lab Invest*, 90, 1661-75.
- Plachno, B. J., Świątek, P., Jobson, R. W., Małota, K. & Brutkowski, W. 2017. Serial Block Face Sem Visualization of Unusual Plant Nuclear Tubular Extensions in a Carnivorous Plant (*Utricularia*, *Lentibulariaceae*). *Ann Bot*.
- Pollreisz, A., Messinger, J. D., Sloan, K. R., Mittermueller, T. J., Weinhandl, A. S., Benson, E. K., Kidd, G. J., Schmidt-Erfurth, U. & Curcio, C. A. 2018. Visualizing Melanosomes, Lipofuscin, and Melanolipofuscin in Human Retinal Pigment Epithelium Using Serial Block Face Scanning Electron Microscopy. *Experimental Eye Research*, 166, 131-139.
- Porter, K. R. & Palade, G. E. 1957. Studies on the Endoplasmic Reticulum lii. Its Form and Distribution in Striated Muscle Cells. *J Biophysic. and Biochem. Cytol.*, 3.
- Powell, P. L., Roy, R. R., Kanim, P., Bello, M. A. & Edgerton, V. R. 1984. Predictability of Skeletal Muscle Tension from Architectural Determinations in Guinea Pig Hindlimbs. *Journal of Applied Physiology*, 57, 1715-1721.
- Puhka, M., Joensuu, M., Vihinen, H., Belevich, I. & Jokitalo, E. 2012. Progressive Sheet-to-Tubule Transformation Is a General Mechanism for Endoplasmic Reticulum Partitioning in Dividing Mammalian Cells. *Mol Biol Cell*, 23, 2424-32.
- Rajagopal, V., Bass, G., Ghosh, S., Hunt, H., Walker, C., Hanssen, E., Crampin, E. & Soeller, C. 2018. Creating a Structurally Realistic Finite Element Geometric Model of a Cardiomyocyte to Study the Role of Cellular Architecture in Cardiomyocyte Systems Biology. *JoVE (Journal of Visualized Experiments)*, e56817.
- Randles, M. J., Collinson, S., Starborg, T., Mironov, A., Krendel, M., Königshausen, E., Sellin, L., Roberts, I. S., Kadler, K. E., Miner, J. H. & Lennon, R. 2016. Three-Dimensional Electron Microscopy Reveals the Evolution of Glomerular Barrier Injury. *Sci Rep*, 6, 35068.
- Rebbeck, R. T., Karunasekara, Y., Board, P. G., Beard, N. A., Casarotto, M. G. & Dulhunty, A. F. 2014. Skeletal Muscle Excitation-Contraction Coupling: Who Are the Dancing Partners? *Int J Biochem Cell Biol*, 48, 28-38.
- Rennie, M. Y., Gahan, C. G., López, C. S., Thornburg, K. L. & Rugonyi, S. 2014. 3d Imaging of the Early Embryonic Chicken Heart with Focused Ion Beam Scanning Electron Microscopy. *Microsc Microanal*, 20, 1111-9.
- Rezakhaniha, R., Fonck, E., Genoud, C. & Stergiopulos, N. 2011. Role of Elastin Anisotropy in Structural Strain Energy Functions of Arterial Tissue. *Biomech Model Mechanobiol*, 10, 599-611.
- Rind, F. C. 1984. A Chemical Synapse between Two Motion Detecting Neurones in the Locust Brain. *J Exp Biol*, 110, 143-167.
- Rind, F. C. 1987. Non-Directional, Movement Sensitive Neurones of the Locust Optic Lobe. *J Comp Physiol A Neuroethol Sens Neural Behav Physiol*, 161, 477-494.
- Rind, F. C. 1996. Intracellular Characterization of Neurons in the Locust Brain Signaling Impending Collision. *J Neurophysiol*, 75, 986-995.
- Rind, F. C. & Bramwell, D. I. 1996. Neural Network Based on the Input Organization of an Identified Neuron Signaling Impending Collision. *J Neurophysiol*, 75.

- Rind, F. C. & Leitinger, G. 2000. Immunocytochemical Evidence That Collision Sensing Neurons in the Locust Visual System Contain Acetylcholine. *Journal of Comparative Neurology*, 423, 389-401.
- Rind, F. C. & Simmons, P. J. 1992. Orthopteran Dcmd Neuron: A Reevaluation of Responses to Moving Objects. I. Selective Responses to Approaching Objects. *J Neurophysiol*, 68, 1655-1666.
- Rind, F. C. & Simmons, P. J. 1997. Signaling of Object Approach by the Dcmd Neuron of the Locust. *American Journal of Physiology*, 1029-1033.
- Rind, F. C. & Simmons, P. J. 1998. Local Circuit for the Computation of Object Approach by an Identified Visual Neuron in the Locust. *Journal of Comparative Neurology*, 395, 405-415.
- Rind, F. C., Wernitznig, S., Pölt, P., Zankel, A., Gutl, D., Sztarker, J. & Leitinger, G. 2016. Two Identified Looming Detectors in the Locust: Ubiquitous Lateral Connections among Their Inputs Contribute to Selective Responses to Looming Objects. *Sci Rep*, 6, 35525.
- Rivera-Alba, M., Vitaladevuni, S. N., Mischenko, Y., Zhiyuan, L., Takemura, S., Scheffer, L. K., Meinertzhagen, I. A., Chklovskii, D. B. & De Polaveija, G. G. 2011. Wiring Economy and Volume Exclusion Determine Neuronal Placement in the Drosophila Brain. *Curr Biol*, 21, 2000-2005.
- Rivlin, P. K. & Raymond, P. A. 1987. Use of Osmium Tetroxide-Potassium Ferricyanide in Reconstructing Cells from Serial Ultrathin Sections. *J Neurosci Methods*, 20, 23-33.
- Roman, W. & Gomes, E. R. 2017. Nuclear Positioning in Skeletal Muscle. *Semin Cell Dev Biol*.
- Roman, W., Martins, J. P., Carvalho, F. A., Voituriez, R., Abella, J. V. G., Santos, N. C., Cadot, B., Way, M. & Gomes, E. R. 2017. Myofibril Contraction and Crosslinking Drive Nuclear Movement to the Periphery of Skeletal Muscle. *Nat Cell Biol*, 19, 1189-1201.
- Roman, W., Martins, J. P. & Gomes, E. R. 2018. Local Arrangement of Fibronectin by Myofibroblasts Governs Peripheral Nuclear Positioning in Muscle Cells. *Dev Cell*.
- Rosen, J. N. & Baylies, M. K. 2017. Myofibrils Put the Squeeze on Nuclei. *Nat Cell Biol*, 19, 1148-1150.
- Rosner, R., Von Hadeln, J., Salden, T. & Homberg, U. 2017. Anatomy of the Lobula Complex in the Brain of the Praying Mantis Compared to the Lobula Complexes of the Locust and Cockroach. *J Comp Neurol*, 525, 2343-2357.
- Rost-Roszkowska, M., Janelt, K. & Poprawa, I. 2019. Fine Structure of the Midgut Epithelium of Thulinus Ruffoi (Tardigrada, Eutardigrada, Parachela) in Relation to Oogenesis and Simplex Stage. *Arthropod Struct Dev*, 49, 128-136.
- Rouquette, J., Genoud, C., Vazquez-Nin, G. H., Kraus, B., Cremer, T. & Fakan, S. 2009. Revealing the High-Resolution Three-Dimensional Network of Chromatin and Interchromatin Space: A Novel Electron-Microscopic Approach to Reconstructing Nuclear Architecture. *Chromosome Res*, 17, 801-10.
- Rowell, C. H. F. 1971. Antennal Cleaning, Arousal and Visual Interneurone Responsiveness in a Locust. *J Exp Biol*, 55, 749-761.
- Rowell, C. H. F. & O'shea, M. 1976. Neuronal Basis of a Sensory Analyser, the Acridid Movement Detector System. Iii. Control of Response Amplitude by Tonic Lateral Inhibition. *J Exp Biol*, 65, 617-625.
- Rowell, C. H. F., O'shea, M. & Williams, J. D. 1977. The Neuronal Basis of a Sensory Analyser, the Acridid Movement Detector System Iv. The Preference for Small Field Stimuli. *J Exp Biol*, 68, 157-185.

- Rozsa, G., Szent-Györgyi, A. & Wyckoff, R. W. G. 1950. The Fine Structure of Myofibrils. *Exp Cell Res*, 1, 194-205.
- Rühling, S., Kramer, F., Schmutz, S., Amor, S., Jiangshan, Z., Schmitz, C., Kipp, M. & Hochstrasser, T. 2019. Visualization of the Breakdown of the Axonal Transport Machinery: A Comparative Ultrastructural and Immunohistochemical Approach. *Molecular Neurobiology*.
- Russell, A. P., Foletta, V. C., Snow, R. J. & Wadley, G. D. 2014. Skeletal Muscle Mitochondria: A Major Player in Exercise, Health and Disease. *Biochim Biophys Acta*, 1840, 1276-84.
- Ryan, M. T. & Hoogenraad, N. J. 2007. Mitochondrial-Nuclear Communications. *Annu Rev Biochem*, 76, 701-22.
- Sabatini, D. D., Bensch, K. & Barnnett, R. J. 1963. Cytochemistry and Electron Microscopy. *J Cell Biol*, 17, 19-58.
- Sabbah, S., Berg, D., Papendorp, C., Briggman, K. L. & Berson, D. M. 2017. A Cre Mouse Line for Probing Irradiance- and Direction-Encoding Retinal Networks. *eNeuro*, 4.
- Safa, B. N., Peloquin, J. M., Natriello, J. R., Caplan, J. L. & Elliott, D. M. 2019. Helical Fibrillar Microstructure of Tendon Using Serial Block-Face Scanning Electron Microscopy and a Mechanical Model for Interfibrillar Load Transfer. *J R Soc Interface*, 16, 20190547.
- Sai, K., Wang, S., Kaito, A., Fujiwara, T., Maruo, T., Itoh, Y., Miyata, M., Sakakibara, S., Miyazaki, N., Murata, K., Yamaguchi, Y., Haruta, T., Nishioka, H., Motojima, Y., Komura, M., Kimura, K., Mandai, K., Takai, Y. & Mizoguchi, A. 2017. Multiple Roles of Afadin in the Ultrastructural Morphogenesis of Mouse Hippocampal Mossy Fiber Synapses. *J Comp Neurol*, 525, 2719-2734.
- Sakaguchi, M., Miyazaki, N., Fujioka, H., Kaneko, O. & Murata, K. 2016. Three-Dimensional Analysis of Morphological Changes in the Malaria Parasite Infected Red Blood Cell by Serial Block-Face Scanning Electron Microscopy. *J Struct Biol*, 193, 162-171.
- Salloum, R. H., Chen, G., Velet, L., Manzoor, N. F., Elkin, R., Kidd, G. J., Coughlin, J., Yurosko, C., Bou-Anak, S., Azadi, S., Gohlsch, S., Schneider, H. & Kaltenbach, J. A. 2014. Mapping and Morphometric Analysis of Synapses and Spines on Fusiform Cells in the Dorsal Cochlear Nucleus. *Front Syst Neurosci*, 8, 167.
- Salo, R. A., Belevich, I., Manninen, E., Jokitalo, E., Gröhn, O. & Sierra, A. 2018. Quantification of Anisotropy and Orientation in 3d Electron Microscopy and Diffusion Tensor Imaging in Injured Rat Brain. *NeuroImage*, 172, 404-414.
- Samejima, K., Booth, D. G., Ogawa, H., Paulson, J. R., Xie, L., Watson, C. A., Platani, M., Kanemaki, M. T. & Earnshaw, W. C. 2018. Functional Analysis after Rapid Degradation of Condensins and 3d-Em Reveals Chromatin Volume Is Uncoupled from Chromosome Architecture in Mitosis. *Journal of Cell Science*, 131.
- Sandow, A. 1952. Excitation-Contraction Coupling in Muscular Response *Yale J. Biol. Med.*, 25, 176-201.
- Sandulescu, T., Spilker, L., Rauscher, D., Naumova, E. A. & Arnold, W. H. 2018. Morphological Analysis and Three-Dimensional Reconstruction of the Smas Surrounding the Nasolabial Fold. *Annals of Anatomy - Anatomischer Anzeiger*, 217, 111-117.
- Santer, R. D., Rind, F. C. & Simmons, P. J. 2012. Predator Versus Prey: Locust Looming-Detector Neuron and Behavioural Responses to Stimuli Representing Attacking Bird Predators. *PLoS One*, 7, e50146.

- Santer, R. D., Yamawaki, Y., Rind, F. C. & Simmons, P. J. 2005. Motor Activity and Trajectory Control During Escape Jumping in the Locust *Locusta Migratoria*. *J Comp Physiol A Neuroethol Sens Neural Behav Physiol*, 191, 965-75.
- Santer, R. D., Yamawaki, Y., Rind, F. C. & Simmons, P. J. 2008. Preparing for Escape: An Examination of the Role of the Dcmd Neuron in Locust Escape Jumps. *J Comp Physiol A Neuroethol Sens Neural Behav Physiol*, 194, 69-77.
- Sassoon, D., Garner, I. & Buckingham, M. 1988. Transcripts of  $\alpha$ -Cardiac and  $\alpha$ -Skeletal Actins Are Early Markers for Myogenesis in the Mouse Embryo. *Development*, 104, 155-164.
- Sattelle, D. B. 1980. Acetylcholine Receptors of Insects. In: BERRIDGE, M. J., TREHERNE, J. E. & WIGGLESWORTH, V. B. (eds.) *Advances in Insect Physiology*. Academic Press.
- Schalek, R., Lee, D., Kasthuri, N., Peleg, A., Jones, T., Kaynig, V., Haehn, D., Pfister, H., Cox, D. & Lichtman, J. W. 2016. Imaging a 1 Mm<sup>3</sup> Volume of Rat Cortex Using a Multibeam Sem. *Microscopy and Microanalysis*, 22, 582-583.
- Schiaffino, S., Ausoni, S., Gorza, L., Saggin, L., Gundersen, K. & Lomo, T. 1988. Myosin Heavy Chain Isoforms and Velocity of Shortening of Type 2 Skeletal Muscle Fibres. *Acta Physiol Scand*, 134.
- Schiaffino, S., Gorza, L., Sartore, S., Saggin, L., Ausoni, S., Vianello, M., Gundersen, K. & Lømo, T. 1989. Three Myosin Heavy Chain Isoforms in Type 2 Skeletal Muscle Fibres. *Journal of Muscle Research and Cell Motility*, 10.
- Schiaffino, S., Hanzlíková, V. & Pierobon, S. 1970. Relations between Structure and Function in Rat Skeletal Muscle Fibers. *The Journal of Cell Biology*, 47, 107-119.
- Schiaffino, S. & Reggiani, C. 2011. Fiber Types in Mammalian Skeletal Muscles. *Physiol Rev*, 91, 1447-531.
- Schiaffino, S., Reggiani, C. & Murgia, M. 2020. Fiber Type Diversity in Skeletal Muscle Explored by Mass Spectrometry-Based Single Fiber Proteomics. *Histol Histopathol*, 35, 239-246.
- Schmeling, F., Tegtmeier, J., Kinoshita, M. & Homberg, U. 2015. Photoreceptor Projections and Receptive Fields in the Dorsal Rim Area and Main Retina of the Locust Eye. *J Comp Physiol A Neuroethol Sens Neural Behav Physiol*, 201, 427-40.
- Schneider, J. P., Wrede, C., Hegermann, J., Weibel, E. R., Mühlfeld, C. & Ochs, M. 2019. On the Topological Complexity of Human Alveolar Epithelial Type 1 Cells. *Am J Respir Crit Care Med*, 199, 1153-1156.
- Schwartz, C. L., Heumann, J. M., Dawson, S. C. & Hoenger, A. 2012. A Detailed, Hierarchical Study of Giardia Lamblia's Ventral Disc Reveals Novel Microtubule-Associated Protein Complexes. *PLoS One*, 7, e43783.
- Seligman, A. M., Wasserkrug, H. L. & Hanker, J. S. 1966. A New Staining Method (Oto) for Enhancing Contrast of Lipid-Containing Membranes and Droplets in Osmium Tetroxide-Fixed Tissue with Osmiophilic Thiocarbohydrazide (Tch). *The Journal of Cell Biology*, 30, 424-432.
- Shami, G. J., Cheng, D., Huynh, M., Vreuls, C., Wisse, E. & Braet, F. 2016. 3-D Em Exploration of the Hepatic Microarchitecture - Lessons Learned from Large-Volume in Situ Serial Sectioning. *Sci Rep*, 6, 36744.
- Shenkman, B. S., Turtikova, O. V., Nemirovskaya, T. L. & Grigoriev, A. I. 2010. Skeletal Muscle Activity and the Fate of Myonuclei. *Acta Naturae*, 2, 59-65.
- Shinomiya, K., Huang, G., Lu, Z., Parag, T., Xu, C. S., Aniceto, R., Ansari, N., Cheatham, N., Lauchie, S., Neace, E., Ogundeyi, O., Ordish, C., Peel, D., Shinomiya, A., Smith, C., Takemura, S., Talebi, I., Rivlin, P. K., Nern, A., Scheffer, L. K., Plaza, S. M. & Meinertzhagen, I. A. 2019. Comparisons

- between the on- and Off-Edge Motion Pathways in the Drosophila Brain. *Elife*, 8.
- Shomorony, A., Pfeifer, C. R., Aronova, M. A., Zhang, G., Cai, T., Xu, H., Notkins, A. L. & Leapman, R. D. 2015. Combining Quantitative 2d and 3d Image Analysis in the Serial Block Face Sem: Application to Secretory Organelles of Pancreatic Islet Cells. *J Microsc*, 259, 155-64.
- Shu, X., Lev-Ram, V., Deerinck, T. J., Qi, Y., Ramko, E. B., Davidson, M. W., Jin, Y., Ellisman, M. H. & Tsien, R. Y. 2011. A Genetically Encoded Tag for Correlated Light and Electron Microscopy of Intact Cells, Tissues, and Organisms. *PLoS Biol*, 9, e1001041.
- Simmons, P. & Rind, F. 1997. *Responses to Object Approach by a Wide Field Visual Neurone, the Lgmd2 of the Locust: Characterization and Image Cues*.
- Simmons, P. J. & Rind, F. C. 1992. Orthopteran Dcmd Neuron: A Reevaluation of Responses to Moving Objects. II. Critical Cues for Detecting Approaching Objects. *J Neurophysiol*, 68, 1667-1682.
- Simmons, P. J., Sztarker, J. & Rind, F. C. 2013. Looming Detection by Identified Visual Interneurons During Larval Development of the Locust *Locusta migratoria*. *J Exp Biol*, 216, 2266-75.
- Slater, C. R. 1982. Postnatal Maturation of Nerve-Muscle Junctions in Hindlimb Muscles of the Mouse. *Dev Biol*, 94, 11-22.
- Smith, M. A., Xia, C. Z., Dengler-Crish, C. M., Fening, K. M., Inman, D. M., Schofield, B. R. & Crish, S. D. 2016. Persistence of Intact Retinal Ganglion Cell Terminals after Axonal Transport Loss in the Dbal2j Mouse Model of Glaucoma. *J Comp Neurol*, 524, 3503-3517.
- Soukup, T., Zacharová, G. & Smerdu, V. 2002. Fibre Type Composition of Soleus and Extensor Digitorum Longus Muscles in Normal Female Inbred Lewis Rats. *Acta Histochem*, 104, 399-405.
- Spano, G. M., Banningsh, S. W., Marshall, W., De Vivo, L., Bellesi, M., Loschky, S. S., Tononi, G. & Cirelli, C. 2019. Sleep Deprivation by Exposure to Novel Objects Increases Synapse Density and Axon-Spine Interface in the Hippocampal Ca1 Region of Adolescent Mice. *The Journal of Neuroscience*, 39, 6613-6625.
- Sparrow, J. C. & Schöck, F. 2009. The Initial Steps of Myofibril Assembly: Integrins Pave the Way. *Nat Mol Cell Bio*, 10, 293-298.
- Spicer, S. S. & Rozsa, G. 1953. An Electron Microscope Study of Contractile Muscle Proteins. *J Biol Chem*, 201, 639-644.
- Stabentheiner, E., Zankel, A. & Pölt, P. 2010. Environmental Scanning Electron Microscopy (Esem)--a Versatile Tool in Studying Plants. *Protoplasma*, 246, 89-99.
- Starborg, T., Kalson, N. S., Lu, Y., Mironov, A., Cootes, T. F., Holmes, D. F. & Kadler, K. E. 2013. Using Transmission Electron Microscopy and 3view to Determine Collagen Fibril Size and Three-Dimensional Organization. *Nat Protoc*, 8, 1433-48.
- Starborg, T., O'sullivan, J. D. B., Carneiro, C. M., Behnsen, J., Else, K. J., Grecis, R. K. & Withers, P. J. 2019. Experimental Steering of Electron Microscopy Studies Using Prior X-Ray Computed Tomography. *Ultramicroscopy*, 201, 58-67.
- Stirling, J. W. 1993. Use of Tannic Acid and Silver Enhancer to Improve Staining for Electron Microscopy and Immunogold Labeling. *J Histochem Cytochem*, 41, 643-648.
- Stucki, D. M., Rueggsegger, C., Steiner, S., Radecke, J., Murphy, M. P., Zuber, B. & Saxena, S. 2016. Mitochondrial Impairments Contribute to Spinocerebellar

- Ataxia Type 1 Progression and Can Be Ameliorated by the Mitochondria-Targeted Antioxidant Mitoq. *Free Radic Biol Med*, 97, 427-40.
- Studer, D. & Gnaegi, H. 2000. Minimal Compression of Ultrathin Sections with Use of an Oscillating Diamond Knife. *J Microsc*, 197, 94-100.
- Sugioka, R., Shimizu, S. & Tsujimoto, Y. 2004. Fzo1, a Protein Involved in Mitochondrial Fusion, Inhibits Apoptosis. *J Biol Chem*, 279, 52726-34.
- Susin, S. A., Lorenzo, H. K., Zamzami, N., Marzo, I., Snow, B. E., Brothers, G. M., Mangion, J., Jacotot, E., Costantini, P., Loeffler, M., Larochette, N., Goodlett, D. R., Aebersold, R., Siderovski, D. P., Penninger, J. M. & Kroemer, G. 1999. Molecular characterization of Mitochondrial Apoptosis-Inducing Factor. *Nature*, 397.
- Svara, F. N., Kornfeld, J., Denk, W. & Bollmann, J. H. 2018. Volume Em Reconstruction of Spinal Cord Reveals Wiring Specificity in Speed-Related Motor Circuits. *Cell Reports*, 23, 2942-2954.
- Svensson, R. B., Herchenhan, A., Starborg, T., Larsen, M., Kadler, K. E., Qvortrup, K. & Magnusson, S. P. 2017. Evidence of Structurally Continuous Collagen Fibrils in Tendons. *Acta Biomater*, 50, 293-301.
- Szczesny, S. E., Caplan, J. L., Pedersen, P. & Elliott, D. M. 2015. Quantification of Interfibrillar Shear Stress in Aligned Soft Collagenous Tissues Via Notch Tension Testing. *Sci Rep*, 5, 14649.
- Szczesny, S. E., Fetchko, K. L., Dodge, G. R. & Elliott, D. M. 2017. Evidence That Interfibrillar Load Transfer in Tendon Is Supported by Small Diameter Fibrils and Not Extrafibrillar Tissue Components. *J Orthop Res*.
- Sztarker, J. & Rind, F. C. 2014. A Look into the Cockpit of the Developing Locust: Looming Detectors and Predator Avoidance. *Dev Neurobiol*, 74, 1078-95.
- Takahashi, M. & Hood, D. A. 1996. Protein Import into Subsarcolemmal and Intermembranous Skeletal Muscle Mitochondria. *Journal of Biological Chemistry*, 271, 27285-27291.
- Takaki, T., Ohno, N., Saitoh, S., Nagai, M. & Joh, K. 2019. Podocyte Penetration of the Glomerular Basement Membrane to Contact on the Mesangial Cell at the Lesion of Mesangial Interposition in Lupus Nephritis: A Three-Dimensional Analysis by Serial Block-Face Scanning Electron Microscopy. *Clinical and Experimental Nephrology*.
- Takeichi, Y., Uebi, T., Miyazaki, N., Murata, K., Yasuyama, K., Inoue, K., Suzaki, T., Kubo, H., Kajimura, N., Takano, J., Omori, T., Yoshimura, R., Endo, Y., Hojo, M. K., Takaya, E., Kurihara, S., Tatsuta, K., Ozaki, K. & Ozaki, M. 2018. Putative Neural Network within an Olfactory Sensory Unit for Nestmate and Non-Nestmate Discrimination in the Japanese Carpenter Ant: The Ultra-Structures and Mathematical Simulation. *Front Cell Neurosci*, 12, 310.
- Takemura, S.-Y., Aso, Y., Hige, T., Wong, A., Lu, Z., Xu, C. S., Rivlin, P. K., Hess, H., Zhao, T., Parag, T., Berg, S., Huang, G., Katz, W., Olbris, D. J., Plaza, S., Umayam, L., Aniceto, R., Chang, L.-A., Lauchie, S., Ogundeyi, O., Ordish, C., Shinomiya, A., Sigmund, C., Takemura, S., Tran, J., Turner, G. C., Rubin, G. M. & Scheffer, L. K. 2017. A Connectome of a Learning and Memory Center in the Adult Drosophila Brain. *eLife*, 6, e26975.
- Takemura, S. Y., Karuppururai, T., Ting, C. Y., Lu, Z., Lee, C. H. & Meinertzhagen, I. A. 2011. Cholinergic Circuits Integrate Neighboring Visual Signals in a Drosophila Motion Detection Pathway. *Curr Biol*, 21, 2077-84.
- Terada, M., Lan, Y. B., Kawano, F., Ohira, T., Higo, Y., Nakai, N., Imaizumi, K., Ogura, A., Nishimoto, N., Adachi, Y. & Ohira, Y. 2010. Myonucleus-Related Properties in Soleus Muscle Fibers of *C57BL/6J* Mice. *Cells Tissues Organs*, 191, 248-259.

- Thai, T. Q., Nguyen, H. B., Saitoh, S., Wu, B., Saitoh, Y., Shimo, S., Elewa, Y. H., Ichii, O., Kon, Y., Takaki, T., Joh, K. & Ohno, N. 2016. Rapid Specimen Preparation to Improve the Throughput of Electron Microscopic Volume Imaging for Three-Dimensional Analyses of Subcellular Ultrastructures with Serial Block-Face Scanning Electron Microscopy. *Med Mol Morphol*, 49, 154-62.
- Thomas, C. I., Keine, C., Okayama, S., Satterfield, R., Musgrove, M., Guerrero-Given, D., Kamasawa, N. & Young, S. M. 2019. Presynaptic Mitochondria Volume and Abundance Increase During Development of a High-Fidelity Synapse. *The Journal of Neuroscience*, 39, 7994-8012.
- Titze, B. & Denk, W. 2013. Automated in-Chamber Specimen Coating for Serial Block-Face Electron Microscopy. *J Microsc*, 250, 101-110.
- Titze, B., Genoud, C. & Friedrich, R. W. 2018. Sbemimage: Versatile Acquisition Control Software for Serial Block-Face Electron Microscopy. *Frontiers in Neural Circuits*, 12.
- Togo, A., Ohta, K., Higashi, R. & Nakamura, K.-I. 2014. En Bloc Staining with Hydroquinone Treatment for Block Face Imaging. *Microscopy*, 63, i34-i35.
- Tondera, D., Grandemange, S., Jourdain, A., Karbowski, M., Mattenberger, Y., Herzig, S., Da Cruz, S., Clerc, P., Raschke, I., Merkwirth, C., Ehse, S., Krause, F., Chan, D. C., Alexander, C., Bauer, C., Youle, R., Langer, T. & Martinou, J. C. 2009. Slp-2 Is Required for Stress-Induced Mitochondrial Hyperfusion. *EMBO J*, 28, 1589-600.
- Totsuka, T., Watanabe, K., Uramoto, I., Sakuma, K. & Mizutani, T. 1998. Muscular Dystrophy: Centronucleation May Reflect a Compensatory Activation of Defective Myonuclei. *Journal of Biomedical Science*, 5, 54-61.
- Tribble, J. R., Vasalauskaitė, A., Redmond, T., Young, R. D., Hassan, S., Fautsch, M. P., Sengpiel, F., Williams, P. A. & Morgan, J. E. 2019. Midget Retinal Ganglion Cell Dendritic and Mitochondrial Degeneration Is an Early Feature of Human Glaucoma. *Brain Commun*, 1, fcz035.
- Trimmer, B. A. 1995. Current Excitement from Insect Muscarinic Receptors. *TINS* 18, 104-111.
- Tsai, W. T., Hassan, A., Sarkar, P., Correa, J., Metlagel, Z., Jorgens, D. M. & Auer, M. 2014. From Voxels to Knowledge: A Practical Guide to the Segmentation of Complex Electron Microscopy 3d-Data. *J Vis Exp*, e51673.
- Tsang, T. K., Bushong, E. A., Boassa, D., Hu, J., Romoli, B., Phan, S., Dulcis, D., Su, C. Y. & Ellisman, M. H. 2018. High-Quality Ultrastructural Preservation Using Cryofixation for 3d Electron Microscopy of Genetically Labeled Tissues. *Elife*, 7.
- Valdez, G., Tapia, J. C., Kang, H., Clemenson, G. D., Jr., Gage, F. H., Lichtman, J. W. & Sanes, J. R. 2010. Attenuation of Age-Related Changes in Mouse Neuromuscular Synapses by Caloric Restriction and Exercise. *Proc Natl Acad Sci U S A*, 107, 14863-8.
- Van Kan, C. M., De Vries, J. I., Lüchinger, A. B., Mulder, E. J. & Taverne, M. A. 2009. Ontogeny of fetal Movements in the Guinea Pig. *Physiol Behav*, 98, 338-44.
- Vandré, D. D. & Burry, R. W. 1992. Immunoelectron Microscopic Localization of Phosphoproteins Associated with the Mitotic Spindle. *Journal of Histochemistry & Cytochemistry*, 40, 1837-1847.
- Vanslebrouck, B., Kremer, A., Pavie, B., Van Roy, F., Lippens, S. & Van Hengel, J. 2018. Three-Dimensional Reconstruction of the Intercalated Disc Including the Intercellular Junctions by Applying Volume Scanning Electron Microscopy. *Histochem Cell Biol*, 149, 479-490.



- Vezzoli, E., Cali, C., De Roo, M., Ponzoni, L., Sogne, E., Gagnon, N., Francolini, M., Braida, D., Sala, M., Muller, D., Falqui, A. & Magistretti, P. J. 2019. Ultrastructural Evidence for a Role of Astrocytes and Glycogen-Derived Lactate in Learning-Dependent Synaptic Stabilization. *Cereb Cortex*.
- Vincent, A. E., Ng, Y. S., White, K., Davey, T., Mannella, C., Falkous, G., Feeney, C., Schaefer, A. M., Mcfarland, R., Gorman, G. S., Taylor, R. W., Turnbull, D. M. & Picard, M. 2016. The Spectrum of Mitochondrial Ultrastructural Defects in Mitochondrial Myopathy. *Sci Rep*, 6, 30610.
- Vincent, A. E., Turnbull, D. M., Eisner, V., Hajnóczky, G. & Picard, M. 2017. Mitochondrial Nanotunnels. *Trends Cell Biol*, 27, 787-799.
- Vincent, A. E., White, K., Davey, T., Philips, J., Ogden, R. T., Lawess, C., Warren, C., Hall, M. G., Ng, Y. S., Falkous, G., Holden, T., Deehan, D., Taylor, R. W., Turnbull, D. M. & Picard, M. 2019. Quantitative 3d Mapping of the Human Skeletal Muscle Mitochondrial Network. *Cell Reports*, 0.
- Vints, K., Vandael, D., Baatsen, P., Pavie, B., Vernailen, F., Corthout, N., Rybakin, V., Munck, S. & Gounko, N. V. 2019. Modernization of Golgi Staining Techniques for High-Resolution, 3-Dimensional Imaging of Individual Neurons. *Scientific Reports*, 9.
- Vishwanathan, A., Daie, K., Ramirez, A. D., Lichtman, J. W., Aksay, E. R. F. & Seung, H. S. 2017. Electron Microscopic Reconstruction of Functionally Identified Cells in a Neural Integrator. *Curr Biol*, 27, 2137-2147 e3.
- Vlahovic, H., Bazdaric, K., Marijancic, V., Soic-Vranic, T., Malnar, D. & Arbanas, J. 2017. Segmental Fibre Type Composition of the Rat Iliopsoas Muscle. *J Anat*, 230, 542-548.
- Vogt, N. & Desplan, C. 2007. The First Steps in Drosophila Motion Detection. *Neuron*, 56, 5-7.
- Von Ardenne, M. 1938. Das Elektronen-Rastermikroskop *Pkysik*, 109, 553-572.
- Walker, A. S., Neves, G., Grillo, F., Jackson, R. E., Rigby, M., O'donnell, C., Lowe, A. S., Vizcay-Barrena, G., Fleck, R. A. & Burrone, J. 2017. Distance-Dependent Gradient in Nmdar-Driven Spine Calcium Signals Along Tapering Dendrites. *Proc Natl Acad Sci U S A*, 114, E1986-E1995.
- Walton, J. 1979. Lead Asparate, an En Bloc Contrast Stain Particularly Useful for Ultrastructural Enzymology. *Journal of Histochemistry and Cytochemistry*, 27, 1337-1342.
- Wang, J. H., Wang, Q. J., Wang, C., Reinholt, B., Grant, A. L., Gerrard, D. E. & Kuang, S. 2015. Heterogeneous Activation of a Slow Myosin Gene in Proliferating Myoblasts and Differentiated Single Myofibers. *Dev Biol*, 402, 72-80.
- Wanner, A. A., Genoud, C. & Friedrich, R. W. 2016a. 3-Dimensional Electron Microscopic Imaging of the Zebrafish Olfactory Bulb and Dense Reconstruction of Neurons. *Sci Data*, 3, 160100.
- Wanner, A. A., Genoud, C., Masudi, T., Siksou, L. & Friedrich, R. W. 2016b. Dense Em-Based Reconstruction of the Interglomerular Projectome in the Zebrafish Olfactory Bulb. *Nat Neurosci*, 19, 816-25.
- Watson, A. H. D. & Burrows, M. 1985. The Distribution of Synapses on the Two Fields of Neurites of Spiking Local Interneurons in the Locust. *J Comp Neurol*, 240, 219-232.
- Webster, P. 2014. Microwave-Assisted Processing and Embedding for Transmission Electron Microscopy. *Methods Mol Biol*, 1117, 21-37.
- Wernitznig, S., Rind, F. C., Pölt, P., Zankel, A., Pritz, E., Kolb, D., Bock, E. & Leitinger, G. 2015. Synaptic Connections of First-Stage Visual Neurons in the

- Locust *Schistocerca Gregaria* Extend Evolution of Tetrad Synapses Back 200 Million Years. *J Comp Neurol*, 523, 298-312.
- Wernitznig, S., Sele, M., Urschler, M., Zankel, A., Pölt, P., Rind, F. C. & Leitinger, G. 2016. Optimizing the 3d-Reconstruction Technique for Serial Block-Face Scanning Electron Microscopy. *J Neurosci Methods*, 264, 16-24.
- West, J. B., Fu, Z., Deerinck, T. J., Mackey, M. R., Obayashi, J. T. & Ellisman, M. H. 2010. Structure-Function Studies of Blood and Air Capillaries in Chicken Lung Using 3d Electron Microscopy. *Respir Physiol Neurobiol*, 170, 202-9.
- White, D. L., Mazurkiewicz, J. E. & Barnett, R. J. 1979. A Chemical Mechanism for Tissue Staining by Osmium Tetroxide-Ferrocyanide Mixtures. *Journal of Histochemistry & Cytochemistry*, 27, 1084-1091.
- White, J. G., Southgate, E., Thomson, J. N. & Brenner, S. 1986. The Structure of the Nervous System of the Nematode *Caenorhabditis Elegans*. *Philosophical Transactions of the Royal Society of London. Series B, Biological Sciences*, 314, 1-340.
- White, R. B., Biérinx, A.-S., Gnocchi, V. F. & Zammit, P. S. 2010. Dynamics of Muscle Fibre Growth During Postnatal Mouse Development. *BMC Dev Biol*, 10.
- White, T. L., Lewis, P., Hayes, S., Fergusson, J., Bell, J., Farinha, L., White, N. S., Pereira, L. V. & Meek, K. M. 2017a. The Structural Role of Elastic Fibers in the Cornea Investigated Using a Mouse Model for Marfan Syndrome. *Invest Ophthalmol Vis Sci*, 58, 2106-2116.
- White, T. L., Lewis, P. N., Young, R. D., Kitazawa, K., Inatomi, T., Kinoshita, S. & Meek, K. M. 2017b. Elastic Microfibril Distribution in the Cornea: Differences between Normal and Keratoconic Stroma. *Exp Eye Res*, 159, 40-48.
- Wilke, S. A., Antonios, J. K., Bushong, E. A., Badkoobehi, A., Malek, E., Hwang, M., Terada, M., Ellisman, M. H. & Ghosh, A. 2013. Deconstructing Complexity: Serial Block-Face Electron Microscopic Analysis of the Hippocampal Mossy Fiber Synapse. *J Neurosci*, 33, 507-22.
- Wilke, S. A., Raam, T., Antonios, J. K., Bushong, E. A., Koo, E. H., Ellisman, M. H. & Ghosh, A. 2014. Specific Disruption of Hippocampal Mossy Fiber Synapses in a Mouse Model of Familial Alzheimer's Disease. *PLoS One*, 9, e84349.
- Wong, M. & Guo, D. 2013. Dendritic Spine Pathology in Epilepsy: Cause or Consequence? *Neuroscience*, 251, 141-150.
- Wool, L. E., Packer, O. S., Zaidi, Q. & Dacey, D. M. 2019. Connectomic Identification and Three-Dimensional Color Tuning of S-Off Midget Ganglion Cells in the Primate Retina. *The Journal of Neuroscience*, 39, 7893-7909.
- Wyckelsma, V. L., Levinger, I., McKenna, M. J., Formosa, L. E., Ryan, M. T., Petersen, A. C., Anderson, M. J. & Murphy, R. M. 2017. Preservation of Skeletal Muscle Mitochondrial Content in Older Adults: Relationship between Mitochondria, Fibre Type and High-Intensity Exercise Training. *J Physiol*, 595, 3345-3359.
- Yadav, S., Williamson, J. K., Aronova, M. A., Prince, A. A., Pokrovskaya, I. D., Leapman, R. D. & Storrie, B. 2017. Golgi Proteins in Circulating Human Platelets Are Distributed across Non-Stacked, Scattered Structures. *Platelets*, 28, 400-408.
- Yam, G. H., Seah, X., Yusoff, N. Z. B. M., Setiawan, M., Wahlig, S., Htoon, H. M., Peh, G. S. L., Kocaba, V. & Mehta, J. S. 2019. Characterization of Human Transition Zone Reveals a Putative Progenitor-Enriched Niche of Corneal Endothelium. *Cells*, 8.
- Yamada, K., Young, R. D., Lewis, P. N., Shinomiya, K., Meek, K. M., Kinoshita, S., Caterson, B. & Quantock, A. J. 2015. Mesenchymal-Epithelial Cell Interactions

- and Proteoglycan Matrix Composition in the Presumptive Stem Cell Niche of the Rabbit Corneal Limbus. *Mol Vis*, 21, 1328-39.
- Yamasaki, R., Lu, H., Butovsky, O., Ohno, N., Rietsch, A. M., Cialic, R., Wu, P. M., Doykan, C. E., Lin, J., Coteleur, A. C., Kidd, G., Zorlu, M. M., Sun, N., Hu, W., Liu, L., Lee, J. C., Taylor, S. E., Uehlein, L., Dixon, D., Gu, J., Floruta, C. M., Zhu, M., Charo, I. F., Weiner, H. L. & Ransohoff, R. M. 2014. Differential Roles of Microglia and Monocytes in the Inflamed Central Nervous System. *J Exp Med*, 211, 1533-49.
- Yang, F., Chen, B., Hashimoto, T., Zhang, Y., Thompson, G. & Robinson, I. 2019a. Investigation of Three-Dimensional Structure and Pigment Surrounding Environment of a Tio(2) Containing Waterborne Paint. *Materials (Basel)*, 12.
- Yang, F., Liu, X., Zhao, Y., Zhang, Y., Wang, P., Robinson, I. & Chen, B. 2018. Investigation of Three-Dimensional Microstructure of Tricalcium Silicate (C(3)S) by Electron Microscopy. *Materials (Basel)*, 11.
- Yang, R., Dzowo, Y. K., Wilson, C. E., Russell, R. L., Kidd, G. J., Salcedo, E., Lasher, R. S., Kinnamon, J. C. & Finger, T. E. 2019b. Three-Dimensional Reconstructions of Mouse Circumvallate Taste Buds Using Serial Blockface Scanning Electron Microscopy: I. Cell Types and the Apical Region of the Taste Bud. *J Comp Neurol*.
- Yao, C. H., Wang, R., Wang, Y., Kung, C. P., Weber, J. D. & Patti, G. J. 2019. Mitochondrial Fusion Supports Increased Oxidative Phosphorylation During Cell Proliferation. *Elife*, 8.
- Youle, R. & Karbowski, M. 2005. Mitochondrial Fission in Apoptosis. *Nat Rev Mol Cell Biol*, 6, 657-663.
- Young, R. D., Knupp, C., Koudouna, E., Ralphs, J. R., Ma, Y., Lwigale, P. Y., Jester, J. V. & Quantock, A. J. 2019. Cell-Independent Matrix Configuration in Early Corneal Development. *Exp Eye Res*, 187, 107772.
- Young, R. D., Knupp, C., Pinali, C., Png, K. M., Ralphs, J. R., Bushby, A. J., Starborg, T., Kadler, K. E. & Quantock, A. J. 2014. Three-Dimensional Aspects of Matrix Assembly by Cells in the Developing Cornea. *Proc Natl Acad Sci U S A*, 111, 687-92.
- Yue, S. & Rind, F. C. 2006. Collision Detection in Complex Dynamic Scenes Using an Lgmd-Based Visual Neural Network with Feature Enhancement. *IEEE Trans Neural Netw*, 17, 705-16.
- Yusuf, M., Chen, B., Hashimoto, T., Estandarte, A. K., Thompson, G. & Robinson, I. 2014. Staining and Embedding of Human Chromosomes for 3-D Serial Block-Face Scanning Electron Microscopy. *Biotechniques*, 57, 302-7.
- Zankel, A., Kraus, B., Poelt, P., Schaffer, M. & Ingolic, E. 2009. Ultramicrotomy in the Esem, a Versatile Method for Materials and Life Sciences. *Journal of Microscopy*, 233, 140-148.
- Zhang, Y., Sher, J. H., Leung, B. & Shafiq, S. A. 1987. An Immunocytochemical Study of Type I Muscle Fibres in Developing Human Skeletal Muscles. *Journal of the Neurological Sciences*, 80, 1-12.
- Zhang, Y., Tsang, T. K., Bushong, E. A., Chu, L.-A., Chiang, A.-S., Ellisman, M. H., Reingruber, J. & Su, C.-Y. 2019. Asymmetric Ephaptic Inhibition between Compartmentalized Olfactory Receptor Neurons. *Nature Communications*, 10.
- Zhao, Y., Liu, X., Chen, B., Yang, F., Zhang, Y., Wang, P. & Robinson, I. 2019. Three-Dimensional Characterization of Hardened Paste of Hydrated Tricalcium Silicate by Serial Block-Face Scanning Electron Microscopy. *Materials (Basel)*, 12.
- Zheng, Z., Lauritzen, J. S., Perlman, E., Robinson, C. G., Nichols, M., Milkie, D., Torrens, O., Price, J., Fisher, C. B., Sharifi, N., Calle-Schuler, S. A., Kmecova,

- L., Ali, I. J., Karsh, B., Trautman, E. T., Bogovic, J. A., Hanslovsky, P., Jefferis, G., Kazhdan, M., Khairy, K., Saalfeld, S., Fetter, R. D. & Bock, D. D. 2018. A Complete Electron Microscopy Volume of the Brain of Adult *Drosophila Melanogaster*. *Cell*, 174, 730-743 e22.
- Zhu, Y., Dewell, R. B., Wang, H. & Gabbiani, F. 2018. Pre-Synaptic Muscarinic Excitation Enhances the Discrimination of Looming Stimuli in a Collision-Detection Neuron. *Cell Rep*, 23, 2365-2378.
- Zhu, Y. & Gabbiani, F. 2016. Fine and Distributed Subcellular Retinotopy of Excitatory Inputs to the Dendritic Tree of a Collision-Detecting Neuron. *J Neurophysiol*, 115, 3101-12.

## Appendix

### Appendix A – Literature Review.

Collection of publications using SBF-SEM found using the search term (((((((serial block face) OR sbfsem) OR sbf-sem) OR sbem) OR sbf-em) OR 3VIEW) OR volume scope)) AND microscopy in PubMed. The category of the publication was defined by the main purpose. Methods describes any paper that described how to prepare (staining), image (technical) and analyse the datasets (analysis), this also included papers which described the method specific to a tissue or aim (experimental). Other papers were designated as either connectomics (neuronal network-based studies) or experimental (for example disease versus control cases). 'Y' Indicated that the raw data are available to download online, and 'N' is not, if the data are available upon request, it is stated as 'upon request'.

Paper	Technique	Details	Software	Segmentation Tool	Sample	Category	Raw Data Online
<i>Denk and Horstmann (2004)</i>	SBF-SEM	FEI QuantaFEG 200	ImageJ and Amira	Manual	Rodent Muscle and Brain	Connectomics/Method (Technical)	Y
<i>Feierbach et al. (2006)</i>	SBF-SEM	FEI QuantaFEG 200	ImageJ	Manual	Mouse Submandibular Ganglia	Experimental	N
<i>Melek et al. (2006)</i>	SBF-SEM	Not Stated	Own Algorithm	Not Stated	Unknown Neural	Method (Analysis)	N
<i>Macke et al. (2008)</i>	SBF-SEM	Not Stated	Own Algorithm Matlab	Automated	Fly Visual System	Method (Analysis)	N
<i>Armer et al. (2009)</i>	FIB-SEM and SBF-SEM	FEI Quanta 3D FEG FIB/SEM and Quanta 200 VP-FEG with Gatan 3View	Amira and Imaris	Not Stated	Zebrafish Embryo	Method (Experimental)	N

<b>Jurru et al. (2009)</b>	SBF-SEM	Not Stated	Insight Segmentation and Registration Toolkit	Manual and Automated	Unknown Brain	Method (Analysis)	N
<b>Rouquette et al. (2009)</b>	SBF-SEM	FEI Quanta 600 VP-FEG with Gatan	Imaris and Amira	Manual	Rat Liver	Method (Experimental)	N
<b>Zankel et al. (2009)</b>	SBF-SEM	Quanta FEG 600 with Gatan 3View	Amira	Thresholding	Polymers and Plant	Method (Technical)	N
<b>Deerinck et al. (2010)</b>	SBF-SEM	Not Stated	None	None	Unknown Brain	Method (Staining)	N
<b>Stabentheiner et al. (2010)</b>	SBF-SEM	Quanta FEG 600 with Gatan 3View	None	None	Plants	Method (Experimental)	N
<b>West et al. (2010)</b>	SBF-SEM	FEI Quanta FEG and Gatan 3view	Amira	Not Stated	Chicken Capillaries Lung	Method (Experimental)	N
<b>Briggman et al. (2011)</b>	SBF-SEM	FEI Quanta FEG 200	KNOSSOS	Manual Skeletonisation	Mouse Retina	Connectomics	N

<b><i>Helmstaedter et al. (2011)</i></b>	SBF-SEM	FEI Quanta FEG 200	KNOSSOS	Manual Skeletonisation	Rabbit and Mouse Retina	Connectomics	Y
<b><i>Lang et al. (2011)</i></b>	SBF-SEM	Not Stated	Neurostruct	Thresholding and automated	Ratn Brain	Method (Analysis)	N
<b><i>Motskin et al. (2011)</i></b>	SBF-SEM	FEI Quanta 600 VP FEG with Gatan 3View	Avizo and Amira	Manual	Human monocyte-macrophages	Experimental	N
<b><i>Mun et al. (2011)</i></b>	SBF-SEM	FEI Quanta FEG 200 with Gatan 3View	IMOD	Not Stated	Melanocytes (Skin)	Experimental	N
<b><i>Rezakhaniha et al. (2011)</i></b>	SBF-SEM	FEI Quanta FEG 200 and Gatan 3View	None	None	Rabbit Artery	Experimental	N
<b><i>Shu et al. (2011)</i></b>	SBF-SEM	FEI Quanta FEG and Gatan 3view	IMOD	Manual	HeLa Cells, C. Elegans and Mouse brain	Method (CLEM)	N
<b><i>Andres et al. (2012)</i></b>	SBF-SEM	FEI Quanta FEG 200	Own Algorithm	Supervoxel/Automated	Mouse Brain	Method (Analysis)	Y (Helmstaedter et al, 2011)



<b>Anttonen et al. (2012)</b>	SBF-SEM	FEI Quanta FEG 250 with Gatan 3View	MIB and Amira	Not Stated	Mouse Cochlea	Experimental	N
<b>Giuly et al. (2012)</b>	SBF-SEM	FEI Quanta with Gatan 3View	Own Algorithm	Automated	Mouse brain	Method (Analysis)	N
<b>Mikula et al. (2012)</b>	SBF-SEM	Zeiss Merlin with Atlas	None	None	Mouse brain	Method (Staining)	N
<b>Mullner et al. (2012)</b>	SBF-SEM	FEI Quanta 600 FEG with Gatan 3View	Fiji and Matlab	Manual	Polymer	Experimental	N
<b>Puhka et al. (2012)</b>	SBF-SEM	FEI Quanta FEG 250 with Gatan 3View	MIB and Amira	Not Stated	Cultured Cells	Experimental	N
<b>Schwartz et al. (2012)</b>	SBF-SEM	FEI Quanta 600 with Gatan 3View	IMOD	Manual	<i>Giardia lamblia</i> trophozoite cells	Experimental	N
<b>Chen et al. (2013)</b>	SBF-SEM	Not stated	Amira	Not Stated	Polymer	Experimental	N

<b><i>Helmstaedter et al. (2013)</i></b>	SBF-SEM	FEI Quanta FEG 200	KNOSSOS	Manual Skeletonisation	Mouse Retina	Connectomics	Y
<b><i>Hermes et al. (2013)</i></b>	SBF-SEM	3View	IMOD	Manual	Mouse Liver	Experimental	N
<b><i>Holcomb et al. (2013)</i></b>	SBF-SEM	FEI Quanta FEG and Zeiss Merlin with Gatan 3View	IMOD	Manual	Mouse Brain	Experimental	N
<b><i>Hughes et al. (2013)</i></b>	SBF-SEM and sTEM	FEI Quanta FEG 250 with Gatan 3View	IMOD and Amira	Manual and Semi-automatic	<i>Trypanosoma brucei</i>	Experimental	N
<b><i>Kalson et al. (2013)</i></b>	SBF-SEM	FEI Quanta FEG 250 with Gatan 3View	IMOD	Manual	Chicken Embryo Tendon	Experimental	N
<b><i>Lafontant et al. (2013)</i></b>	SBF-SEM	FEI Quanta FEG 200 with Gatan 3View	Amira	Not Stated	Zebrafish Cardiac Muscle	Experimental	N
<b><i>Pinali et al. (2013)</i></b>	SBF-SEM	FEI Quanta FEG 250 with Gatan 3View	Fiji and IMOD	Contrast Based and Manual	Sheep and Rat Cardiac Muscle	Experimental	N

<b>Starborg et al. (2013)</b>	SBF-SEM	FEI Quanta FEG 250 with Gatan 3View	IMOD, ImageJ	Manual	Animal and Human Tendons, Skin, Kidney and Cardiac and Smooth Muscle	Method (Experimental)	Y (portion)
<b>Titze and Denk (2013)</b>	SBF-SEM	FEI Quanta FEG 200 and Zeiss Merlin	None	None	Various Neural Tissue	Method (Technical)	Y (portion)
<b>Wilke et al. (2013)</b>	SBF-SEM	FEI Quanta FEG with Gatan 3View	IMOD	Manual	Mouse Brain	Experimental	N
<b>Wong and Guo (2013)</b>	SBF-SEM	FEI Quanta FEG with Gatan 3View	IMOD and Amira	Not Stated	Mouse Cardiomyocytes	Experimental	N
<b>Anttonen et al. (2014)</b>	SBF-SEM	FEI Quanta FEG with Gatan 3View	MIB and Amira	Manual and semi-automated	Mouse hair cells (ear)	Experimental	N
<b>Arkill et al. (2014)</b>	SBF-SEM and FIB-SEM	FEI Quanta FEG 250 with Gatan 3View	ImageJ, IMOD, Amira and Fiji	Not Stated	Rat and Human Kidney	Method (Experimental)	N
<b>Bohórquez et al. (2014)</b>	SBF-SEM	Zeiss Sigma VP with Gatan 3View	Imaris	Manual	Mouse Intestine	Experimental	N

<b>Bushong et al. (2014)</b>	SBF-SEM	Zeiss Merlin with Gatan 3View	None	None	Mouse Brain	Method (CLEM)	N
<b>Dettmer et al. (2014)</b>	SBF-SEM	FEI Quanta FEG 250 with Gatan 3View	MIB and Amira	Not Stated	<i>Arabidopsis</i> root	Experimental	N
<b>Dziasko et al. (2014)</b>	SBF-SEM	Zeiss Sigma VP with Gatan 3View	Amira	Manual	Human Cornea Cells	Experimental	N
<b>Gillies et al. (2014)</b>	SBF-SEM	Zeiss Sigma VP with Gatan 3View	IMOD and ANALYZE	Manual and Thresholding	Mouse Skeletal Muscle	Method (Experimental)	N
<b>Hammer et al. (2014)</b>	SBF-SEM	Not Stated	Fiji (TrakEM2)	Manual	Mouse Retina	Experimental	N
<b>Hughes et al. (2014)</b>	SBF-SEM	3View	Fijie and Avizo	Not Stated	Polymer	Experimental	N
<b>Lipke et al. (2014)</b>	ssTEM and SBF-SEM	JEOL JEM 1011 TEM and FEI Quanta FEG 250 with Gatan 3View	Amira	Manual	<i>Philodromus</i> Spermatozoa	Method (Experimental)	N

<b>Majaneva et al. (2014)</b>	SBF-SEM	FEI Quanta FEG 250 with Gatan 3View	MIB	Not Stated	Cryptomonads	Experimental	N
<b>Miyazaki et al. (2014)</b>	SBF-SEM	Zeiss Sigma VP with Gatan 3View	Amira	Manual	Yeast	Experimental	N
<b>Mustafi et al. (2014)</b>	SBF-SEM	FEI Quanta FEG 200 with Gatan 3View	Reconstruct	Auto Training and Manual	Mouse Retina	Method (Experimental)	N
<b>Perez et al. (2014)</b>	SBF-SEM	Not Stated	IMOD	Own Algorithm	Unknown Brain	Method (Analysis)	N
<b>Pinali and Kitmitto (2014)</b>	SBF-SEM	FEI Quanta FEG 250 with Gatan 3View	Fiji and IMOD	Manual and Thresholding	Sheep and Rat Cardiac Muscle	Method (Experimental)	N
<b>Pingel et al. (2014)</b>	SBF-SEM	FEI Quanta FEG 250 with Gatan 3View	IMOD	Not Stated	Human Tendon	Experimental	N
<b>Salloum et al. (2014)</b>	SBF-SEM	Zeiss Sigma VP with Gatan 3View	Fiji (TrakEM2) and Blender (Neuromorph)	Manual	Hamster Cochlear	Experimental	N

<b>Togo et al. (2014)</b>	SBF-SEM	Quanta 3D FEG	None	None	Mouse liver	Method (Staining)	N
<b>Tsai et al. (2014)</b>	SBF-SEM, FIB-SEM and TEM	Gatan 3View	Chimera, Amira and Matlab	Manual, Semi-Automatic and Automated	Plant, Bacteria, Eukaryote cells, mammary glands, inner ear hair cell	Method (Analysis)	N
<b>Wilke et al. (2014)</b>	SBF-SEM	FEI Quanta FEG SEM	IMOD	Manual and Interpolation	Mouse Brain	Experimental	N
<b>Yamasaki et al. (2014)</b>	SBF-SEM	Zeiss Sigma VP with Gatan 3View	Fiji(TrakEM2)	Manual	Mouse Spinal Cord	Experimental	N
<b>Young et al. (2014)</b>	SBF-SEM and FIB-SEM	FEI Quanta 3D FE FIB and FEI Quanta FEG 250 with Gatan 3View	ImageJ/Fiji	Manual	Chicken Embryonic Cornea	Experimental	N
<b>Yusuf et al. (2014)</b>	SBF-SEM	FEI Quanta FEG 250 with Gatan 3View	Avizo	Manual	Cultured Lymphocytes	Method (Experimental)	N
<b>Bellesi et al. (2015)</b>	SBF-SEM	Zeiss Sigma VP with Gatan 3View	Fiji (TrakEM2)	Manual	Mouse Brain	Experimental	N

<b>Berning et al. (2015)</b>	SBF-SEM	FEI Quanta FEG 200	SegEM	Automated	Mouse Retina	Method (Analysis)	N
<b>Biazik et al. (2015a)</b>	SBF-SEM	FEI Quanta FEG 250 with Gatan 3View	IMOD	Manual	Cultured Cells	Method (Experimental/CLEM)	N
<b>Biazik et al. (2015b)</b>	SBF-SEM	FEI Quanta FEG 250 with Gatan 3View	IMOD	Manual	Rat Kidney Cultured Cells	Experimental	N
<b>Blumer et al. (2015)</b>	SBF-SEM	FEI Quanta FEG 200 with Gatan 3View	Own Algorithm	Automated	Unknown Brain	Method (Analysis/CLEM)	N
<b>Bohórquez et al. (2015)</b>	SBF-SEM	Zeiss Sigma VP with Gatan 3View	Imaris	Manual	Mouse Colon	Method (Experimental/CLEM)	N
<b>Breidenbach et al. (2015)</b>	SBF-SEM	Not Stated	IMOD	Interpolation and Manual	Mouse Tendon	Experimental	N
<b>Chavan et al. (2015)</b>	SBF-SEM	Zeiss Sigma VP with Gatan 3View	Fiji(TrakEM2)	Not Stated	Mouse Brain	Experimental	N

<b>Chuang et al. (2015)</b>	SBF-SEM and FIB-SEM	3View and FEI Helios Nanolab 650	IMOD	Not Stated	Mouse Retina	Experimental	N
<b>Dow et al. (2015)</b>	SBF-SEM	Zeiss Sigma VP with Gatan 3View	Fiji, Blender and Reconstruct	Manual	Zebrafish Nerve Cells (hair cell)	Experimental	N
<b>Gluenz et al. (2015)</b>	SBF-SEM	FEI Quanta FEG 250 with Gatan 3View	IMOD and Amira	Manual and Thresholding	<i>Trypanosoma brucei</i> and <i>Leishmania mexicana</i>	Method (Experimental)	N
<b>Hammer et al. (2015)</b>	SBF-SEM	Zeiss Sigma VP with Gatan 3View	Fiji(TrakEM2)	Manual	Mouse Retina	Experimental	N
<b>Hanlon et al. (2015)</b>	SBF-SEM	FEI Quanta FEG 250 with Gatan 3View	Amira	Not Stated	Mouse Cornea	Experimental	N
<b>Ichimura et al. (2015)</b>	FIB-SEM and SBF-SEM	Helios Nanolab 650 and Zeiss Sigma VP with Gatan 3View	Amira	Not Stated	Rat Kidney	Experimental	N
<b>Jungreuthmaier et al. (2015)</b>	SBF-SEM	FEI Quanta FEG 600 with Gatan	ImageJ	Not Stated	Polymer	Experimental	N



<b>Kleesattel et al. (2015)</b>	SBF-SEM	Zeiss Sigma VP with Gatan 3View	Reconstruct	Not Stated	Mouse Optic Nerve	Experimental	N
<b>Kreshuk et al. (2015)</b>	SBF-SEM	Quanta 200 VP FEG with Gatan 3View	Own Algorithm	Automated	Rat Nerve	Method (Analysis)	N
<b>Mikula and Denk (2015)</b>	SBF-SEM	FEI Quanta FEG 200 and Zeiss Merlin	None	None	Mouse brain	Method (Staining)	Y
<b>Neves and Reichert (2015)</b>	SBF-SEM	FEI Quanta FEG 200 with Gatan 3View	Fiji(TrakEM2 )	Manual	<i>Symbion Pandora</i>	Experimental	N
<b>Ou et al. (2015)</b>	SBF-SEM	FEI Quanta FEG or Zeiss Merlin with Gatan 3View	IMOD	Manual and Interpolation	Cells	Method (CLEM)	N
<b>Pallotto et al. (2015)</b>	SBF-SEM	FEI NanoSEM 450	Knossos	Automated and Skeletonisation	Mouse Brain and Retina	Method (Staining)	Y
<b>Pfeifer et al. (2015)</b>	SBF-SEM	Zeiss Sigma VP with Gatan 3View (HV)	Amira	Manual	Mouse Pancreas	Experimental	N

<b><i>Pinali et al. (2015)</i></b>	SBF-SEM	FEI Quanta FEG 250 with Gatan 3View	IMOD and Fiji	Not Stated	Sheep heart	Experimental	N
<b><i>Shomorony et al. (2015)</i></b>	SBF-SEM	Zeiss Sigma VP with Gatan 3View (HV)	Amira	Not Stated	Mouse Pancreas	Method (Experimental)	N
<b><i>Szczesny et al. (2015)</i></b>	SBF-SEM	Zeiss Merlin VP with Gaan 3View 2XP	Fiji	Matlab Algoritihim	Rat Tendon	Experimental	N
<b><i>Wernitznig et al. (2015)</i></b>	SBF-SEM	FEI Quanta FEG 600 ESEM	Amira	Manual	Locust Optic Lobe	Connectomics	N
<b><i>Yamada et al. (2015)</i></b>	SBF-SEM	Zeiss Sigma VP with Gatan 3View	ImageJ and Amira	Manual and Automated	Rabbit and Human Cornea	Experimental	N
<b><i>Belevich et al. (2016)</i></b>	SBF-SEM	FEI Quanta FEG 250 with Gatan 3View	MIB	Manual, Semi-Automatic and Automated	Cultured cells, plant roots and mouse cochlea	Method (Analysis)	N
<b><i>Booth et al. (2016)</i></b>	SBF-SEM	Not Stated with Gatan 3View	Amira	Masking, Thresholding, Magic Wand and Blow Tools	Cultured Cells	Method (CLEM)	N

<b><i>Brama et al. (2016)</i></b>	SBF-SEM	Zeiss Sigma VP with Gatan 3View	None	None	HeLa Cells	Method (CLEM)	Y
<b><i>Büsse et al. (2016)</i></b>	SBF-SEM	FEI Quanta FEG 250 with Gatan 3View	Amira	Not Stated	Arthropod	Experimental	Y
<b><i>Ding et al. (2016)</i></b>	SBF-SEM	Quanta FEG 200 and custom made ultramicrotome	Webknossos	Manual (skeletonisation)	Mouse Retina	Connectomics	N
<b><i>Feng et al. (2016)</i></b>	SBF-SEM	Zeiss Sigma VP with Gatan 3View	Fiji and IMOD	Manual and Interpolation	Prawn Spermatozoa	Experimental	N
<b><i>Han et al. (2016)</i></b>	SBF-SEM	FEI Quanta FEG 250 with Gatan 3View	IMOD	Manual	Human Pancreas	Experimental	N
<b><i>Hashimoto et al. (2016)</i></b>	SBF-SEM	FEI Quanta FEG 250 with Gatan 3View	Not Stated	Thresholding	Polymer	Method (Experimental/Technical)	N
<b><i>Hondow et al. (2016)</i></b>	SBF-SEM	FEI Quanta FEG 250 with Gatan 3View 2XP	Fiji and Imaris	Not Stated	Cells	Method (Technical)	N

<b><i>Jakob et al. (2016)</i></b>	SBF-SEM	FEI Quanta FEG 250 with Gatan 3View 2XP	IMOD	Not Stated	<i>Trypanosoma brucei</i>	Experimental	N
<b><i>Kaiser et al. (2016)</i></b>	SBF-SEM	FEI Quanta FEG 250 with Gatan 3View 2XP	Fiji	Not Stated	<i>Plasmodium berghei</i> Parasite in HeLa Cells	Experimental	N
<b><i>Kaji et al. (2016)</i></b>	SBF-SEM	Zeiss Sigma VP and Merlin with Gatan 3View	Imaris	Not Stated	Tanaid Crustacean	Experimental	N
<b><i>Kittelmann et al. (2016)</i></b>	SBF-SEM	Zeiss Merlin VP with Gatan 3View 2XP	Various Use	Range	Plant Cell Membrane	Method (Experimental/Technical)	N
<b><i>Lewis et al. (2016)</i></b>	SBF-SEM	Zeiss Sigma VP System with Gatan 3View2	Amira	Not Stated	Human Cornea	Experimental	N
<b><i>Mukherjee et al. (2016)</i></b>	SBF-SEM	Zeiss Sigma VP with Gatan 3View	Fiji (TrakEM2)	Manual	Mouse Brain	Experimental	N
<b><i>Nguyen et al. (2016)</i></b>	SBF-SEM	Zeiss Sigma VP and Merlin with Gatan 3View	Fiji(TrakEM2 ) and Amira	Not Stated	Mouse Brain and Kidney	Method (Staining)	N

<b>Nkwe et al. (2016)</b>	SBF-SEM	Zeiss Sigma VP with Gatan 3View	Amira and Fiji (TrakEM2)	Manual	Infected Human Macrophage	Experimental	N
<b>Pipkin et al. (2016)</b>	SBF-SEM	FEI Quanta FEG and Zeiss Merlin with Gatan 3View	IMOD and Fiji	Manual	Leech Nervous System	Experimental	N
<b>Randles et al. (2016)</b>	SBF-SEM	FEI Quanta FEG 250 with Gatan 3View	IMOD	Manual	Mouse Kidney	Experimental	N
<b>Rind et al. (2016)</b>	SBF-SEM	FEI Quanta FEG 600 ESEM with Gatan 3View	Amira	Not Stated	Locust Optic Lobe	Connectomics	N
<b>Sakaguchi et al. (2016)</b>	SBF-SEM	Zeiss Merlin with Gatan 3View	Amira	Manual and Automated	Cultured Parasite in Human Red Blood Cell	Experimental	N
<b>Shami et al. (2016)</b>	SBF-SEM	Zeiss Sigma VP with Leica Microtome	ImageJ and IMOD	Manual	Rat Liver	Method (Experimental/CLEM)	N
<b>Smith et al. (2016)</b>	SBF-SEM	Zeiss Sigma VP with Gatan 3View	Synapse Web Reconstruct	Not Stated	Mouse Retina	Experimental/Connectomics	N

<b>Stucki et al. (2016)</b>	SBF-SEM	FEI Quanta FEG 250 with Gatan 3View 2XP	UCSF Chimera and IMOD	Not Stated	Mouse Cerebellum	Experimental	N
<b>Thai et al. (2016)</b>	SBF-SEM	Zeiss Sigma or Merlin with Gatan 3View	Fiji (TrakEM2) and Amira	Not Stated	Mouse Skeletal Muscle, Cerebrum and Kidney	Method (Staining)	N
<b>Vincent et al. (2016)</b>	SBF-SEM	Zeiss Sigma with Gatan 3View	IMOD	Manual	Human Muscle	Experimental	N
<b>Wanner et al. (2016a)</b>	Wanner et al. (2016a) SBF-SEM	FEI Quanta FEG 200 with Gatan 3View	PyKnossos	Manual	Zebrafish Olfactory Bulb	Connectomics	Y
<b>Wanner et al. (2016b)</b>	SBF-SEM	FEI Quanta FEG 200 with Gatan 3View	PyKnossos	Manual+E86	Zebrafish Olfactory Bulb	Connectomics	N
<b>Wernitznig et al. (2016)</b>	SBF-SEM	FEI Quanta FEG 600 ESEM	Amira and Own Tool	Manual and Semi-automatic	Locust Optic Lobe	Connectomics	N
<b>Agrawal et al. (2017)</b>	SBF-SEM	Zeiss Sigma VP with Gatan 3View	Amira	Not Stated	Mouse Eye	Experimental	N

<b><i>Bellesi et al. (2017)</i></b>	SBF-SEM	Zeiss Sigma VP with Gatan 3View	Fiji (TrakEM2)	Manual	Mouse Brain	Experimental	N
<b><i>Boergens et al. (2017)</i></b>	SBF-SEM	FEI Quanta with Custom Built SBEM	Webknossos	Manual and Semi-automatic	Mouse Brain	Connectomics	N
<b><i>Bouwer et al. (2017)</i></b>	SBF-SEM	FEI Quanta FEG 250 with Gatan 3View	None	None	Unknown Brain	Method (Technical)	N
<b><i>Cabezón et al. (2017)</i></b>	SBF-SEM	FEI Quanta FEG 250 with Gatan 3View	Imaris	Not Stated	Mouse Brain	Method (Experimental)	N
<b><i>Chai et al. (2017)</i></b>	SBF-SEM	Zeiss Sigma VP with Gatan 3View	Reconstruct	Not Stated	Mouse Brain	Experimental	N
<b><i>Chen et al. (2017)</i></b>	SBF-SEM	FEI Quanta FEG 250 with Leica Ultramicrotome	Avizo	Not Stated	Cultured Cells	Experimental	N
<b><i>Chung et al. (2017)</i></b>	SBF-SEM	FEI Quanta FEG 250 with Gatan 3View	Avizo	Intensity-based Thresholding	Rat Lung	Experimental	N

<b>Colman et al. (2017)</b>	SBF-SEM	FEI Quanta FEG 250 with Gatan 3View	IMOD and Fiji	Manual and Thresholding	Sheep Cardiac Muscle	Experimental	N
<b>Daum et al. (2017)</b>	SBF-SEM	FEI Quanta and Zeiss Merlin with Gatan 3View	Fiji (TrakEM2)	Manual	Mouse Retina	Experimental	N
<b>Dorkenwald et al. (2017)</b>	SBF-SEM	FEI Quanta FEG 200 and Zeiss Merlin	Own Algorithm	Automated	Zebrafish, Songbird and mouse brain	Method (Analysis)	N
<b>Fredericksen et al. (2017)</b>	SBF-SEM	Zeiss Sigma VP with Gatan 3View	Avizo and Amira	Deep Learning Model	Fungal Parasite in Ant Muscle	Experimental	Y
<b>Gan et al. (2017)</b>	SBF-SEM	Zeiss Sigma with Gatan 3View	IMOD	Not Stated	Mouse Pancreas	Experimental	N
<b>Giarmarco et al. (2017)</b>	SBF-SEM	Zeiss Sigma VP with Gatan 3View 2XP	Fiji (TrakEM2)	Manual	Zebrafish Retina	Experimental	N
<b>Gillies et al. (2017)</b>	SBF-SEM	Zeiss Sigma	IMOD	Manual	Mouse Skeletal Muscle	Experimental	N



<b>Godwin et al. (2017)</b>	SBF-SEM	FEI Quanta FEG 250 with Gatan 3View	UCSF Chimera	Not Stated	Mouse Cartilage	Experimental	N
<b>Hoover et al. (2017)</b>	SBF-SEM and ssSEM	Zeiss Sigma VP with Gatan 3View and ATUMtome	Imaris	Manual	Mouse Intestine	Method (Experimental/CLEM)	N
<b>Hughes et al. (2017)</b>	SBF-SEM	FEI Quanta FEG 250 with Gatan 3View	Amira	Manual and Thresholding	<i>Trypanosoma brucei</i>	Experimental	N
<b>Ichimura et al. (2017)</b>	FIB-SEM and SBF-SEM	FEI Helios Nanolab 650 or Hitachi MI4000L and Zeiss Sigma VP with Gatan 3View	Amira	Not Stated	Rat Kidney	Experimental	N
<b>Kornfeld et al. (2017)</b>	SBF-SEM	Zeiss Ultraplus	Knossos	Manual	Bird Brain	Connectomics	Y
<b>Liang et al. (2017)</b>	SBF-SEM	Zeiss Sigma VP with Gatan 3View	Fiji (TrakEM2)	Manual	Mouse Brain	Experimental	N
<b>Martin et al. (2017)</b>	SBF-SEM	Zeiss Sigma VP with Gatan 3View	Fiji (TrakEM2)	Manual	Mouse Brain	Experimental/Connectomics	N

<b>Meyer et al. (2017)</b>	SBF-SEM	FEI Magellan 400 with Gatan 3View	Imaris	Intensity Thresholding and Size Filtering	Mouse Liver	Experimental	N
<b>Nakao et al. (2017)</b>	SBF-SEM	Zeiss Merlin with Gatan 3View	Fiji, Reconstruct and Amira	Not Stated	Mouse Brain	Experimental	N
<b>Nixon et al. (2017)</b>	SBF-SEM	FEI Quanta FEG 250 with Gatan 3View	Amira	Manual	HeLa Cells	Experimental	N
<b>Palaologou et al. (2017)</b>	SBF-SEM	FEI Quanta FEG 250 with Gatan 3View	Amira	Thresholding	Human Placenta	Experimental	N
<b>Pinali et al. (2017)</b>	SBF-SEM	FEI Quanta FEG 250 with Gatan 3View	IMOD	Not Stated	Pig Cardiac Muscle	Experimental	N
<b>Plachno et al. (2017)</b>	SBF-SEM	Zeiss Sigma with Gatan 3View	Imaris	Manual	Plant Cell	Experimental	N
<b>Sabbah et al. (2017)</b>	SBF-SEM	Quanta FEG 200 and custom made ultramicrotome	Knossos	Manual	Mouse Retina	Experimental/Connectomic	N

<b>Sai et al. (2017)</b>	SBF-SEM	Zeiss Merlin and JEOL JSM-7800F with Gatan 3View	Amira	Manual	Mouse Brain	Experimental	N
<b>Svensson et al. (2017)</b>	FIB-SEM and SBF-SEM	FEI Quanta FEG 3D and FEI Quanta FEG 250 with Gatan 3View	Amira	Manual	Human and Mouse Tendon	Experimental	N
<b>Szczesny et al. (2017)</b>	SBF-SEM	Zeiss Merlin VP with Gatan 3View 2XP	Amira	Region Growing Algorithm	Rat Tendon	Experimental	N
<b>Walker et al. (2017)</b>	SBF-SEM	JEOL JSM-7100F with Gatan 3View 2XP	Fiji (TrakEM2) and Blender (Neuromorph)	Manual	Mouse Brain	Experimental	N
<b>White et al. (2017a)</b>	SBF-SEM	Zeiss Sigma VP with Gatan 3View2	Amira	Not Stated	Mouse Cornea	Experimental	N
<b>White et al. (2017b)</b>	SBF-SEM	Zeiss Sigma VP with Gatan 3View2	Amira	Not Stated	Human Cornea	Method (Experimental/Staining)	N
<b>Yadav et al. (2017)</b>	SBF-SEM	Zeiss Sigma VP with Gatan 3View	Digital Micrograph	Only Aligned	Human Platelets	Experimental	N

<b>Attiger et al. (2018)</b>	ssTEM and SBF-SEM	FEI Quanta FEG 250 with Gatan 3View	Fiji (TrakEM2) and Imapis	Manual	Trophoblasts	Experimental	N
<b>Bleck et al. (2018)</b>	FIB-SEM and SBF-SEM	ZEISS Crossbeam 540 using the ZEISS Atlas 5 software and Zeiss Sigma VP with Gatan 3View	Ilastik	Semi-automatic (pixel classifier)	Mouse Skeletal and Cardiac Muscle	Experimental	N
<b>Bleckert et al. (2018)</b>	SBF-SEM	Zeiss Sigma VP with Gatan 3View	TrakEM2 and KNOSSOS	Manual	Mouse Retina	Experimental	N
<b>Boergens et al. (2018)</b>	SBF-SEM	FEI Quanta with Custom Built SBEM	KNOSSOS, webKNOSS OS and Amira	Manual (skeletonisation)	<i>Drosophila melanogaster</i> Brain	Connectomics	Y
<b>Bolasco et al. (2018)</b>	SBF-SEM	Zeiss Gemini 330VP with Gatan 3View	Fiji, IMOD and Blender	Manual	Mouse Brain	Experimental	N
<b>Cetina et al. (2018)</b>	SBF-SEM and FIB-SEM	FEI Quanta with Gatan 3View	Own Algorithm	Semi-automatic/Automated	Mouse Brain	Method (Analysis)	Y

<b>Chung et al. (2018)</b>	ssTEM and SBF-SEM	FEI Tecnai G2 Spirit BioTWIN and Zeiss with Gatan 3View	Amira	Manual	HeLa Cells	Experimental (CLEM)	N
<b>Clarke and Royle (2018)</b>	SBF-SEM	Unknown	Unknown	Not Stated	Unknown	Not Known	N
<b>Cocks et al. (2018)</b>	SBF-SEM	Zeiss Sigma VP with Gatan 3View	Fiji (TrakEM2), MIB and Amira	Manual and Semi-automatic	Locust Optic Lobe and Guinea Pig Muscle	Method (Analysis)	Y
<b>Deerinck et al. (2018)</b>	SBF-SEM	Zeiss Gemini 300 and Merlin with Gatan 3View	None	None	Culture Cells and various Tissue	Method (Technical)	N
<b>Drawitsch et al. (2018)</b>	SBF-SEM	Custom SBEM microtome in FEI Verios	KNOSSOS	Skeletonisation	Mouse Brain	Experimental/Connectomics. Methods	Y
<b>Eustaquio et al. (2018)</b>	SBF-SEM	Zeiss Merlin VP with Gatan 3View 2XP	IMOD and Amira	Manual	Mouse Frontal Cortex	Experimental	N
<b>Feeney et al. (2018)</b>	SBF-SEM	Zeiss Merlin Compact with Gatan 3View	IMOD	Manual	Arabidopsis	Experimental	N

<b><i>Funke et al. (2018)</i></b>	SBF-SEM, FIB-SEM and ssTEM	FEI Quanta FEG 200, Philips Tecnai 12	Own Algorithm (3D-Unet)	Flood filling	Drosophila and Mouse Brain	Method (Analysis)	N
<b><i>Genoud et al. (2018)</i></b>	SBF-SEM	Zeiss Merlin VP with Gatan 3View and Quanta 200 VP FEG	None	None	Zebrafish Brain	Method (Experimental)	N
<b><i>Giacci et al. (2018)</i></b>	SBF-SEM	Zeiss Sigma VP with Gatan 3View 2XP	MIB	Not Stated	Rat Optic Nerve	Experimental/Connectomics	N
<b><i>Gjoni et al. (2018)</i></b>	SBF-SEM	Zeiss Merlin with Gatan 3View	Fiji (TrakEM2) and Blender (Neuromorph)	Manual	Mouse Brain	Connectomics	N
<b><i>Godwin et al. (2018)</i></b>	SBF-SEM	Quanta FEG 250 with Gatan 3View	IMOD and Amira	Manual	Bovine Eye	Experimental	N
<b><i>Graydon et al. (2018)</i></b>	SBF-SEM	Quanta FEG 200 and custom made ultramicrotome	Webknossos	Manual (skeletonisation)	Mouse Retina	Experimental/Connectomics	N)
<b><i>Grillo et al. (2018)</i></b>	SBF-SEM	JEOL JSM-7100F with Gatan 3View 2XP	Fiji (TrakEM2) and Blender (Neuromorph)	Manual	Mouse Brain	Experimental	N

<b>He et al. (2018)</b>	SBF-SEM	Zeiss Sigma VP with Gatan 3View	IMOD and Amira	Not Stated	Mouse Liver	Method (Technical)	N
<b>Hussain et al. (2018)</b>	SBF-SEM	FEI Teneo VolumeScop e and Zeiss Sigma VP with Gatan 3View	Own Algorithm	Manual, Semi-Automated and Automated	Rat Cardiac Muscle	Method (Analysis)	Y (portion)
<b>Januszewski et al. (2018)</b>	SBF-SEM	FEI QuantaFEG 200	Own Algorithm	Flood filling	Mouse Brain	Method (Analysis)	N
<b>karthik et al. (2018)</b>	SBF-SEM	Quanta FEG 250 with Gatan 3View	Imaris	Not Stated	Zebrafish Embryo	Experimental (CLEM)	N
<b>Kerov et al. (2018)</b>	SBF-SEM	Zeiss and Gatan 3View	Not Stated	Not Stated	Mouse Retina	Experimental	N
<b>Maclachlan et al. (2018)</b>	SBF-SEM	Zeiss Merlin with Gatan 3View	Fiji (TrakEM2)	Manual	Mouse Brain	Method (Technical)	N
<b>McBride et al. (2018)</b>	SBF-SEM	Zeiss Sigma VP with Gatan 3View	Amira	Manual	Human Platelets	Method (Technical)	N

<b>McGlynn et al. (2018)</b>	SBF-SEM	Zeiss Merlin VP with Gatan 3View	IMOD	Manual	Microbials	Experimental (CLEM)	N
<b>Mutha et al. (2018)</b>	SBF-SEM	Zeiss Sigma with Gatan 3View	Amira	Manual	Bacteria	Experimental	N
<b>Navarro et al. (2018)</b>	SBF-SEM	FEI Quanta FEG 200 with Gatan 3View	Fiji (TrakEM2)	Manual	Human Brain	Experimental	N
<b>Neuhaus et al. (2018)</b>	SBF-SEM and FIB-SEM	Zeiss Sigma VP with Gatan 3View and Crossbeam Auriga 40 and 60	ImageJ and Amira	Not Stated	Human Bladder	Experimental	N
<b>Nguyen et al. (2018)</b>	SBF-SEM	Zeiss Sigma or Merlin with Gatan 3View	Fiji (TrakEM2)	Manual	Mouse Brain	Experimental	N
<b>Pipkin et al. (2018)</b>	SBF-SEM	Zeiss Merlin VP with Gatan 3View	Fiji (TrakEM2)	Manual	Leech Nervous System	Connectomics	N
<b>Pollreisz et al. (2018)</b>	SBF-SEM	Zeiss Sigma VP with Gatan 3View	Fiji/ImageJ	Plugins	Human Eyes	Experimental	N



<b>Rajagopal et al. (2018)</b>	SBF-SEM	Unknown	Unknown	Not Stated	Unknown	Not Known	N
<b>Salo et al. (2018)</b>	SBF-SEM	Quanta FEG 250 with Gatan 3View	MIB	Not Stated	Rat Brain	Experimental	N
<b>Samejima et al. (2018)</b>	SBF-SEM	Gatan 3View	Amira	Manual and Semi-automatic	Cells	Experimental	N
<b>Sandulescu et al. (2018)</b>	SBF-SEM	Zeiss Sigma	AutoCAD	Not Stated	Human Skin	Experimental	N
<b>Svara et al. (2018)</b>	SBF-SEM	Zeiss Ultraplus	KNOSSOS	Manual	Zebrafish Larval Spinal Cord	Connectomics	N
<b>Takeichi et al. (2018)</b>	SBF-SEM	Zeiss Sigma VP and Marlin with Gatan 3View	Amira	Manual	Ants, <i>Camponotus japonicus</i> , olfactory	Experimental	N
<b>Titze et al. (2018)</b>	SBF-SEM	Zeiss SEM with Gatan 3View	None	None	Example Brain	Method (Technical)	Y

<b><i>Tsang et al. (2018)</i></b>	SBF-SEM	Zeiss Merlin with Gatan 3View	IMOD	Manual	Drosophila Antenna and Mouse brain	Method (Staining)	N
<b><i>Vanslebrouck et al. (2018)</i></b>	SBF-SEM and FIB-SEM	Zeiss Merlin with Gatan 3View2 and Zeiss Crossbeam 540 with Atlas5	Fiji (TrakEM2), MIB and Imaris	Manual	Mouse Cardiac Muscle	Experimental	N
<b><i>Yang et al. (2018)</i></b>	SBF-SEM	Zeiss Sigma VP with Gatan 3View	None	None	Polymer	Experimental	N
<b><i>Abdollahzadeh et al. (2019)</i></b>	SBF-SEM	FEI Quanta 250 with Gatan 3View	MIB and Own algorithm	Automated	Rat Brain	Experimental/Method (Analysis)	N
<b><i>Alvarez et al. (2019)</i></b>	SBF-SEM and FIB-SEM	Helios G4 UX Systems and Teneo Volume Scope	None	None	Polymer	Experimental	N
<b><i>Booth et al. (2019)</i></b>	SBF-SEM	FEI Quanta 250 FEG with Gatan 3View	Amira	Blow Tool	Mice Cultured Cells (Dorsal Root Ganglia)	Method (CLEM)	N
<b><i>Buchacker et al. (2019)</i></b>	SBF-SEM	Zeiss Merlin VP with Gatan 3View	Own Algorithm	Semi-Automated	Mouse Capillary Lung	Experimental/Method (Analysis)	N

<b><i>Cali et al. (2019)</i></b>	SBF-SEM	Gatan 3view with FEI Quanta 200	Fiji, TrakEM2, Ilastik and Blender	Semi-automated and manual	Rat Brain	Experimental	N
<b><i>Courson et al. (2019)</i></b>	SBF-SEM	Mira 3 with Gatan 3View	Amira	Manual	Mouse Cornea	Experimental	N
<b><i>de Vivo et al. (2019)</i></b>	SBF-SEM	Zeiss Sigma VP with Gatan 3View	Fiji (TrakEM2)	Manual	Mouse brain	Experimental	N
<b><i>Fischbach et al. (2019)</i></b>	SBF-SEM	Zeiss Sigma VP with Gatan 3View	Reconstruct	Not Stated	Mouse Brain	Experimental	N
<b><i>Graves et al. (2019)</i></b>	SBF-SEM	Zeiss Merlin VP with Gatan 3View	IMOD and Amira	semi-automated (thresholding and interpolation)	Cultured Cells and virus	Experimental	N
<b><i>Guérin et al. (2019)</i></b>	SBF-SEM and FIB-SEM	Not Stated	None	None	Root	Method (Technical)	N
<b><i>Harwood et al. (2019)</i></b>	SBF-SEM	Zeiss Sigma VP with Gatan 3View	Avizo	Manual	Plant (Wheat and Chickpea)	Experimental	N

<b>Hayes et al. (2019)</b>	SBF-SEM	Zeiss Sigma VP with Gatan 3View	IMOD	Not Stated	Mouse Retina	Experimental	N
<b>Ju et al. (2019)</b>	SBF-SEM	Zeiss Merlin with Gatan 3View	IMOD	Manual	Rat Optic Nerve	Experimental	Y (portion)
<b>Khadangi et al. (2019)</b>	SBF-SEM	FEI Teneo VolumeScope and Zeiss Sigma VP with Gatan 3View	Ilastik and own Algorithm	Semi-automated	Rat Heart	Method (Analysis)	N
<b>Koudouna et al. (2019)</b>	SBF-SEM	FEI Quanta FEG 250 with Gatan 3View	ImageJ	Manual	Human Eye	Experimental	N
<b>Lai et al. (2019)</b>	SBF-SEM	Zeiss Sigma VP with Gatan 3View	Reconstruct and Amira	Manual	Human Eye	Experimental	N
<b>Liu et al. (2019)</b>	SBF-SEM	FEI Teneo VolumeScope	IMOD	Manual	Parasite <i>Plasmodium knowlesi</i>	Experimental	N
<b>Mantani et al. (2019)</b>	SBF-SEM	Jeol JSM 7800F with Gatan 3View	IMOD	Not Stated	Rat Intestine	Experimental	N

<b>Matsumoto et al. (2019)</b>	SBF-SEM	Unknown	Unknown	Not Stated	Mouse brain	Experimental	N
<b>Melia et al. (2019)</b>	SBF-SEM	Zeiss Sigma VP and Gatan 3View	Segmentation (Fiji) and Amira	Manual and semi-automatic	Viral infected cells	Experimental	Y
<b>Pain et al. (2019)</b>	SBF-SEM	Zeiss Merlin with Gatan 3View	IMOD and Amira	Manual	Arabidopsis	Experimental	N
<b>Parker et al. (2019)</b>	SBF-SEM	Not Stated	Not Stated	Not Stated	<i>stracod carapace</i> Eye	Experimental	N
<b>Patterson et al. (2019)</b>	SBF-SEM	Zeiss Sigma VP with Gatan 3View	Viking and Matlab (RenderApp)	Manual and Skeletonisation	Macaque retina	Connectomic	N
<b>Rost-Roszkowska et al. (2019)</b>	SBF-SEM	Gatan 3View	None	None	<i>Thulinus ruffoi</i> (Tardigrade)	Experimental	N
<b>Rühling et al. (2019)</b>	SBF-SEM	Zeiss Sigma with Gatan 3View	Reconstruct and BioVis3D	Not Stated	Mouse and Human Brain	Experimental	Y

<b>Safa et al. (2019)</b>	SBF-SEM	Apereo VolumeScope	Seg3D	Manual	<i>Rat Tendon</i>	Experimental	N
<b>Schneider et al. (2019)</b>	SBF-SEM	Zeiss Merlin VP with Gatan 3View	Fiji and IMOD	Manual	Human lung	Method (Experimental)	N
<b>Spano et al. (2019)</b>	SBF-SEM	Unknown	Unknown	Not Stated	Mouse brain	Not Known	N
<b>Starborg et al. (2019)</b>	SBF-SEM	FEI Quanta 250 with Gatan 3View	None	None	Murine, heart, worm head	Method (Technical)	N
<b>Takaki et al. (2019)</b>	SBF-SEM	Zeiss Merlin or Sigma with Gatan 3View	Fiji (TrakEM2), MIB and Amira	Manual and Semi-automatic	Human Kidney	Experimental	N
<b>Thomas et al. (2019)</b>	SBF-SEM	Unknown	Unknown	Not Stated	Mouse brain	Not Known	N
<b>Tribble et al. (2019)</b>	SBF-SEM	Zeiss Sigma with Gatan 3View	Fiji (TrakEM2)	Manual	Human Retina	Experimental	N

<b>Vezzoli et al. (2019)</b>	SBF-SEM	FEI Quanta FEG 200 with Gatan 3View	Ilastik and Amira	Manual and Semi-automated	Mouse brain	Experimental	N
<b>Vincent et al. (2019)</b>	SBF-SEM	Zeiss Sigma VP with Gatan 3View	IMOD, MIB and Amira	Manual	Human and Mouse Muscle	Experimental	N
<b>Vints et al. (2019)</b>	SBF-SEM	Zeiss Sigma VP with Gatan 3View	ImageJ	Semi-Automated	Mouse Brain	Method (Staining)	N
<b>Wool et al. (2019)</b>	SBF-SEM	Unknown	Unknown	Not Stated	Mouse brain	Not Known	N
<b>Yam et al. (2019)</b>	SBF-SEM	Zeiss Sigma VP with Gatan 3View	Imaris	Manual	Human Cornea	Experimental	N
<b>Yang et al. (2019a)</b>	SBF-SEM	FEI Quanta 250 with Gatan 3View	None	None	Polymer	Experimental	N
<b>Yang et al. (2019b)</b>	SBF-SEM	Zeiss Sigma with Gatan 3View	ImageJ, Reconstruct and Blender	Manual	Mouse Tongue	Experimental	N

<b>Young et al. (2019)</b>	SBF-SEM	Zeiss Sigma with Gatan 3View	Fiji and Amira	Not Stated	Mouse Cornea	Experimental	N
<b>Zhang et al. (2019)</b>	SBF-SEM	Zeiss Gemini and Merlin with Gatan 3View (Onpoint Detector)	IMOD	Automated	Drosophila melanogaster Brain	Experimental	N
<b>Zhao et al. (2019)</b>	SBF-SEM	Zeiss Sigma VP with Gatan 3 View	ImageJ and Avizo	Manual and Semi- automatic	Polymer	Experimental	Y



## Appendix B – Locust Protocol

1. Dissolve compounds as listed and fill up to 500ml ddH<sub>2</sub>O for Insect Ringer Solution:
  - a. NaCl 5.1 g
  - b. KCl 0.36 g
  - c. CaCl<sub>2</sub> 0.11 g
  - d. MgCl<sub>2</sub> 6H<sub>2</sub>O 0.43 g
  - e. NaHCO<sub>3</sub> 0.035 g
  - f. Na<sub>2</sub>HPO<sub>4</sub> 2H<sub>2</sub>O 0.15 g
  - g. C<sub>6</sub>H<sub>12</sub>O<sub>6</sub> H<sub>2</sub>O 3.85 g
2. Dissect Brains in cold insect Ringer solution.
3. 2% Formaldehyde, 2.5% glutaraldehyde in 0.1M sodium cacodylate buffer for minimum of 24hrs.
4. Wash in 0.1M sodium cacodylate pH7.4
  - a. 100 ml of 0.2M Sodium Cacodylate (21.4g sodium cacodylate in 500ml ddH<sub>2</sub>O)
  - b. 5ml of 1M HCL.
  - c. Made up to 200ml with ddH<sub>2</sub>O and pH 7.4
5. Place in solution of 1% osmium tetroxide and 3% potassium ferrocyanide in d ddH<sub>2</sub>O for 30 minutes at RT.
6. 3 x 5minute washes in ddH<sub>2</sub>O.
7. Filtered 10% Thiocarbohydrazide for 1hr at RT.
8. 3 x 5minute washes in ddH<sub>2</sub>O.
9. 1% osmium tetroxide in ddH<sub>2</sub>O for 30 minutes at RT.
10. 3 x 5minute washes in ddH<sub>2</sub>O.
11. In 1% Uranyl Acetate in ddH<sub>2</sub>O for 2h at 60°C.
12. 3 x 5minute washes in ddH<sub>2</sub>O.

13. Lead Aspartate Solution made prior to next step as follows:
  - a. Lead nitrate, 0.12g
  - b. Aspartic acid solution, 0.03M 20ml
  - c. 30mins at 60°C.
14. Tissue in Lead Aspartate Solution overnight at RT.
15. 3 x 5minute washes in ddH<sub>2</sub>O.
16. 50% Acetone for 30mins.
17. 75% Acetone for 30mins.
18. 2 x 100% Acetone for 1hr.
19. 25% Resin (TAAB 812) in Acetone for 1hr.
  - a. Hardener Resin Component 812 Resin-Premix, 52g
  - b. Resin Component 812 Resin-Premix, 48g
  - c. Accelerator TAAB812-Ter-Araldite Resin Premix, 2.5ml
20. 50% Resin in Acetone for 1hr
21. 75% Resin in Acetone for 1hr.
22. 3 x 100% Resin for 1hr.
23. 100% Resin for minimum of 3hrs.
24. Embed in 100% resin and placed in oven at 60°C for minimum of 72hrs.

## Appendix C – Guinea Pig Protocol

1. Dissect muscle in 2% glutaraldehyde in 0.1M sodium cacodylate buffer for minimum of 24hrs.
2. Wash in 0.1M sodium cacodylate pH7.4
  - a. 100 ml of 0.2M Sodium Cacodylate (21.4g sodium cacodylate in 500ml ddH<sub>2</sub>O)
  - b. 5ml of 1M HCL.
  - c. Made up to 200ml with ddH<sub>2</sub>O and pH 7.4
3. Place in solution of 2% osmium tetroxide and 3% potassium ferrocyanide in ddH<sub>2</sub>O for 1hr at RT.
4. 3 x 5minute washes in ddH<sub>2</sub>O.
5. Filtered 10% Thiocarbohydrazide for 20 minutes at RT.
6. 3 x 5minute washes in ddH<sub>2</sub>O.
7. 2% osmium tetroxide in ddH<sub>2</sub>O for 1hr at RT.
8. 3 x 5minute washes in ddH<sub>2</sub>O.
9. In 1% Uranyl Acetate in ddH<sub>2</sub>O overnight at 4°C
10. 3 x 5minute washes in ddH<sub>2</sub>O.
11. Lead Aspartate Solution made prior to next step as follows:
  - d. Lead nitrate, 0.12 g
  - e. Aspartic acid solution, 0.03M 20 ml
  - f. 30mins at 60°C.
12. Tissue in Lead Aspartate Solution for 30 minutes at 60°C.
13. 3 x 5minute washes in ddH<sub>2</sub>O.
14. 50% Acetone for 30mins.
15. 75% Acetone for 30mins.
16. 2 x 100% Acetone for 1hr.

17. 25% Resin in Acetone for 1hr.

a. Hardener Resin Component 812 Resin-Premix, 52g

b. Resin Component 812 Resin-Premix, 48g

c. Accelerator TAAB812-Ter-Araldite Resin Premix, 2.5ml

18. 50% Resin in Acetone for 1hr

19. 75% Resin in Acetone for 1hr.

20. 3 x 100% Resin for 1hr.

21. 100% Resin for minimum of 3hrs.

22. Embed in 100% resin and placed in oven at 60°C for minimum of 72hrs.

**Appendix D – Chemical List**

<b>Reagent</b>	<b>Company</b>	<b>Product Code</b>
NaCL	Sigma-Aldrich	S9888
KCL	Sigma-Aldrich	P3911
CaCl <sub>2</sub>	Sigma-Aldrich	C1016
MgCl <sub>2</sub> 6H <sub>2</sub> O	Sigma-Aldrich	M2670
NaHCO <sub>3</sub>	Sigma-Aldrich	S6014
Na <sub>2</sub> HPO <sub>4</sub> 2H <sub>2</sub> O	Sigma-Aldrich	71643
C <sub>6</sub> H <sub>12</sub> O <sub>6</sub> H <sub>2</sub> O	Sigma-Aldrich	49158
Formaldehyde	TAAB Laboratories Equipment Ltd	F017
Glutaraldehyde	TAAB Laboratories Equipment Ltd	G003
Cacodylate Buffer	Agar Scientific	R1104
Osmium Tetroxide	TAAB Laboratories Equipment Ltd	O014
Potassium Ferrocyanide	Sigma-Aldrich	244023
Thiocarbohydrazide	Sigma-Aldrich	223220
Uranyl Acetate	Agar Scientific	AGR1260A
Lead Nitrate	Sigma-Aldrich	228621
Aspartic Acid	Sigma-Aldrich	A9256
Acetone	Fisher Scientific	A/0560/PC17
TAAB 812 Hard Epoxy Resin	TAAB Laboratories Equipment Ltd	T030

## **Appendix E – Image Analysis Protocol**

### *1.1 Conversion from DM3 to Tiff*

For use by the programs the image datasets had to be first converted into a file type different from the ones produced by Gatan digital micrograph, DM3 and DM4. This was performed in Fiji by following the procedure below:

1. Import into Fiji by selecting 'File' > 'Import' > 'Image Sequence' in Fiji.
2. Select first image, or entire folder of images, a new dialogue box appears.
3. Check the number of images to be imported and ensure nothing else is ticked.
4. Convert 16-bit images to 8-bit images, to speed up the processing of the images and reduce the final size of the data.
5. Image stack opens.
6. Normalise contrast by selecting 'Process' > 'Enhance Contrast'.
7. Change saturated pixels to 1% and select 'Normalize' and 'Process All'.
8. Enhance contrast by going to 'Image' > 'Adjust' > 'Brightness/Contrast'.
9. Manually adjust brightness and contrast by moving the sliders.
10. Change image parameters by selecting 'Image' > 'Properties'.
11. The parameters for x and y are always correctly registered in Fiji; however, the z parameter needs to be changed to the correct thickness of slices taken.
12. Adjust images, if required, using filters (such as denoising) found in 'Process' > 'Noise' or 'Process' > 'Filters' for all the other filter options.
13. Save adjusted images as a series of TIFF files by clicking 'File' > 'Save as Image Sequence'.

### *1.2. Fiji/TrakEM2 Analysis Method*

1. Open image stack in Fiji, as detailed above.
2. To create a new TrakEM2 file, select 'File' > 'New' > 'TrakEM2 (Blank)'.
3. Two new windows open; object window and analysis window.
4. Import the open stack by right-clicking and selecting 'Import' > 'Import Stack' in the analysis window.
5. To add objects and start the segmentation, right-click in the object organiser window and selecting 'Anything' > 'Add New Child' > 'Area\_List'.
6. Dragging 'Anything' into the middle column creates a new folder; dragging 'Area List' creates a new object in that folder.
7. Rename object by right-clicking and selecting 'Area\_List' > 'Rename'.
8. Object appears under the 'Z Space' tab in the analysis window; select to begin segmentation.
9. Using the brush tool, draw an outline around the selected object on the image.
10. Hold the shift button and click in the centre of the outline to fill in the outline.
11. Repeat over each slice and segment each object.
12. Once the segmentation of an object (s) is completed, view results in the 3D viewer, by right-clicking in either of the windows and selecting 'Show in 3D'.
13. The 3D reconstruction(s) appear in a new window and can be checked.
14. Save model as an .obj file to be exported to other packages if required.
15. 3D reconstructions created in Fiji can be analysed in Blender.

### *1.3. Blender Reconstruction*

1. Install Neuromorph tools in Blender: 'Install from File' > 'File' > 'User Preferences'.
2. The tools are found in the side panel in the main interface under 'Misc'.
3. To open the .obj file of interest, select 'Scene' tab on the right-hand side and click 'Import Object'.
4. The object appears in the display.
5. Using the neuromorph tools, the volume and surface area of each object can be measured.



#### 1.4. Microscopy Image Browser (MIB)

MIB can be opened through MATLAB or as a standalone program, and the information on how to do either is found on the MIB website (<http://mib.helsinki.fi/>).

##### 1. Opening Dataset and Starting Segmentation

- I. Use the 'Directory Contents' to navigate to the location where the files are stored.
- II. Open the images to be analysed by highlighting them all, then right-clicking and selecting 'Combine Selected Datasets'.
- III. The image stack opens in the image window.
- IV. Change dataset parameters by going to 'Dataset' > 'Parameters'.
- V. Start segmentation by clicking 'Create' in the 'Segmentation' panel and either selecting 63 or 255 models (depending on how many objects are to be segmented).
- VI. Add each material to the 'Segmentation' panel by clicking the 'plus' button, then changing the name of the material; it appears in the material column.
- VII. In MIB, pixels can only be selected and assigned to one material at a time, so segmentation has to be performed one at a time.
- VIII. Change the chosen colour for each material by double clicking on the coloured square to the left of the material name.
- IX. A variety of tools are used for the segmentation.

##### 2. Manual Segmentation

- I. Below the material panel is the segmentation tool drop down list. The default when the program is started is the 'Brush' tool, a manual segmentation tool.
- II. Use the brush tool to trace the outline of an object and repeat over each slice. Press Shift and F to fill the object throughout all the slices.

- III. Hold down the Ctrl button to turn the brush tool into an eraser to remove any errors.
- IV. The selected pixels appear as green on the image.
- V. Assign the selected pixels to the correct material by ticking the material under the 'Add to' column and pressing Shift and A.

### 3. Watershed/SLIC

- I. Select the 'Brush' tool; two more options of segmentation appear called 'Watershed' and 'SLIC'.
- II. When using the 'Watershed' tool the pixels in the image are combined into superpixels, based upon boundaries and changes in contrast.
- III. The size of the superpixels is adjusted by changing the 'N' number, the higher the number, the larger the superpixel.
- IV. The 'SLIC' option is a similar tool but the pixels are grouped into superpixels based on similar contrast; the smaller the N number, the larger the resulting superpixel.
- V. By clicking on the image using the brush tool the superpixels appear on the image as pink outlines; the superpixels are selected by moving over them using the brush tool.
- VI. The superpixels only appear in the area of the image seen in the 'Image View' and not over the entire image.

### 4. Interpolation

- I. Use the brush tool to segment the object on every  $n$ th slice; 'Selection' > 'Interpolation', or click 'I', to fill in the gaps in the segmentation.
- II. Check segmentation and correct any errors.

## 5. Thresholding

- I. With thresholding the pixels are selected based on a user inputted contrast range and in MIB there are two types, B/W thresholding and the Magic Wand tool.
- II. Select 'B/W Thresholding' from the menu. Alter the range of contrast by adjusting the two sliders until the correct selection is seen on the image in green on the first slice.
- III. Click 'All' to apply the B/W thresholding to all images.
- IV. Select the 'Magic Wand-Region growing' tool to change the variation and radius of the selection tool.
- V. Use the tool to click on a single pixel in the object; select all the pixels within the range and radius around the selected pixel; alter the variation and radius until the desired selection is made.
- VI. Select '3D' in the 'Selection' panel to apply the thresholding to the whole stack.
- VII. Correct any errors using the brush tool.

## 6. Saving file

- I. Once segmentation is finished (by whichever chosen process) the model is saved as a separate file by going to 'Model'>'Save Model'.
- II. During the segmentation process, save as the suggested MATLAB file format (.model) and the model will be automatically saved in this format each time.
- III. Once the segmentation is complete, the model file is also saved in an .am file format to open in Amira.

### 1.5. Amira

#### 1. Opening Dataset and Starting Segmentation

- I. Import images by selecting 'Open data', highlighting all the TIFF images and clicking open.
- II. A new window appears, and the voxel measurements change to the pixel measurements.
- III. In the main interface, a file appears corresponding to the image stack and a single orthoslice automatically appears in the main viewing area.
- IV. The segmentation is started by right-clicking on the main file and selecting 'Edit New Label' or switching to the 'Segmentation Panel'.
- V. New objects are added by clicking 'Add' in the segmentation panel, the name is changed by double-clicking on the new object and the colour altered by right-clicking on it.
- VI. The segmentation tools are found at the bottom of the right-hand panel.

#### 2. Manual Segmentation and Interpolation

- I. Select the brush symbol to manually highlight the objects.
- II. Annotate every  $n$ th slice manually and then select 'Interpolate' under the 'Selection' tab.
- III. The selection appears as red upon the image.
- IV. Assign the selection to the correct label by selecting the 'plus' sign, and to add the selection from all slices select 'Volume' instead of 'Current Slice'.
- V. Remove the selection by selecting the 'minus' sign and correct any errors by holding down the 'shift' key and using the brush tool.

#### 3. Thresholding

- I. Select the magic wand thresholding tool by selecting the 'magic wand' symbol in the panel.
- II. When selected, a graph appears in the panel with sliders.

- III. When a pixel is selected on the image, a pointer appears on the graph to show where on the contrast scale that specific pixel sits.
- IV. Adjust the sliders around this point until the correct pixels are selected.
- V. Tick '3D' to perform the action across all slices.
- VI. During the segmentation, view the rough object by choosing the four-panel viewer above the viewing window.

#### 4. Reconstruction

- I. Once the segmentation is complete, select the project panel tab to go back to the view when Amira was first opened; the new label file (.label) is created and is found connected to the first image file.
- II. To create the surface for reconstruction, right-click the .Labels file and select 'Generate Surface' > 'Apply' selected.
- III. A .surf file appears, connected to the .Labels file.
- IV. View the surface by right clicking the .surf file and selecting 'Surface view'.

## **Appendix F – Published Paper**

# A guide to analysis and reconstruction of serial block face scanning electron microscopy data

E. COCKS\* , M. TAGGART\*, F.C. RIND† & K. WHITE‡

\*Institute of Genetic Medicine, Newcastle University, Central Parkway, Newcastle upon Tyne, NE1 3BZ, UK

†Institute of Neuroscience, Newcastle University, Framlington Place, Newcastle upon Tyne, NE2 4HH, UK

‡Electron Microscopy Research Services, Newcastle University Medical School, Framlington Place, Newcastle upon Tyne, NE2 4HH, UK

**Key words.** Amira, blender, Fiji, image analysis, microscopy image browser, serial block face scanning electron microscopy, skeletal muscle.

## Summary

Serial block face scanning electron microscopy (SBF-SEM) is a relatively new technique that allows the acquisition of serially sectioned, imaged and digitally aligned ultrastructural data. There is a wealth of information that can be obtained from the resulting image stacks but this presents a new challenge for researchers – how to computationally analyse and make best use of the large datasets produced. One approach is to reconstruct structures and features of interest in 3D. However, the software programmes can appear overwhelming, time-consuming and not intuitive for those new to image analysis. There are a limited number of published articles that provide sufficient detail on how to do this type of reconstruction. Therefore, the aim of this paper is to provide a detailed step-by-step protocol, accompanied by tutorial videos, for several types of analysis programmes that can be used on raw SBF-SEM data, although there are more options available than can be covered here. To showcase the programmes, datasets of skeletal muscle from foetal and adult guinea pigs are initially used with procedures subsequently applied to guinea pig cardiac tissue and locust brain. The tissue is processed using the heavy metal protocol developed specifically for SBF-SEM. Trimmed resin blocks are placed into a Zeiss Sigma SEM incorporating the Gatan 3View and the resulting image stacks are analysed in three different programmes, Fiji, Amira and MIB, using a range of tools available for segmentation. The results from the image analysis comparison show that the analysis tools are often more suited to a particular type of structure. For example, larger structures, such as nuclei and cells, can be segmented using interpolation, which speeds up analysis; single contrast structures, such as the nucleolus, can be segmented using the contrast-based thresholding tools. Knowing the nature of the tissue and its specific structures (complexity, contrast, if there are distinct membranes, size)

will help to determine the best method for reconstruction and thus maximize informative output from valuable tissue.

## Introduction

Electron microscopy (EM) has evolved to incorporate different preparation techniques for the imaging of a wide variety of samples. Transmission and scanning EM (TEM and SEM, respectively) are regularly used to analyse biological material in order to reveal structural information, which may relate to function. Yet, there are limitations. For example, SEM generally images the surface topography of cells and tissues but not intracellular structures (unless freeze-fracture techniques are used). On the other hand, TEM provides information on spatial arrangements within cells to within 1 nm resolution. However, this is accomplished by examining a single ultrathin section, typically 50–100 nm, from a much larger sample, which could range from  $\sim 10 \mu\text{m}$  (single cells) to several millimetres (tissues). Therefore, important information regarding spatial arrangements of structures of interest through the depth of a cell or tissue is difficult to obtain. Manual serial-sectioning can be combined with TEM to create 3D stacks and visualizations of data (Andersson-Cedergren, 1959; Kristen & Stevens, 1988; Bock *et al.*, 2011; Takemura, 2015; Lee *et al.*, 2016). However, this is extremely time-consuming, requires a high level of experience in microtomy and manual image alignment and, even then, often results in damaged or lost sections whose ‘missing’ information has to be interpolated.

The desire within the EM community to obtain data in three spatial dimensions ( $x$ – $y$ – $z$ ) at the ultrastructural level led to the development of a rudimentary automated system for serial sectioning coupled with EM imaging by Kuzirian and Leighton (1983). Although it was another two decades before the procedure known as serial block face SEM (SBF-SEM) was described in published form by (Denk & Horstmann, 2004). It consists of a mini-ultramicrotome with diamond knife inside an SEM chamber. The knife cuts ultrathin sections from a piece of tissue embedded in a resin block, an electron beam scans

Correspondence to: E. Cocks, Newcastle University, Institute of Genetic Medicine, Central Parkway, Newcastle upon Tyne NE1 3BZ, UK. Tel: 07713 583726; e-mail: E.Cocks2@newcastle.ac.uk

the block surface and a detector records the backscattered electrons, producing a digital image. This process is repeated at an operator-specified depth to produce a digitized stack of aligned images. It is possible to obtain tens to hundreds of serial sections from resin blocks, and aligned images, in a few hours. In addition to SBF-SEM, there are other methods of 3D volume collection that have been developed, such as array tomography and focused ion beam scanning EM (FIB-SEM) (reviewed by Peddie & Collinson, 2014; Titze & Genoud, 2016). All techniques produce large quantities of data, which are difficult to manage and time-consuming to analyse. In this manuscript, we concentrate on data obtained by SBF-SEM but the same analyses we describe may be applied to datasets obtained by other methods.

The stack of images obtained from biological samples allows researchers to follow cell-to-cell arrangements, or intracellular structures, in the z-axis in a number of ways. First, this can be achieved by simply scrolling through the images for qualitative assessment of the features of interest. Second, image analysis software can be used to create 3D reconstructions of the data. These can aid the qualitative assessment of the data, for example, creating movies that show the reconstructions on rotating axis (Kasthuri *et al.*, 2015). Third, such tools can also be used for detailed quantification of the biological data. The image analysis can be the most complex and time-consuming portion of the whole process.

In many ways, the challenges of 3D EM have now shifted from how to capture the difficult-to-measure to what to do with all this data? At the outset of an experiment one, ideally, it needs to know how the resultant images are to be analysed. These considerations vary from simple to complex, depending upon the experimental question, the tissue or cell constituency, the resolutions of structures of interest and their contrast to neighbouring structures.

The most likely requirement is the creation of 3D reconstructions of the image stacks, whether for qualitative or quantitative assessment. There are a number of image analysis packages that assist with creating reconstructions (for a recent review of these, see Borrett and Hughes (2016)), each requiring segmentation as a first step. Segmentation is the process of annotating a specific structure on each image so as to follow it in each consecutive image in the z-axis. There are two main ways of accomplishing this. In one case, the object(s) is highlighted manually by adding a coloured layer(s) on top of the image. An alternative process involves assigning individual image pixels to only one object, which means if a pixel is reselected during another segmentation, it will be reassigned.

The methods of segmentation can be further divided into manual, semiautomated and automated categories. Manual segmentation tools require the user to annotate the object, e.g. by colouring, over every slice. Semiautomated tools use a combination of user input and programme predictions, to highlight a structure. An example of this is interpolation. The user manually annotates the structure every *n*th slice and the

programme will fill in the empty slices using the annotated image as a guide to predict the possible shape of the object. Another is the thresholding tool, which selects pixels based on the contrast limits set by the user. These limits allow for the selection of light or dark pixels depending on the appearance of the object. There is the option available in some programmes for machine learning automated segmentation. Here, the programme 'learns' object selection based on trial runs performed by the user on a sample dataset. These settings are then automatically applied to the full dataset to be analysed and can be implemented on other datasets as well.

The complexity of SBF-SEM datasets, and scenario-specific analysis requirements, can make it difficult to know which image analysis tools and procedures to follow to make best interpretations of the data. Therefore, the purpose of this paper is to compare three popular image analysis programmes, and the segmentation tools they offer, for the qualitative and quantitative analysis of SBF-SEM data. We provide detailed protocols for the data handling and analyses. In doing so, we aim to provide direction to researchers new to SBF-SEM by drawing attention to advantages and limitations of the software packages and tools. A similar comparison was done by Tsai *et al.* (2014), which details data reconstruction from multiple volume EM techniques. However, the in-depth workflow from these techniques may appear daunting for those new to image analyses. This paper is aimed at researchers with no or little experience using image analysis software and SBF-SEM and provides a simple workflow for deciding which methods to use.

The material analysed is predominantly guinea pig skeletal muscle, chosen because it exhibits regular, well-defined intracellular structures by EM that allowed us to test the effectiveness of each software tool. From the results, we developed a decision-making map that can be applied to the analysis of any structure from any sample type and will help researchers choose the workflow to apply to their SBF-SEM data. By following this workflow, the researcher will ensure that they are in the best position to address the aims of their study and maximize the output from this relatively new technique.

## Method

### *Tissue preparation for SBF-SEM*

Skeletal muscle tissue (psoas and soleus muscles) and hearts, from Duncan Hartley guinea pigs, were terminated under licenced procedures according to the Animals Scientific Procedures Act 1986 (ASPA). They were then microdissected into 2% glutaraldehyde with 0.1M sodium cacodylate buffer and left for a minimum of 12 h in the fixative at 4°C. The samples then undergo a heavy metal staining protocol (Wilke *et al.*, 2013). The tissues were washed in 0.1M sodium cacodylate pH7.4 followed by a solution of 3% potassium ferricyanide with 2% aqueous osmium tetroxide in ddH<sub>2</sub>O for 1 h. Then,



followed by filtered 10% thiocarbonylhydrazide, TCH, for 20 min and then secondary 2% osmium tetroxide for 30 min. The samples were then placed in 1% uranyl acetate at 4°C overnight followed by lead aspartate solution, 0.12 g of lead nitrate in 20 mL aspartic acid for 30 min.

The brain from an adult locust (*Locusta migratoria*) was sacrificed by ice, dissected in cold saline and placed in 2% paraformaldehyde, 2.5% glutaraldehyde in 0.1M sodium cacodylate buffer. It was processed with an adapted version of the Wilke *et al.* (2013) protocol described in Wernitznig *et al.* (2016). The main differences to the above protocol are the use of reduced osmium (1%) and a shorter time in uranyl acetate but at 60°C.

Between each step, all samples were washed in several changes of ddH<sub>2</sub>O. The samples were dehydrated with acetone, from 25% to 100% and then impregnated with increasing concentrations of Taab 812 hard resin in acetone with several changes of 100% resin. The samples were embedded into 100% resin and left to polymerize at 60°C for a minimum of 36 h.

The resin blocks were trimmed using a razor blade to form a trapezoid block face. Using a diamond knife, 1 µm sections are taken and stained with toluidine blue and viewed under a light microscope. Several 70 nm sections were taken, placed on a copper grid and viewed on a CM100 TEM (FEI), to check tissue morphology and orientation and penetration of the staining. This is done to ensure that the tissue has been adequately processed for viewing by SBF-SEM. The blocks were then further trimmed to approximately 0.75 mm × 0.75 mm and glued onto a pin. In order to reduce sample charging within the SEM, the block was painted in silver Dag and sputter-coated with a 5 nm layer of gold.

#### SBF-SEM settings and image analysis

The specimens were placed into a Zeiss Sigma SEM (Zeiss, Cambridge, UK) incorporating the Gatan 3View (Gatan inc., Abingdon, UK) as the SBF-SEM system. For this particular project, the following parameters were used. For each sample, the images were obtained at 2.5–5 kV accelerating voltage, with an aperture of 30 µm, in variable pressure ranging from 20 to 53 Pa. The blocks were sectioned (unless stated otherwise) at a thickness of 70 nm and the images recorded at a range of magnifications with a resolution of 1024 × 1024 pixels or 3000 × 3000 pixels with a 20 µs/pixel dwell time and at resolution ranging from 5 to 20 nm.

Gatan Digital Micrograph was used to collect digitized images of each experimental run in a DM3 format. The data were then analysed using three different image analysis programmes (Fig. 1). These are Fiji (<http://fiji.sc/>), Amira (<http://www.fei.com/software/amira-3d-for-life-sciences/>) and Microscopy Image Browser, MIB (<http://mib.helsinki.fi/>). Fiji, via the plugin TrakEM2 (Cardona *et al.*, 2012), is primarily an operator-driven programme that is freely available. For a

comparison of the programmes see Table 1. Amira and MIB (Belevich *et al.*, 2016) have the capacity for using semiautomated tools: Amira requires a commercial license and MIB is freely available. Amira enables visualization of all analysed data, whereas FIJI and MIB are purely analytical programmes with basic visualization and require a secondary programme to perform computational analysis of the segmentations. Blender (<https://www.blender.org/>) is one such programme, it is a free graphics software which can be used to reconstruct the objects created in Fiji with the aid of Neuromorph Tools (Jorstad *et al.*, 2015) (<http://cvlab.epfl.ch/NeuroMorph>) and perform computational analysis. These were developed specifically to import the objects from Fiji and perform quantification analysis. Opening the segmented 3D objects via these tools also ensures that the dimensions are consistent with the parameters from the raw data. In MIB, the segmentation model file can be exported in a variety of formats to different programmes, and in this protocol, Amira is used as the example.

#### Protocols for image file handling and analyses

The protocols below are applied initially to the examination of a skeletal muscle SBF-SEM dataset and the steps in each process illustrated in the accompanying video file tutorials (Supporting files S1–S5). The raw datasets used in the videos can be accessed via the EMPIAR website: <http://www.ebi.ac.uk/pdbe/emdb/empir/> (Accession code: EMPIAR-10092). The analysis is performed on a Toshiba laptop with Intel® Core i7-5500U CPU, 2.40 GHz, 16 GB RAM and 64 bit.

#### Converting DM3 to TIFF (video Fiji image processing)

The raw data are saved as a DM3 file format from Gatan Digital Micrograph, GDM, which cannot be opened in all imaging analysis programmes. The first step therefore is to convert the images into a TIFF format. During this conversion process, image contrast can be lost and a normalization step is carried out to prevent this.

- (1) An image sequence is imported by selecting 'File' > 'Import' > 'Image Sequence' in Fiji (*Supplementary file S1*).
- (2) Select the first image, or entire folder of pertinent images and a new window will appear.
- (3) Check the number of images to be imported and ensure that nothing else is ticked.
- (4) At this point, the 16 bit images can be converted into 8 bit images, to speed up the processing of the images and reduce the final size of the data.
- (5) The image stack will open.
- (6) Normalize the contrast by selecting 'Process' > 'Enhance Contrast'.

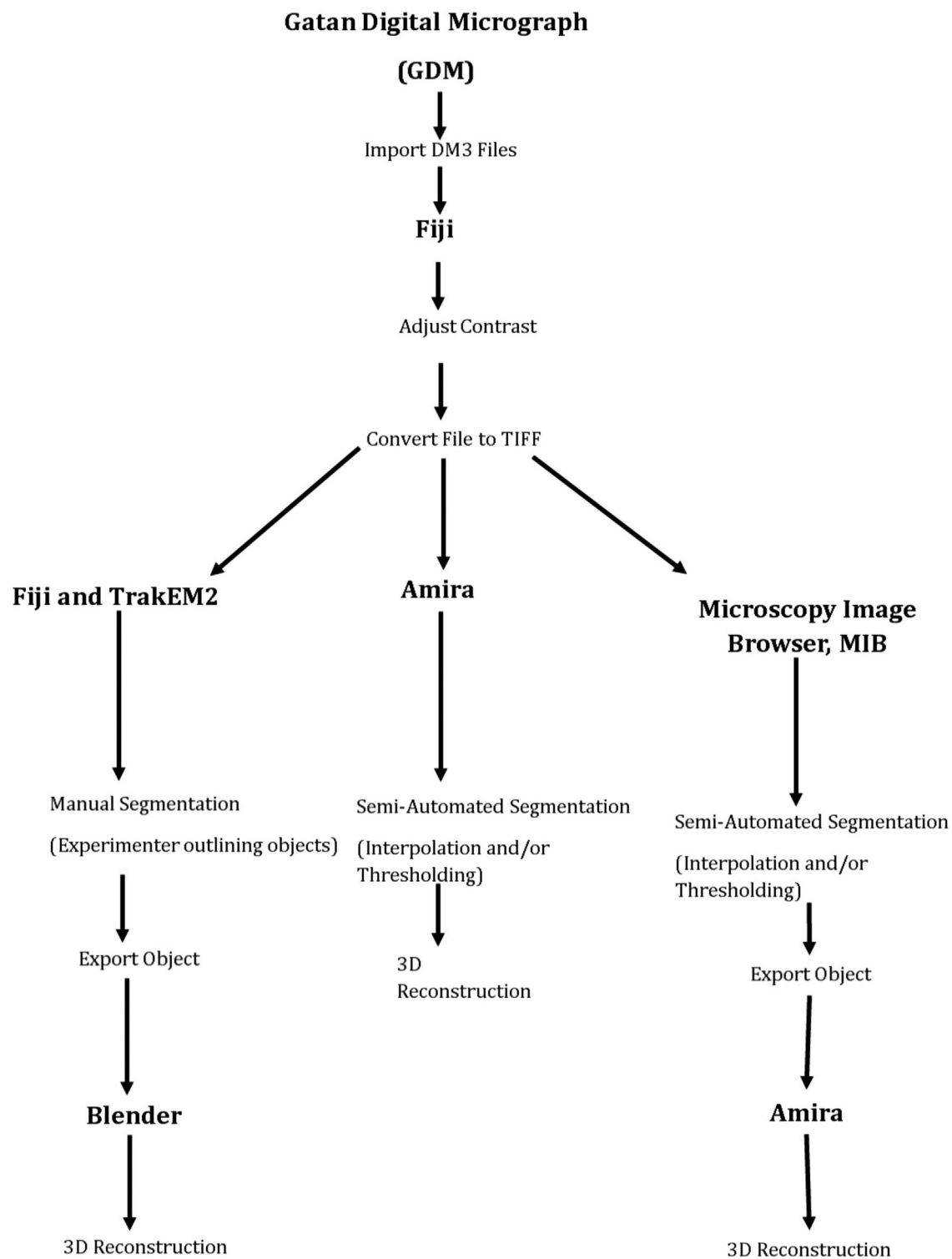


**Fig. 1.** Flow chart showing the steps for the image analysis comparison. The first step is to adjust the contrast and convert the images from DM files formats to TIFF. The stack of TIFFs is then analysed in each of the three programmes, and the examples of the segmentations used in each are also shown. The final step in the process is to reconstruct the segmentations into a 3D model.

- (7) Change saturated pixels to 1% and select 'Normalize' and 'Process All'.
- (8) Contrast can be further enhanced by going to 'Image' > 'Adjust' > 'Brightness/Contrast'.
- (9) Manually adjust the brightness and contrast by moving the sliders.
- (10) The image parameters have to be changed by selecting 'Image' > 'Properties'.
- (11) The parameters for the  $x$  and  $y$  are always correctly registered in Fiji; however, the  $z$  parameter will need to be changed to the correct thickness of slices taken.
- (12) The images are adjusted, if required, using filters (such as denoising) found in 'Process' > 'Noise' or 'Process' > 'Filters' for all the other filter options.
- (13) Save the adjusted images as TIFF by clicking 'File' > 'Save as Image Sequence'.

The following steps are then undertaken in each programme to segment each of the image stacks:

(1) *Fiji/TrakEM2 (Image Analysis Fiji)*

- (i) The image stack to be analysed is opened in Fiji, as detailed above.
- (ii) To create a new TrakEM2 file, select 'File' > 'New' > 'TrakEM2 (Blank)' (*Supplementary file S2*).
- (iii) Two new windows will open. One is the object window and the other is the analysis window.
- (iv) Right click and select 'Import' > 'Import Stack' in the analysis window to import the images.
- (v) Right click in the object organizer window and select 'Anything' > 'Add New Child' > 'Area List'.
- (vi) Drag 'Anything' into the middle column to create a new folder and then drag 'Area List' to create a new object in that folder.
- (vii) Rename the object by right-clicking and selecting 'Area List' > 'Rename'.
- (viii) The object will appear under the 'Z Space' tab in the analysis window and select it to begin segmentation.
- (ix) Use the brush tool to draw an outline around the selected object on the image.
- (x) Fill the object by holding the shift button and clicking in the centre of the outline.
- (xi) Repeat this over each slice and for each user-defined object to be segmented.
- (xii) Once the segmentation of a defined object (s) is completed, the results can be viewed in the 3D viewer. Right click in either of the windows and select 'Show in 3D'.
- (xiii) The 3D reconstruction(s) will appear in a new window.
- (xiv) The model is saved as an .obj file and to be exported to other packages if required.

- (xv) 3D reconstructions created in Fiji can be analysed in Blender.

(2) *Blender v2.76 (Blender)*

- (i) To install the Neuromorph tools, go to 'Install from File' > 'File' > 'User Preferences' (*Supplementary file S3*).
- (ii) The tools are found in the side panel in the main interface under 'Misc'.
- (iii) To open the .obj file of interest select the 'Scene' tab on the right hand side and then 'Import Object'.

(3) *Microscopy Image Browser, MIB v2.1 (Image Analysis MIB)*

MIB can be opened through Matlab or as a standalone programme, and the information on how to do either is found on the MIB website (<http://mib.helsinki.fi/>).

- (i) Navigate to the location of the TIFF image stack to be imported by using the 'Directory Contents' (*Supplementary file S4*).
- (ii) Highlight all the images to be analysed, right-click and select 'Combine Selected Datasets'.
- (iii) The image stack will open.
- (iv) Change the dataset parameters by going to 'Dataset' > 'Parameters'.
- (v) Click 'Create', in the 'Segmentation' panel and select 63 or 255 models, depending on how many objects will be segmented, to start the segmentation.
- (vi) Add a material to the 'Segmentation' panel by clicking the 'plus' button, change the name of the material and it will appear in the column.
- (vii) In MIB, pixels can only be selected and assigned to one material at a time, so segmentation has to be done one at a time.
- (viii) Double click on the coloured square to the left of the material name to change the colour.
- (ix) A variety of tools can then be used for the segmentation.

## Manual

- (1) Below the material panel is the segmentation tool drop down list. The default when you start the programme will be the 'Brush' tool, a manual segmentation tool.
- (2) Use the brush tool to trace the outline of the object and repeat this over each slice. Press Shift and F to fill the object throughout all the slices.
- (3) Hold the Ctrl button to turn the brush tool into an eraser and remove any errors.
- (4) The selected pixels will appear green on the image.
- (5) Assign the selection to the ticking the correct material in the 'Add to' box and pressing Shift and A.

**Table 1.** Comparison of imaging programmes. Examples of the different types of image formats and segmentation tools offered by three analysis programmes.

	Fiji	Amira	MIB
Image import format	.tif, .dm3, .png, .bmp	.tif, .png, .bmp	.tif, .dm3, .dm4, .png, .bmp
Object export format	.obj	.am, .surf	.am, .tif, .mat, .model, .stl, .mrc, .mod, .nrrd, .h5
Manual Brush	✓	✓	✓
Interpolation		✓	✓
B/W thresholding		✓	✓
Magic wand thresholding		✓	✓
Watershed/SLIC segmentation			✓

### Watershed/SLIC

- (1) When the 'Brush' tool is selected, there are two more options of segmentation that can be found 'Watershed' and 'SLIC'.
- (2) The 'Watershed' tool combines the pixels in the image into superpixels, based upon boundaries and changes in contrast.
- (3) The size of the superpixels is adjusted by changing the 'N' number, the higher the number, the larger the superpixel.
- (4) Click on the image using the brush tool and the superpixels appear on the image, as pink outlines, select the superpixels by moving over them using the tool.
- (5) The 'SLIC' option is a similar tool but the pixels are grouped into superpixels based on similar contrast and instead the smaller the N number, the larger the pixel.
- (6) The superpixels will only appear in the area of the image seen in the 'Image View' and not over the entire image.

### Interpolation

- (1) Using the brush tool manually, draw on every *n*th slice and then click 'I' or go to 'Selection' > 'Interpolation' and the gaps in the segmentation will be filled in.
- (2) Check and correct any errors that have occurred.

### Thresholding

- (1) Thresholding is the selection of pixels based on a user inputted contrast range and there are two types, B/W thresholding and the Magic Wand tool.
- (2) Select 'B/W Thresholding' from the menu. Alter the range by adjusting the two sliders until a correct selection is made over the entire image.

**Table 2.** Timing analysis results. The table shows the results from the timing analysis performed on a small portion of the total skeletal muscle dataset (20 slices) in each of the programmes shown in seconds. It was performed on Toshiba laptop with Intel® Core i7-5500U CPU, 2.40 GHz, 16 GB RAM and 64 bit.

		Fiji	Amira	MIB
Foetal	Nucleus	6.29	3.21	2.12
	mitochondria	9.14	9.22	26.44
Adult	Nucleus	10.52	5.35	3.07
	mitochondria	37.14	4.28	62.39

- (3) Click 'All' for B/W thresholding to be applied to the stack of images.
- (4) Chose the 'MagicWand-Regiongrowing' tool, change the variation and radius of the selection tool.
- (5) Click on a single pixel in the object, pixels within the range and radius will be selected, alter the variation and radius until the desired selection is made.
- (6) Select '3D' in the 'Selection' panel to apply the thresholding to the stack.
- (7) Check for any errors and correct using the brush tool.

### Saving file

- (1) Once segmentation is finished (by whichever chosen process) go to 'Model' > 'Save Model' to save the model file in the preferred format.
- (2) Recommended file format for the duration of the segmentation the Matlab file format (.model) is preferred and the model will automatically save in this format.

### Saving for opening in Amira

- (1) Save the model file to open in Amira go to 'Model' > 'Save Model As'.
- (2) Select any of the '.am' file types.
- (3) The new model file can now be opened in Amira (see Reconstruction under Amira).
- (4) *Amira v6.0 (Image Analysis Amira)*
  - (i) Select 'Open data', highlight all the TIFF images and click open to import the images (*Supplementary file S5*).
  - (ii) In the new window change the voxel measurements to the pixel measurements, as mentioned at the beginning.
  - (iii) In the main interface, a file will appear which corresponds to the image stack and a single orthoslice will automatically appear in the viewing area on the right.
  - (iv) Right click on the main file and select 'Edit New Label' to start segmentation and switch to the 'Segmentation Panel'.



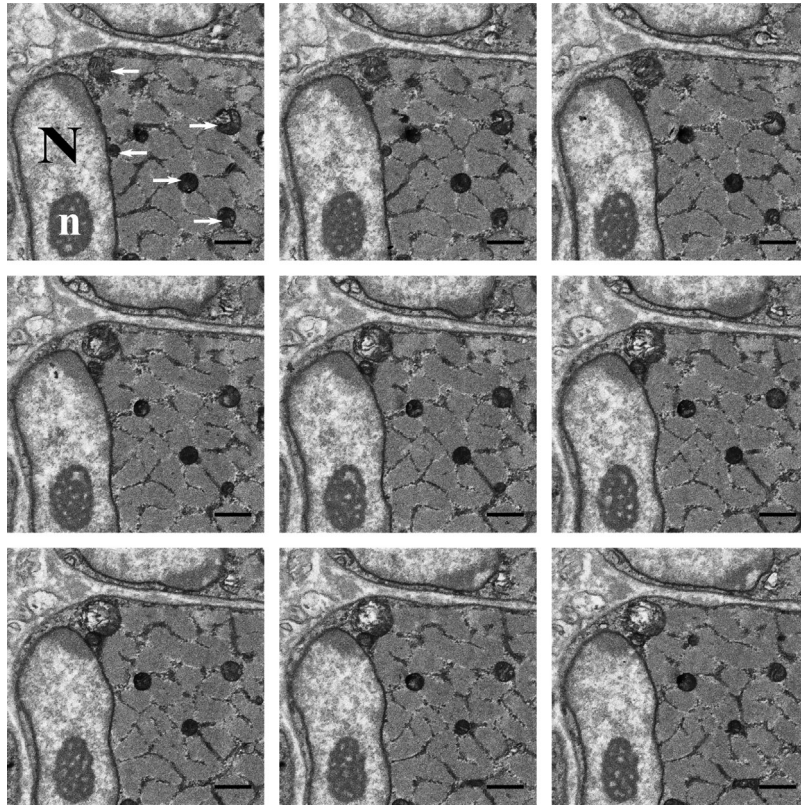


**Fig. 2.** Example of SBF-SEM image series. Nine consecutive images (viewed from left to right) from a stack of 93 serial images of a portion of a muscle cell from the skeletal muscle psoas from a late foetus guinea pig. In the first image, the nucleus can be seen, labelled with an 'N', as well as the nucleolus, white 'n', and the mitochondria, labelled with white arrows. Over each slice, of 70 nm, the structures change shape, as shown in the images. The images were taken at 12k $\times$  magnification, 7 nm resolution and an image size of 1024  $\times$  1024 pixels. All scale bars are 1  $\mu$ m.

- (v) Click 'Add' to add new objects to the segmentation panel, double-click on it to change the name and right click to change the colour and appearance.
- (vi) The segmentation tools are at the bottom of the right-hand panel.

#### Manual and interpolation

- (1) Select the brush symbol for the manual tool to highlight objects.
- (2) Manfully annotate every  $n$ th slice and select 'Interpolate' under the 'Selection' tab.
- (3) Assign the selection to a label by selecting the 'plus' sign, to add selection from all slices select 'Volume' and just for the one slice select 'current slice'.
- (4) To remove the selection click the 'minus' sign.

#### Thresholding

- (1) Click on the magic wand symbol to use the magic wand thresholding tool.
- (2) A graph will appear with sliders.

- (3) Select a pixel on the image and a pointer will appear on the graph to show where on the contrast scale that pixel appears.
- (4) An area will be highlighted and manually adjust the sliders to change the pixels selected until the correct selection is made.
- (5) Tick '3D' to perform the action across all slices.
- (6) To view the object on 3D in the segmentation panel choose the four-panel viewer above the viewing window.

#### Reconstruction

- (1) Select the project panel tab once the segmentation is complete, where there will be a secondary file connected to the original image file with .labels extension (corresponding to the new objects created in the segmentation panel).
- (2) Right click the .Labels file and select 'Generate Surface' > 'Apply'.
- (3) Another file will appear connected to the .Labels file, a .surf file.

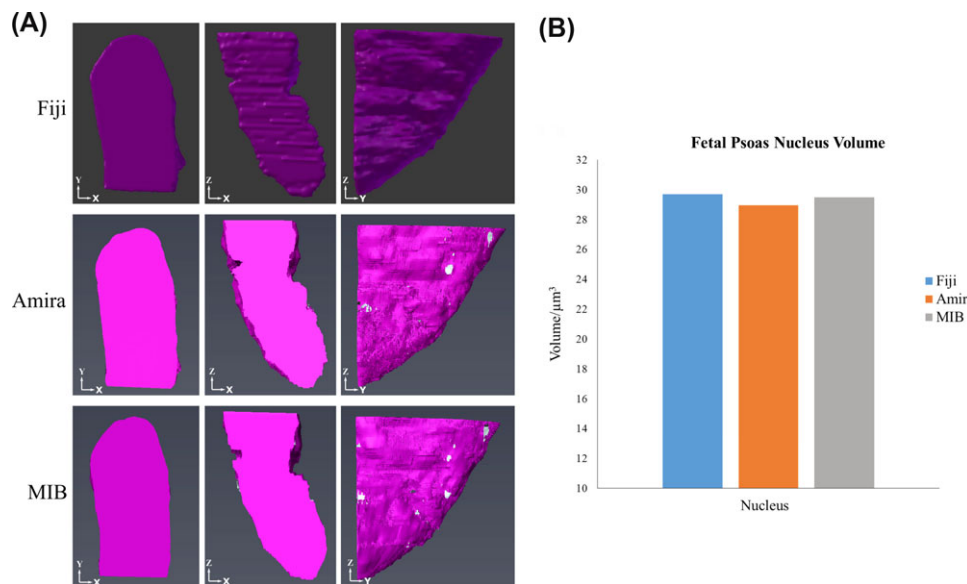


**Fig. 3.** Examples of digital reconstruction of nuclear volume. (A) Reconstructions of the nucleus from foetal psoas at different orientations from the segmentations performed in Fiji, Amira and MIB. The reconstructions of the nuclei show no differences between the different programmes. (B) Volume measurements of the nucleus from each of the programmes, which again are similar between each of the programmes used to reconstruct the nucleus.

- (4) Right click the .surf file and select 'Surface View', a render of the 3D model will appear in the viewing window.

## Results

Figure 2 illustrates a montage of serial-sectioned raw data SBF-SEM images from the psoas skeletal muscle (late foetus). Nine consecutive images are shown that are part of a larger dataset of 93 serial images. This dataset was used to illustrate the application of the different image analysis programmes and protocols. From the data, the nucleus, nucleolus, chromatin and mitochondria were all segmented and reconstructed using the tools detailed in the methods. Further information on which tool was specifically used for each structure is included in the following results and figures. The methods of segmentation can be further divided into manual, semiautomated and automated categories. Manual segmentation tools require the user to annotate the object, e.g. by colouring over every slice. Semiautomated tools use a combination of user input and programme predictions to highlight a structure. Automated segmentation requires no user input, although some machine learning is often involved; however, this method is not used in this analysis.

A timing analysis was also performed over 20 slices for each different method used to segment the nuclei and mitochondria (see Table 2). Interpolation was used to segment the nuclei in MIB and Amira, which was quicker than the manual segmentation performed in Fiji, with MIB being the fastest between all three programmes. The thresholding method in Amira was the quickest method to segment the mitochondria. Overall

the semiautomated tools, Amira specifically, segmented the structures fastest, when combining the nuclei and mitochondria timing analysis. Note that the speed of the semiautomated procedures will be dependent on computing ability.

### Segmentation of cellular structures

The nucleus of the cell was segmented first. This was done manually in Fiji and with the use of interpolation in Amira and MIB. Visually, the 3D models of the nuclei are similar and the volumes are also similar between each of the programmes (Fig. 3). Although using interpolation speeds up the segmentation process, errors did occur on the slices that were interpolated and correcting these added to the time taken to segment. Further analysis was performed to test the accuracy of the interpolation in MIB, comparing the uncorrected interpolated nucleus to a manually segmented one (Fig. 4). There was a differing level of detail between each of the models. Specifically, the folds of the nuclear membrane were not as detailed in the interpolated models as in the manually segmented one. However, the volumes of the nuclei from the quantification analysis were similar, with only 1.98% difference between the corrected and the every 10th slice (1.37% difference between the corrected and the every 5th slice). Therefore, for bulk quantification analysis, corrections may not be required. If, however, finer details are required for qualitative analysis, the interpolation errors will need to be corrected.

After the nucleus, the darker and dense chromatin within the nucleus was segmented. The segmentation and the final reconstruction can be seen in Figure 5(A). Thresholding was

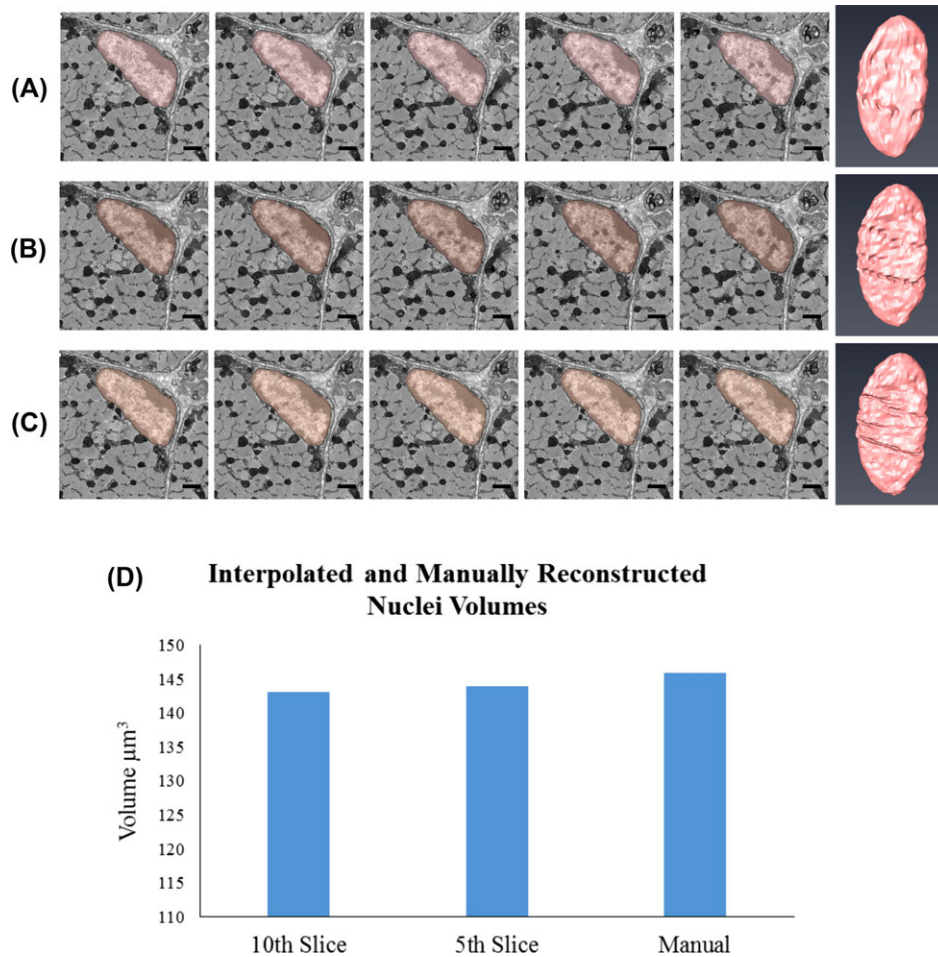


**Fig. 4.** Analysis of accuracy of interpolation method for segmentation. (A), (B) and (C) each show five images with the nucleus segmented and the final reconstruction of the nucleus, from late foetal psoas all performed in MIB. (A) Shows the nucleus segmented using interpolation when every 10th slice has been manually segmented, (B) from every fifth slice and (C) is a nucleus which has been segmented manual. In the images, there appear to be small differences between the segmentations, either the selection has not reached the boundary or goes over it. In the reconstructions, the nuclear folds are not as detailed in (A) and (B) when compared to the manual reconstruction in (C). (D) Volumes from each of the segmentations. The images are cropped from a total image size of  $3000 \times 3000$  pixels taken at  $2k\times$  magnification and  $13\text{ nm}$  resolution. All scale bars are  $1\text{ }\mu\text{m}$ .

used in MIB and Amira to select the darker pixels that correspond to the chromatin. During the thresholding of the chromatin in both Amira and MIB, there were some errors in the selection. In this case, the thresholding was not restricted to a specific structure, and the nuclear boundary was also selected. In order for the thresholding procedure to be effective, there also needs to be sufficient contrast within the images. Manual alterations can be made after thresholding to ensure that the correct selection is made although one has to be careful not to introduce user bias in object selection.

The next feature to be segmented was the nucleolus. The segmentation had to be performed in this order due to the nature of the segmentation in MIB and Amira. As mentioned earlier, in these two programmes, the pixels can only be assigned to a single structure. After the initial segmentation of the nucleus, all pixels were assigned to it. Then, when the chromatin is

segmented, the thresholded pixels were reassigned from the nucleus to the chromatin. However, when the chromatin was thresholded, the nucleolus was also selected, as the pixels are of a similar contrast. By segmenting the nucleolus after the chromatin, the pixels were reassigned to the nucleolus. This has to be kept in mind whenever segmenting a larger structure (nucleus) and the inner detail of it (chromatin and nucleoli) when using programmes such as Amira and MIB.

The segmented image and reconstruction of a nucleolus is shown in Figure 5(B). As seen in the raw images, the nucleoli appeared in a range of contrasts, with light and dark pixels. When thresholded, only the darker pixels were selected, which caused gaps in the model, whereas when it was manually segmented, the entire nucleolus area was segmented. This is one example of when thresholding can be used to show intricate internal structures of an object.



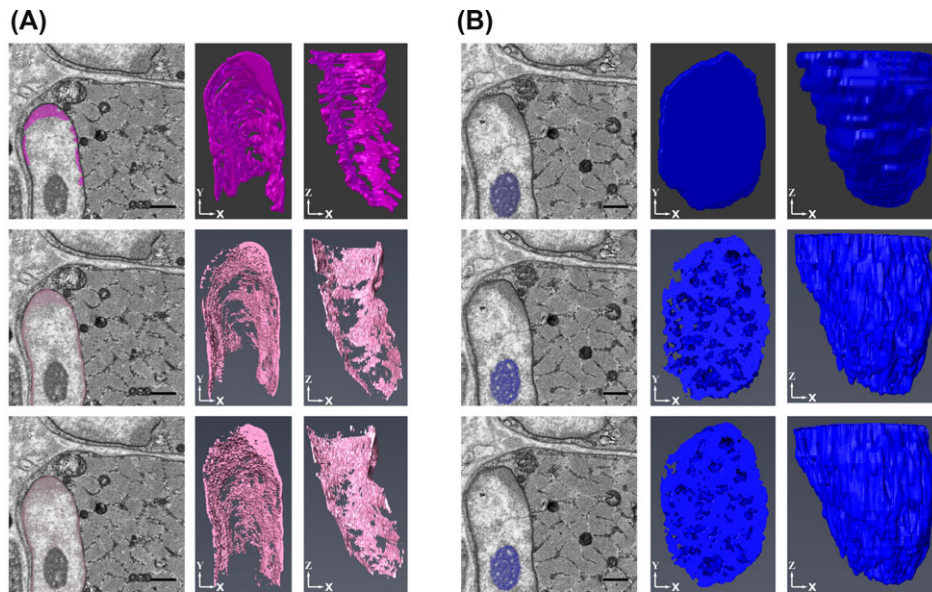


**Fig. 5.** Examples of reconstruction of chromatin and nucleoli. (A) Three single snapshots from the data series with the chromatin segmented and the reconstructions at different orientations performed in each of the image programmes, Fiji, Amira and MIB. (B) Three single snapshots from the data series with the nucleolus segmented and reconstructions of the nucleolus from the three programmes. The nucleoli reconstructed in Amira and MIB show more detail of the 'web-like' appearance of the nucleolus. All scale bars are 1  $\mu\text{m}$ .

Once the nuclei and associated structures were completed, the mitochondria were segmented. The decision was made not to interpolate the mitochondria due to their small size and complex nature, as highlighted in Figures 6(A) and 6(B). Instead, the mitochondria were thresholded in Amira and MIB. On comparing, the three models there were differences (Fig. 6C). Mitochondria consist of a range of contrasts and in the raw images, the detail of the cristae (appearing as dark inner membranes) can be seen. When thresholded, only the darker pixels, the outer membrane and cristae, were selected, which gave the thresholded models a broken appearance. However, the location and arrangement of the mitochondria could still be discerned and with further user input (e.g. using the fill feature), the appearance was improved. However, this is further evidence that the thresholding tool is case-dependent and often cannot be relied upon on its own but should be used in conjunction with other segmentation tools.

A second dataset was taken at a higher resolution, higher magnification and thinner section thickness, specifically to attempt to reconstruct the mitochondria with greater detail. Figure 7 presents the results from the reconstruction of these datasets, showing that it was possible for the cristae of the mitochondria to be reconstructed in detail. However, importantly, quantitative analysis of the thresholded mitochondria resulted in a smaller volume than the manually segmented mitochondria, due to only the darker pixels being segmented. Therefore, if quantification of mitochondrial volume is required, a manual method will have to be used to ensure that correct measurements are made.

The final reconstructions incorporating all segmented features of the skeletal muscle are shown in Figure 8. Although the general appearances of the models were similar in each of the programmes, there were some differences caused by the methods used to segment the structures of interest. For example, the mitochondria were more fragmented in the MIB and Amira models as they had been thresholded compared to the more dense structures seen with Fiji's manual segmentation. The devised workflow from these analyses is shown in Figure 9.

### Validation

The workflow was then implemented onto two other tissue types: guinea pig cardiac muscle and a region of the optic lobe from locust brain. This was done to test the workflow and validate that it was applicable to other tissues and structures.

The mitochondria in the cardiac muscle were dark and dense, with high contrast to surrounding features (Fig. 10A). It had a different appearance when compared to the mitochondria in the skeletal muscle, which, as shown already, exhibited varied contrasts. By following the workflow (3D Reconstruction > Yes > Quantification > Yes > Contrast > Simple > Threshold), it was determined that a form of thresholding, either b/w or the magic wand in MIB or Amira, could be used to segment the cardiac mitochondria. This was done and the segmentation and subsequent reconstructions are shown in Figures 10(B) and (C).

For the cardiac muscle nucleus, the same segmentation procedure was used as for the skeletal muscle. The



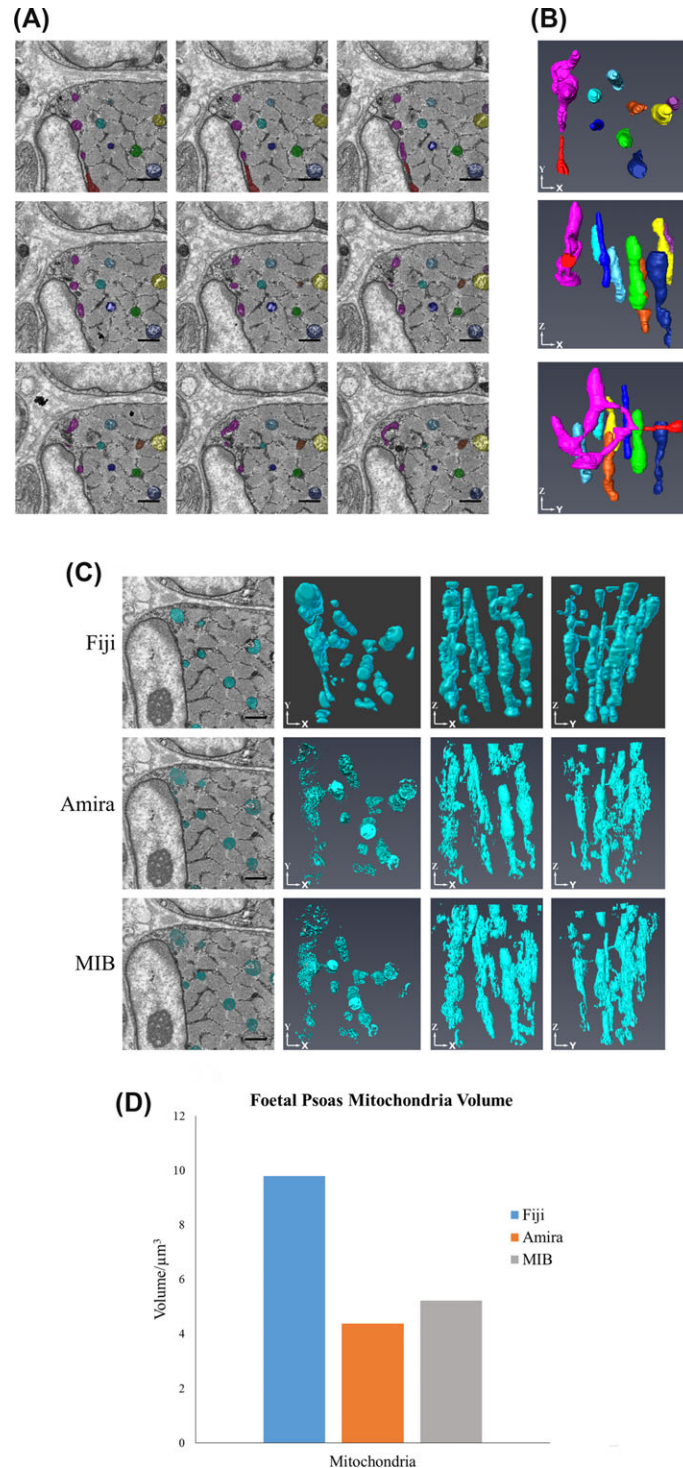


**Fig. 6.** Examples showing the complex morphology of mitochondria. (A) Nine consecutive images from the late foetal psoas (viewed from left to right). The mitochondria have been segmented individually in different colours, in MIB, and their corresponding 3D reconstructions, from Amira, can be seen in (B). Showing how mitochondria change over each 70 nm slice, requiring observation from the user to ensure that the correct structure is selected. All scale bars are 1  $\mu\text{m}$ . (C) Three single snapshots from the data series with the mitochondria segmented and the reconstructions of the mitochondria at different orientations. The mitochondria, reconstructed in Amira and MIB, appear broken due to the selection method used. (D) Volume measurements of the mitochondria, which show that there is a large difference between the Fiji segmentation and the Amira and MIB segmentations, due to the broken appearance seen in the reconstructions. The images were taken at 12k $\times$  magnification, 7 nm resolution and an image size of 1024  $\times$  1024 pixels. All scale bars are 1  $\mu\text{m}$ .

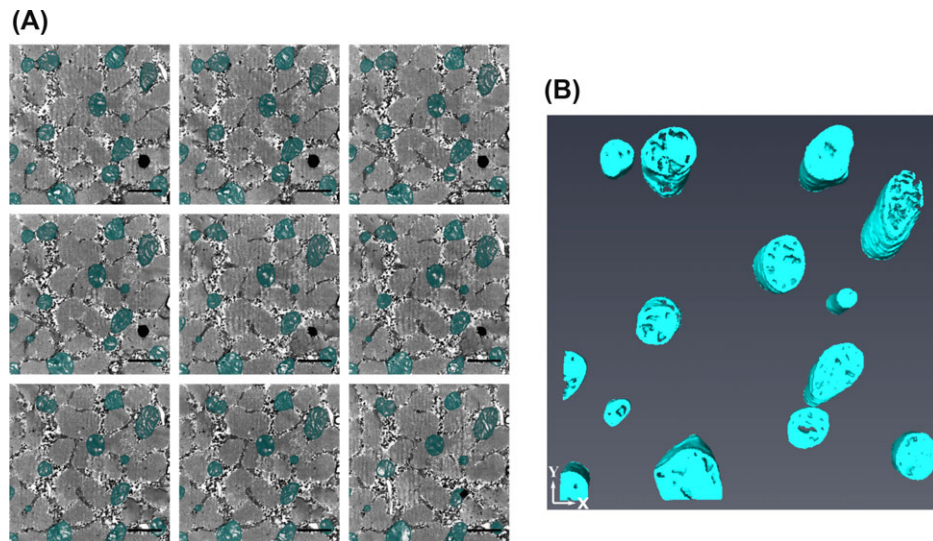


**Fig. 7.** Digital reconstruction of mitochondria from a dataset with thinner sectioning and higher magnification. (A) Nine consecutive images (viewed from left to right) from a larger dataset from the foetal psoas muscle. The images were taken at high magnification ( $18k\times$ ), high resolution (5 nm) and the block was sliced at 40 nm section thickness. (B) The subsequent reconstructions from a portion of the total stack to highlight the reconstruction of the cristae of the mitochondria using the thresholding tool in MIB and Amira to reconstruct the mitochondria. Scale bar is 1  $\mu\text{m}$ .

workflow was (3D Reconstruction>Yes>Quantification>Yes>Contrast>Varied>Size> Large>Distinct Border>Yes>Automated Method (Watershed Segmentation in MIB)). The dataset was composed of only 100 slices, image size  $1024 \times 1024$  pixels, and the nucleus was only present for a portion of the stack. As automated segmentation can be a time-consuming method due to computational demands, it is not efficient for small objects or datasets. Thus, the decision was made to use manual segmentation combined with interpolation. So, the nucleus was manually segmented over every fifth slice, interpolated in between and any errors manually corrected (Fig. 11).

A similar dilemma was found in the dataset from the locust optic lobe of the Lobula Giant Movement Detector 2 (LGMD2) neuron. This tissue was vastly different from the skeletal and cardiac muscle already shown, as it was densely packed with a variety of cells. The dataset analysed (100 slices at  $6000 \times 6000$  pixels) was also much larger than the muscle data. The aim, on this occasion, was rather different: to segment out an entire dendrite and the following workflow was followed 3D Reconstruction>Yes>Quantification>Yes>Contrast>Varied>Size> Large>Distinct Border>Yes>Automated Method (Watershed Segmentation in MIB). As mentioned earlier, this method takes time but there is a semiautomated version of the watershed segmentation combined with the brush tool in MIB, as described in the methods. Using this method, the dendrite was selected and selection was repeated every fifth slice and interpolation was used (Fig. 12). This tool could be used when analysing nuclei, however, it is best used on larger and more complex structures that would take time to manually segment, such as large dendrites like the LGMD2.

## Discussion

Serial block face SEM is a powerful tool for cellular examination and, when combined with image analysis software, can provide detailed qualitative and quantitative data. Since its release in 2004, the use SBF-SEM has steadily grown. In 2016, there were 39 articles published and so far in 2017, there have been 24 publications using this technique. The articles were found by searching 'serial block face scanning EM' in PubMed (<https://www.ncbi.nlm.nih.gov/pubmed/>) and only selecting those that use the technique for their research, not a review of the technique. With this burgeoning interest, there has been an increased demand for training in the analysis of data. This has drawn attention to the need for clarity and consistency in the reporting of methods of data analysis and interpretation, both qualitative and quantitative. However, getting started with the software is not easy for new researchers and there is a risk they will underutilize their data. Here, we have explained the terminology of many analytical features found in the programmes and provided step-by-step protocols to instruct users.

We have compared manual and semiautomated segmentation methods in order to help researchers choose the best options for their analysis. The results show that the semiautomated methods are less time-consuming but are not always accurate, as shown by the quantification results of the mitochondria segmentations. However, this segmentation was performed with the thresholding tools, which work best on structures of a single contrast that are distinct from their surroundings. Thresholding can be a useful way to highlight the finer details of structures, such as the cristae of the mitochondria, the web-like appearance of the nucleolus and the chromatin within the

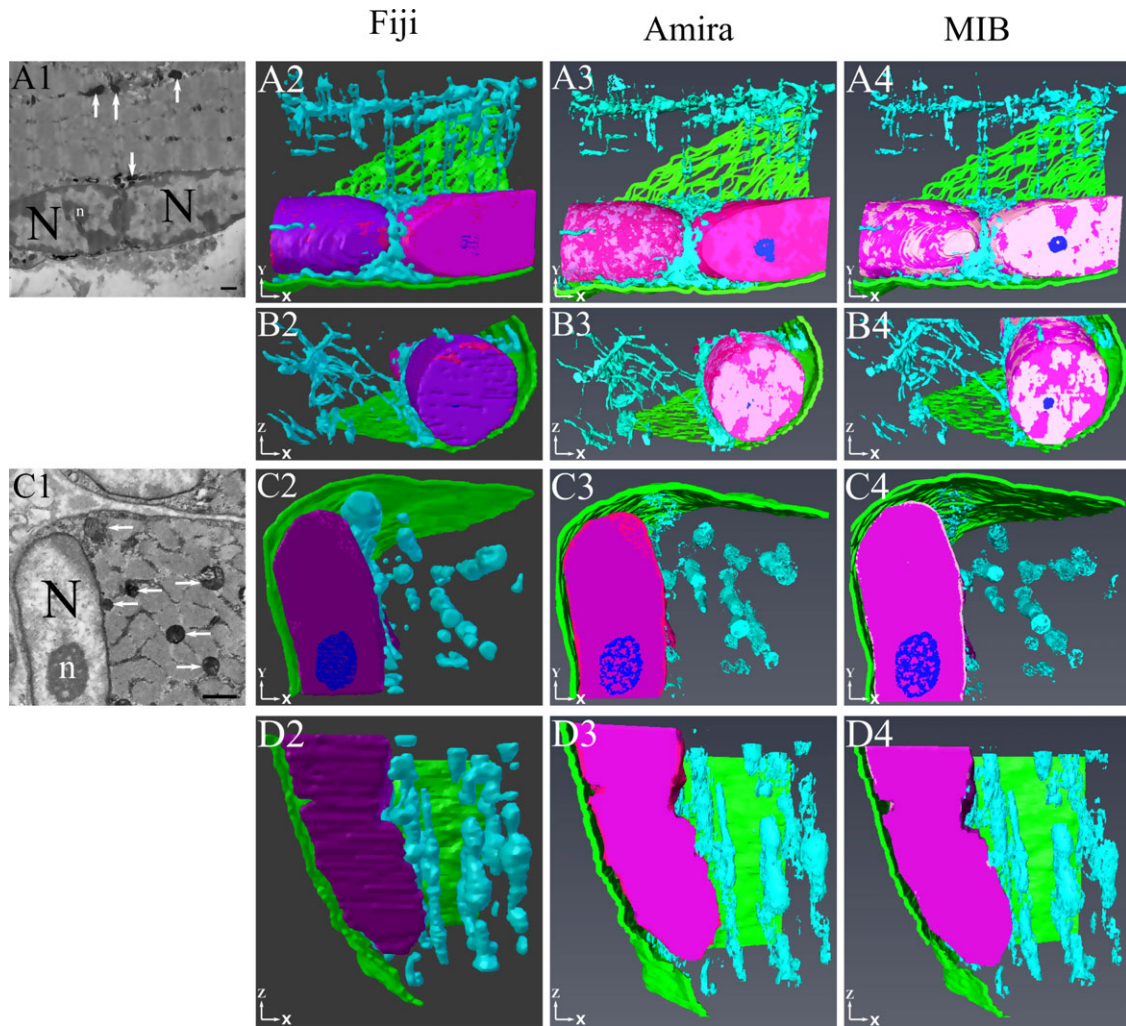


**Fig. 8.** Examples of 3D reconstructions of segmented structures. This diagram depicts examples of the assembled reconstructions of all segmented features from two separate skeletal muscle SBF-SEM datasets. Rows (A) and (B) show results from adult soleus muscle (from X serial sections; panel A1 indicates a snapshot SBF-SEM image). Rows C and D show results from foetal psoas muscle (from X serial sections; panel B1 indicates a snapshot SBF-SEM image). (C) and (D) The following features are colour-coded in the reconstructions: mitochondria, light blue; nuclei, dark pink/purple; chromatin, light pink; nucleoli, dark blue; plasmalemma, green. All scale bars are 1  $\mu\text{m}$ .

nucleus. In all cases, these semiautomated tools require some form of manual input and manual correction. A prime example of this is when using interpolation, which is best suited to larger structures that do not change much over each slice, like the nucleus of a cell, a whole cell or a large portion of the tissue. To optimize results, each object of interest should be assessed individually in terms of the segmentation method. The tools mentioned in this paper, whilst commonly used, are just some that are available. There are many other possibilities some of which have been briefly mentioned in this paper (e.g. creation of masks, smoothening, smart watershed and graph cut segmentation) for users more familiar with the programmes. Using a range of tools to efficiently and accurately segment, multiple structures in a sample will give better results than trying to use a 'one-method-fits-all' approach.

Although the results shown here are derived mostly from guinea pig skeletal muscle, the described approaches have been repeated on other types of tissue (guinea pig cardiac muscle and locust optic lobe), which validate the findings shown. From the results, a workflow was devised, Figure 9, to aid researchers new to image analysis. It provides recommendations for segmentation tools based on a variety of factors, such as the contrast and size of the structure, presence of any membrane boundaries, the size of the dataset and most importantly the objective of the analysis. The result can be qualitative, quantitative or both and knowing which is required prior to analysis is important. Knowing the objective is not only important for the image analysis but also prior to that, when the datasets are collected. For example, if low-resolution images are collected to reconstruct a whole cell, it is no good deciding after collection



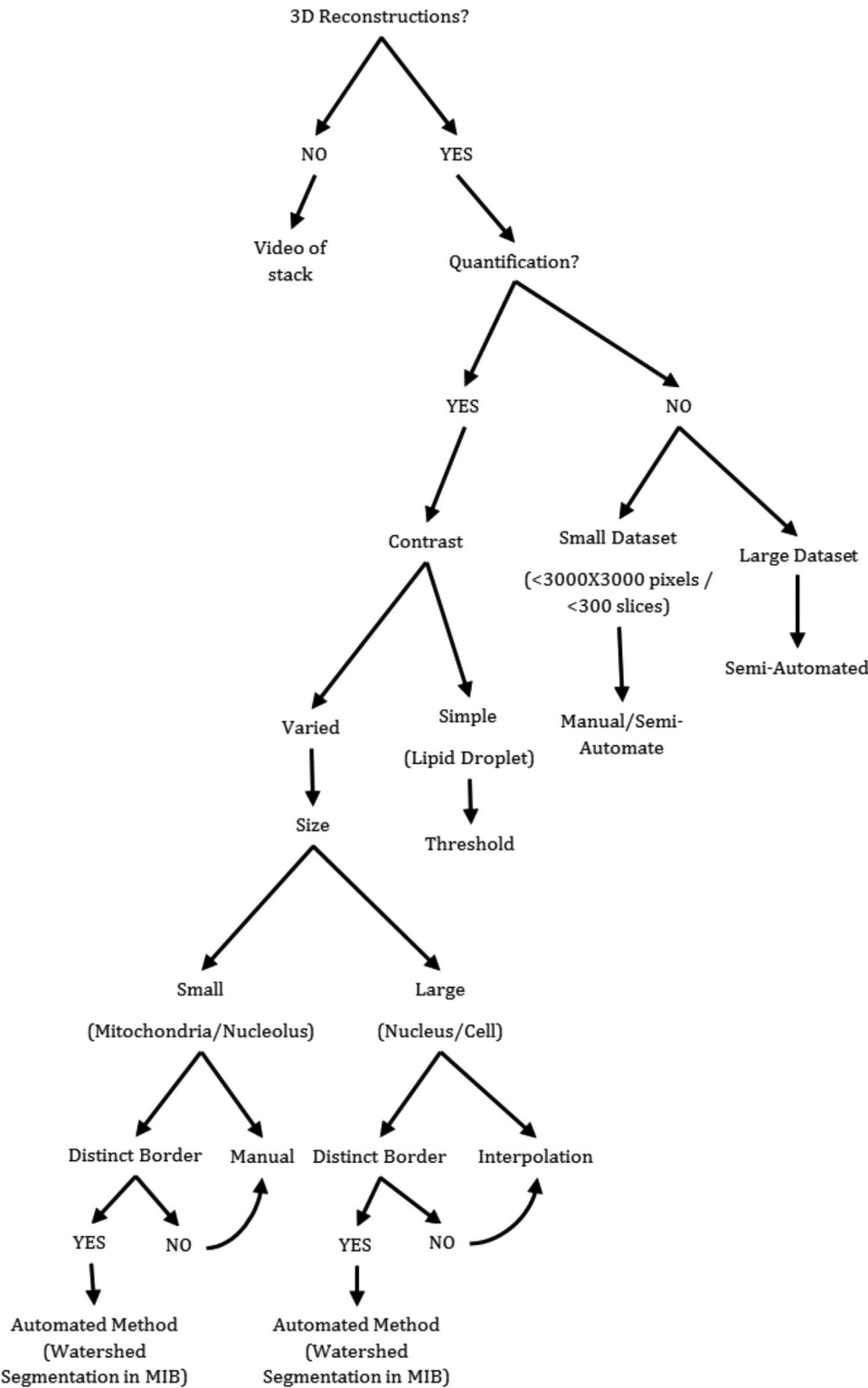
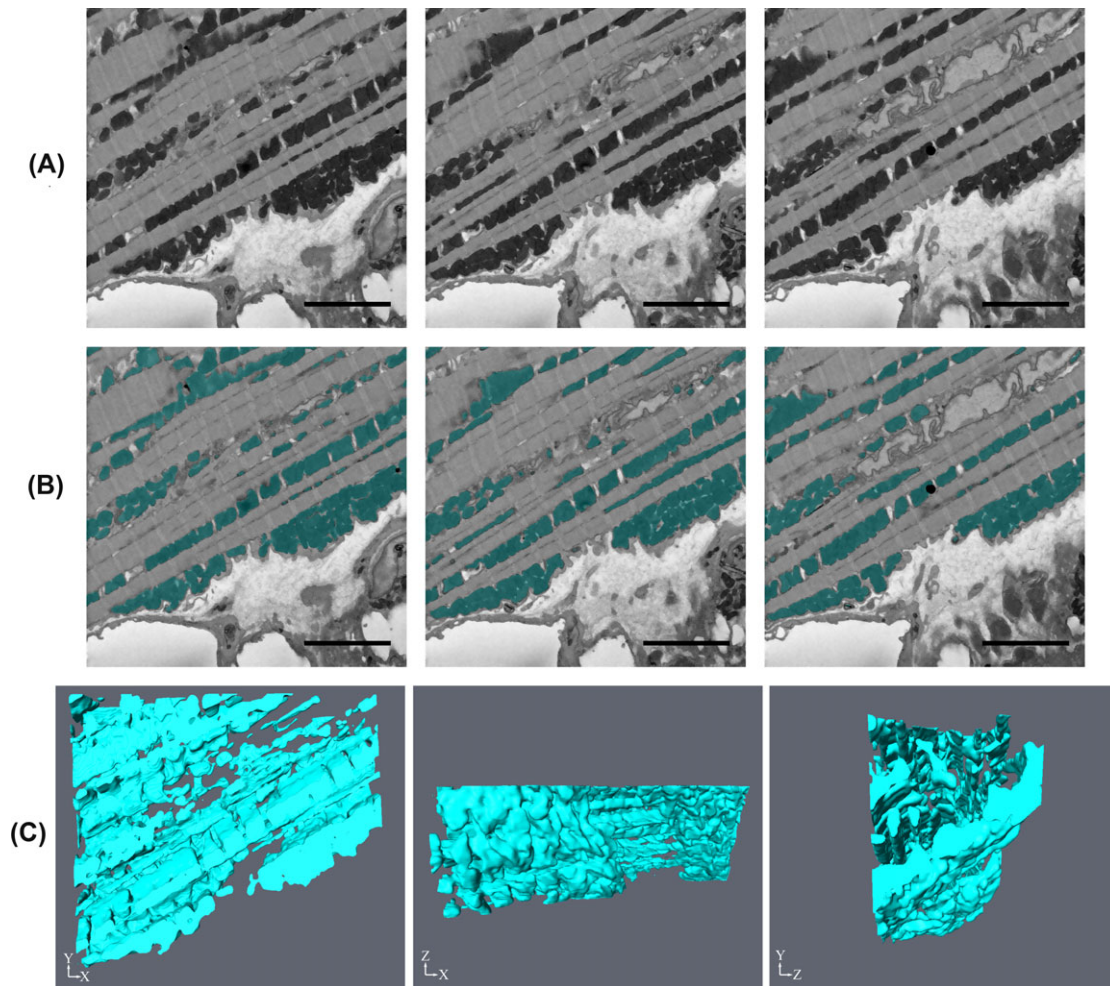


Fig. 9. Proposed workflow to aid in decision making when choosing appropriate segmentation methods for analysis of SBF-SEM data. The majority of these segmentation methods can be used in MIB and Amira, with some exceptions, the watershed segmentation which is not shown in this paper. The decision to use either MIB or Amira to perform the segmentations will depend on user preference and access to the software, as previously shown, the two programmes yield similar results.



**Fig. 10.** Segmentation and reconstruction of mitochondria from cardiac muscle. (A) Shows three raw images that are five slices apart from each other, (B) is the same raw images with the segmentation of the mitochondria shown and (C) is the subsequent reconstructions at different orientations. The images were taken at  $5k\times$  magnification, 18 nm resolution and an image size of  $1024 \times 1024$  pixels. Scale bars are  $1 \mu\text{m}$ .

that the organelles should also be reconstructed, as they may have insufficient clarity. The resolution of the image collection should be determined by the smallest structure likely to be of interest. However, although decisions on how to collect data in pursuit of biological questions are made at the time of SBF-SEM scanning, the outcomes are only revealed upon viewing the serially collected digital images. Indeed, this is one of the key benefits of SBF-SEM. Therefore, if tissue is plentiful, an iterative approach to SBF-SEM data collection and analysis can be beneficial in revealing much new biological information from complex cell/tissue structures.

Before the data collection starts, the settings of the SBF-SEM have to be adjusted to the needs of the researcher, for example, the accelerating voltage and pressure. The voltage and pressure are closely linked, if one is dropped, the other has to be dropped; otherwise, there is a loss of contrast to the image. We have found that at a lower kilovolts and lower pascals, the amount of charging by the electron beam is reduced and

imaging at settings as low as 2.5 kV and a pressure between 20 and 25 pa can yield excellent results. High vacuum can also be used to give high-resolution images; however, it is limited to dense tissues, as the electron beam affects the resin, the image 'jumps' and the datasets have to be aligned. However, these parameters can be tissue- and machine-dependent. It is likely that different versions of SBF-SEM systems can operate at high vacuum better than others and we recommend researchers test a combination of kilovolts and pascals to find one that suits their tissue and their objective.

By adjusting the data collection parameters – section thickness, magnification and number of pixels – the resulting images will have different resolution, thus altering the appearance of the final reconstructions. A thinner section thickness will result in a more detailed reconstruction, as smaller changes in structures will be imaged. A higher resolution results in a clearer image, so a better distinction between cellular structures and higher detail of the structures is achieved. The

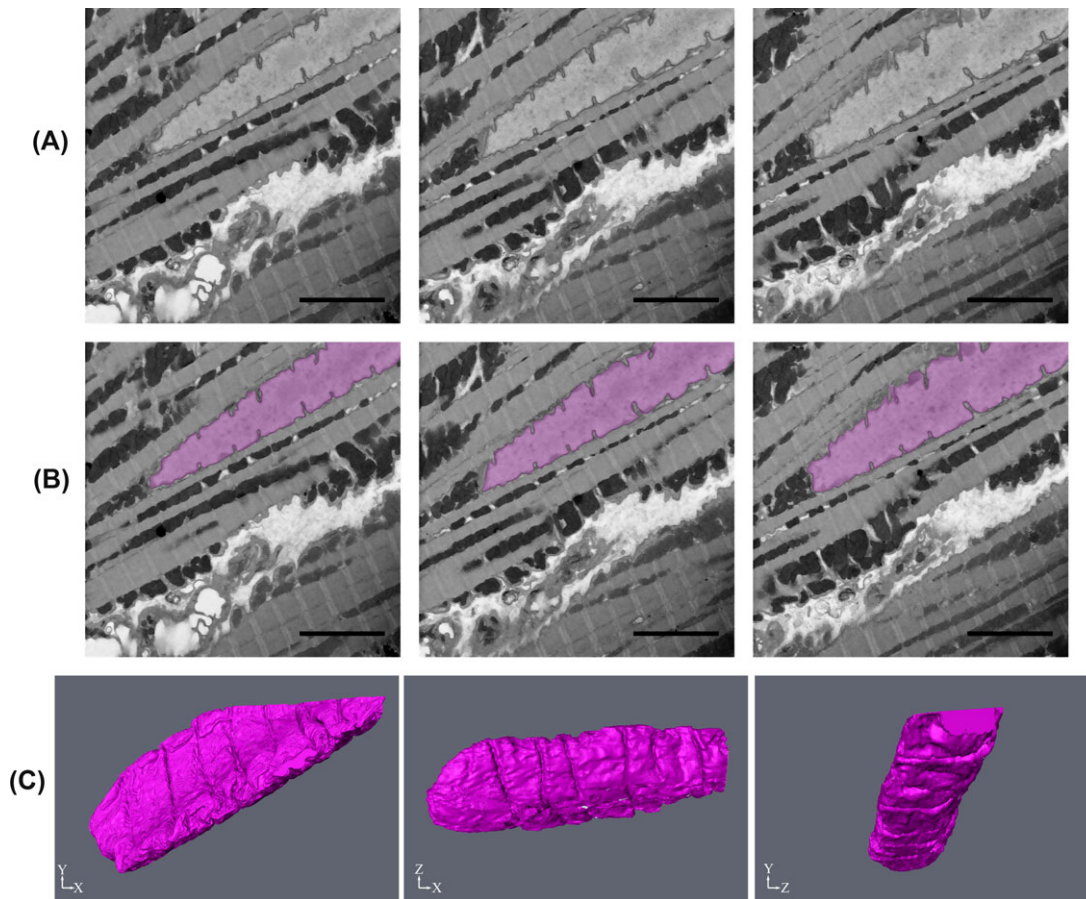


**Fig. 11.** Segmentation and reconstruction of nucleus from cardiac muscle. (A) Shows three raw images that are five slices apart from each other, (B) is the same raw images with the segmentation of the nucleus shown and (C) is the subsequent reconstructions at different orientations. The images were taken at  $5k\times$  magnification, 18 nm resolution and an image size of  $1024 \times 1024$  pixels. Scale bars are  $1 \mu\text{m}$ .

resolution, magnification and number of pixels are all linked. A higher magnification results in a higher resolution image but this decreases the field of view. To maintain the same field of view but still increase resolution, the number of pixels can be increased. However an increase in pixel number also increases the resulting image file size, which can be difficult to handle without a high-powered computer. For the majority of this analysis the datasets were  $<3000 \times 3000$  pixels and  $<300$  slices, so a laptop with 16 GB RAM and 2.4 GHz processing speed could cope. However for larger datasets (e.g.  $>3000 \times 3000$  pixels and  $>400$  slices) a more high powered computer, such as with 64 GB RAM and 3.2 GHz processing speed may be needed. In addition, if the time taken to collect an image is very high, the electron dose can have a detrimental effect on the resin and cause subsequent sectioning artefact. An alternative would be multiple regions of interest (ROIs) at a higher magnification but lower pixel number. However, ROIs that overlap might be affected by the increased exposure to the electron beam, as the areas are scanned repeatedly. Thus, some compromise may be required to balance

the need for high-resolution images but also images free from sectioning and imaging artefacts.

We have provided a workflow to recommend segmentation tools and also a detailed step-by-step protocol for four programmes, one of which is recently developed (MIB). The aim is to provide a resource for researchers to refer to when starting their analysis. Although there have been several publications using SBF-SEM, the detail about the segmentation methods is limited. We carried out a survey of the recent literature (Supplementary file S6) where SBF-SEM has been utilized and found that although all papers stated which programme they had used, only around half stated the specific tools utilized. Of these, the majority simply stated the type of segmentation and only a small number of the articles described the segmentation process in detail (Supplementary file S6). From the literature survey, it was also apparent that different terms were used to describe the segmentation tools, for example, manual segmentation was sometimes referred to 'by hand' and thresholding as 'intensity-based' (Meyer *et al.*, 2017) or 'contrast-based selection' (Pinali & Kitmitto, 2014). This could lead to confusion



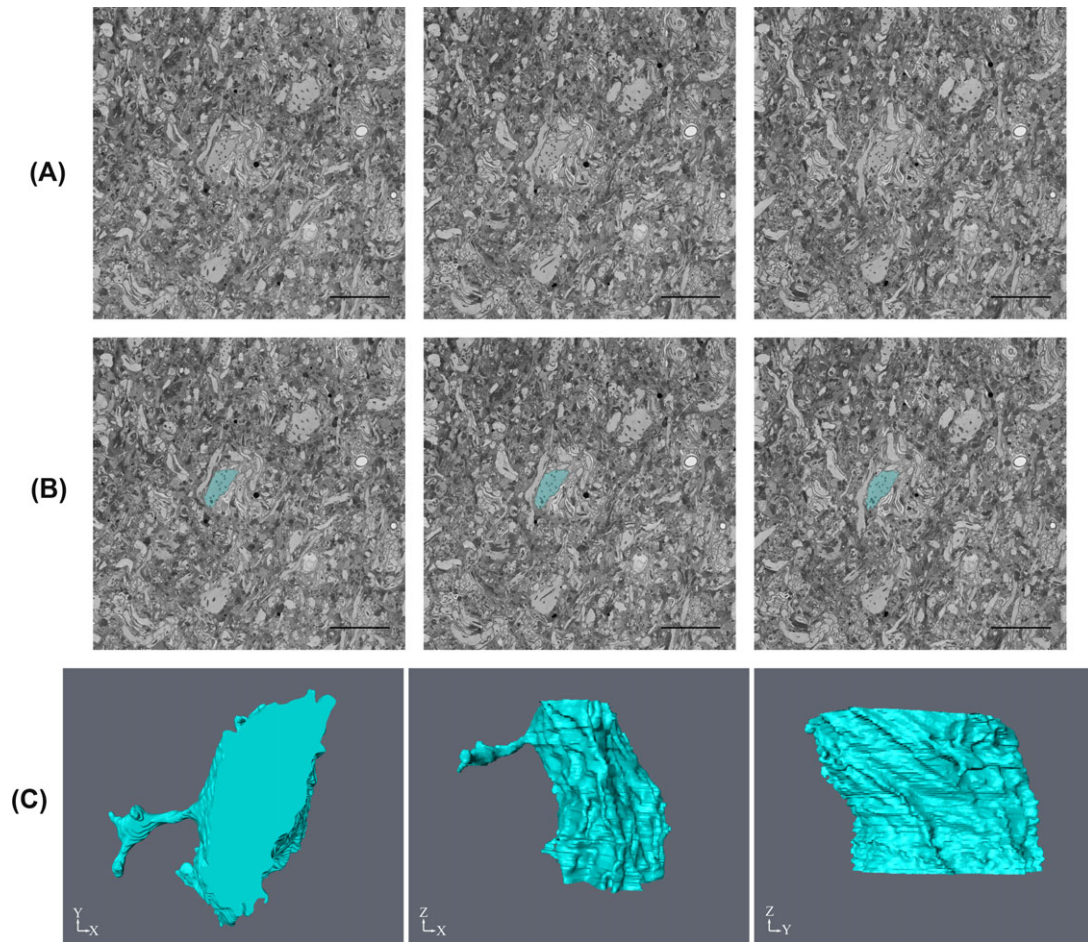


**Fig. 12.** Segmentation and reconstruction of the LGMD2 neuron from the optic lobe of the locust. (A) Shows three raw images that are five slices apart from each other, (B) is the same raw images with the segmentation of the LGMD2 shown and (C) is the subsequent reconstructions at different orientations. The images were taken at 1.5k $\times$  magnification, 9 nm resolution, section thickness of 60 nm and an image size of 6000  $\times$  6000 pixels. Scale bars are 5  $\mu$ m.

for those new to this type of analysis. An article by Borrett and Hughes (2016) reviewed earlier publications and they also noted that there was often a lack of information given in articles on the methods used to analyse data from SBF-SEM. From the analysis of the literature, manual segmentation appears to be the preferred method. However, this could be from a lack of knowledge or confidence rather than it being the most suitable method of segmentation. For a detailed analysis of the different software programmes and their functionalities, the reader is directed to Kittelmann *et al.* (2016).

In addition, we recognize that this is a fluid research environment where advances in computational analysis tools are rapid. Therefore, our provision of openly accessible raw datasets enables researchers who are developing novel/improved analysis approaches to compare the functionality of new tools with those used here. All researchers should be encouraged to deposit future SBF-SEM datasets at <https://www.ebi.ac.uk/pdbe/emdb/empiar/>, or similar open-access repositories. We have not only provided detailed step-by-step protocols but also videos to run alongside these

protocols. We have found that when teaching others to use new programmes, it is much easier for them to learn with textual and visual explanations available in tandem.

In conclusion, SBF-SEM is a powerful tool for analysing cellular structures with high resolution in  $x$ - $y$ - $z$  planes. However, current publications do not always give enough information on the data analyses involved and with the myriad of programmes and tools available, it can be a daunting task for new researchers to train themselves. By following a logical workflow such as that provided here, it is possible to obtain qualitative and quantitative data on multiple structures from a single dataset, maximizing output from valuable tissue.

### Acknowledgements

The Research was funded by BBSRC grant BB/M012093/1.

Raw data can be accessed from <http://www.ebi.ac.uk/pdbe/emdb/empiar/> with Accession code: EMPIAR-10092 and EMPIAR-10152.

## References

- Andersson-Cedergren, E. (1959) Ultrastructure of motor end plate and sarcoplasmic components of mouse skeletal muscle fiber as revealed by three-dimensional reconstructions from serial sections. *J. Ultrastruct. Res.* **2**, 5–191.
- Belevich, I., Joensuu, M., Kumar, D., Vihinen, H. & Jokitalo, E. (2016) Microscopy image browser: a platform for segmentation and analysis of multidimensional datasets. *PLoS Biol.* **14**, e1002340.
- Bock, D.D., Lee, W.-C.A., Kerlin, A.M. *et al.* (2011) Network anatomy and in vivo physiology of visual cortical neurons. *Nature* **471**, 177–182.
- Borrett, S. & Hughes, L. (2016) Reporting methods for processing and analysis of data from serial block face scanning electron microscopy. *J. Microsc.* **263**, 3–9.
- Cardona, A., Saalfeld, S., Schindelin, J. *et al.* (2012) TrakEM2 software for neural circuit reconstruction. *PLoS One* **7**, e38011.
- Denk, W. & Horstmann, H. (2004) Serial block-face scanning electron microscopy to reconstruct three-dimensional tissue nanostructure. *PLoS Biol.* **2**, e329.
- Jorstad, A., Nigro, B., Cali, C., Wawrzyniak, M., Fua, P. & Knott, G. (2015) NeuroMorph: a toolset for the morphometric analysis and visualization of 3D models derived from electron microscopy image stacks. *Neuroinformatics* **13**, 83–92.
- Kasthuri, N., Hayworth, K.J., Berger, D.R. *et al.* (2015) Saturated reconstruction of a volume of Neocortex. *Cell* **162**, 648–661.
- Kittlmann, M., Hawes, C. & Hughes, L. (2016) Serial block face scanning electron microscopy and the reconstruction of plant cell membrane systems. *J. Microsc.* **263**, 200–211.
- Kristen, M.H. & Stevens, K. (1988) Study of dendritic spines by serial electron microscopy and three-dimensional reconstructions. In: *Intrinsic Determinants of Neuronal Form and Function* (ed. by R.J. Lasek, & M.M. Black), pp. 179–199. Liss, Cleveland, Ohio.
- Kuzirian, A.M. & Leighton, S.B. (1983) Oxygen plasma etching of entire block faces improves the resolution and usefulness of serial scanning electron microscopy images. *Scan. Electron. Microsc.* **4**, 1877–1885.
- Lee, W.A., Bonin, V., Reed, M., Graham, B.J., Hood, G., Glattfelder, K. & Reid, R.C. (2016) Anatomy and function of an excitatory network in the visual cortex. *Nature* **532**, 370–374.
- Meyer, K., Ostrenko, O., Bourantas, G. *et al.* (2017) A predictive 3D multi-scale model of biliary fluid dynamics in the liver lobule. *Cell Syst.* <https://doi.org/10.1016/j.cels.2017.02.008>. [Epub ahead of print].
- Peddie, C.J. & Collinson, L.M. (2014) Exploring the third dimension: volume electron microscopy comes of age. *Micron* **61**, 9–19.
- Pinali, C. & Kitmitto, A. (2014) Serial block face scanning electron microscopy for the study of cardiac muscle ultrastructure at nanoscale resolutions. *J. Mol. Cell Cardiol.* **76**, 1–11.
- Takemura, S.Y. (2015) Connectome of the fly visual circuitry. *Microscopy (Oxf)* **64**, 37–44.
- Titze, B. & Genoud, C. (2016) Volume scanning electron microscopy for imaging biological ultrastructure. *Biol. Cell* **108**, 307–323.
- Tsai, W.T., Hassan, A., Sarkar, P., Correa, J., Metlagel, Z., Jorgens, D.M. & Auer, M. (2014) From voxels to knowledge: a practical guide to the segmentation of complex electron microscopy 3D-data. *J. Vis. Exp.* e51673.
- Wernitznig, S., Mariella, S., Urschler, M., Zankel, A., Pöhl, P., Rind, F.C. & Leitinger, G. (2016) Optimizing the 3D-reconstruction technique for serial block-face scanning electron microscopy. *J. Comp. Neurol.* **523**, 298–312.
- Wilke, S.A., Antonios, J.K., Bushong, E.A. *et al.* (2013) Deconstructing complexity: serial block-face electron microscopic analysis of the hippocampal mossy fiber synapse. *J. Neurosci.* **33**, 507–522.

## Supporting Information

Additional Supporting information may be found in the online version of this article at the publisher's website:

- S1. Image Processing Fiji.** Converting from DM3 to Tiff.  
**S2. Fiji/TrakEM2.** Image analysis in Fiji and TrakEM2.  
**S3. Blender.** How to use Blender to show reconstructions.  
**S4. Microscopy Image Browser (MIB).** Image analysis in MIB.  
**S5. Amira.** Image analysis in Amira.  
**S6. Analysis Tools for SBF-SEM Datasets in Recent Literature.** Articles published between 2015 and 2017 including SBF-SEM experimentation were assessed for the detail they provided on the segmentation process used, including any software programmes and specific tools.